Electron Beam Deposited Nanotools for Nanomanipulation and Biological Applications

Beard, James

Award date:
2011

Awarding institution:
University of Bath

Electron Beam Deposited Nanotools for Nanomanipulation and Biological Applications

submitted by

James David Beard

for the degree of Doctor of Philosophy

of the

University of Bath

Department of Physics

March 2011

Abstract

This thesis describes the fabrication of a variety of "nanotool" structures which are fabricated on Atomic Force Microscope (AFM) probe tips. The structures are fabricated on standard AFM probes using a method of electron beam induced deposition (EBID), forming an amorphous carbon structure on the probe tip. Experiments are described which demonstrate the successful application of these probes for a variety of different manipulation applications, focussing on the nanomanipulation of biological cells.

A variety of tools are described, including "nanoscalpel" probes able to cut and section biological materials on very small scales, "nanoneedles" which function as high aspect ratio AFM probes or as probes of intracellular structures, "nanotweezers" and a "nanotome" which can be used to remove thin layers of material from a biological sample.

A variety of techniques to fabricate complex nanotool structures and to strengthen the structures against large applied forces are described. Using these tools, the investigation of a variety of cell types including smooth muscle cells, megakaryocytes and corneocytes has been performed. Results are presented showing the "nanodissection" of these cells to expose their internal structures for *in situ* AFM imaging, and the detection of the mechanical properties of intracellular structures by indentation using nanoneedle probes. Extraction of samples from the outer cornified envelope of corneocyte cells using a nanoneedle probe is also demonstrated.

The mechanical properties of the amorphous carbon making up these nanotools are also characterised using AFM manipulation, and their elastic bending modulus determined using models based on the Euler-Bernoulli beam bending equation. The structures are shown to be highly flexible, with thin nanoneedle structures able to buckle elastically under large tip-sample forces in a manner similar to the high aspect ratio carbon nanotubes which are currently used as AFM probes.

Contents

1 Introduction **8**

2 Background **12**

2.1 Scanning Probe Microscopy 12

2.2 Electron Beam Induced Deposition 14

2.2.1 Discovery 14

2.2.2 Interaction of the Electron Beam and Sample 16

2.2.3 Deposition 16

2.2.4 Replenishment of Precursor Supply 18

2.2.5 Other Similar Techniques 19

2.2.6 Applications 19

2.2.7 Modification of AFM Probes 21

2.3 Indentation 22

2.3.1 Development of Indentation Models 22

2.3.2 Indentation of Biomaterials 25

2.4 Nanomanipulation of Cells 26

2.5 Descriptions of Biological Cells 30

2.5.1 Smooth Muscle Cells 30

2.5.2 Megakaryocytes 30

2.5.3 The Stratum Corneum 31

3 Methodology **33**

3.1 Atomic Force Microscopy 33

3.2 Scanning Electron Microscopy 33

3.3 Electron Beam Induced Deposition 34

3.3.1 Freestanding structures 34

3.3.2 Stabilisation . . . 34
3.4 Cantilever calibration . . . 34
3.5 Indentation . . . 37
3.5.1 Calibration . . . 37
3.5.2 Determination of sample deformation . . . 38
3.5.3 Decontamination of AFM Probes . . . 41
3.6 Manipulation with AFM . . . 41
3.6.1 Incisions . . . 42
3.6.2 Surface removal . . . 42

4 Fabrication of Nanotools by Electron Beam Induced Deposition 44
4.1 Fabrication Process . . . 45
4.2 Nanoscalpel . . . 45
4.3 Carbon Blade Dimensions . . . 49
4.4 Effect of Primary Beam Current . . . 51
4.5 Structure of a Carbon Blade . . . 52
4.6 Observation of cut off in extended structures . . . 55
4.7 Nanoneedles . . . 58
4.8 Other nanotool designs . . . 60
4.9 Summary and Conclusions . . . 64

5 Nanoneedles 66
5.1 Growth of Nanoneedles . . . 67
5.2 Nanoneedle Probes for AFM Imaging . . . 69
5.3 Growth of Needles with Small Tip Radii . . . 70
5.4 Effect of Exposure after Growth . . . 72
5.5 Buckling Effects in Nanoneedle Probes . . . 78
5.6 Buckling Mechanics . . . 80
5.7 Biological Applications of Nanoneedles . . . 83
5.8 Combining Needles with Other Nanotools . . . 83
5.9 Conclusions . . . 85

6 Characterisation of Nanotools 89
6.1 Elastic Modulus of EBID Nanostructures . . . 90
6.2 Modelling the Bending of a Cantilever Beam . . . 93

6.3 Experimental Results 98
6.4 Shape of Deflected Blades 100
6.5 Discussion of Results 100
6.6 Other Applications 103
6.7 Conclusions 103

7 Nanoindentation **105**
7.1 Procedure 107
7.2 Force Curves 107
7.3 Depth of Penetration 110
7.4 Elastic Moduli at Surface 112
7.4.1 Effect of Indenter Diameter 116
7.5 Multiple Indents 117
7.6 Elastic Moduli of Internal Structure 120
7.6.1 Derivation of Model 120
7.6.2 Results from Analysis Incorporating Viscoelasticity 123
7.7 Double Indentation 127
7.8 Discussion of Mechanical Tomography of Corneocytes 129
7.9 Effect on Corneocyte 131
7.10 Changes in Elastic Modulus of SLS-Treated Corneocytes 134
7.10.1 Discussion of Results from SLS Treated Skin 137
7.11 Conclusions and Summary of Results 138

8 Manipulation of Biological Structures **143**
8.1 Incisions 144
8.1.1 Force feedback 147
8.1.2 Depth of Incisions 148
8.2 Surface Removal 150
8.2.1 Nanotome 154
8.3 Manipulation with Nanoneedles 157
8.4 Conclusions 161

9 Conclusions **163**
9.1 Summary of Results and Conclusions 163
9.2 Concluding Remarks 167

9.3 Publications 167

A Biological Protocols **169**

A.1 Isolation of Smooth Muscle Cells 169

A.1.1 Cell Culture 169

A.1.2 Fixation for AFM Imaging 170

A.2 Preparation of Megakaryocyte Samples 170

A.2.1 Preparation of Substrates 170

A.2.2 Megakaryocyte Preparation 172

A.3 Isolation of Corneocytes 172

B Program for Integration of Beam Bending Equations **175**

Acknowledgements

I would like to thank the following people and organisations for their help, teaching and support during the work described in this thesis.

From the Department of Physics, University of Bath:
Dr SN Gordeev
Dr AV Moskalenko
Dr DJ Burbridge
Mr O Dudko

From the Department of Chemistry, University of Bath:
Dr F Marken
Dr S Dale

From the Department of Pharmacy and Pharmacology, University of Bath:
Prof RH Guy
Dr A Mackenzie
Dr SV Smirnov
Dr MB Delgado-Charro
Dr C Hobbs
Mrs P Iarova
Miss SF Cordery
Mrs Q Yang

Engineering and Physical Sciences Research Council (EPSRC)

List of Abbreviations

The following table lists abbreviations used in this thesis.

AFM	Atomic Force Microscope
BSA	Bovine Serum Albumin
CNT	Carbon Nanotube
EBID	Electron Beam Induced Deposition
EBIE	Electron Beam Induced Etching
EBL	Electron Beam Lithography
ESEM	Environmental Scanning Electron Microscope
GUI	Graphical User Interface
IPA	Isopropyl Alcohol
HOPG	Highly Ordered Pyrolytic Graphite
IBID	Ion Beam Induced Deposition
IBIE	Ion Beam Induced Etching
MFM	Magnetic Force Microscopy
PFM	Photonic Force Microscope
OT	Optical Tweezers
SEM	Scanning Electron Microscope
SLS	Sodium Lauryl Sulphate
NEMS	Nanoelectromechanical Systems
SMC	Smooth Muscle Cell
SPM	Scanning Probe Microscopy
STEM	Scanning Transmission Electron Microscope
STM	Scanning Tunneling Microscope
TEWL	Trans-Epidermal Water Loss
TCE	Trichloroethylene
TEOS	Tetra-ethyl-ortho-silicate
TREC	Topography and Recognition Imaging

Chapter 1

Introduction

In recent years there has been great interest in the manipulation of biological cells at a nanoscale level. Advances in many techniques, particularly those developed for nanofabrication and investigation of artificial structures and materials, have expanded this capacity. It is now possible to manipulate single cells, individual organelles, and even single membrane proteins, leading to many new insights into the structure and function of cells and other biological structures.

Of the many different techniques available to biologists, the Atomic Force Microscope (AFM) offers the highest precision in both imaging and manipulation. AFM is a scanning probe technique which can both image and manipulate biological samples under a wide range of conditions, including in liquids at physiological temperatures, with a resolution of a few nanometres. AFM has been widely applied for manipulation and nanoscale dissection of cells and biological structures. In particular, AFM has been applied for measurement of elastic modulus and other mechanical properties of cells and tissues by indentation. These properties are of interest as they reflect the internal cellular organisation, in particular its cytoskeleton. Reorganisation and disruption of the internal cell structure, and the associated changes in mechanical properties, are known to be a symptom of disease states such as malaria, sick cell anaemia and cancer; therefore the cell mechanical properties can serve both as a diagnostic marker and a means to investigate the pathology of these diseases.

However, the shape of standard AFM probes is typically not ideal for high-precision manipulation; in particular the low aspect ratio of the tip prevents it penetrating deep into cells without inflicting damage to the cell over a large area.

This prevents, for example, mapping of mechanical properties of intracellular structures with high resolution; this would be desireable as the cell internal organisation is hierarchical, comprising many structures of a range of sizes from the microscopic to the nanoscale. Several groups have investigated approaches to improve the aspect ratio of AFM probes, modifying them to create needle-like structures which can penetrate deep into cells without significant damage to the cell, allowing it to remain viable and unperturbed.

This thesis discusses experiments to modify AFM probes for a variety of applications to the manipulation of biological structures. The probes are modified by fabrication of specialised structures on the tip apex using a method of electron beam induced deposition (EBID). These structures are composed of amorphous carbon whose source is the adventitious hydrocarbon molecules present as adsorbed contamination in the electron microscope system used for the nanofabrication. Decomposition of these hydrocarbons using an electron beam allows the deposition of solid material to form a three-dimensional structure on the probe tip. A variety of applications of these probes are discussed and demonstrated on different cell types, especially corneocyte cells from the outer layer of skin (the stratum corneum).

EBID has great versatility in the variety of probe shapes that can be created. Described in this thesis are the fabrication of probes incorporating high-aspect ratio "nanoneedles", blade-like "nanoscalpels", "nanotweezers" and a "nanotome" capable of separating thin layers of material from the surface of a biological structure. The nanoscalpel probes can be used to cut and section biological structures with nanometre precision, and the nanoneedles can penetrate cells to large depths without significant loss of lateral precision.

It is proposed that indentation using nanoneedle probes could allow the measurement and mapping of mechanical properties with high lateral precision over a range of depths below the cell surface, described as "mechanical tomography". The nanoneedles could also be used to target specific intracellular structures (especially if AFM measurements were combined with optical imaging techniques) such as organelles or cytoskeletal structures and measure their mechanical properties *in situ*.

Other nanotools such as a the nanoscalpel and nanotome can be used for the "nanodissection" of biological structures, removing their outer layers to expose

their intracellular structure for imaging using AFM techniques. Experiments showing these applications are also described in this thesis, and some possible techniques for nanodissection have been developed and discussed.

Chapter 2 discusses the background knowledge important to the work described in this thesis. The principles of AFM imaging, and the process of electron beam induced deposition (including its discovery, mechanism, and applications) are described. Relevant models used for analysis of indentation data are also described. A brief description of the structure and function of the cell types used for the experiments in this thesis is also included. Chapter 3 then describes the experimental and analytical techniques used for AFM imaging, indentation and manipulation and EBID nanofabrication.

Chapter 4 describes in more detail the methods used to fabricated AFM "nanotool" probes using a method of electron beam induced deposition. Experiments investigating the effects of the deposition rate and primary electron beam current on the dimensions of the resulting structures are described. The fabrication of a variety of different "nanotool" structures is described in detail.

Chapter 5 is devoted to the nanoneedle structures fabricated on AFM probes as tools for imaging, manipulation and nanoindentation. Thin nanoneedles are shown to undergo elastic buckling above a critical tip-sample force, which is an advantage as it limits the tip-sample force and therefore prevents damage to the AFM probe and sample. The dynamics of this buckling are compared to a model based on the buckling of homogeneous columns obeying the Euler-Bernoulli beam equations and shown to be in good agreement. Techniques for the stabilisation of the nanoneedles against buckling so that they can exert larger forces on a sample are described, and the applications of these nanoneedle probes for studies of biological cells are discussed.

Chapter 6 describes the experiments carried out to measure the elastic modulus of nanoscale cantilevers fabricated using EBID. A numerical method is used to model the nonlinear bending behaviour of the cantilevers at large deflections. The structures are shown to be highly flexible; their application as nanoscale springs, nanoelectromechanical system (NEMS) components or cantilever-based sensing devices is proposed.

Chapter 7 describes experiments using nanoneedle probes as indentation tools. Indentation experiments suggest that they can be used to measure the mechanical

properties of corneocyte cells, and are sensitive to the mechanical properties of structures beneath the surface as well as to the viscoelastic effects which occur during deformation of these cells. This suggests that they can be used as probes to investigate the intracellular structure and mechanical properties of biological cells.

Chapter 8 describes other experiments performed using modified AFM probes for the manipulation of biological cells, or "nanosurgery". These experiments suggest that AFM manipulation can be used for many purposes to investigate the cell structure, including the removal of material from the outer layers of a cell. This allows the extraction of samples from a cell, and the imaging by AFM of intracellular structures beneath the surface layer of cells.

Chapter 9 summarises the work described in this thesis and the most important conclusions drawn from the experiments carried out. It also discusses some possible future work which would further extend the experiments carried out and support the conclusions drawn.

The work in this thesis presents also several novel probe designs such the nanotome probe, together with applications of these modified AFM probes. Furthermore, while high-aspect ratio nanoneedle probes have been applied by several groups for microinjection of biomolecules into cells, they have not previously been used for the measurement of mechanical properties of cell structures. The elastic buckling of these structures has also not been previously described or systematically studied. In addition, the methods of characterisation of the mechanical properties of the deposited carbon have not been applied to EBID structures before, and the observed flexibility of EBID structures has not previously been reported (although it has been observed in structures deposited using focussed ion beams).

These new designs and applications of specialised AFM probes could find application in many areas of cell biology. The thesis also proposes other novel applications for the elastic nanostructures such as nanocantilever sensing devices and components for NEMS systems.

Chapter 2

Background

2.1 Scanning Probe Microscopy

Scanning probe microscopy (SPM) refers to a set of techniques distinct from electron and optical microscopy. An SPM system typically consists of a microfabricated probe which is scanned across the surface of a sample using a piezoelectric positioning system, sensing interactions between the probe and sample. In 1981, while working for IBM, Gerd Binnig and Heinrich Rohrer developed the scanning tunneling microscope (STM), which is regarded as the first SPM device. The STM operates using a fine conducting probe able to measure tunneling currents between the probe and a conductive sample. This instrument was the first to achieve atomic resolution imaging, and as a result Binnig and Rohrer were awarded the Nobel Prize in 1986, which they shared with Ernst Ruska for his work in the invention of the electron microscope. [1]

From its earliest days, artifacts arose in STM imaging resulting from other interactions between the probe and sample. Observation of these effects led to the development of the Atomic Force Microscope (AFM) in 1986. [2, 3] Instead of a conducting tip, the AFM uses a microfabricated cantilever which acts as a force sensor. Attached to the cantilever is a sharp tip which is placed close to the sample surface. Forces acting between tip and sample cause displacement of the cantilever end leading to a deflection of the cantilever.

A variety of different techniques can be used to detect the deflection; the earliest AFM used an STM tip mounted above the cantilever. Other techniques which have been used include detection of piezoelectric and piezoresistive effects

in the cantilever itself and changes in capacitance between the cantilever and a separate electrode. However, the deflection of the cantilever is most often detected using optical methods, via a laser beam reflected from the back of the AFM cantilever (the back of which is sometimes coated with a thin aluminium or gold layer to increase its reflectivity). The deflection can then be measured using interferometric techniques, or using a split photodiode which detects small displacements of the laser spot. [3]

AFM systems can operate in a number of different modes for different imaging applications. In static or contact mode AFM, the cantilever deflects under the action of tip-sample forces. For small deflections, the deflection is proportionate to this force. The probe tip is scanned over the sample surface using a piezoelectric scanner; as it is scanned in the x and y directions, an electronic feedback loop controls its z-position to keep the deflection fixed at a certain value (the "setpoint" value). This allows the tip to trace an accurate profile of the surface of a rigid sample.

AFM systems can also operate in dynamic mode, in which the cantilever is oscillated using an external driving force at a frequency close to its resonance. [4] In this mode, tip-sample force gradients act to create shifts in the cantilever amplitude, phase or oscillation frequency; these are then used as the controlled setpoint for AFM profiling. The advantage of this technique compared to static mode AFM is that the tip-sample forces are much smaller, and lateral friction between tip and sample is almost eliminated, allowing the imaging of delicate samples which would otherwise be damaged by the AFM probe. This mode is often used for the imaging of biological cells and other delicate structures. In this mode, the AFM can operate in non-contact mode (sensing Van der Waals interactions without surface contact) or intermittent contact mode (also called Tapping Mode) where the tip apex touches the surface during each cycle of oscillation.

AFM demonstrates significant advantages over other microscopy techniques, including other SPM techniques such as Scanning Tunneling Microscopy. The attainable resolution is determined by the probe tip size, typically a few nanometres, and so is comparable to that attainable using electron microscopy techniques. Since it is the tip-sample force and not the tunneling current which is measured, surface profiling can be performed on insulating, semiconducting and conducting substrates, unlike STM which is limited by the electron transport properties of

the samples.

Using dynamic mode imaging, soft samples such as biological materials can be imaged without damage. [5] The ability to image in liquid even allows the imaging of living cells, which would not survive imaging techniques requiring high vacuum (such as electron microscopy). [6–9] By capturing successive AFM images, dynamic processes such as the extension of cytoplasmic processes (lamellipodia and filopodia) from the cell can be observed. [5, 10] By using appropriately designed or modified tips, AFM systems can also detect, measure and map different forces acting close to the surface of a sample. For example, a tip containing magnetic material can be used to detect magnetic forces (a technique known as Magnetic Force Microscopy or MFM), [11, 12] or a tip coated with biological ligands can detect specific binding forces associated with receptor sites on the surface of a cell (a technique known as Topography and Recognition Imaging or TREC). [13]

2.2 Electron Beam Induced Deposition

2.2.1 Discovery

It was noted from the earliest days of experimentation with electron beams that deposits of material formed on surfaces irradiated by the electron beam. [14–18] It was discovered that these deposits arose as a result of decomposition of contaminants present in the vacuum chamber of electron-beam systems by the electron beam. [17, 19] Originally considered to be a disadvantage of electron microscopy techniques, since it decreased resolution and contaminated samples, it was later used as a technique for the deposition of material to fabricate nanoscale structures. Christy demonstrated the deposition of insulating thin films using this technique [20], and Baker *et al* are credited as the first to use it for the deposition of metallic structures. [21] Broers *et al* later used EBID contamination to form etch masks on Au-Pd films with 8-nm resolution. [22] Since these early experiments, modern experimentation has led to widespread research into EBID applications and techniques, and it is becoming a mainstream nanofabrication technique which promises higher attainable resolution than conventional electron-beam lithography techniques as well as greater versatility in the range of structures which can be fabricated. [23]

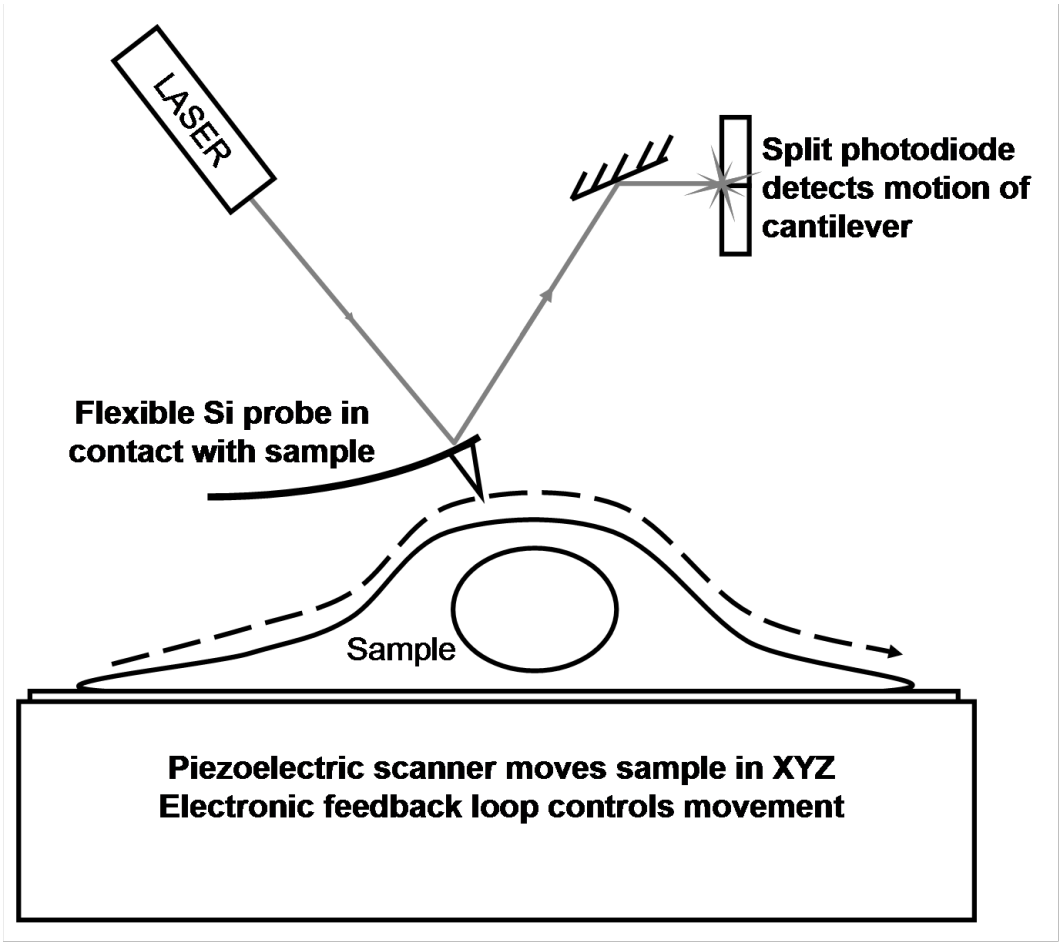

Figure 2-1: Schematic of a typical AFM system (not to scale).

2.2.2 Interaction of the Electron Beam and Sample

When a high-energy beam of electrons is incident on an atom in a sample, a number of different effects can occur. The electron may not be deflected significantly and may pass close to the atom without significant scattering (transmitted electrons). Some electrons are scattered, sometimes by very large angles of up to 180 degrees (backscattered electrons).

The electrons in the beam (referred to as "primary electrons") may also cause the emission of shell electrons from the atom. In some cases, energy is transferred from a primary electron to a K-shell electron, which can be ejected from the atom as a result. These emitted electrons are termed "secondary electrons". These electrons have much lower energies than those in the primary beam, typically having energy of 1-50 eV. This also causes the emission of x-ray radiation as outer shell electrons undergo transitions to fill the vacancy left by the ejected secondary electron; alternatively, the transition energy can be transferred to an outer shell electron, which is also ejected from the atom (these electrons have energies corresponding to the electron energy transitions in the atom and are known as "Auger electrons"). Other significant effects caused by the arrival of an electron beam on a sample include the induction of surface plasmons, induced currents, emission of continuum or *bremsstrahlung* X-ray radiation, heating of the sample, and even the emission of visible light (cathodoluminescence). [24]

2.2.3 Deposition

The energy of electrons interacting with a substrate can be transferred to molecules adsorbed on its surface, referred to as precursor molecules or precursors. These molecules can be present as contamination arising from the environment; for instance contamination arising from greases in vacuum systems and outgassing of contaminants from the vacuum chamber walls. [17, 19] They can also be deliberately introduced to the vacuum chamber.

The energy of the electron beam can cause decomposition of these molecules; heavier fractions of the molecule then remain on the substrate, while lighter fractions are able to evaporate from the surface. In the case of hydrocarbon contamination, the heavier carbon-rich fractions of the molecule remain on the surface, becoming polymerised into a carbonaceous residue. The resulting deposit

is composed of amorphous carbon, [17] usually also containing some hydrogen and oxygen.

There is considerable evidence that deposition is mainly caused by the secondary electrons which are produced when the primary electron beam interacts with atoms in the sample. The size of deposits usually extends some distance around the primary electron beam spot, which is usually smaller than 1 nm in diameter. [25] The width of the deposited structures is instead noted to correlate with the penetration range of secondary electrons. [26] In addition, the interaction cross-section of hydrocarbon precursor molecules is significantly larger for lower energy electrons. [26, 27] The dissociation energies of these bonds lie in the range of 50-100 eV. [27, 28] These energies are much closer to those of the secondary electrons, resulting in a greater probability that a secondary electron will induce breakdown of these bonds and decompose the precursor molecules. These results indicate that the secondary electrons generated from the substrate atoms are the primary contributors to the deposition process. However, despite the evidence that the secondary electrons are the dominant cause of electron-beam induced deposition, it is recognised that some deposition is also caused by primary and backscattered electrons. [29]

Growth of high aspect ratio structures by EBID usually uses one of two techniques. Irradiation of a single spot on a flat substrate using a stationary electron beam deposits carbon around the beam spot. Over time, carbon accumulates to form a pillar. [30–36] Alternatively, the beam spot can be focused onto a substrate close to an edge, and then moved slowly beyond the edge into free space. This deposits a line of carbon; due to induction of deposition by the secondary electrons, the carbon is deposited around and ahead of the beam spot. When the deposition reaches the edge of the substrate some deposition occurs beyond the edge, creating a structure on which further deposition can occur. This results in the fabrication of a freestanding pillar or plate-like structure extending out from the substrate edge. [37–43] These two different techniques are illustrated schematically in figure 2-2.

A third technique for the fabrication of high-aspect ratio filaments is to irradiate a large area of a strongly insulating surface using the electron beam, causing the growth of branching, tree-like structures. Random irregularities in the deposition process create sharper points on the deposit. Due to the insulating

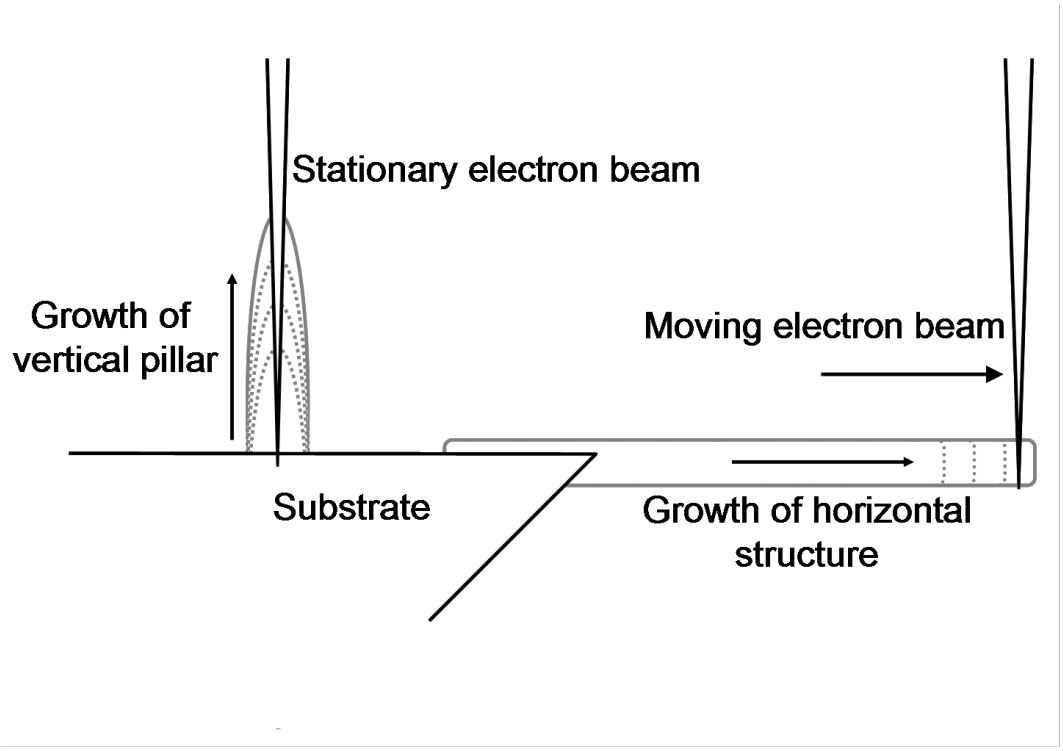

Figure 2-2: Illustration of two main techniques used to fabricate high-aspect ratio structures using electron-beam induced deposition. The most commonly used technique is to focus a stationary beam at a point on a flat substrate, creating a vertical pillar along the beam axis. A second method is lateral growth of a pillar from a substrate edge by moving the electron beam spot.

substrate, charge accumulation from the primary beam creates a strong electric field around these points, attracting precursor molecules ionised by the beam. The result is the increased growth of EBID carbon from each point, creating a branching structure. [44–49] This method generally can only fabricate randomly branching, "dendritic" (tree-like) structures composed of many nanoscale filaments.

2.2.4 Replenishment of Precursor Supply

The source of carbon or other materials for deposition by EBID is the precursor molecules which adsorb onto the substrate surface. This imposes a limit on the quantity of available precursor, which must be replenished after depletion by the electron beam. Replenishment occurs by diffusion processes, either along

the surface of the substrate or by diffusion from traces of gaseous precursor in the surrounding vacuum. Of these two routes, there is significant evidence that surface diffusion is the dominant process; for example, deposition over an area of a flat substrate results in a structure with raised edges due to more rapid replenishment of the precursor at the deposit edges by diffusion across the surface. Further evidence of the importance of surface diffusion during deposition was shown in experiments using EBID to fabricate concentric rings on surfaces; which reduces the growth rate of structures grown inside the ring immediately afterwards. [50,51] This can be explained by the depletion of precursor molecules during the deposition of the ring structure, which reduces the supply of surface-adsorbed precursor molecules available for deposition inside the ring. Finally, in our experiments we have found that free-standing carbon filaments will not grow beyond a certain length as the surface diffusion path becomes longer and the surface density of the precursor decreases. More detail on these experiments can be found in chapter 4. All of these effects suggest that surface diffusion plays the major role in the replenishment of the precursor supply.

2.2.5 Other Similar Techniques

It is possible to achieve similar effects to EBID deposition using ion beams, a technique known as ion-beam induced deposition (IBID). This technique has even been used to fabricate nanosized three-dimensional scale models, including one of the Starship *Enterprise*. [52] Ion beams can also be used to directly etch material from a substrate; electron beams generally cannot achieve this as the momentum of electrons at energies normally used in SEM systems is not sufficient to displace atoms from the substrate. In some cases, particularly if the adsorbed molecules present on a surface contain oxygen (e.g. water), then an electron or ion beam can induce an etching reaction between these molecules and the substrate. This technique is known as electron- or ion-beam induced etching (EBIE or IBIE). [53]

2.2.6 Applications

As a direct-write nanolithography process, EBID has been applied to fabricate or modify a wide variety of nanoscale structures. EBID has been used to fabricate nanoscale dots, [54, 55] nanowires, [38, 56, 57] and more complex structures

including three-dimensional structures. [40, 58] EBID structures have been used in the fabrication of Hall sensors, [59] superconducting quantum interference devices, [60] photonic crystals, [61] and electronic devices. [23] It has been used for the repair of lithographic masks, [62] for the deposition of high-resolution resist patterns onto substrates prior to etching, [22] and for the modification of AFM probes (see subsection 2.2.7).

EBID can also be used for the immobilisation of nanostructures, depositing a carbon layer to "weld" them onto the substrate. This has been used for EBID fixation of nanowires and nanotubes to AFM probes and microcantilevers, either for measurement of their mechanical and electrical properties under tension [58, 63–65] or in order to improve tip aspect ratio. It has also been used to join carbon nanotubes and nanowires [38,66], and to increase the binding strength of specific nanoparticles in monolayers to their substrate so that a nanoparticle pattern can be formed after removal of the unwelded particles. [67]

Control of the precursor gas content allows the deposition of a wide variety of different materials. Modifying SEM systems or using Environmental SEMs (ESEMs) allows introduction of different precursor gases and control of the gas concentration and pressure within the SEM chamber. Using a metallocene or metal halide compound as a precursor, for example, will result in the deposition of a metal-containing structure by EBID. [54, 68, 69] Metals deposited by this technique in previous experiments include tungsten, copper, [43] gold, [38, 56] cobalt, [59] platinum, [61, 70, 71], palladium, molybdenum, rhenium and chromium. [37] It is also possible to deposit silicon-based structures using this technique. [42, 72] Usually, deposition using metal-containing precursors results in a metal-carbon composite; however, pure metallic structures have been successfully fabricated by EBID techniques. One mechanism proposed for the formation of pure metallic structures is the heating of the sample by the beam, which decomposes and desorbs light contaminant molecules. [43] Deposition in an atmosphere including water vapour has also been reported to produce structures with solid gold cores. [38, 56, 58] Post-processing by heating the deposited structures can also be used to remove carbon impurities. [37, 71]

The resolution attainable by EBID suggests that it can be used to produce extremely small structures, even smaller than those attainable by "resist-based" electron beam lithography (EBL). Using thin substrates, short exposure times,

and high primary beam energies, sub-nanometre dots have been fabricated using electron beam induced deposition. [69, 73] These resolutions were achieved using high energy primary electron beams in a Scanning Transmission Electron Microscope (STEM) system, and by fabricating nanodots on thin substrates which limit the volume in which the primary electrons are scattered (and so therefore decreases the volume of the substrate which generates secondary electrons). Theoretical predictions suggest that these techniques could be used on thick substrates as well. [74] These nanodots are fabricated using very small beam dwell times; this generally means that high-aspect ratio structures with diameters this small cannot be fabricated by EBID. However, using high-energy beams, high-aspect ratio structures with a lateral size of ∼10 nm can be fabricated. [40, 75] One group has reported the fabrication by EBID of ∼5 nm diameter pillars; in this study larger-diameter metal-carbon composite pillars were initially deposited by ion beam induced deposition and then used as a support for the fabrication of the thin pillars using EBID. These results indicate that EBID has great future potential for fabrication of nanodevices at scales smaller than those attainable by conventional EBL techniques. [76]

2.2.7 Modification of AFM Probes

EBID is also widely used for the modification of AFM and STM probes. By fabricating a pillar on the probe tip, a high-aspect ratio probe is created, capable of profiling surface features with steep gradients such as vertical steps. These cannot be profiled accurately using standard unmodified probes, which typically have a pyramidal shape.

In order to produce a high-aspect ratio probe, deposition is usually performed using a stationary beam spot to fabricate a pillar on the tip. [30–35, 68] Carbon is deposited around the beam spot, forming a pillar which grows along the axis of the beam. The pillar is usually cylindrical with a conical tip, with a radius determined by the escape depth of the secondary electrons produced around the primary beam path through the central axis of the pillar. During this growth process, the radius of the pillar is enlarged until its radius reaches the limit of the escape depth of the secondary electrons. [25, 26, 33] Once this radius is reached, the secondary electrons generated along the central axis of the pillar can no longer

reach the surface of the pillar to cause further deposition.

Wendel *et al* were able to improve the tip radius of EBID probes using oxygen plasma etching after growth, creating tips which could be applied for both imaging and lithography. [35] Recently, our group applied EBID to fabricate blade-like structures on the apex of AFM probes; this structure was applied as a "nanoscalpel", which could be used for mechanical lithography on metal films, and as a nanoscale surgical scalpel for the dissection of biological objects. [77] We have also been able to fabricate very slender (<15 nm diameter) high-aspect ratio "nanoneedle" AFM probes using this technique. [78]

2.3 Indentation

2.3.1 Development of Indentation Models

Indentation techniques are now widely used to characterise the elastic and other mechanical properties of solid materials. The materials which have been characterised by indentation include glasses, metals, polymers, and biological materials including cells and tissues. Indentation techniques can be applied at a nanoscale level, a technique known as nanoindentation; nanoindentation can be applied to thin or heterogeneous samples due to the small indentation depth and probe size. Indentation works by pressing a highly rigid indenter of known geometry into the material to be tested; mechanical properties such as the tensile elastic modulus of the material can then be calculated from its deformation at a given applied indentation force. [79] Nanoindentation studies can be performed using purpose-designed nanoindenter systems, but are often performed instead using AFM systems which provide very precise force and displacement sensing combined with simultaneous high resolution imaging of the sample.

The deformation due to elastic contact between spheres was first analysed by Hertz and Boussinesq, whose work became the foundation of the "contact mechanics" used to model indentation studies. Hertz considered the problem of two elastic spheres being pressed together by a loading force and the resulting deformation. By assuming one sphere to be infinitely large (approximating a flat surface), and one to be absolutely rigid (infinite elastic modulus) then the model can be applied to the case of a rigid spherical indenter which elastically deforms a

comparatively soft flat surface. In this simplified model, the relationship between the applied indentation force and the depth of indentation is given by

$$F = \frac{4}{3}\frac{E}{1-\nu^2}\sqrt{R}h^{\frac{3}{2}} \tag{2.1}$$

where F is the force applied during loading or unloading, h is the vertical deformation of the sample by the indenter, R is the indenter radius of curvature, and ν is the Poisson Ratio of the sample. This relation can be used to calculate the tensile elastic modulus of the sample, E, from the force-deformation curve.

This model was then generalised to other indenter geometries by Sneddon, who calculated the deformation as a function of applied force for other indenter geometries including conical and cylindrical indenters. [80] For conical indenters,

$$F = \frac{2Etan\theta}{\pi(1-\nu^2)}h^2 \tag{2.2}$$

where θ is the half-cone angle of the indenter, and for cylindrical indenters

$$F = \frac{2ERh}{1-\nu^2} \tag{2.3}$$

In general, a material will deform purely elastically until its "elastic limit" is reached, after which permanent deformation occurs. This is referred to as "plastic" deformation, which does not disappear when the applied indentation force is removed. Indentation studies are often made using forces which cause plastic deformation of the sample.

It is often assumed that all plastic deformation occurs during the loading period where the applied force is raised from zero to a maximum value, and that all deformation during the unloading of the indenter is elastic. Therefore, the elastic modulus can be determined from the deformation during the unloading process. This procedure is often performed using the method developed by Doerner and Nix [81] and refined by Oliver and Pharr [82]. Their technique, known as the "compliance method", calculates the elastic modulus from the gradient S of the force-deformation curve during the unloading process, at the point of maximum force F_{max} (see fig 2-3).

$$S = \frac{dF}{dh} = \frac{2}{\sqrt{\pi}}E_r\sqrt{A} \tag{2.4}$$

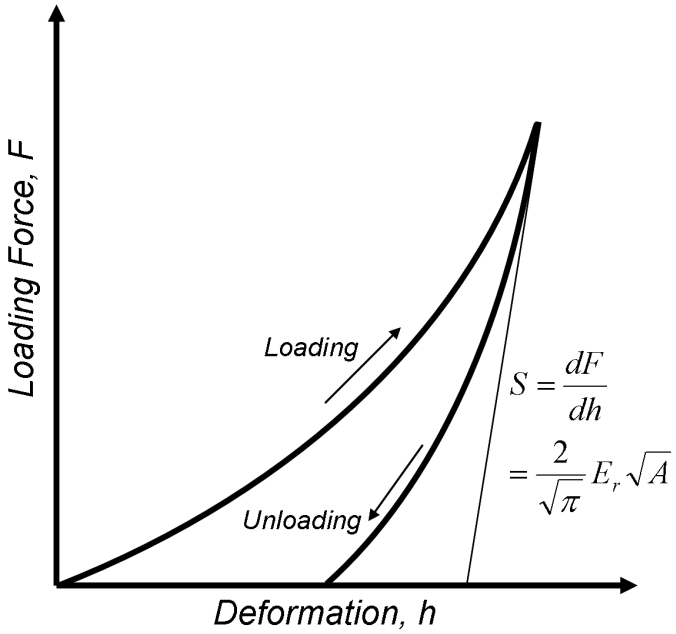

Figure 2-3: Schematic of typical force-displacement curve used to measured elastic modulus using the "compliance model".

where E_r is the "reduced elastic modulus" and A is the "projected contact area" (projected area of the indenter surface in contact with the sample) at the point of maximum load.

E_r is defined by

$$\frac{1}{E_r} = \frac{1-\nu^2}{E} + \frac{1-\nu_i^2}{E_i} \tag{2.5}$$

where E_i and ν_i are respectively the elastic modulus and Poisson ratio of the indenter. For a highly rigid indenter, E_i is often considered infinite, reducing the equation to

$$E_r = \frac{E}{1-\nu^2} \tag{2.6}$$

The deformation rate of many materials depends not only on the applied load but the rate at which the load is applied. This is referred to as viscoelastic or viscoplastic behaviour, and is not included in the models described above. This

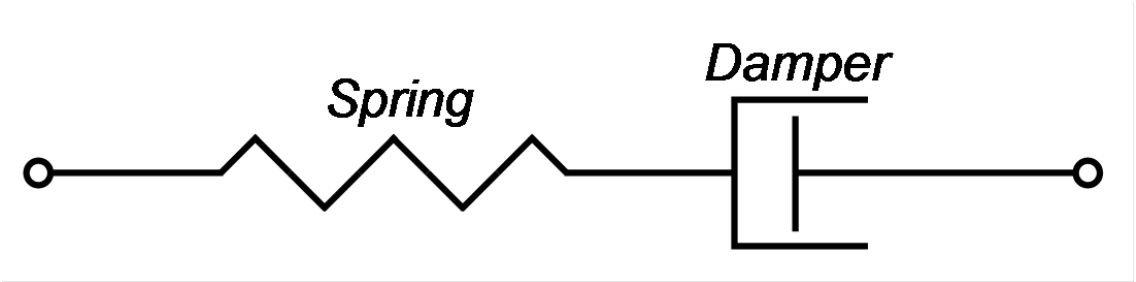

Figure 2-4: Schematic illustration of the Maxwell model which considers a material as an elastic spring and damping element which simulates the sample viscoelasticity.

behaviour is common in biological cells and tissues. [5, 83–88]

In order to compensate for this behaviour Oyen and Cook suggested a model for conical indenters which considers the deformation as a linear sum of viscoelastic, elastic and plastic deformation. Deformation by the indenter in this case can be considered as a convolution of elastic, plastic and viscoelastic deformation, and a number of models can be used to calculate the effect of each on the sample deformation.

Oyen and Cook [87, 89] derived a model for conical indenters taking into account viscous effects, based on the "Maxwell model" which assumes that viscoelastic deformation can be modeled as a spring and damper linked in series (shown schematically in figure 2-4). In chapter 7, a model is derived for cylindrical indenters based on the Oyen-Cook model; this has been applied to the deformation of corneocyte cells using AFM probes with "nanoneedle" structures fabricated on the AFM tip using electron beam induced deposition. These probes can indent to large depths within cells without loss of lateral precision, and measure mechanical properties of structures deep within the cell.

2.3.2 Indentation of Biomaterials

In recent years, a great many studies have used AFM nanoindentation techniques to determine mechanical properties of biological cells and other biological materials. Some of the earliest research in this area was pioneered by measurements on cells by Weisenhorn *et al* [90] and on bone by Tao *et al* [91] Further developments in this area have led to investigations of many different cell types using

AFM. [92, 93] The AFM probe can be used to induce controlled deformation of the cell structure, simultaneously measuring the applied force. The techniques described in section 2.3.1 can be used to determine elastic modulus and other mechanical properties of the cell. The measured properties reflect the cell's internal structure, especially its "cytoskeleton", the network of polymerised protein filaments threaded throughout the cell, which provides a structural support for the cell as well as providing a driving force for cellular locomotion, cell division and morphological changes. [94] There is significant evidence that the mechanical properties of cells can be used to determine the overall state of the cell. Several groups have recorded a decrease in elastic modulus in cancer cells compared to healthy cells of the same type. [88, 95, 96] Changes in mechanical properties have also been reported between metastatic cells (cancer cells which are able to migrate and spread the disease beyond its original site) and non-metastatic cancer cells. [97] The same study reported that different types of healthy cell could also be distinguished by their different mechanical properties, and proposed the use of cell deformability as a criterion for the sorting of large populations of cells by cell type. Many other diseases can cause changes in stiffness and other mechanical properties of various cell types, including arthritis, asthma, cancer, malaria, sickle cell anaemia, and also spherocytosis and elliptocytosis (two conditions in which the shape of red blood cells is altered and their function impaired). [98] In some cases, the change in mechanical properties is a cause of the disease symptoms; for example the increased stiffness of malaria-infected erythrocytes (red blood cells) prevents them from deforming to traverse narrow vascular capillaries. It is likely that these changes arise from the re-organisation of the cellular organisation (such as the cytoskeleton structure) that occurs due to these disease states. In many cases (particularly cancer) early diagnosis is vital for the treatment of disease, and so there is potential application of nanomechanical measurements as a tool for the early detection of the onset of these conditions.

2.4 Nanomanipulation of Cells

"Nanosurgery" refers to the manipulation of biological cells on extremely small scales. A diverse range of techniques exist for this purpose; for many years, micropipettes have been used to hold cells in place using negative pressure or for

injection of biomolecules (including DNA) into cells. [99, 100] In recent years, a wider array of techniques have been used for direct manipulation on cellular and subcellular scales, including optical tweezers, laser microscalpels, and the atomic force microscope. A major advantage of these techniques is their ability to operate on subcellular levels, with a precision comparable to the size of intracellular organelles, which decreases damage to the cell structure as a whole.

Optical tweezers (OTs) use a focused laser beam to confine a dielectric particle at the beam focus; this confinement occurs due to the transfer of momentum from the scattered light, and the electric field gradient which will tend to draw polarised particles to the beam focus. [101] The use of OTs to manipulate cells has attracted great interest in recent years; they have been used for the confinement of single cells in suspension allowing them to be imaged or examined using optical spectroscopy over long periods of time, [102, 103] or repositioned to form a cell cluster. OTs are also widely applied for cell sorting and for the "stretching" of cells in order to investigate their mechanical properties; for a review see Zhang *et al.* [104]

In general OTs have been applied for manipulation of whole cells rather than individual intracellular structures; however, some groups have created "nanotool" structures which can be manipulated using optical tweezers which could be used for manipulation of smaller structures in cells. [105] In addition, particles trapped in OTs have been used as force-sensitive probes which can profile and image biological samples, with additional application to mapping of their elastic and viscoelastic properties. This application is known as a "photonic force microscope" (PFM). [106–108] Optical tweezers have also been used to manipulate organelles isolated from cells using other nanosurgical techniques. [109] However, the manipulation of subcellular structures has generally been demonstrated using other techniques, such as laser microscalpels or AFM.

Laser microscalpels are usually short-duration pulsed lasers which are used to cut or destroy intracellular structures. Ablation of biological structures by a laser beam occurs due to generation of plasma in ionisation cascades induced by the beam energy [110] or by selective heating of the sample. [111] These have been used to selectively delete organelles or cut cytoskeleton filaments within cells, and also to make incisions in the cell membrane [111–115] or the cell wall of plant cells. [116] Laser microscalpels have also been used to dissect isolated chromosomes.

[117] Similar results can be achieved using focussed ion beams as microscalpels to remove material from a biological sample. Laser microscalpels can also be used to destroy single organelles within cells without affecting cell viability; this has been used to demonstrate that mitochondria in the cells studied were discrete entities rather than a linked network as had previously been believed, [118] as well as to destroy single chloroplasts in plant cells. [116] Using a combination of a laser microscalpel and optical tweezers, single organelles have also been isolated from cells using nanosurgery. [109] The cells targeted in these experiments were often observed to suffer no loss of viability after nanosurgery.

There are limits to the precision attainable using laser microscalpels. Firstly, optical techniques are subject to diffraction limits, which determine the minimum beam spot size. However, the distribution of energy across the beam spot (often Gaussian) can confine the highest energy densities to a region smaller than the beam spot. [111] A certain threshold energy is required to initiate the ablation effects; Maxwell *et al* demonstrated that increasing the beam energy will cause the ablation of material over a larger volume. [118] Therefore, the minimum incision width is limited to that attainable at the threshold energy for ablation; TEM measurements of incisions on fixed cells showed that $\sim$200 nm-wide incisions could be attained close to the threshold energy. The requirement to exceed the threshold energy and the focussing limits of the laser beam would suggest that this approaches the minimum incision width, and therefore the limit of lateral precision, attainable using a laser microscalpel. In addition to this limitation, laser scalpels can induce heating and bubble formation in cells, which can induce significant damage to the overall cell structure.

The atomic force microscope has also found widespread application in the manipulation of biological structures including cells. AFM has been used in the dissection of chromosomes, [117, 119] plasmids [120, 121], virus particles [122], bacterial photosynthetic reaction centres in isolated membranes [123, 124] and collagen fibrils. [125] The successful dissection of collagen fibrils in the study cited here using AFM indicates its usefulness as a "nanoscalpel", which was used to make incisions on a collagen fibril, and then manipulate its upper layers to enlarge the incisions and expose its internal structures for AFM imaging. AFM manipulation has also been used to dissect outer layers of bacterial cell walls *in situ*, exposing the periodic peptidoglycan strands which comprise the cell

wall ultrastructure for AFM imaging. [126] Using a spherical AFM tip coated with phospholipidase enzyme, Alfin *et al* were able to selectively break down the phospholipid structure of the cell membrane, creating holes of several micron diameter. [127] Following fixation of the cells using glutaraldehyde, it was possible to image intracellular filament structures using AFM and SEM. AFM has also been used to extract material from biological samples; for example, extracting DNA from isolated human chromosomes [119] and the mRNA from the cytoplasm of cells. [128]

Compared to optical techniques, the AFM is capable of much higher precision as the tip has a radius of a few nm, and can be positioned with sub-nanometre accuracy. This allows manipulation to be performed at the level of individual biological molecules, or at the level of the nanoscale structures, such as cytoskeleton filaments, found within biological cells. However, while the AFM tip itself is small, the pyramidal shape of the tip decreases its precision if the tip penetrates deeper into a sample. [77] This loss of precision not only decreases the accuracy of the manipulation but also inflicts significant damage on the target structure. In the case of a cell, this can affect its living processes or even kill it. [129] Just as in macroscopic surgery and dissection, high precision tools are therefore desireable in nanosurgery.

In order to improve the lateral precision of AFM probes, various approaches have been used to improve the AFM probe aspect ratio for biological nanomanipulation. "Nanoneedle" AFM tips have been produced using focussed-ion beam milling to modify the tip shape, and have been applied for the injection of molecules into cells, including the injection of DNA into the nuclei within living cells. [130–133] These tips demonstrate far less effect on the cell structure, and the survival rate for cells after nanosurgery using nanoneedles is high. Similar nanoneedles for biological applications have been fabricated using carbon nanotube probes; [129] these probes are often stiffened by application of carbon [134] or polymer coatings [135] to prevent them buckling during nanomanipulation. Nanoneedle probes for cellular manipulation have also been fabricated by attaching cadmium sulphide nanorods to microbeads which can be manipulated using optical tweezers. [105]

2.5 Descriptions of Biological Cells

This section describes in brief the structure and function of the cells used in the experiments described in this thesis. Details of the protocols used to isolate and prepare cells in our experiments can be found in appendix A.

2.5.1 Smooth Muscle Cells

Smooth muscle cells make up a muscular layer (thicker in arteries than in veins) that surrounds the thin epithelium and internal space (or lumen) of blood vessels. Contraction of these muscles causes vasoconstriction (narrowing of the blood vessel) which is used to maintain homeostasis of blood pressure in the circulatory system. The cells have a well-developed internal cytoskeleton which interfaces with a membrane skeleton lying just beneath the cell membrane. The membrane skeleton consists of two "subdomains"; dense plaque regions and regions possessing many small invaginations of the cell surface (caveolae). The plaque regions form "adherens junctions" which bind to other nearby cells and to the underlying cytoskeleton. The cytoskeleton forms the structural support for the smooth muscle cell, composed of filaments of polymerised actin and vimentin protein. The actin filaments are able to interact with myosin protein filaments, forming contractile structures which provide the driving force for the contraction of the muscle cell. [136]

2.5.2 Megakaryocytes

Megakaryocytes are cells found in bone marrow; these cells are responsible for the biogenesis of blood platelets (small cell-like objects 2-3 μm in diameter found in blood which facilitate blood clotting, also called thrombocytes). The cells produce blood platelets in a process which first involves the enlargement of the cell to $\sim$100 μm in size, followed by the formation of a "demarcation membrane system" in which the cell extrudes numerous tubules of cell membrane. These tubules form small bud-like "proplatelets" at the end of the tubules. The tubules are able to form multiple branches, increasing the number of proplatelets, a process described as "proplatelet amplification". Eventually (after 4-10 hours) the whole cell structure is composed of this tubule network, with tubules reaching

lengths of 200-250 μm (the cell nucleus is actually extruded out of the cell as part of this process). The proplatelets eventually detach, forming true blood platelets. [137, 138]

2.5.3 The Stratum Corneum

The stratum corneum is a thin (in humans, $\sim$20 μm thick) tissue which forms the outermost layer of the skin in mammals. It acts as a barrier to evaporative water loss from the body as well as protecting from harmful pathogens and environmental conditions. Species lacking such a waterproof layer (such as amphibians or those with genetic defects that prevent its formation) cannot survive in conditions of low humidity as they rapidly dehydrate. The stratum corneum is a highly sophisticated and complex tissue. In humans, the stratum corneum is composed of 40-50 layers of cells known as corneocytes. These cells are generated in a basal layer of keratinocyte cells, and migrate upwards towards the outer skin surface during their life cycle. During this process, their internal structure is replaced by a matrix of keratin filaments, while a polymerised protein layer forms at the cell surface. [139] This renders the corneocyte impermeable to water. The continual upward migration of corneocytes allows rapid replacement of the layer if damaged; corneocytes continually detach in the stratum corneum surface layers and are eventually lost to the surrounding environment. Corneocytes are bound to one another by corneodesmosome structures; these are protein clusters which span the cornified envelopes of adjacent corneocytes and maintain adhesion between the cells. [140]

The corneocytes are surrounded by lipids covalently bound to the corneocyte envelope. [141] The overlapping corneocytes embedded in this lipid matrix together form a structure described as a "brick and mortar" model. This structure is highly resistant to water loss from diffusion; the overlapping corneocytes increase the length of the diffusion path so that it is much larger than the thickness of the stratum corneum itself, and the lipid molecules resist the passage of water due to their hydrophobicity. [142]

Monolayers of corneocytes can be easily isolated from the skin surface using an adhesive stripping procedure. Adhesive tape, or a glass slide coated with an adhesive, is pressed onto the skin surface and then peeled away, removing with

it a layer of corneocyte cells. [143] Since the stratum corneum provides a strong diffusion barrier against water loss from the underlying tissue, and this barrier function remains approximately constant with depth [144], the removal of the stratum corneum by tape stripping increases trans-epidermal water loss (TEWL) due to evaporation. Thus, measurement of TEWL can be used to accurately determine the depth from which the corneocytes have been isolated.

Modelling the stratum corneum as a homogeneous membrane, Fick's 1st Law can be used to describe the diffusion across the stratum corneum. This can be used to derive

$$\frac{1}{T_x} = \frac{H - x}{K\Delta C} \tag{2.7}$$

where T_x is the TEWL measured after a thicknes x of stratum corneum has been removed, H is the total stratum corneum thickness, ΔC is the concentration gradient across the stratum corneum, and K is a constant determined by the properties of the stratum corneum and the diffusivity of water. [144, 145] If T_0 is the TEWL of the unstripped skin surface, where $x = 0$, then

$$T_0 = \frac{K\Delta C}{H} \tag{2.8}$$

therefore the percentage of the stratum corneum removed is given by

$$\frac{x}{H} = 1 - \frac{T_0}{T_x} \tag{2.9}$$

In our experiments, TEWL measurements were used to control the depth from which corneocyte samples were taken from the skin.

Chapter 3

Methodology

3.1 Atomic Force Microscopy

The experiments described in this thesis were carried out using a Veeco Multimode IIIa Atomic Force Microscope (AFM), controlled by dedicated Nanoscope software. The images were analysed using the freeware WSxM program created by Nanotec Electronica S.L. Manipulation was perfomed using predefined macros included with the Nanoscript function in the Nanoscope software; these macros were incorporated into programs written using C++. Samples were imaged in air at room temperature in a clean room environment.

Imaging and manipulation were carried out in Tapping Mode using standard Tapping Mode cantilevers, with a spring constant of ∼40 N/m and a resonant frequency of ∼300 kHz. For determination of the critical buckling force of thin nanoneedle probe tips (see chapter 5) lateral force microscopy tips with a spring constant of ∼3 N/m and a resonant frequency of ∼75 kHz were used.

3.2 Scanning Electron Microscopy

Scanning Electron Microscope (SEM) imaging was carried out using a Hitachi S4300-SE Scanning Electron Microscope. For normal imaging, a beam current of 70-150 pA and an accelerating voltage of 20 kV were used. The beam current can be controlled by adjusting the SEM condenser lens setting.

3.3 Electron Beam Induced Deposition

Electron-beam induced deposition (EBID) was used in the experiments described in this thesis to fabricate three-dimensional nanostructures.

3.3.1 Freestanding structures

Freestanding structures were grown in the AFM system using programs written in the Raith nanolithography software. This software controls the Raith lithography system which has been installed as part of the SEM. Structures were grown using the same range of beam conditions (current and accelerating voltage) as were used for imaging. Before deposition, beam currents were measured using the "Faraday cup" built into the SEM stage.

3.3.2 Stabilisation

Stabilisation of "nanoneedle" structures by depositing additional amorphous carbon (described in more detail in chapter 5) was performed by imaging them at high magnification (150,000-300,000x) in the SEM under high beam current conditions (100-150 pA).

3.4 Cantilever calibration

In order to calculate the force applied to a sample by the AFM probe, it is necessary to know the cantilever spring constant k_c. The spring constant is specified by the probe manufacturer within certain tolerances; however, between individual probes of the same type it can vary considerably. It is therefore necessary to calculate the spring constant of individual probes used for nanomanipulation if the tip-sample force is to be determined.

If the dimensions and resonant frequency of the cantilever *in vacuo* are known, the spring constant can be determined using

$$k_c = 0.2427 \rho_c b h L \omega_v^2 \tag{3.1}$$

where ρ_c is the density of the cantilever material, b is the width of the cantilever, h is the cantilever thickness, L the cantilever length, and ω_v the cantilever

resonance *in vacuo*. However, equation 3.1 relies on highly accurate measurement of the vacuum resonance frequency, which is often difficult to achieve.

Due to this difficulty, a variety of other methods have been used to determine the spring constant in previous AFM studies. Sader *et al* investigated how equation 3.1 could be modified for cantilevers oscillating in air, and derived a method of calculating k_c using only the cantilever dimensions and resonance peak properties in air. [146,147] This method relies on a model of the hydrodynamic damping properties of the AFM probe in a fluid environment. For a rectangular cantilever, the resonant frequency when oscillating in fluid is given by

$$\omega_v = \omega_f(1 + \frac{\pi\rho_f b}{4\rho h}\Gamma_r(\omega_f)) \tag{3.2}$$

The cantilever thickness, h, is also often difficult to measure and so Sader makes use of the relationship

$$\rho h = \frac{\pi\rho_f b}{4}[Q\Gamma_i(\omega_f) - \Gamma_r(\omega_f)] \tag{3.3}$$

which can be substituted into equation 3.2 to eliminate ρh. In equations 3.2 and 3.3, ω_f is the cantilever resonant frequency in fluid, Q is the quality factor of the oscillation, ρ_f is the fluid density, and Γ_r and Γ_i are the real and imaginary components of the "hydrodynamic damping function" Γ.

The Γ function for a cylindrical beam, Γ_{circ}, is given by [146]

$$\Gamma_{circ} = 1 + \frac{4iK_1(-i\sqrt{iRe})}{\sqrt{iRe}K_0(-i\sqrt{iRe})} \tag{3.4}$$

where $i^2 = -1$, K_0 and K_1 are modified Bessel functions of the second kind, and Re is Reynold's Number, given by

$$Re = \frac{\rho_f\omega_f b^2}{4\eta} \tag{3.5}$$

where η is the fluid viscosity. However, AFM cantilevers are rarely cylindrical. Sader therefore modified the Γ function to apply it to cantilevers with rectangular cross-sections by adding a correction factor $\Omega(\omega_f)$, which is a sum of real and imaginary polynomials of τ where $\tau = log_{10}Re$. Therefore, $\Gamma = \Omega(\omega_f)\Gamma_{circ}(\omega_f)$. $\Omega(\omega_f)$ is a 12th-order polynomial and therefore rather complex; for full details see Sader's paper. [146]

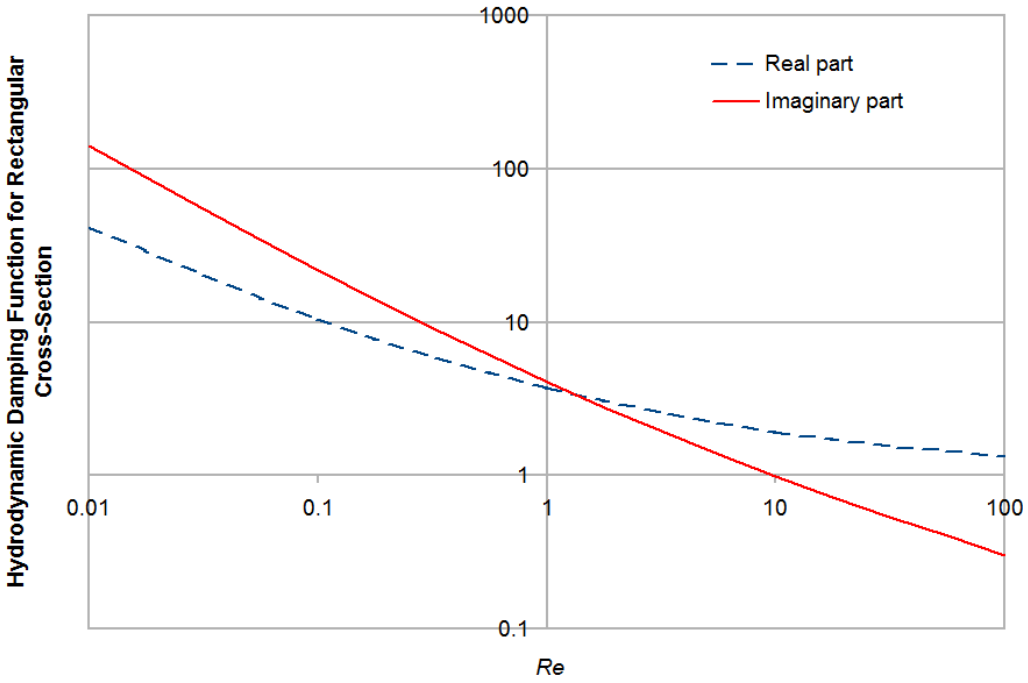

Figure 3-1: Hydrodynamic damping function calculated using Sader's method.

Although this calculation is complex, it is based on only a small number of initial variables (L, b, Q and ω_f) which can be measured to a high degree of accuracy. The resulting error on the cantilever spring constant is therefore quite small. The calculation is also independent of the material or composition of the cantilever. Cantilevers are often inhomogeneous due to metal coating on the upper side to improve laser reflectivity; since the Sader method is independent of the cantilever composition, it can be used without taking the cantilever coating into account.

In our experiments, measurement of Q and ω_f were carried out using the Autotune function in the Nanoscope AFM control software. b and L were measured using the SEM system for each cantilever used for manipulation. The cantilever tuning was carried out in air at room temperature, and standard values of ρ_f and η for air at room temperature were used. Calculation of the spring constant based on this data was calculated using a spreadsheet template in Microsoft Excel. Figure 3-1 shows the damping function calculated using this spreadsheet for a range of Re values; this curve is identical to that in Sader's paper indicating

that the calculation is accurate.

3.5 Indentation

Nanoindentation on the surface of biological cells was carried out using a dedicated program written using the NanoScript package, which forms part of the Nanoscope software. A graphical user interface (GUI) was implemented in these programs to allow the user to control the indentation parameters such as the approach rate and applied force. The program first retracts the AFM probe 100-200 nm from the surface, then moves it downwards towards the sample surface. When the probe contacts the surface, the tip-sample force causes a deflection of the AFM cantilever, increasing the deflection signal detected at the AFM photodiode. The indentation program monitors and outputs the cantilever deflection and amplitude signal from the AFM system, and stops the approach when a chosen target deflection signal (corresponding to a certain applied indentation force) is attained. Approach rates in the range of 2-1000 nm/s were used to perform indents on cells.

The force applied to a sample during indentation can be determined by

$$F = k_c D \tag{3.6}$$

where D is the cantilever deflection and k_c is the cantilever spring constant. k_c was determined in our experiments using the method developed by Sader, described in section 3.4. [147]

3.5.1 Calibration

Deflection of the AFM cantilever is detected using a four-quadrant photodiode built into the AFM system, which detects a laser beam which is reflected from the back side of the AFM probe cantilever. During initial alignment of the laser system, the laser beam spot is positioned on the photodiode such that the difference between the signal detected on the diode quadrants is minimised. Deflection of the cantilever causes a displacement of the beam spot, which is detected as a change in the signal from the different quadrants.

In order to accurately determine the force applied to a sample it is necessary to determine the deflection of the probe from the deflection signal. The actual deflection of the cantilever can be determined by measuring the signal recorded as the probe tip is pressed down on a rigid surface which does not significantly deform under the applied force. An example of such a calibration curve is shown in figure 3-2. Since there is no deformation of the sample, the vertical movement of the sample by the piezoelectric scanner will be equal to the deflection of the cantilever; the sample movement can be accurately determined from the scanner calibration. This allows a "cantilever calibration factor" to be determined as the rate of increase of the deflection signal for a given scanner displacement. Our AFM system gave a typical calibration factor of 0.1 V/nm deflection; due to different positioning of the cantilever, different laser alignments and different cantilever geometries this could vary from 0.07-0.12 V/nm for different experiments.

In our experiments, silicon wafers were used to provide a sufficiently rigid surface for this calibration process. The wafers were cleaned before use by low powered sonication for ∼3-5 minutes each in acetone and isopropyl alcohol (IPA).

3.5.2 Determination of sample deformation

The deformation of a sample beneath the AFM probe can be determined using the cantilever deflection recorded during the calibration curve and during the indent on the sample. During the calibration curve, the deformation of the sample is assumed to be negligible as it is recorded on a rigid sample; during an indent on a softer sample such as a cell, there is also deformation of the sample and so the AFM scanner travels a greater distance in the z-direction before the target cantilever deflection is attained. A comparison between a calibration curve recorded on a rigid surface and a softer sample (a corneocyte cell) is shown in figure 3-3. The difference in this z-axis movement for a given cantilever deflection (corresponding to a given applied indentation force) between the calibration and indentation curves gives the vertical deformation of the sample.

The deformation can be calculated using

$$h = [z_i(D) - z_1] - [z_1 - z_c(D)] \tag{3.7}$$

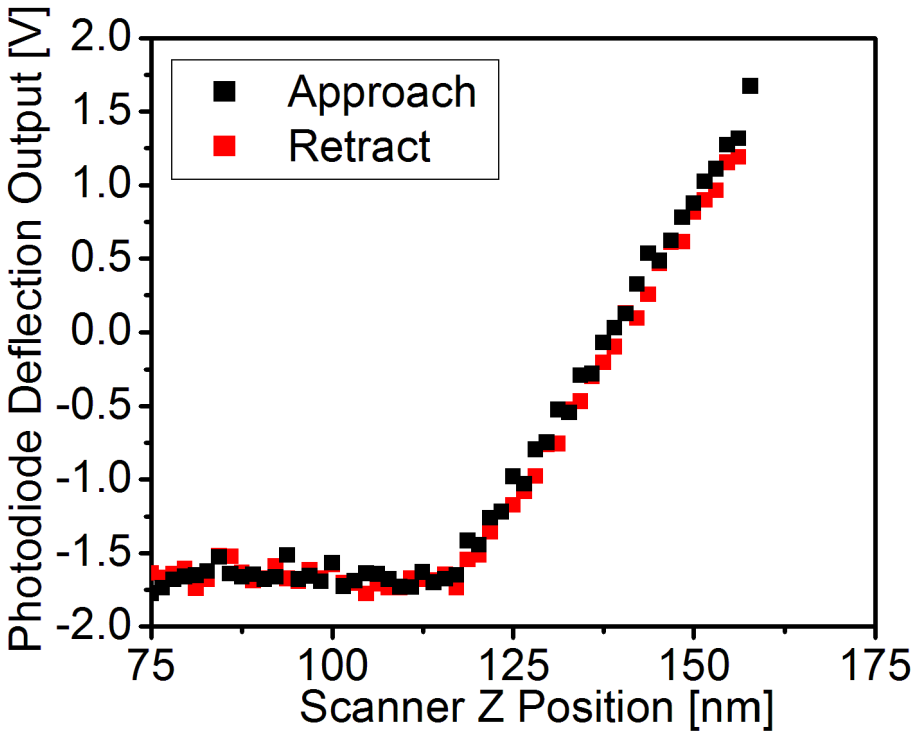

Figure 3-2: Outputted deflection signal from AFM system during calibration indent on rigid sample surface (a clean silicon wafer).

where h is the vertical deformation of the sample, z_1 is the point of contact with the sample surface, $z_i(D)$ is the z-position of the scanner during the indent for a given deflection, and $z_c(D)$ is the scanner z-position during calibration. For the calibration curve, the z-movement of the scanner is equivalent to the cantilever deflection D; substituting $D = z_1 - z_c(D)$ reduces this to

$$h = z_i(D) - z_1 - D \tag{3.8}$$

In chapter 6, this procedure is used to determine the vertical deformation of EBID carbon blades fabricated on AFM probes during nanomanipulation. The blades are fabricated on the side of AFM probe tips, and deformed by bending them against a 200 nm step on the sample surface. The principle here is exactly the same, except that part of the probe (the carbon blade) deforms rather than the sample; a calibration curve is recorded far from the step without deformation

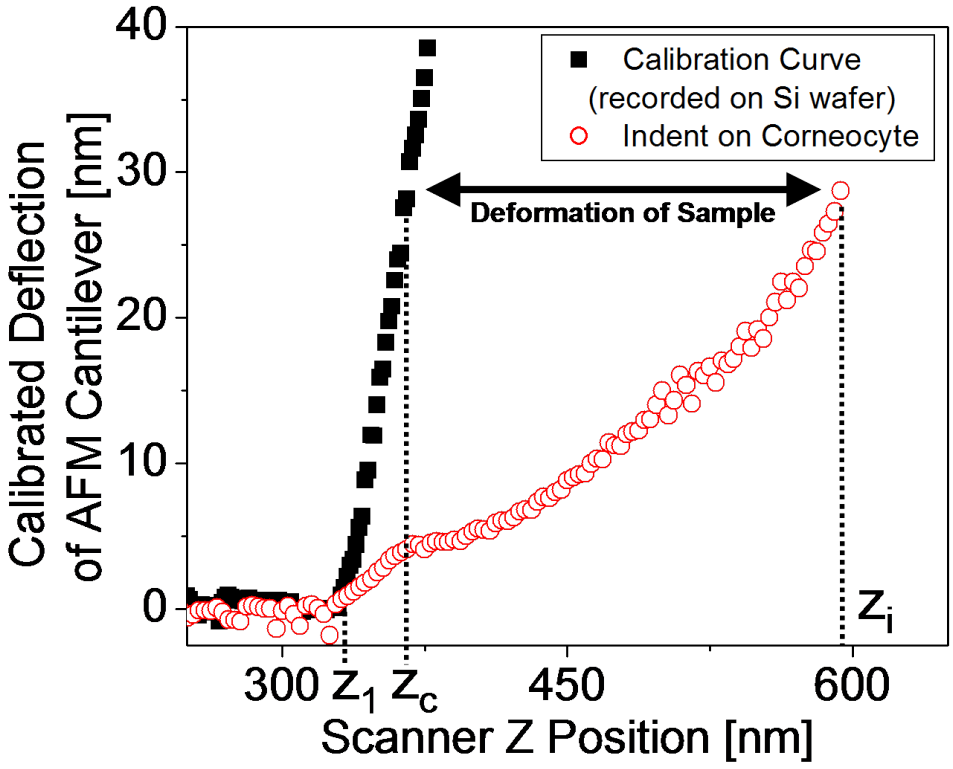

Figure 3-3: Calibrated deflection data during calibration curve recorded on a silicon wafer and during indentation on a corneocyte cell.

of the carbon blade, and then the deformation of the blade against the step is determined with reference to the calibration curve using the method presented here. For more details of this process see chapter 6.

The residual depth of the indentation can be regarded as the inelastic deformation of the sample. This is the depth of penetration of the needle when the applied tip-sample force returns to zero during the retraction of the AFM probe, in other words at $D = 0$. The inelastic deformation h_i can therefore be calculated by

$$h_i = z_2 - z_1 \tag{3.9}$$

where z_2 is the z-position of the scanner when the cantilever deflection returns

to zero during the retraction of the probe. Finally, the elastic recovery of the sample h_e in the vertical direction can be determined by

$$h_e = h - h_i \tag{3.10}$$

3.5.3 Decontamination of AFM Probes

During imaging and manipulation of biological samples, a commonly encountered problem is the adhesion of biological contamination to the tip apex. This can alter the probe shape; in the case of an EBID-modified probe, this can cancel out the specialised shape of the probe tip. In nanoindentation experiments, soft material adhering to the probe tip can deform during the indent instead of the sample, creating a misleading result when the sample deformation is calculated.

To remove contamination the AFM probes were cleaned after performing 6-10 indents. The following cleaning procedure, based on a standard procedure used to clean silicon wafers before photolithographic patterning, was found to be highly effective. The probes were placed in a purpose-built brass holder and cleaned using gentle sonication at room temperature in trichloroethylene (TCE) for 5-10 minutes, followed by acetone for 3-5 minutes and finally isopropyl alcohol for 3-5 minutes. The probes were then allowed to dry in air at room temperature in a clean room environment. This procedure was also used to clean contaminated probes prior to electron microscopy imaging (as the deposition of carbon would otherwise cause "welding" of the contamination to the probe tip, making it much harder to remove).

3.6 Manipulation with AFM

In the course of the experiments discussed in this thesis, the suitability of EBID-modified AFM probes for manipulation of biological samples was investigated. "Nanoscalpel" probes were used to create incisions in biological structures, and several methods were tested which could be applied to remove outer layers from biological samples to expose underlying structures for AFM imaging.

3.6.1 Incisions

In order to create an incision on the surface of a biological sample, a program was developed which could cut into the sample with a chosen cutting force, which would be maintained at a constant setpoint during the cut. This allowed the depth of the cut to be controlled, and prevented the force on the AFM tip becoming too large, which could damage the tip.

Incisions were made using the following procedure:

1) The manipulation program stops the AFM scan and moves the probe to the centre position of the AFM scan, with feedback enabled.
2) The probe is passed back and forth along the intended cut path with the feedback still enabled. This allows the profile of the undamaged sample surface to be recorded.
3) Feedback is disabled and the probe is raised a short distance (100-300 nm) above the surface.
4) The probe is lowered down a distance that takes it below the sample surface, cutting into a soft sample. The tip-sample force causes a deflection of the cantilever. This approach stops when a target deflection signal (corresponding to a desired cutting force) has been attained.
5) The probe is moved slowly (at a rate of 5-20 nm/s) along the cutting path. A feedback loop implemented in the manipulation program controls the z-scanner position so that the deflection signal is kept at a constant setpoint value (see chapter 8 for more details on the operation of the feedback loop).
6) The probe is retracted from the sample surface; feedback is re-enabled and normal imaging resumes.
During stages 4-6, the cantilever deflection and amplitude, scanner z-position and the correction in the z-position implemented by the feedback program are all recorded.

3.6.2 Surface removal

A number of methods were tested to remove the surface layer from cell samples. The results of these experiments, including images of structures revealed by this "nanodissection" technique, are shown in chapter 8. The first method which was

tried was the use of the Interleave controls in the AFM system to increase the tip-sample force during the Retrace scan. Each AFM scan line consists of two scans, a "Trace" scan along the initial scan path and then another in the opposite direction along the same path, the "Retrace" scan. The Interleave controls can be used to set different parameters during the Retrace scan; for example, the probe can be lifted a short distance (known as the "Lift Height") above the surface during the Retrace scan in order to sense long-range forces (for example magnetic forces if a tip containing magnetic material is used). [148]

By setting a Lift Height less than zero, the probe can be pressed into the surface during the Retrace scan to increase the tip-sample force, displacing material from the surface. Scanning areas of the surface of fixed cells using negative Lift Height was therefore used to remove material from the cell surface to expose internal structures for AFM imaging.

Another method that was used was a "raster scan"-type technique using the AFM NanoScript program to sweep the tip over both Trace and Retrace paths, scanning a rectangular area with large tip-sample force. This also displaces material from the surface to expose internal structures.

Surface removal using the "nanotome" tool (described in detail in chapter 4) was performed in the same manner as the nanoscalpel incisions described in section 3.6.1. After making an incision on the surface using this tool, the surface layer is separated from the layers beneath; this layer can then be moved aside using the tip of the AFM probe by passing it across the surface perpendicular to the initial incision.

Chapter 4

Fabrication of Nanotools by Electron Beam Induced Deposition

Electron beam induced deposition (EBID) is a nanofabrication process which allows the growth of nanoscale structures using a single-stage process within a standard unmodified SEM system. Using this technique (which is described in more detail in chapter 2), AFM tips can be easily modified to improve their aspect ratio or suitability for mechanical lithography by fabricating nanostructures on the AFM tip apex. [30–36] This chapter describes the design and fabrication of a number of novel EBID probes optimised for nanomanipulation and imaging applications. In particular, this chapter discusses the fabrication and application of "nanoscalpel" and "nanotome" probes, which can be used to make incisions on the surfaces of biological objects and for nanosurgical removal of the outer layers of biological structures. EBID probes have not previously been applied for these purposes; however, they demonstrate several advantages over standard AFM probes due to their optimisable shape and robust mechanical properties.

The basis of the EBID growth procedure described here is the fabrication of free-standing blade-like or needle-like structures, which can then be modified by further EBID processes for different applications. When fabricated on AFM probe tips, these specialised structures have a wide range of different applications as "nanotools", which can be used for AFM imaging, lithography, indentation, and the manipulation of biological objects ("nanosurgery"). [77]

4.1 Fabrication Process

In order to create a free-standing structure, the electron beam is focused on a point a short distance (∼100 nm) from the edge of the deposition substrate (typically a silicon wafer or AFM tip apex), and then a line of amorphous carbon is deposited by moving the beam toward and then beyond the edge at a rate of 1-10 nm/s. This process is shown in figure 4-1. Interaction of the primary beam electrons with atoms in the sample produces secondary electrons; these secondary electrons cause deposition of carbon in a radius of 10-30 nm around the primary beam spot, as described in more detail in chapter 2. When the beam reaches the edge of the substrate, carbon is deposited beyond the edge ahead of the primary beam creating a structure on which further deposition can occur. [37, 39, 40, 42, 58, 68, 70, 72, 149, 150] The result is the fabrication of a free-standing structure extending beyond the substrate edge; an array of free-standing structures fabricated on the edge of a silicon wafer is shown in 4-2.

The electron beam is moved in small steps (1 nm in our experiments) along a path which in our experiments ranged from 0.3-1.5 μm in length. The beam spot position, velocity and total path length are controlled using a standard electron-beam lithography system. It is possible to control the velocity at which the beam spot is moved by varying the time taken for each step (beam dwell time), which for these experiments is typically of the order of 100-1000 ms per step. Deposition occurs wherever the secondary electrons generated along the primary beam path are able to reach the surface, as long as there are adsorbed molecules present to provide the precursor supply. Growth therefore occurs around the entry and exit points of the beam on the top and bottom of the deposited structure. Some secondary electrons generated inside the structure are able to exit through the sides as well, increasing the lateral thickness of the deposited structure. Finally, deposition occurs at the tip of the structure ahead of the primary beam.

4.2 Nanoscalpel

Figure 4-3 shows a carbon blade fabricated on an AFM probe using this process. This probe had previously been damaged during its use in AFM imaging; in most of our experiments, damaged probes were used for this process so that

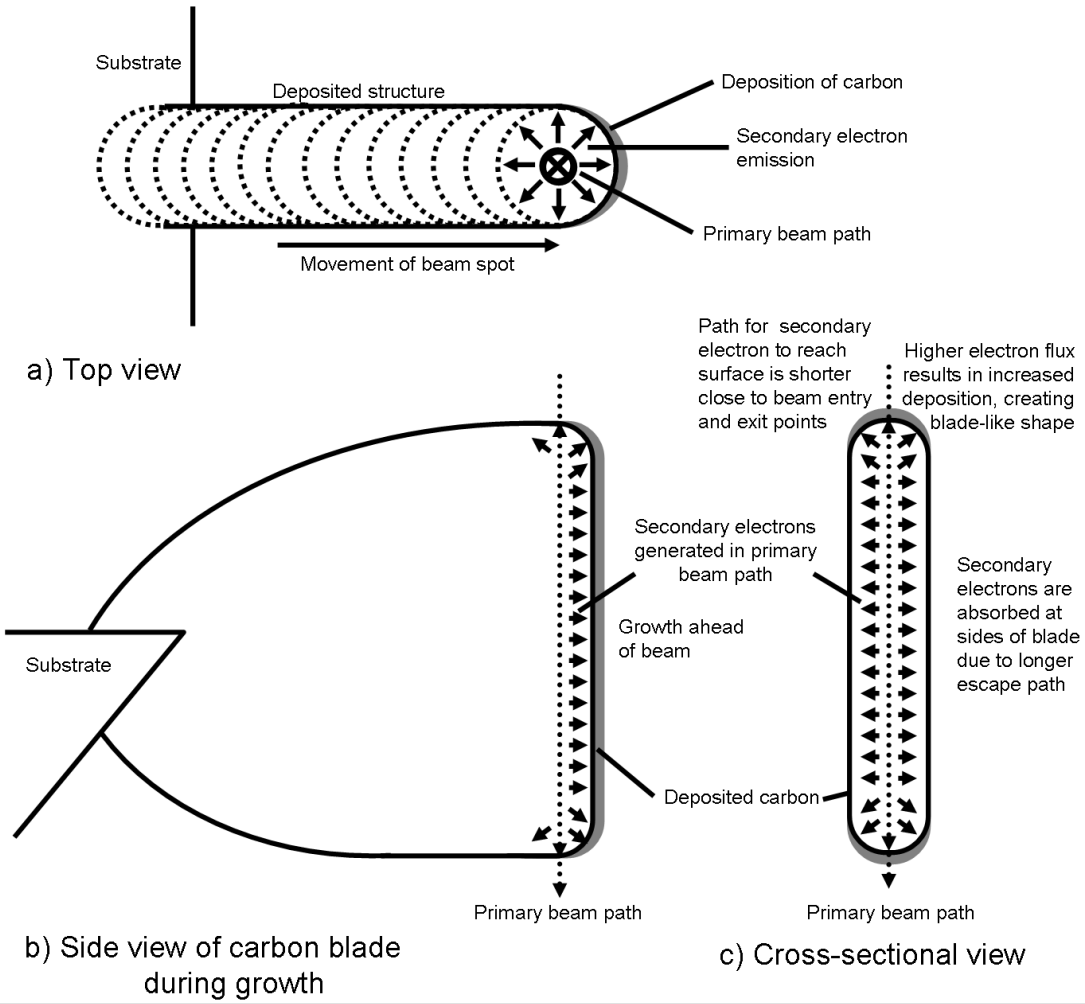

Figure 4-1: Growth process for carbon blade, shown from b) top (parallel to beam direction), b) side and c) in cross-section. The blade-like shape results from the absorption of the secondary electrons in the deposited material at the sides of the carbon blade, restricting its growth in this direction, while deposition occurs around the beam spot at the top and bottom of the structure.

they could be "recycled" by fabrication of structures on the tip. Due to their blade-like shape and applications, these structures are termed "nanoscalpels" by our group. When fabricated on AFM probes, it was previously demonstrated by our group that these nanoscalpels can be used to cut nanoscale objects, for example creating nanoscale gaps in metal films which can be used as contacts in nanoelectronic devices. [77] It is difficult to reproducibly create such gaps by conventional nanolithography techniques such as photolithography and electron

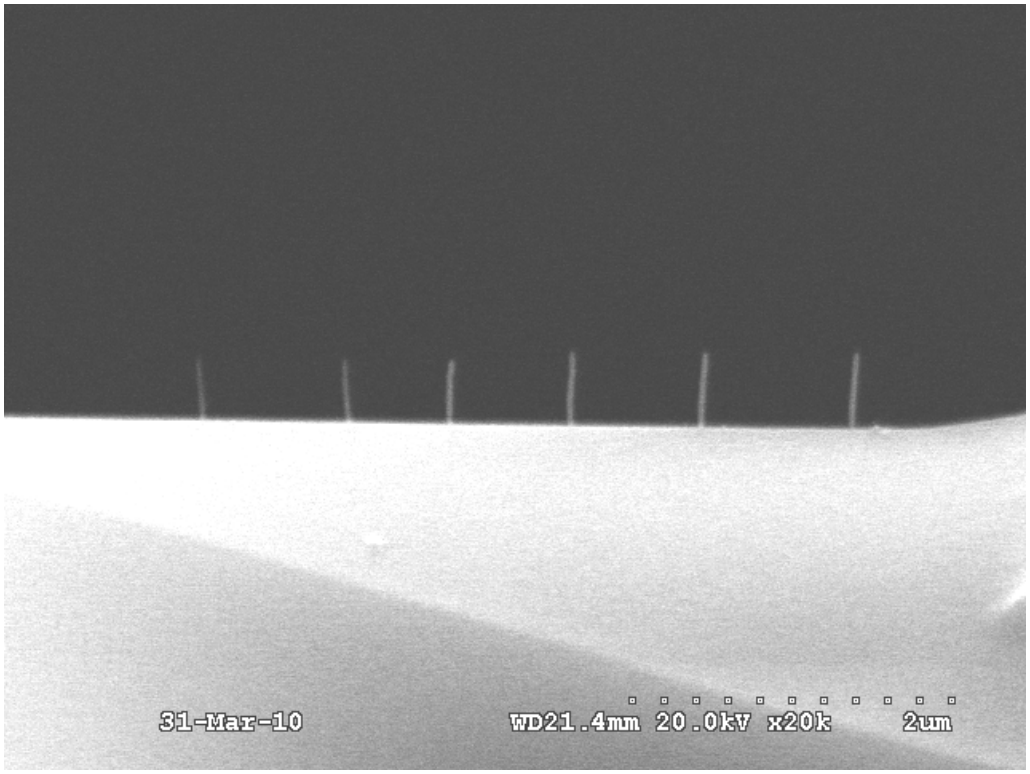

Figure 4-2: Array of free-standing carbon structures grown from the edge of a silicon substrate.

beam lithography. Chapter 8 describes how these nanoscalpels can be used in the manipulation of biological structures ("nanosurgery") where they have a function similar to a macroscopic surgical scalpel.

Amorphous carbon is a robust material compared to the more brittle, crystalline silicon or silicon nitride used in standard AFM probes, which are often damaged during nanomanipulation. This means that the nanoscalpel blades can be used for manipulation without any detectable damage to the carbon blade. Their shape and high aspect ratio also allows them to cut a sample down to large depths without loss of lateral precision, which is impossible using standard AFM probes due to their pyramidal shape which results in a wider incision as the cut depth increases. [77]

a)

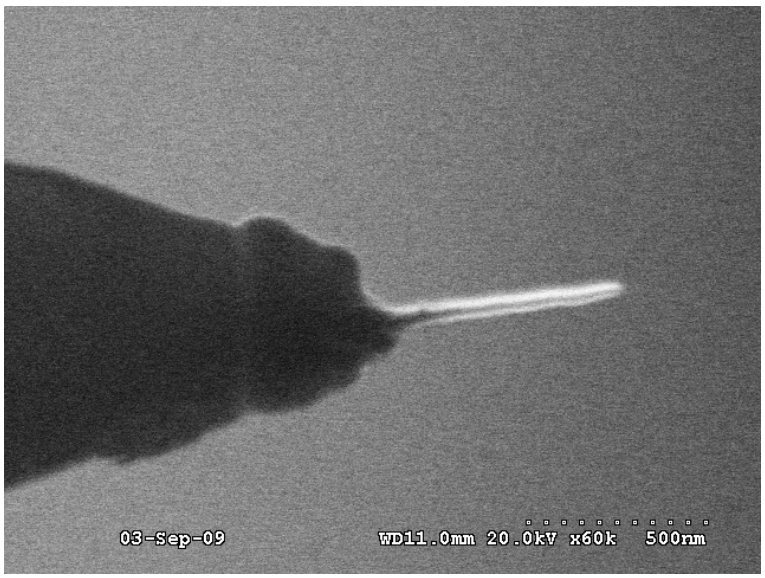

b)

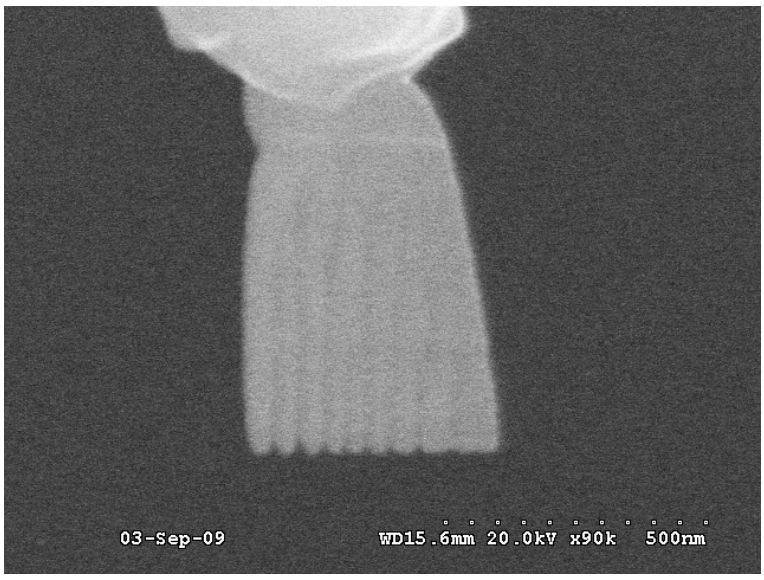

Figure 4-3: Carbon blade imaged from the edge immediately after growth on a damaged AFM probe (a) and from the side after re-mounting the probe rotated 90 degrees (b). Note the presence of parallel striations in the surface of the carbon blade, which appear a short distance from the blade base.

4.3 Carbon Blade Dimensions

The lateral thickness of the deposited blade depends on the escape depth of the secondary electrons. Due to their low energy, these electrons are not able to travel far from the primary beam path through the deposited structure. This means that the growth of the structure is restricted in the lateral direction. However, secondary electrons are able to escape more easily close to the entry and exit points of the primary beam, meaning that more rapid growth occurs on the top and bottom of the structure. This results in a flat, blade-like structure which grows in the plane of the primary beam. The growth process is shown in the diagram in figure 4-1.

In our experiments, we investigated the effect of time for each step of the deposition process (beam dwell time) on the dimensions of the carbon blades. Increasing the dwell time increases the time available for the deposition of carbon. Deposition on the upper and lower edge results in an increased blade width with increased beam dwell time (shown in figure 4-4). The thickness of the blade is also increased at lower beam spot velocities.

Figure 4-4 shows the evolution of the thickness of the deposited blade as a function of the beam dwell time. The thickness is observed to follow a very similar trend to that often observed in the fabrication of other structures by electron-beam induced deposition, such as nanopillars grown by stationery beams [19,26,29,33]; an initial nucleation phase followed by rapid growth and saturation. Similar evolution of thickness was noted by Gazzadi *et al* in the deposition of free-standing structures. [42] The lateral thickness of the blade saturates due to the limitations of secondary electron escape depth, which prevents the secondary electrons reaching the blade surface at the sides of thicker blade.

In figure 4-5, the same results for the blade width and thickness are presented as a function of the beam spot velocity (which is inversely proportional to beam dwell time). Of interest is that a regime exists at high beam spot velocity where the width and thickness are similar; the resulting structure has a high-aspect ratio "needle-like" shape which makes an ideal probe for AFM imaging of steep topographic features on a sample surface. These structures are discussed in more detail in section 4.7 and in chapter 5.

For very small dwell times, no growth extends beyond the substrate edge. This

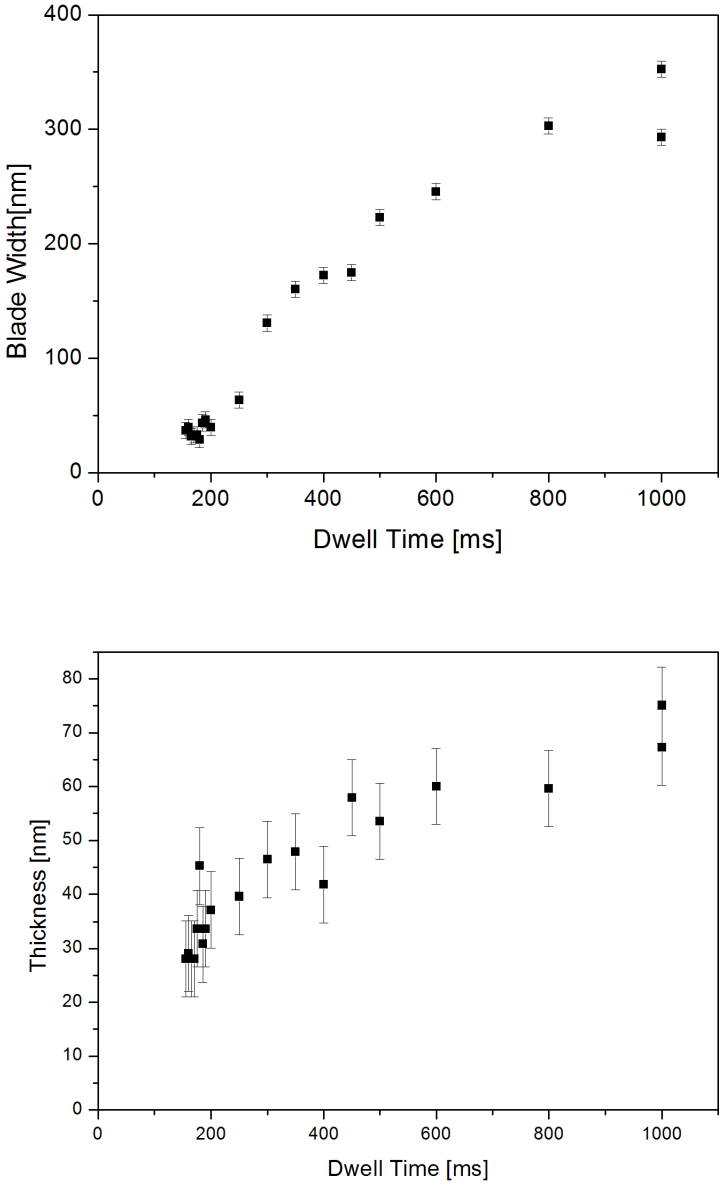

Figure 4-4: Width and thickness of the deposited carbon blades as a function of beam dwell time.

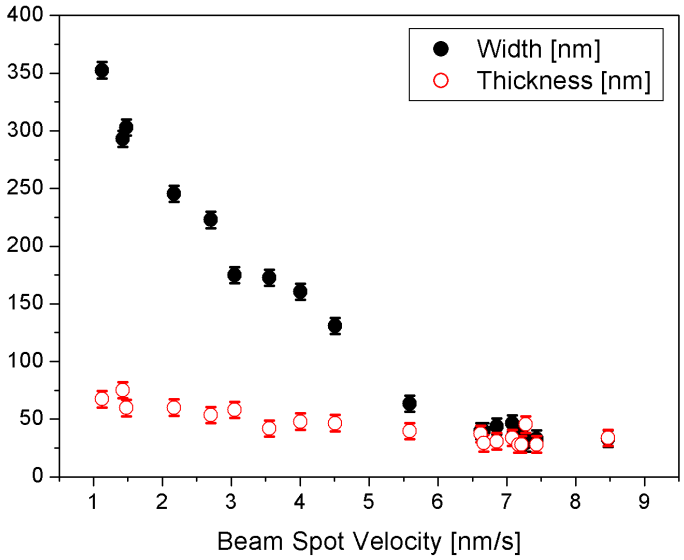

Figure 4-5: Effect of beam spot velocity on dimensions of deposited carbon blades. At high beam spot velocity, "nanoneedle" structures are fabricated with a circular cross-section.

indicates that the beam has overtaken the rate of deposition of carbon, probably because there is insufficient time the formation of enough deposit beyond the substrate edge to support the structure.

4.4 Effect of Primary Beam Current

Increasing beam current could be expected to increase the rate of deposition of carbon by increasing the primary electron flux, and therefore increasing the rate of production of secondary electrons. However, several studies have showed that this applies only at small beam currents (∼10 pA); at larger beam currents, the deposition rate decreases with increasing current [33, 35]. This has been attributed to heating effects from the primary beam causing a decrease in precursor concentration [33].

In contrast, our experiments indicated a clear increase in carbon blade width with increased beam current, even for currents from 80-150 pA. This is shown in figure 4-6. This result contradicts the findings of previous authors; however,

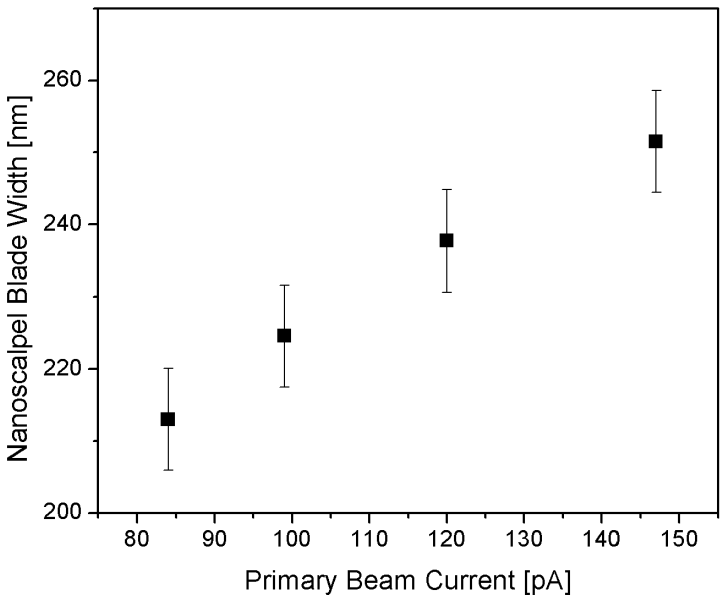

Figure 4-6: Effect of primary beam current on the width of the deposited carbon blades.

their experiments concentrated on the growth of pillars parallel to the electron beam using a stationary beam spot, which results in the whole structure being irradiated by the primary electron beam for the full duration of the growth. If heating effects are the cause of the decreased deposition rate, it would be expected that these would be more significant in this situation. Deposition of a free-standing structure using a moving beam spot (as in our experiments) exposes only part of the whole structure to the beam at any time, and the exposure time of any one part of the structure to the primary beam is shorter. This would tend to reduce the impact of heating effects. With the depletion of the precursor molecules as a result of heating reduced, the increased secondary electron flux at higher beam currents causes an increase in the rate of deposition.

4.5 Structure of a Carbon Blade

The structure of the deposited blades is of interest since wider blades are observed to grow as an array of parallel filaments, which can grow close enough to form a

blade, or separately. [37,40,42,58,149] A carbon blade composed of such filaments produced in our experiments is shown in figure 4-3. This phenomenon has not yet been satisfactorily explained. It was noted by Gazzadi *et al* that filaments did not form in deposited platinum structures but were visible in structures deposited using a tetra-ethyl-ortho-silicate (TEOS) precursor, while Mølhave *et al* observed them in gold nanostructures. [42, 58] The separation into filaments often occurs after the blade has already grown some distance from the substrate, suggesting that the effect is due to decreasing precursor supply as precursor molecules are decomposed in the deposition process. Möllenstedt suggested that diffusion of the precursor causes a reduction in precursor concentration around growth sites, preventing growth in the regions between filaments. [149]

Another effect that occurs occasionally when fabricating free-standing structures is the growth of several separated parallel structures in place of a single blade. This tends to occur when the growth substrate does not possess a well-defined edge to support the growth. The high-energy primary electron beam can penetrate deep into the growth substrate, and deposition can occur at any point where the secondary electrons generated are able to reach the surface. Using the formulae derived by Kanaya and Hawakatsu [151, 152], it can be shown that the penetration range of a 20 kV electron beam into both amorphous carbon and silicon is $\sim$5 μm.

When growing free-standing structures by the method described above, it is therefore possible that there is more than one site where secondary electrons reach the substrate surface, creating multiple parallel growths. This effect is particularly pronounced when attempting to grow a carbon blade on a pre-existing blade, as the corrugations observed in the first blade create multiple deposition sites for the growth of subsequent blades. Examples of both these effects are shown in figure 4-7. Similar parallel growths were observed by Lui *et al* and Mølhave *et al* when growing free-standing tungsten structures from thin substrates and vertical pillars, which were also attributed to the presence of more than one growth site. [40, 58] This technique has been exploited to deliberately produce multiple structures in a single exposure. [153]

The parallel growths which are produced tend to remain separated and do not merge during growth. These blades are also tend to be narrow, creating a fragile structure which is not generally suitable as a tool for nanomanipulation

a) 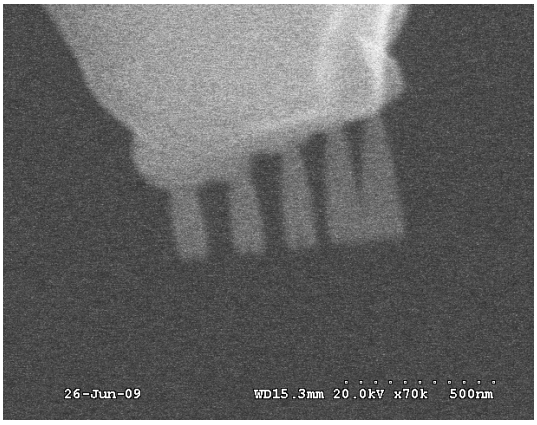

b) 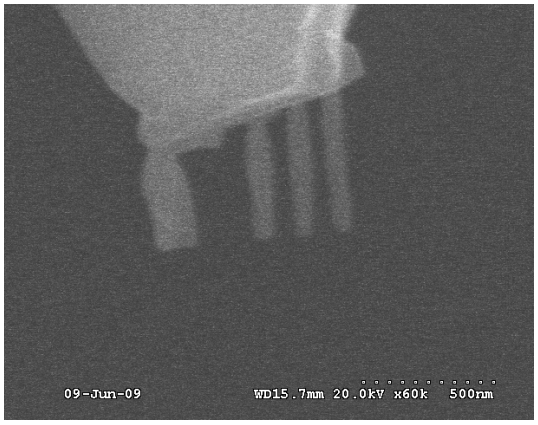

c) 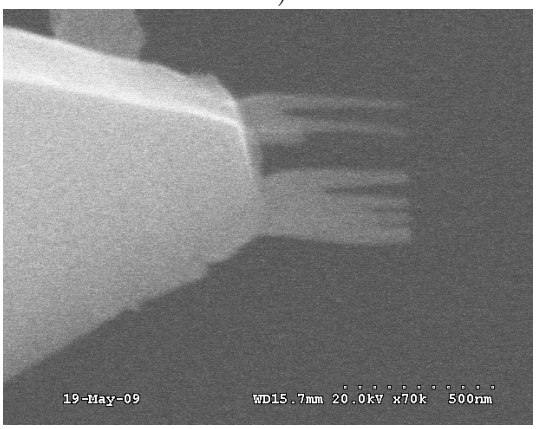

Figure 4-7: Growth of multiple carbon structures on AFM tips. a) and b) show multiple growths forming on the same tip due to the present of multiple sites for the nucleation of carbon. c) shows the division of growing structures into separate carbon filaments.

since it is too delicate, and not suitable for use as an AFM probe due to the presence of multiple blades which create imaging artifacts. This may be caused by the accumulation of charge close the the beam spot during the deposition, which would tend to repel secondary electrons (and possibly also ionised precursor molecules) and so prevent deposition in the gaps between the blades. This effect has also been proposed as an explanation of the formation of the filament-like structures in single blades. [42]

It is possible that these two phenomena are related, with the uneven deposition resulting in an increased number of nucleation sites for growth, each of which grows a filament.

Since the resulting multiple growths are generally too brittle for use in nanoma-

nipulation, it is desirable to avoid these effects. This requires that the substrate edge from which a carbon blade is grown is relatively sharp, with only a single site from which the growth will originate. This can be achieved by careful selection of the growth site and probe shape; however, if the nanotool is to be fabricated on a damaged probe this is not always possible.

Therefore, in our experiments we developed a process which produces a well-defined growth site by the initial growth of a short pillar on a tip, which is then used as the growth site. The pillar is grown using a spot exposure to a height of ∼100 nm; an example is shown in part a) and b) of figure 4-8. Following this, the probe is remounted to image the pillar from the side, and a carbon blade is grown from the pillar (see part c) of figure 4-8). It can be seen in part d) of this figure that this process results in the growth of a single wide blade due to the well-defined single growth site. This method unfortunately will result in a nanoscalpel with a very narrow, brittle base. However, the base can be strengthened by the deposition of further carbon"buttress" structures to reinforce adhesion of the carbon blade to the AFM tip; this is shown in figure 4-9.

4.6 Observation of cut off in extended structures

When attempting to grow free-standing structures by electron-beam induced deposition, it was observed that structures tended not to grow beyond ∼500 nm for small beam dwell times. In order to grow longer structures, it is necessary to increase the beam dwell time, decreasing the beam spot velocity. [58] This effect, and the maximum stable length attained for filaments grown with different beam spot velocities, is shown in figure 4-10. This limit on the length of free-standing structures grown by this technique was also noted by Mølhave *et al*, Gazzadi *et al* and Lui *et al*. [40,42,58] Lui *et al* noted that it could be exploited to create structures with very small tip diameters (1-2 nm) since the diameter of the deposited filament decreases as the precursor is depleted. In chapter 5, the fabrication of nanoneedles with very small diameters is demonstrated using this technique.

Since it occurs most significantly in rapidly-grown structures, this cut-off effect cannot be attributed to instabilities due to drift in the electron beam lithography

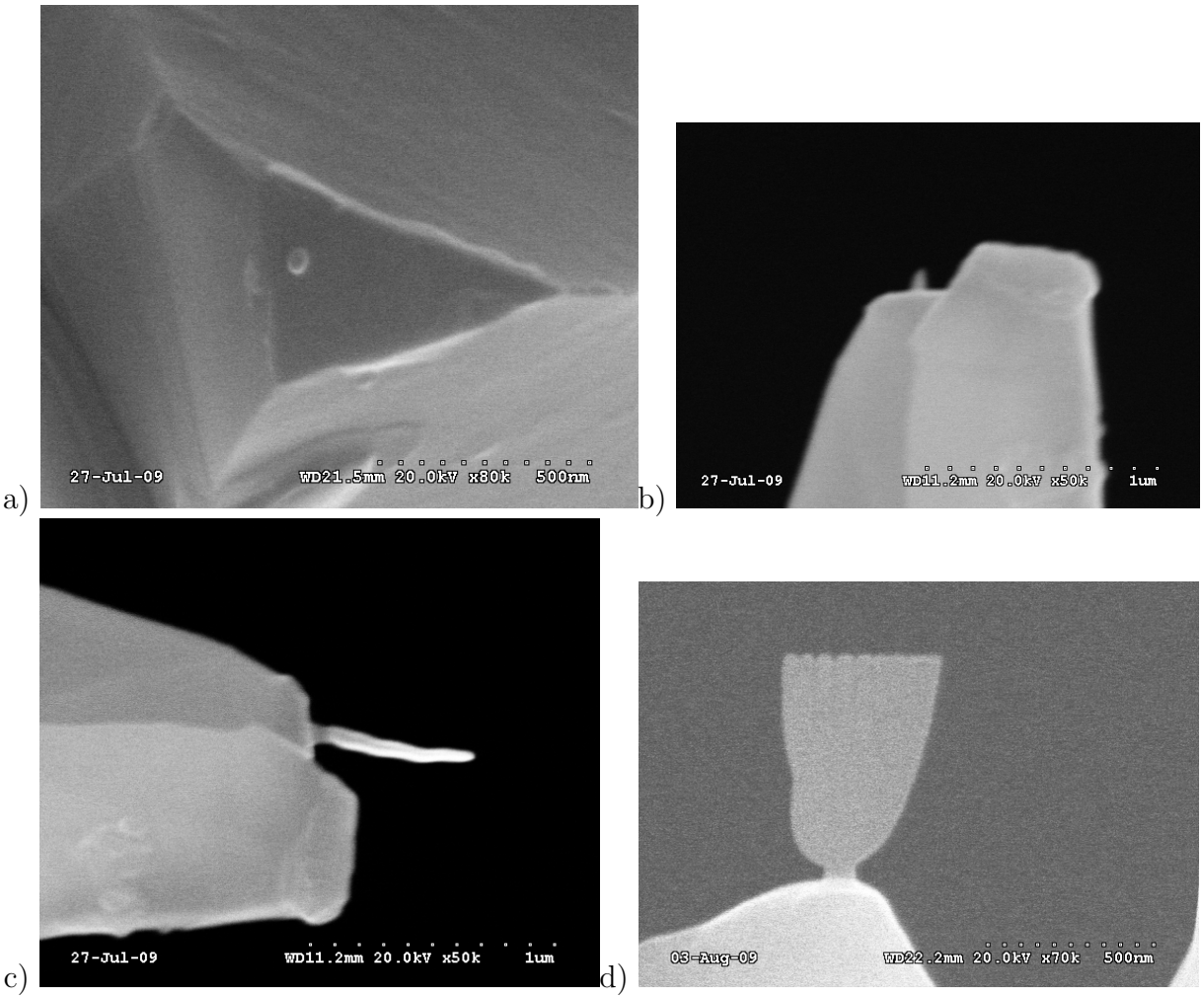

Figure 4-8: a) Growth of short pillar on damaged AFM probe apex using stationary spot exposure. b) Pillar imaged from side. c) Growth of carbon blade on pillar imaged immediately after growth. d) Image of blade from side.

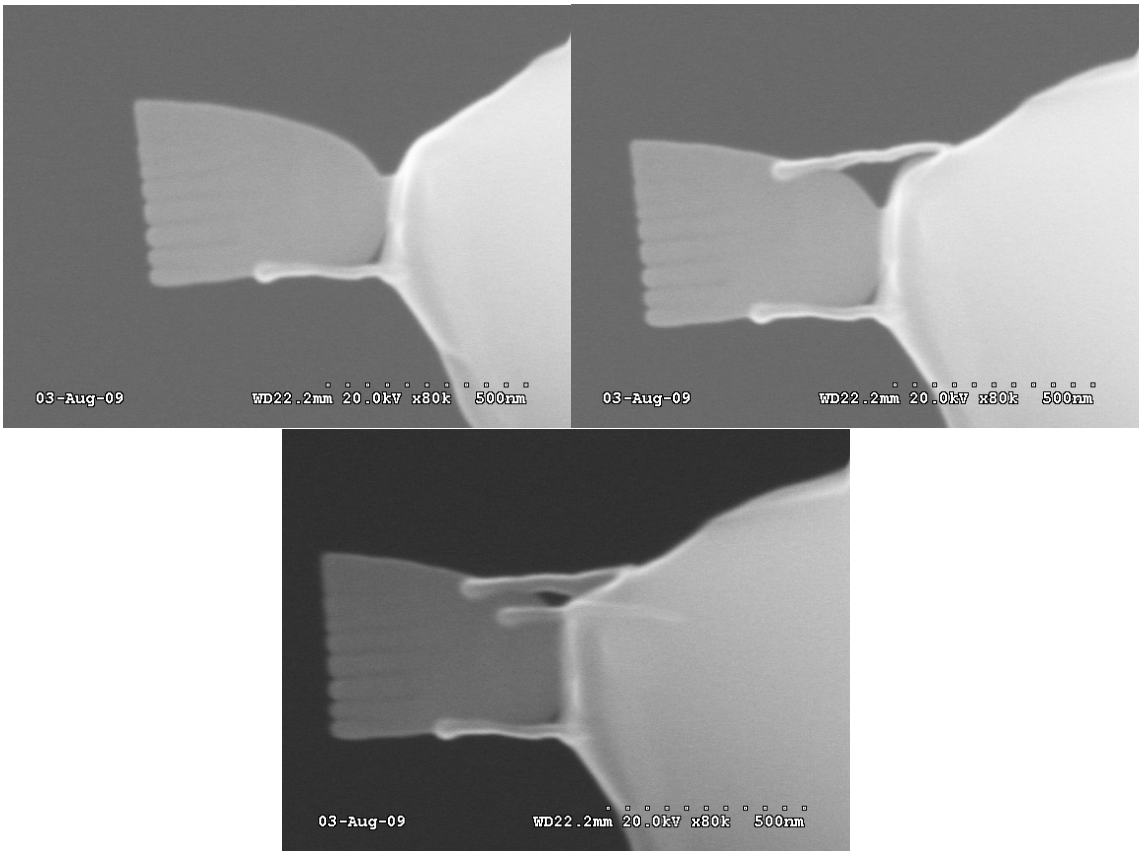

Figure 4-9: Growth of additional carbon structures reinforcing adhesion of a carbon blade to the AFM probe. The three images show reinforcement of the same carbon blade shown in figure 4-8.

system, as drift effects should become more significant for slower beam spot velocities. It is most likely that this effect occurs due to depletion of precursor molecules to the extent that no further growth can occur. In the case of rapid growth, there is insufficient time for the diffusion of hydrocarbon molecules to replenish the available precursor.

There is significant evidence that the principle route of replenishment of hydrocarbons for EBID is the diffusion of adsorbate molecules across the substrate surface, rather than diffusion of gaseous contaminants present in free space within the vacuum chamber. [50, 51] In the case of longer free-standing structures, the increased length of the diffusion path further restricts the supply of precursor molecules, and the precursor supply decreases as the filament becomes longer. Eventually, the deposition is not sufficient to create a stable free-standing structure and the filament growth stops.

4.7 Nanoneedles

In figure 4-5, it is clear that there is a regime of growth at the highest beam spot velocities in which the carbon nanostructures deposited by EBID have approximately equal width and thickness. These structures have a circular cross-section with a diameter of 20-40 nm. When fabricated on AFM tips, these structures can be used as high-aspect ratio AFM probes with a small tip radius. These slender "needle-like" probes demonstrate elastic buckling behaviour under large tip-sample forces, similar to probes modified by attaching a carbon nanotube to the probe tip. [154,155] This behaviour protects the tip and sample from damage by limiting the tip-sample force.

Imaging these structures after their fabrication results in the deposition of more carbon around the needle, increasing its diameter. This stabilises the needle and prevents buckling, allowing it to exert larger forces on the sample. This also allows the strengthened needle to function as a rigid indenter which can be used to determine mechanical properties of samples, including biological structures. This application of the nanoneedle probe is discussed in more detail in chapter 7.

Nanoscale needles mounted on AFM tips fabricated by other techniques such as focussed ion-beam milling have also been used in previous studies for other

a)

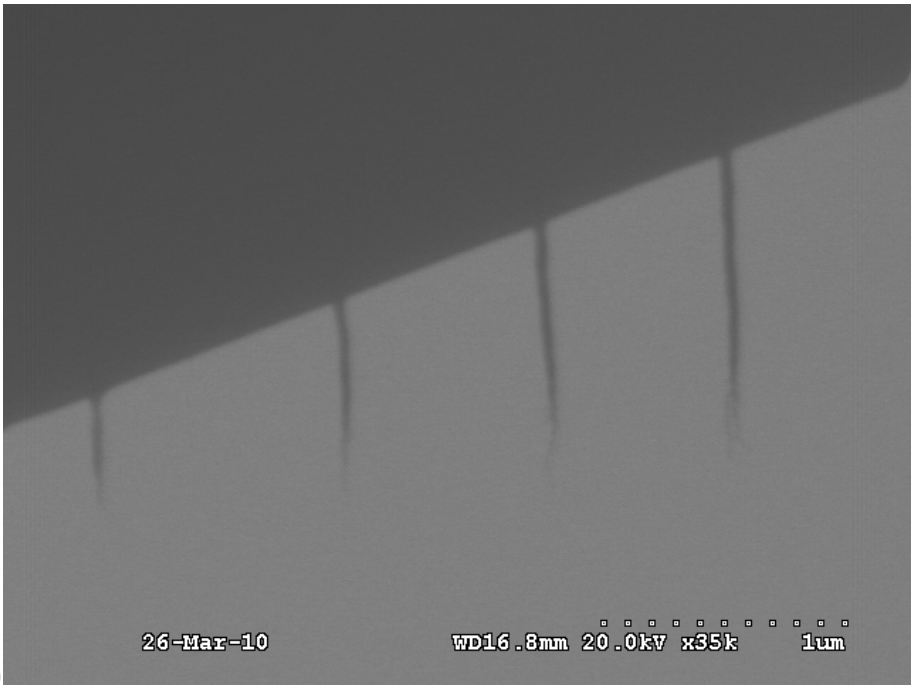

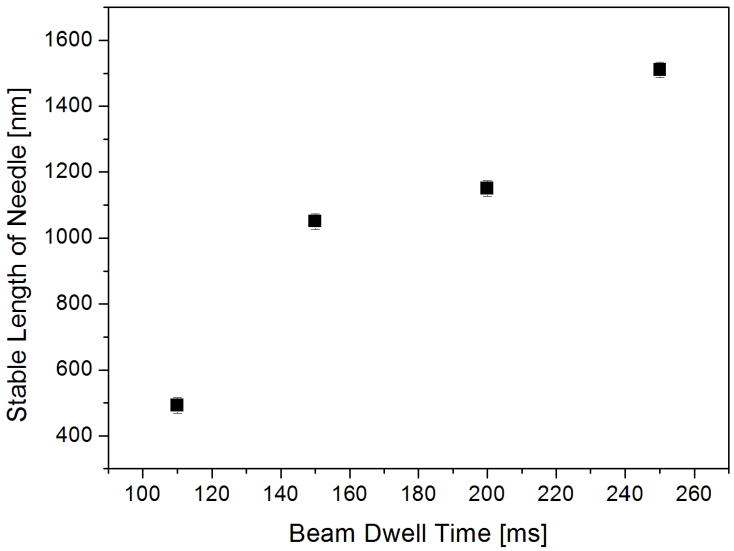

b)

Figure 4-10: a) Filaments growth using different beam dwell times. In each case, the target length of the filament was 1.5 μm. b) Attainable lengths of free-standing structures at different beam dwell times.

biological applications such as the injection of biomolecules adsorbed onto the needle into biological cells, in a similar manner to a macroscopic hypodermic

needle. [130–132] Carbon nanotube probes stabilised against buckling by polymer- or carbon-coating [134, 135] have also been applied for this purpose, and EBID nanoneedles and other nanostructures have been used for the extraction of DNA from cell nuclei. [153]

The fabrication, buckling dynamics and applications, including biological applications, of nanoneedle AFM probes are discussed in more detail in chapter 5.

4.8 Other nanotool designs

One application of AFM manipulation is the removal of surface layers of biological objects to reveal underlying structures for imaging and further manipulation. [125, 126] A variety of techniques for achieving this goal using AFM nanosurgery are discussed in chapter 8. It is desirable to achieve this goal as quickly as possible due to both experimental time constraints and the drift in AFM systems, and therefore a nanotool which can remove an area of surface quickly would be useful for this application.

In order to fabricate such a tool, the EBID process described here was used to fabricate two parallel blades supporting a single suspended filament of amorphous carbon, which can separate surface layers from a biological object in the manner of a vegetable peeler. The parallel blades separate the sides of the layer from the surrounding surface while the suspended filament cuts beneath the layer to separate it from the structures underneath. This structure has been termed a "nanotome" by our group.

This structure was fabricated by first depositing the two parallel blades at the apex of an AFM tip, and then remounting the tip after rotating it so that a carbon filament can be deposited across the tips of the blades. Rotating the tip ensures that only a single point on each blade is exposed to the primary beam, preventing the growth of multiple filaments originating from different deposition sites (see section 4.5 for more information on this phenomenon). The diagrams in figure 4-11 show the fabrication process for this structure. Examples of these structures are shown in figures 4-12. Similar suspended structures have been previously fabricated by EBID on pre-existing EBID structures, though usually supported by cylindrical pillars rather than flat blades. [40, 70, 72]

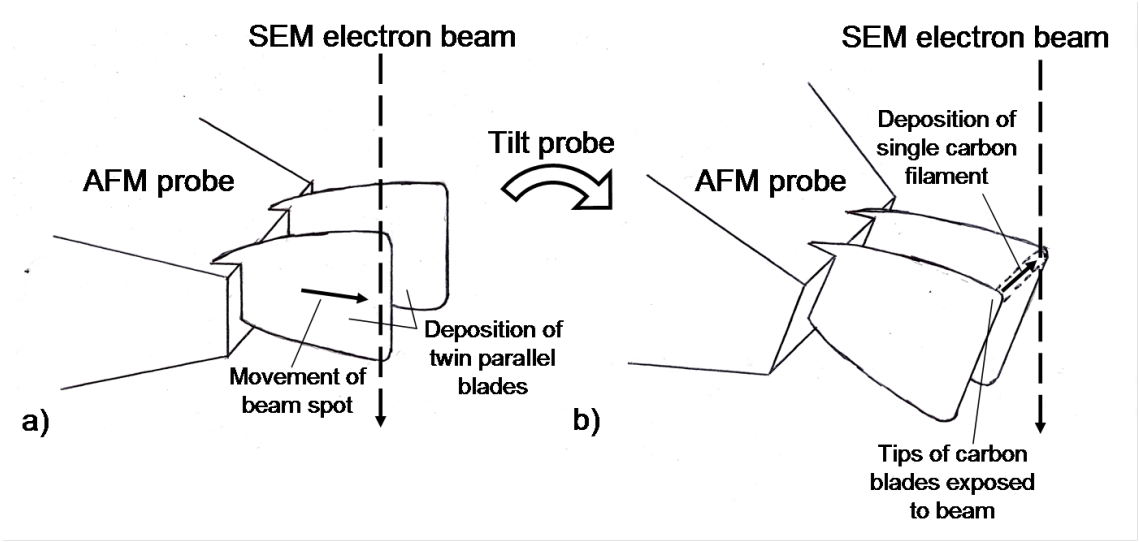

Figure 4-11: Two stages of the process of fabricating a suspended carbon filament "nanotome". a) Deposition of parallel carbon blades on an AFM probe tip. b) Deposition of a single carbon filament across carbon blades after rotating the structure such that only the tips of the carbon blades are exposed to the primary beam.

As well as its applications in nanomanipulation, this structure could also be applied as a nanoscale resonator. Tranverse oscillations could be induced in the flexible, elastic carbon filament by periodic excitation e.g. mechanical or electromechanical oscillation. The fundamental resonant frequency of a 500 nm-long, 20 nm-diameter filament of carbon suspended in this way would be ~120 MHz assuming an elastic modulus for the deposited carbon of ~28 GPa (as measured in chapter 6). [156] The potential applications and advantages of EBID structures as resonating components in nanoelectromechanical sensing systems are discussed in more detail in chapter 6.

The flexible nature of the carbon blades also suggests that they can be used as nanomechanical elements in a tweezer-like device fabricated on an AFM tip. Such devices have been fabricated previously using EBID structures, and also carbon nanotubes, as the jaws of the tweezers. These can be opened and closed using piezoelectric elements, thermal expansion effects, or by charging the tweezers such that they are opened by electrostatic repulsion and close elastically when the charging potential is switched off. [157–159] Such tweezers have been used for the manipulation of nanospheres and other nanoscale objects.

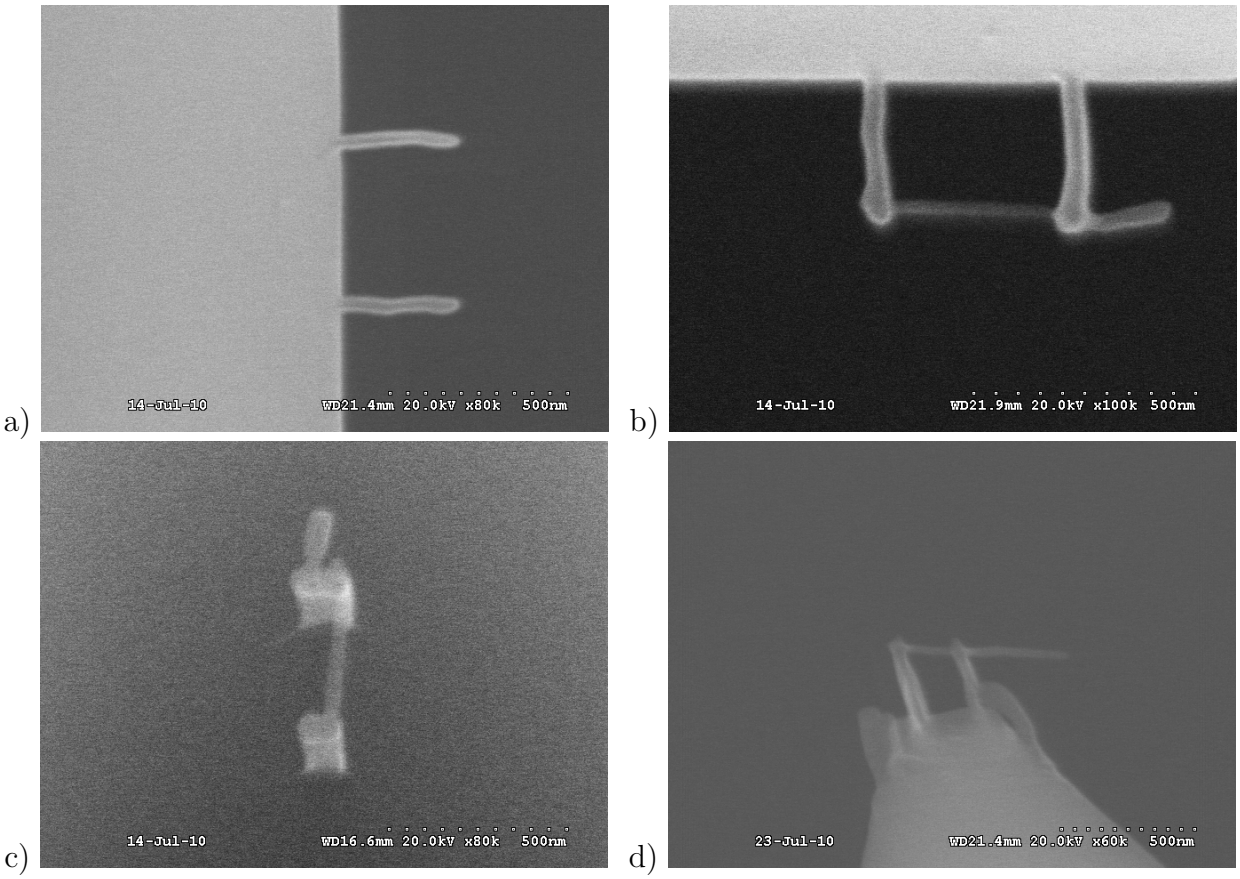

Figure 4-12: a) Parallel growths on edge of silicon wafer. b) Suspended filament growth between carbon blades shown in a) after tilting the structure to expose the tips of the carbon blades. c) Same structure imaged from above using SEM, showing that only a single carbon filament extends between the upright carbon blades. d) Suspended filament and carbon blades on AFM tip, forming a nanotool which can be used to remove layers of surface material from a cell.

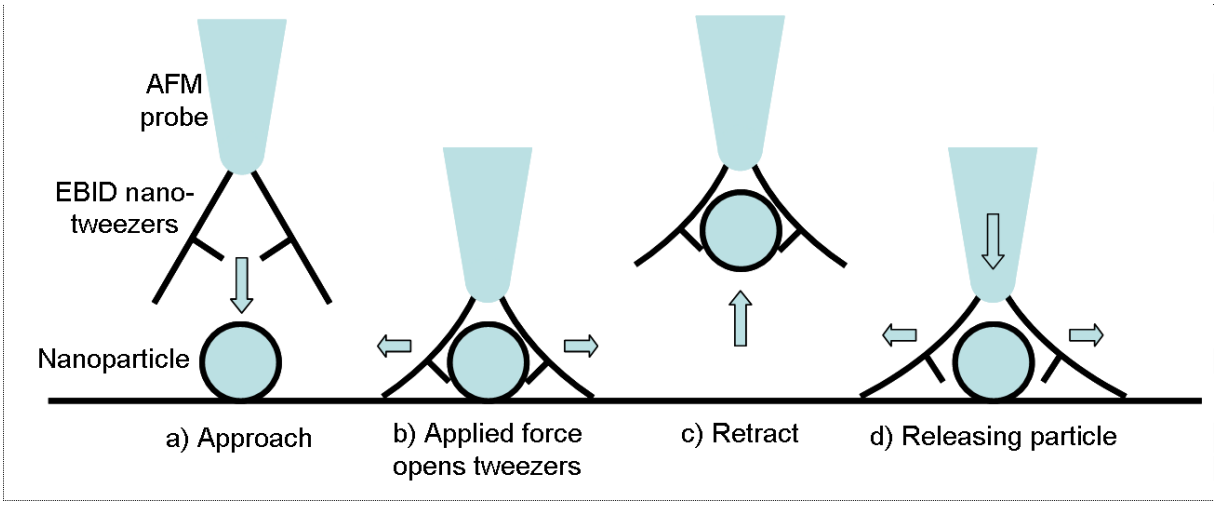

Figure 4-13: Process of picking up a nanoparticle using mechanical EBID nanotweezers. Force applied to the probe opens the tweezers around the nanoparticle, and their elasticity closes them around the particle when the force is removed. The same process is used to release the particle at a chosen site.

Another route proposed here for the actuation of such nanotweezers is purely mechanical actuation based on the flexibility of the carbon blades. A carbon structure could be fabricated such that the jaws of the tweezers are forced open when a large force is applied to the nanotool using the AFM system. When this force is removed, the elasticity of the blades would cause them to return to their original shape, closing the tweezers around the nano-object to be manipulated. This elastic behaviour would allow them to maintain a firm grip on the nanoobject until it is released at a desired site by further application of sufficient force. The process of picking up and releasing a nano-object using such a nanotweezer device is shown in figure 4-13.

Figure 4-14 shows the fabrication process for the proposed mechanical nanogripper. Initially, two diverging carbon blades are fabricated from the edge of silicon wafer used as a test substrate. In order to be used for nanomanipulation, such a structure could be fabricated on an AFM tip instead. In the second growth stage, additional growths are deposited on the carbon blades, which act as the "jaws" of the nanogripper, creating a gap of $\sim$200 nm.

The ability to fabricate these different structures for different nanomanipulation applications illustrates the adaptability of EBID structures for a wide variety of different purposes. The flexibility of the carbon blades would also allow them to

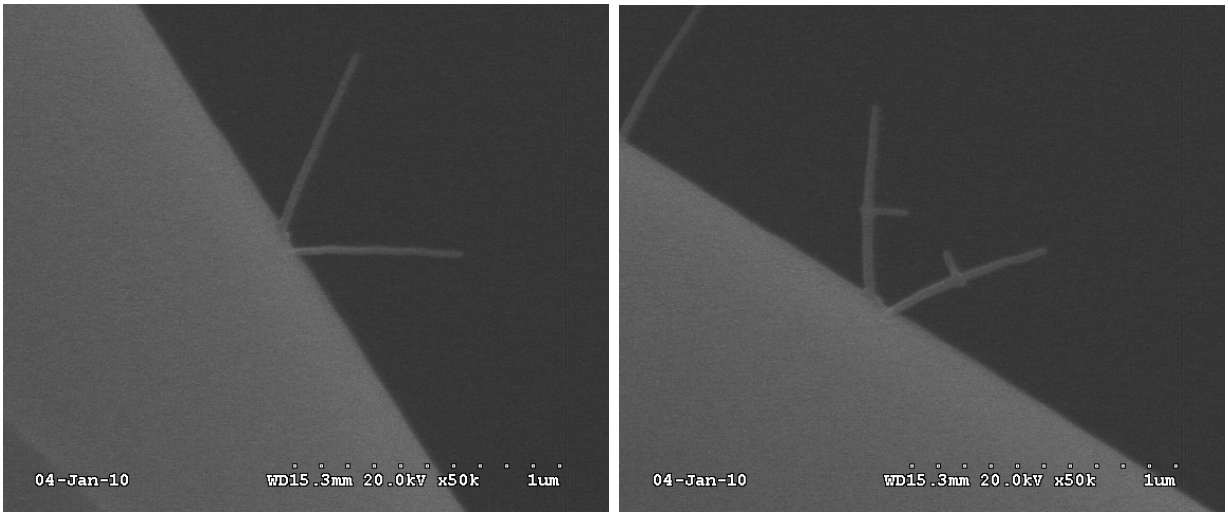

Figure 4-14: Fabrication of "nanotweezers".

act as components in nanomechanical devices, including sophisticated mechanical nanotools such as a the nanotweezers described above.

4.9 Summary and Conclusions

This chapter describes the fabrication processes for a variety of free-standing structures using a method of electron-beam induced deposition (EBID). This technique can be used to modify AFM probes for different manipulation applications, creating nanoscale tools. These tools demonstrate several advantages over standard unmodified AFM probes; their shape can be controlled and optimised for specialised applications, and the amorphous carbon that makes up the probes is robust compared to the comparatively brittle silicon or silicon nitride used in standard AFM probes.

Fabrication of a free-standing blade-like carbon structure on an AFM probe creates a "nanoscalpel" probe which can be used to cut and dissect objects imaged in an atomic force microscope. Their use in manipulation of biological cells is discussed in more detail in chapter 8. The dimensions of this structure can be controlled by varying the beam current and beam spot velocity used in the growth process. Optimisation of this process can create a "nanoneedle" probe with a circular cross-section, small diameter and tip radius, and high aspect ratio, all of which are highly desirable properties for AFM probes. These probes are

further discussed in chapter 5.

A diverse range of other nanotools can be fabricated for different nanomanipulation applications, including "nanotweezers" and a novel "nanotome" device consisting of a suspended carbon filament supported between two nanoscalpel blades. The nanotome is designed to separate the upper layers of a biological sample from those underneath, in order to expose internal structures for imaging *in situ*.

It is therefore shown that electron beam induced deposition can be used to fabricate a wide variety of specialised "nanotool" AFM probes for different applications. These tools can be applied for AFM imaging, nanomanipulation and nanoindentation studies, and present advantages over standard AFM probes due to their robust nature and specialised design.

Chapter 5

Nanoneedles

In chapter 4 it was noted that free-standing carbon blades fabricated using electron-beam induced deposition became thinner and narrower when grown more rapidly, due to decreased time for the deposition of carbon and replenishment of the precursor supply. At higher beam spot velocities, a regime of growth is observed in which the thickness and width of the deposited structure are very similar, resulting in a filament-like or needle-like structure with a circular cross-section, instead of a flat blade. This effect can be seen in figure 4-5.

The resulting structures are termed "nanoneedles" by our group. These structures are of diameters ∼20–40 nm, and function as ideal high-aspect ratio AFM probes for tapping mode imaging. These structures can be fabricated with tip diameters <10 nm. It is advantageous for an AFM probe tip to have a high aspect ratio as this allows it to accurately profile steep gradients on sample surfaces, such as high vertical steps. Typically, these cannot be accurately profiled using standard AFM probes due to the probes' pyramidal shapes. The modification of AFM probes to improve their aspect ratio has been achieved in the past by electron-beam induced deposition, [30–36] by focussed ion beam milling, [130,131] and by the attachment of carbon nanotubes to the AFM tip. [154, 155, 160, 161] Of these techniques, EBID provides the simplest method for the fabrication of very thin needles, requiring only a single growth stage.

The flexibility of the deposited nanoneedles also gives them advantages when used as AFM probes. In our experiments we were able to show that the needle will buckle if the force applied to it by the AFM system becomes too large, and that much of this deformation recovers elastically when this load is removed.

This suggests that thin nanoneedle tips are resistant to breaking, since they will bend and recover elastically under large forces rather than break, similar to the behaviour observed for probes using a carbon nanotube as the AFM tip. [154,155]. This property of high-aspect ratio probes is similar to that which is often observed in carbon nanotube AFM probes, which are also subject to buckling under large forces.

Nanoneedle probes can be used for biological applications, as discussed in section 5.7. Similar needle-like probes fabricated by focussed ion beam milling or attachment of carbon nanotubes have been used to inject small quantities of biomolecules (such as DNA) into cells or cell nuclei. [130–135] In chapter 7 it is demonstrated that the nanoneedle probes can also be used as indenter tools to probe the mechanical properties (e.g. elastic modulus) of biological structures. Due to their shape, they can penetrate deep into such objects to measure the properties of their internal structures, without causing extensive damage to the cell structure. However, the buckling of the needle limits the maximum force which can be exerted by the needle. In order to stabilise the nanoneedle probe against buckling so that it can exert large forces on a sample, additional carbon can be deposited onto it by SEM imaging after fabrication. This coats the needle, increasing its diameter. This stabilisation process is described in section 5.4.

5.1 Growth of Nanoneedles

In a similar manner to the fabrication of a carbon blade, a nanoneedle is fabricated by moving an electron beam beyond the edge of the growth substrate or AFM tip, causing deposition of a free-standing carbon filament extending into the vacuum of the SEM chamber. If the beam spot velocity is high, the resulting structure is not blade-like but instead forms a thin filament with an approximately circular cross-section. Figure 5-1 shows a nanoneedle fabricated on an AFM probe tip.

For very high beam spot velocities, no growth extends beyond the substrate edge. This indicates that the beam has overtaken the rate of deposition of carbon, probably because there is insufficient time for diffusion processes to replenish the precursor supply. The thinnest nanoneedles can be grown close to this cut-off point where the beam spot velocity is highest.

The circular cross-section of the filaments grown with high beam spot velocity

a)

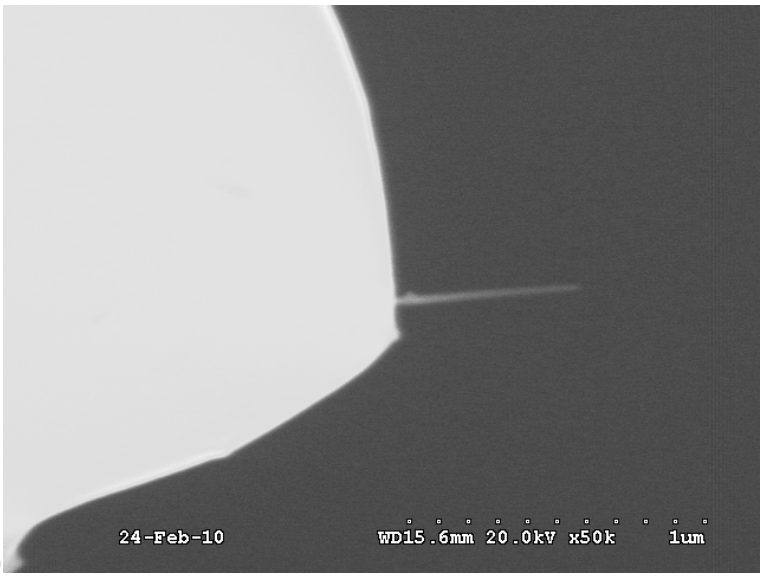

b)

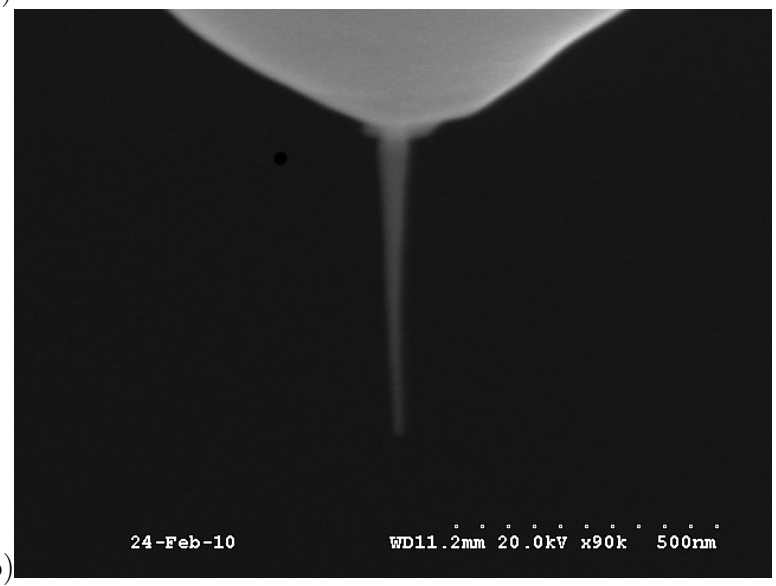

Figure 5-1: Nanoneedle fabricated on AFM probe imaged from side immediately after growth (a) and front after rotating 90 degrees (b).

suggests that deposition is occurring at a uniform rate on all sides of the structure, indicating that the secondary electron flux is also uniform around the needle circumference. This may be due to the small diameter of these structures, which means that regardless of their point of origin along the primary beam path, and the path they take in order to escape from the structure, the secondary electrons will not be absorbed in the deposited structure but will instead reach the surface. This results in a uniform secondary electron flux, and therefore deposition rate, around the circumference of the needle.

This method of fabrication of nanoneedle tips is significantly different from the widely-used technique of growing the needle parallel to the beam direction. In the case of growth of a needle parallel to the beam, a stationary electron beam is used to create a pillar of deposited carbon which grows around the beam spot, as described in chapter 2. [29,30,33,35] The technique of growing a free-standing needle perpendicular to the electron beam axis has several advantages over this method; pillars grown by a stationary beam spot generally grow more slowly, and so their shape is subject to greater distortion due to drift and instabilities in the electron beam system. In addition, the diameter of longer pillars is determined by the maximum escape depth of the secondary electrons and so the pillars are generally thicker. Fabrication of thinner pillars by this method requires additional post-processing stages such as sharpening the probe using etching techniques. [35]

In contrast, the technique presented here can produce much thinner needles more quickly. The quicker fabrication reduces the effect of drift on the shape of the needle, making it easier to produce straight needles. The resulting straight needles with a small tip radius are ideal for application as AFM probes.

5.2 Nanoneedle Probes for AFM Imaging

In our experiments, we were able to use nanoneedles fabricated on AFM probes as tips for the imaging of samples in dynamic (Tapping) mode. The needle acts as a high-aspect ratio AFM probe, allowing the accurate profiling of high, vertical features on the surface of a sample.

For high-resolution AFM imaging, it is desirable that the tip has a small effective tip radius. In order to determine the tip radius of the fabricated nanoneedles, gold nanoparticles with a known, narrow size distribution (∼20 nm diam-

eter) were deposited from solution on a freshly cleaved highly-ordered pyrolytic graphite (HOPG) surface, and imaged using a nanoneedle probe. An example of an image of these particles is shown in figure 5-2. The tip radius can be determined from these images using a simple calculation, modeling the tip apex as a spherical surface. This method of tip characterisation is often used to determine AFM tip sharpness. [162] In this experiment, the tip radius was calculated to be 13 ± 3 nm. To demonstrate the capability of EBID nanoneedle probes to image samples with high, steep features, a standard AFM calibration grid sample was successfully imaged in Tapping Mode using these probes (an example of such an image is shown in figure 5-3.)

It has been shown that it is possible to grow free-standing structures of smaller diameters (8-10 nm) using high-energy electron beams in scanning transmission electron microscopes (STEM) [40, 75], and that the sharpness of EBID probes can be improved by oxygen plasma etching [35] after growth. This would allow the creation of probes with even smaller tip radii for higher resolution imaging. In section 5.3, experiments in the fabrication of thinner needles using our EBID technique are described.

It is possible to obtain high-aspect ratio carbon nanotube tips with very small tip radii (1-2 nm) but their fabrication is more complex compared to single-stage fabrication of a nanoneedle probe by EBID. Typically, carbon nanotubes are either fabricated separately and then manipulated onto the tip using micromanipulation systems [154] or grown on the tip apex *in situ* using chemical vapour deposition techniques [160, 161]. The latter requires prior patterning using photolithography or electron beam lithography to deposit a catalyst onto the tip apex. Both of these are multi-stage, time-consuming processes, compared to the rapid fabrication of EBID nanoneedles using a single pass of the electron beam.

5.3 Growth of Needles with Small Tip Radii

It is possible to fabricate very thin needles by exploiting the decreasing surface precursor concentration as the needle grows longer. This is due to the increasing length of the diffusion path for the precursor molecules along the needle surface, and is discussed in more detail in chapter 4. Figure 5-4 shows a needle the diameter of which decreases significantly towards the tip, resulting in a very

a)

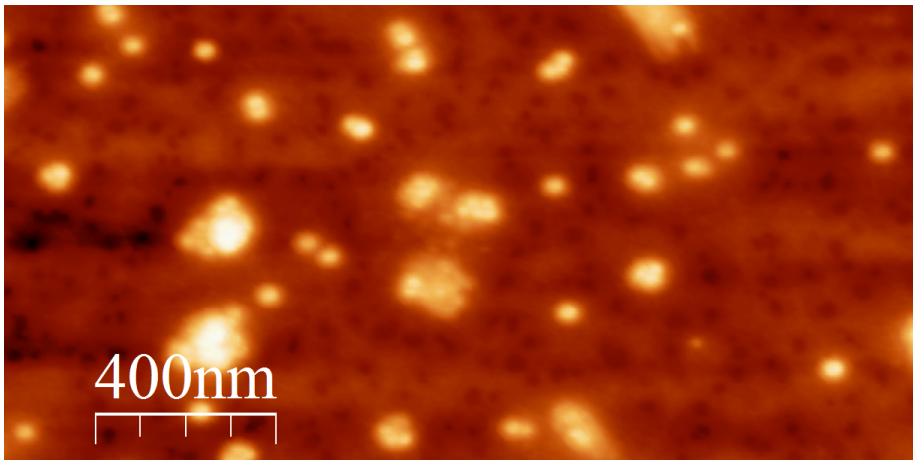

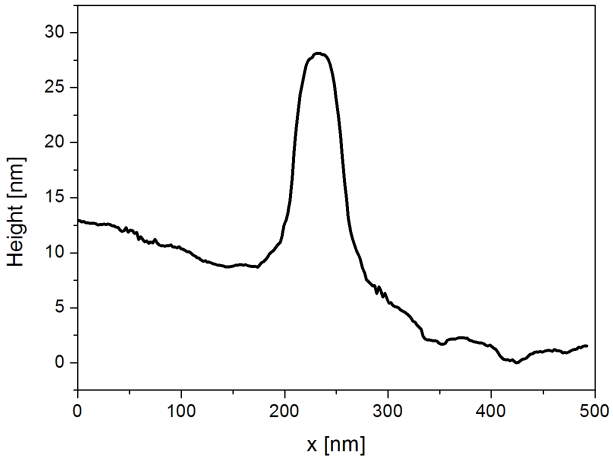

b)

Figure 5-2: a) Image of gold nanoparticles deposited onto HOPG surface, captured using nanoneedle AFM probe. b) Topographic profile of a single nanoparticle.

a) 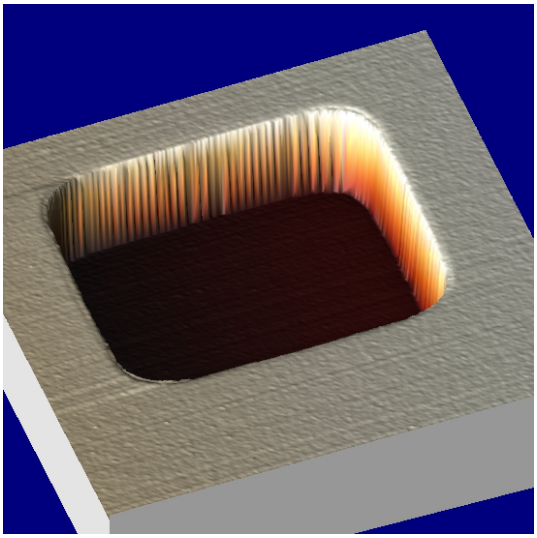 b) 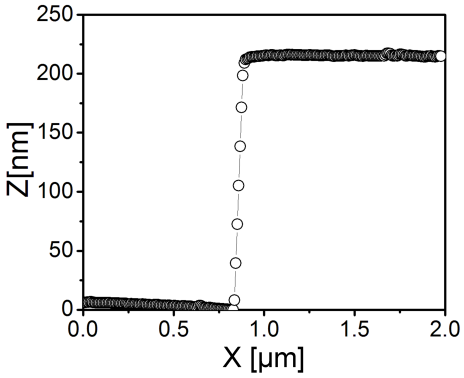

Figure 5-3: a) Calibration sample pit imaged using nanoneedle AFM probe. (Imaged area is 8x8 μm.) b) Profile across edge of pit.

small tip radius (measured in the SEM as <5 nm.) Therefore, if a very long needle is fabricated, its diameter will decrease as it becomes longer. This effect was noted by Liu *et al*, who suggested it could be used to produce structures with very small tip radii. [40] Figure 5-5 shows a needle fabricated with a long target length.

Using this technique, nanoneedles could potentially be produced with tip radii as small as those attainable using carbon nanotube AFM probes (1-2 nm). This would allow nanoneedle probes to be used for high resolution imaging of samples with very steep surface gradients.

5.4 Effect of Exposure after Growth

Carbon deposits will form on almost any structure irradiated by the electron beam. [14–16, 19] If a fabricated structure is exposed to the primary electron beam after growth by imaging using the SEM in normal scanning mode, additional carbon is deposited. The structure is enlarged, increasing in both width and thickness, as shown in figure 5-6. It can be seen from figure 5-7 this effect preserves the shape of the structure's cross-section; nanoneedle structures retain their circular cross-section, although their diameter is enlarged.

a) 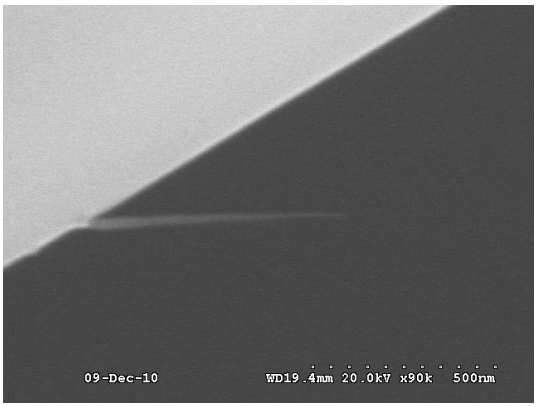

b) 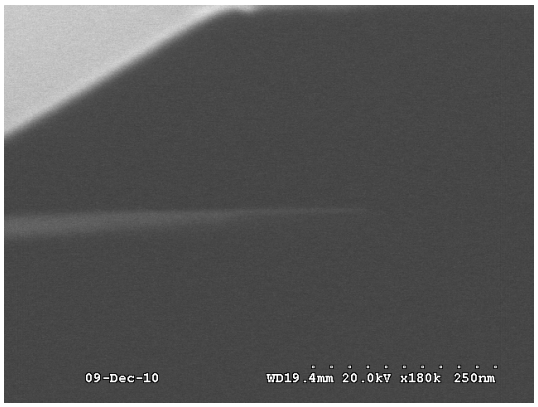

Figure 5-4: a) SEM image of needle grown with very small tip radius. b) Image with increased magnification. Measurement in the SEM showed that the tip radius is <5 nm.

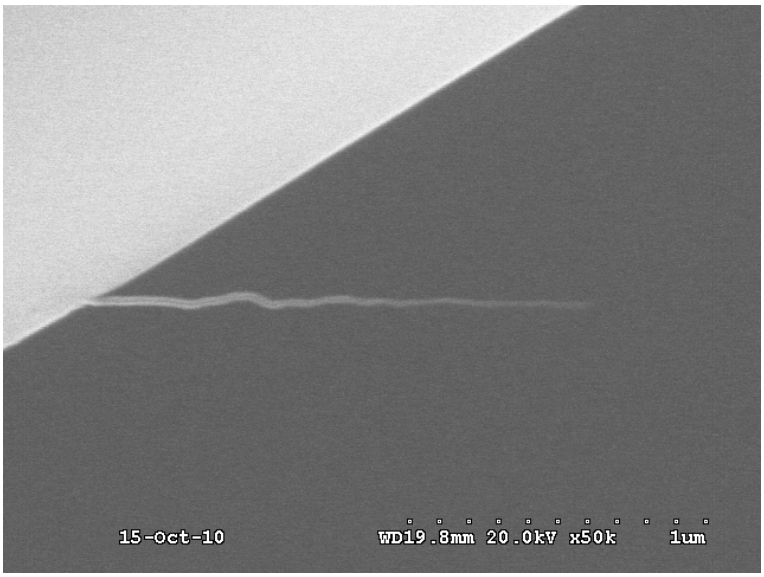

Figure 5-5: Needle grown to a length of 1.5 μm. The needle diameter decreases as the growth extends further from the substrate due to decreasing surface precursor concentration.

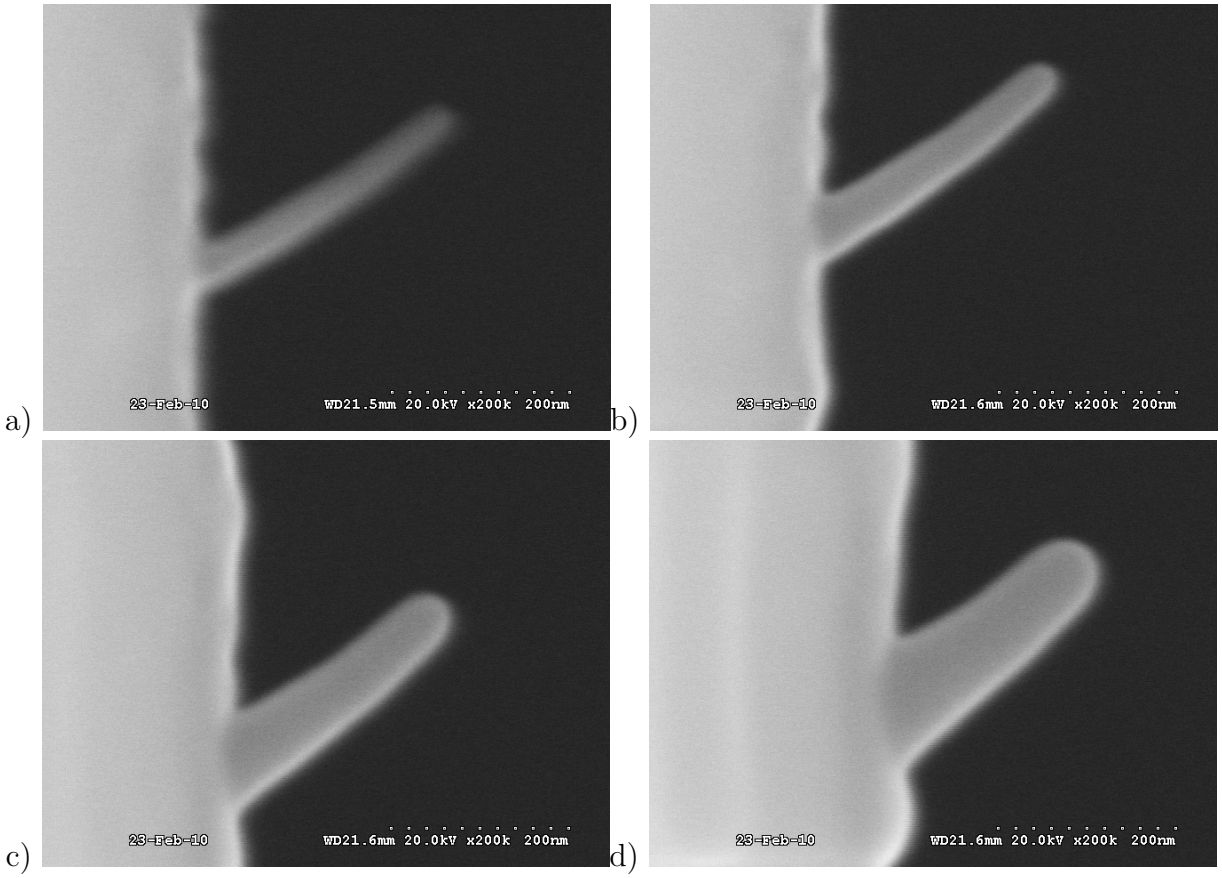

Figure 5-6: Process of thickening nanoneedle by imaging using SEM to deposit additional carbon. Image a) shows the needle immediately after growth; images b)-d) show the effect of b) 5 minutes, c) 15 minutes, and d) 30 minutes exposure.

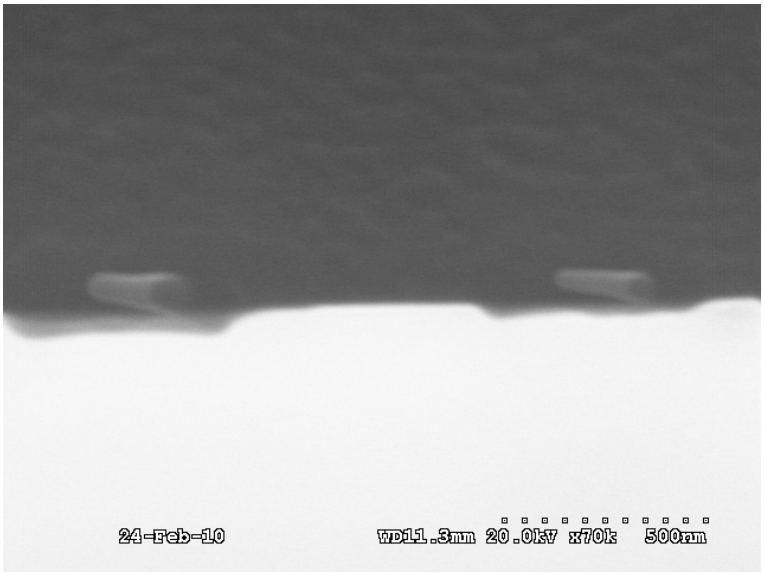

Figure 5-7: Thickened needles on the edge of of a silicon wafer imaged along the needle axis, showing circular cross-section.

Enlarging a nanoneedle would seem to be detrimental to its usefulness as an AFM probe because the tip radius is increased. Smaller tip radii are generally desirable for AFM probe tips as they improve the attainable resolution of an AFM image. However, the increased diameter increases the resistance of the needle to bending, allowing it to exert larger forces on the sample. Specifically, the critical buckling force which will cause the needle to begin bending is significantly increased, even if the diameter of the enlarged needle is as little as 40 nm, as discussed in section 5.6. Such a needle can be used as a rigid indenter to determine mechanical properties of a sample, such as the hardness or elastic modulus, from analysis of AFM force curves. An example of a needle fabricated on an AFM probe and then stabilised in this way is shown in figure 5-8.

The preservation of a circular cross-section during exposure suggests that the rate of carbon deposition is uniform on all sides of the deposited structure, and not concentrated only on the surfaces irradiated directly by the primary electron beam. Scanning the beam over the structure during imaging stimulates secondary electron production at all points on the exposed upper surface of the structure. Due to their high energy, the electrons in the primary beam penetrate the structure without significant attenuation and cause production of secondary electrons at both their entry and exit points, meaning that deposition also occurs

a) 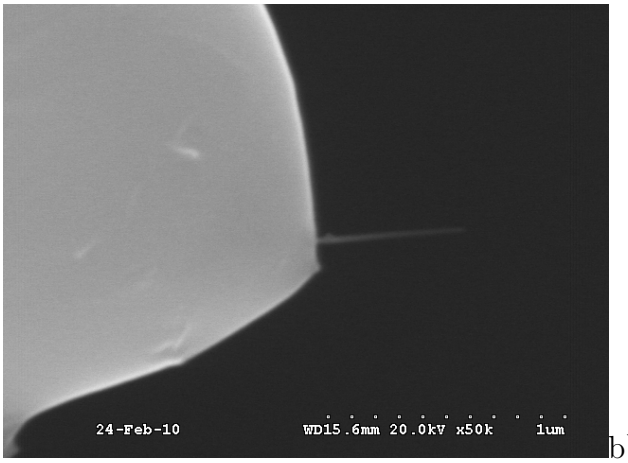

b) 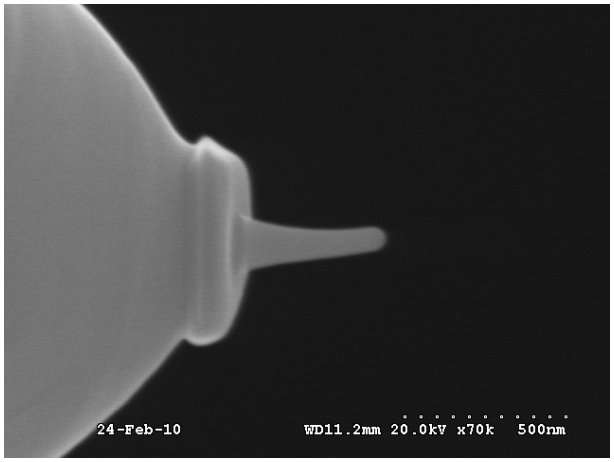

Figure 5-8: Nanoneedle on AFM probe a) before and b) after exposure for ∼25 minutes (depositing additional carbon). The needle diameter has increased from 30 nm to 75 nm at the tip. Note that a ring of additional carbon is deposited around the needle base due to exposure of the AFM tip itself to the beam during imaging.

at the same rate on the lower face of the structure which is not directly exposed to the primary beam.

Figure 5-9 shows the evolution of the needle dimensions as a function of exposure time. The needle diameter initially increased rapidly, but gradually the rate becomes slower as the supply of precursor molecules absorbed onto the needle is depleted by the primary beam faster than they can be replenished by diffusion effects.

There is also a tendency for initially relatively cylindrical nanoneedle structures to become thicker at the needle base during exposure. This effect can be explained if one considers the depletion of the concentration of adsorbed precursor on the surface of the needle by the deposition process. Once depleted, the precursor is replenished by diffusion of molecules across the structure and substrate surface, resulting in a gradient of precursor concentration with the greatest concentration, and therefore the highest deposition rate, near the needle base. This effect is similar to that noted in many experiments during the deposition of carbon over an area by imaging in the SEM, where the deposition rate is highest at the edges of the exposed area. This increased deposition rate can be explained due to more rapid replenishment of the precursor supply at the edges of the exposed area. This replenishment is mainly due to surface diffusion of precursor

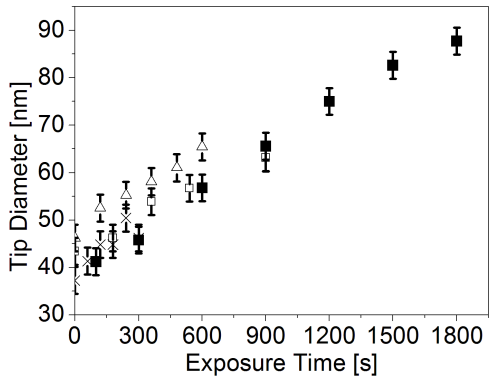

a)

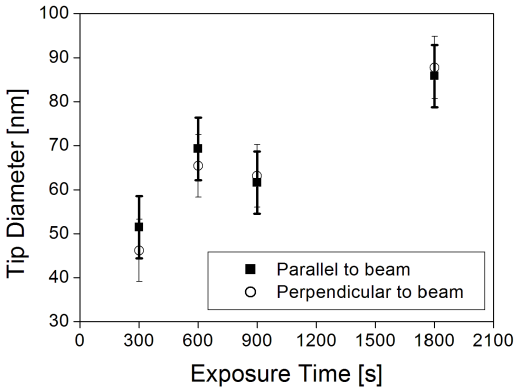

b)

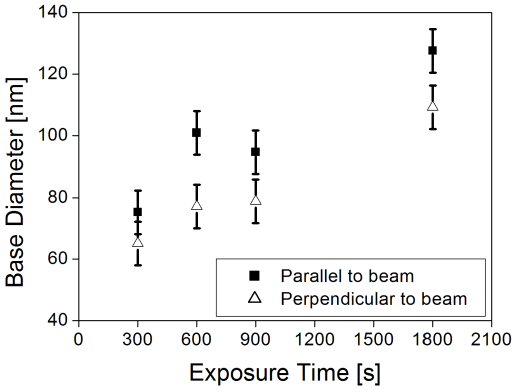

c)

Figure 5-9: a) Evolution of tip diameter measured for 4 different nanoneedles thickened by exposure to electron beam. (Different symbols indicate different needles.) b) Final tip diameters measured parallel and perpendicular to beam, indicating circular cross-section of the resulting needles. c) Diameter of needle base.

molecules and therefore occurs more rapidly at the edges of the deposit due to diffusion of precursors from the surrounding substrate. [50, 51, 64]

5.5 Buckling Effects in Nanoneedle Probes

In the case of a high-aspect ratio nanoneedle probe, the flexibility and elasticity of the carbon filament makes the probe much more resistant to damage than its fragile appearance would suggest. In the event of the AFM tip-sample force becoming too large, the nanoneedle will buckle rather than break.

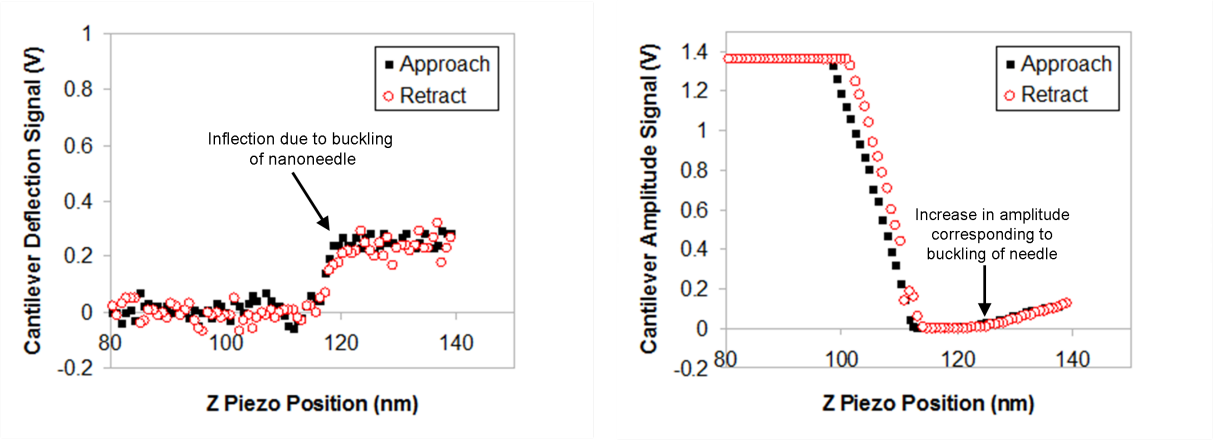

Figure 5-10: Variation of cantilever deflection and amplitude during indentation on a rigid substrate using a nanoneedle AFM probe of ~20 nm diameter. The saturation of the deflection curve is caused by buckling of the nanoneedle probe, preventing the tip-sample force from increasing above the critical buckling force. Note the lack of significant hysteresis in the curves (particularly the deflection curve) indicating elastic recovery of the needle. The small hysteresis observed in the amplitude curve is most likely due to drift in the AFM piezoelectric scanner during the indent.

The force curves shown in figure 5-10 demonstrate the buckling of the nanoneedle during an indent on a rigid silicon wafer. The probe was approached toward the surface in tapping mode, with the cantilever oscillated close to its resonant frequency. On making contact with the surface, the amplitude of the oscillating cantilever drops to zero. Once the amplitude reaches zero, the cantilever deflects. The tip-sample force is increased until the needle buckles (the inflection point labeled in the deflection curve in figure 5-10). After buckling, an increase in the

oscillation amplitude is noted as the buckling of the needle allows the cantilever to oscillate again (at the point labeled in the amplitude curve in figure 5-10).

On withdrawal from the surface after a small deformation of the needle, both the deflection and amplitude recover without hysteresis in the force curve, indicating that the needle has returned to its original length. This indicates that the needle is deformed elastically. Similar buckling behaviour is observed for carbon nanotubes mounted on AFM probes, which demonstrate similar force curves [155].

When the deformation of the needle becomes larger, hysteresis is observed in the deflection curve. However, only very small hysteresis occurs in the amplitude curve between the approach and retract. This would indicate that the needle is still deformed elastically as it is able to return to its original length. The hysteresis in the deflection curve is therefore attributable to slipping of the needle tip across the surface when the buckling effect becomes large enough. This effect is shown in figure 5-11. In region A of the force curve in this figure, no buckling occurs; once the force increases, the needle buckles. Under small tip-sample forces, the needle tip is stabilised against slipping across the surface during buckling by friction and adhesion forces (region B of the curve). As the tip-sample force increases, the lateral force on the needle tip overcomes this and the needle tip becomes free to slide over the surface. This reduces its resistance to deformation, allowing some of the cantilever deflection to relax; this is observed in region C of the deflection curve. During the retract, the needle does not return to the state shown in diagram B of figure 5-11, and this results in a different force response of the AFM cantilever which is observed as a hysteresis effect in the deflection curve (region D). However, the needle is still able to recover its original length elastically (diagram E).

At very large deformations, the needle undergoes some inelastic deformation. In our experiments the threshold for inelastic deformation seemed to be vertical deformation equal to $\sim$60% of the length of the nanoneedle, determined by the onset of hysteresis between the approach and retract amplitude curves recorded during buckling of the needle.

If the needle is fabricated not on the tip apex but instead offset by a few hundred nm, then the bending of the needle under an applied force eventually brings the rigid silicon tip into contact with the surface, preventing further bend-

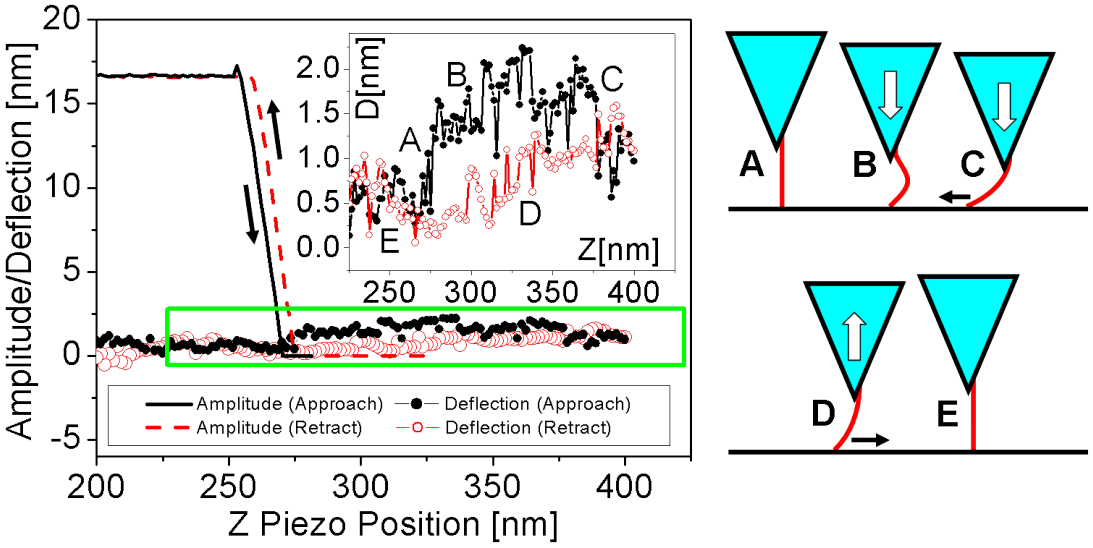

Figure 5-11: Effect of a ∼30 nm diameter nanoneedle tip becoming free to slide across the surface during buckling, resulting in a hysteresis effect between approach and retract deflection curves. Diagrams A-E correspond to different regions of the deflection curve, showing the shape of needle during buckling (region outlined on main graph, enlarged in inset). These regimes are discussed further in the main text.

ing of the needle. This prevents the needle from bending enough that it deforms inelastically or breaks, or exerts sufficient strain on the needle base to detach it from the AFM tip. This means that in the event of a "tip crash", where the tip-sample force becomes large enough that the tip or sample might be damaged, the needle will remain unbroken and can be used for further AFM imaging.

5.6 Buckling Mechanics

If a thin column is subjected to a load parallel to its longest axis (described as an "axial load") then the Euler-Bernoulli equation predicts that column will begin to bend if the load exceeds a maximum value, described as the "critical buckling force", F_c. This force is given by the equation [163]

$$F_c = \frac{\pi^2 EI}{(KL)^2} \tag{5.1}$$

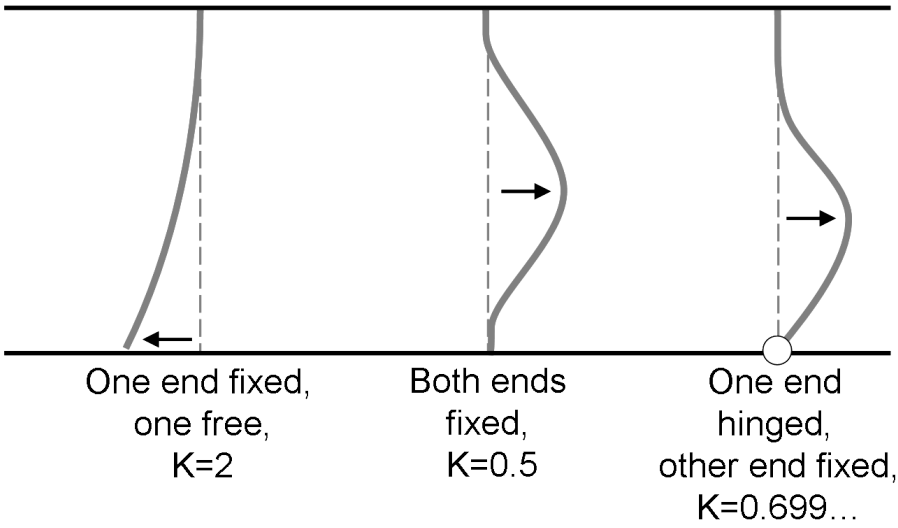

Figure 5-12: Illustration of some different conditions for buckled columns and the corresponding values of the column effective length factor K. Dashed line indicates column in non-buckled state.

where L is the column length and K is the "column effective length factor". K varies with the anchorage of the column ends; $K = 0.5$ for a column with fixed ends, $K = 2.0$ with one end fixed and the other free to move laterally, and $K = 0.699...$ if one end is fixed and the other is able to rotate freely about its base. Figure 5-12 shows these different conditions and the corresponding values of K. [163]

Equation 5.1 shows that the critical buckling force is proportionate to I, the area moment of inertia of the column. For a cylindrical column, $I = \pi r^4/4$ and so increases with the fourth power of the needle diameter. A small increase in diameter can therefore prevent the needle from buckling, allowing the exertion of larger forces on a sample. In section 5.4, a process is described which deposits additional carbon onto nanoneedle tips, increasing their diameter. Chapter 7 shows that these enlarged needles can be used for nanoindentation studies on corneocyte cells. Due to their shape, these needles are able to penetrate the sample down to depths of several hundred nanometres and measure the elastic modulus of structures at these depths.

Similar techniques have been used for the stabilisation of carbon nanotubes, in particular to allow them to be used for microinjection of biomolecules into biological cells. In this case, the carbon nanotube is stabilised by coating with a

polymer or by deposition of a carbon coating using chemical vapour deposition techniques. [134, 135]

Figure 5-13a shows approach curves measured for nanoneedle tips with different diameters fabricated using EBID. For diameters larger than 40 nm, buckling is not observed over the range of forces tested. The linearity of the approach curve after contact in these cases suggests that there is no deformation of these thicker needles within this force range. For thinner needles, the failure of the needle due to buckling can be seen as a saturation of the cantilever deflection as the buckled nanoneedle no longer supports the cantilever.

Using equation 5.1 the critical buckling forces for the nanoneedles could be estimated, assuming the needle to be a homogeneous prismatic column. For this calculation, a value of $K = 0.7$ (the case of a needle fixed at one end and hinged at the other) was taken to correspond closely to the nanoneedle in contact with the substrate surface at one end and bonded to the AFM probe at the other. The best fit to the experimentally measured critical buckling forces was attained for an elastic modulus E=18 GPa. A comparison of the calculated and experimentally measure buckling forces is shown in figure 5-13b.

This value is close to the value of $E = 28 \pm 10$ GPa determined by controlled bending of carbon blades by AFM manipulation, which is described in chapter 6. However, it is slightly lower; there are a number of possible reasons for this discrepancy. As discussed further in chapter 6, the elastic moduli of nanostructures are often measured to decrease in smaller structures due to the increased dominance of surface effects over bulk properties. [164–166] As the nanoneedles have a smaller cross-section than the carbon blades studied in chapter 6, surface effects could be expected to be more significant in the case of the smaller nanoneedle probes. Furthermore, the properties of amorphous carbon deposited using EBID vary with the deposition conditions; [64, 167] the rapidly grown needles receive only a small electron dose and this could result in different mechanical properties (as discussed further in chapter 6).

Finally, it can be seen in equation 5.1 that the critical buckling force is strongly dependent on how the ends of the column are fixed, which determines the column effective length factor, K. Our calculations assumed the ideal case corresponding to $K = 0.7$. If a value of $E = 28$ GPa is assumed, a value of $K = 0.87$ produces good agreement between the calculated and experimental buckling forces.

Therefore, the elastic modulus of the carbon which comprises the nanoneedle and that of the carbon blades examined in chapter 6 may be more similar than the calculated values would suggest.

5.7 Biological Applications of Nanoneedles

Nanoneedle probes produced using focussed ion beam (FIB) milling to modify silicon probes have previously been applied for indentation on cells [130] as well as for microinjection of DNA into cell nuclei [131]. Similar experiments have also been performed using carbon nanotubes stabilised by the deposition of polymer or carbon coatings onto the nanotube. [134, 135] The EBID technique can be used to fabricate needles of smaller diameters than those previously fabricated using FIB milling, and is less complex than the multi-stage processing needed to fabricate stabilised carbon nanotube probes.

The small size of nanoneedle probes decreases the damage to the cell structure as a whole, allowing penetration of living cells without affecting their viability. Their high aspect ratio allows penetration deep into the cell, and also means they can maintain high lateral precision even when penetrating a sample to a large depth, unlike standard AFM probes whose pyramidal shape results in a loss of lateral precision as the indentation depth increases. Chapter 7 describes a method for the use of nanoneedles to determine mechanical properties of biological cells, particularly if reinforced by exposure to the primary beam after growth. Standard AFM probes are also used for this process; however, the nanoneedle probes demonstrate advantages over unmodified AFM probes due to their small size and high aspect ratio. In chapter 7, results are presented which suggest that they can be used to measure mechanical properties of structures deep inside the cell, as well as those on the surface of cells.

5.8 Combining Needles with Other Nanotools

A disadvantage of many of the AFM nanotools discussed in this thesis (e.g. the "nanoscalpels" and "nanotome" described in chapter 4) is that the AFM tip shape is altered, decreasing the resolution of the AFM image and introducing distortion of the image due to convolution with the tip shape. This is a problem

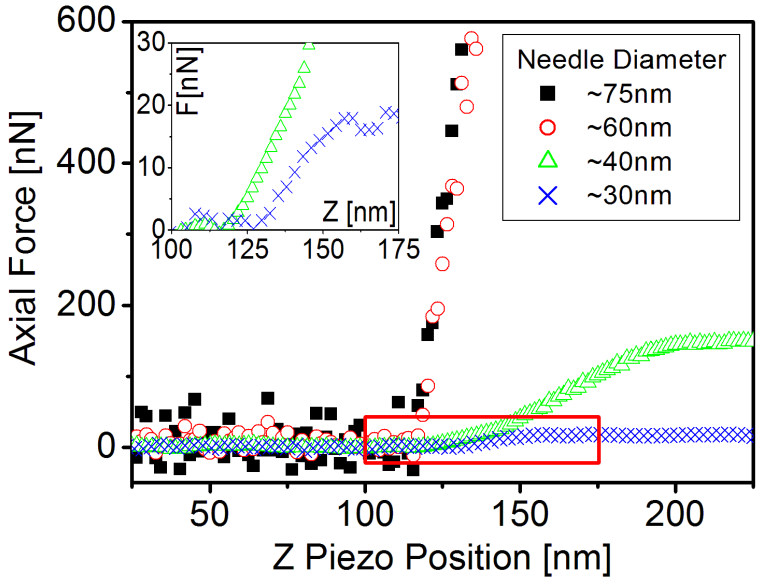

a)

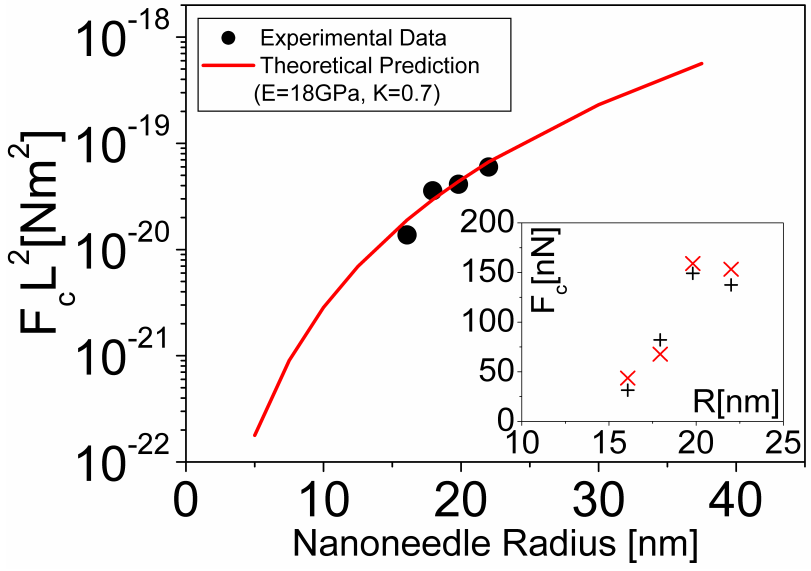

b)

Figure 5-13: a) Force curves for AFM probes with nanoneedles of different diameters. For diameters >40 nm, no buckling effect is observed. Inset shows enlargement of curves for 30 nm and 40 nm diameter needles. b) Critical buckling forces multipled by needle length squared (L^2) to compensate for variations in L between different needles and illustrate dependendence on needle radius alone. Inset shows comparison of critical buckling forces for needles of 30-40 nm diameter to theoretical prediction without compensation for L.

since the use of the nanotool probe for normal AFM imaging allows the alignment of the tip at the required manipulation site and subsequent imaging of the sample after manipulation. To obtain a high resolution image of the sample after nanomanipulation it is often necessary to replace the AFM tip with an unmodified, sharp probe, which is a time-consuming process as the new tip must be re-aligned over the site where the manipulation has been performed. In the case of a time-dependent sample like a biological cell, it might be almost impossible to replace the tip in time to observe the results of the manipulation.

This problem does not occur for thin nanoneedle probes; these are effectively ideal AFM probes due to their small tip radius and high aspect ratio. In addition, if a nanoneedle probe is fabricated on the same tip as another nanotool, then it can be used for normal imaging until the applied force is increased for nanomanipulation. At this point, the needle will buckle and fold away from the main tip. When the manipulation has been performed and the tip is retracted, the elasticity of the nanoneedle causes it to spring back to its original shape, allowing the area where the manipulation has been performed to be imaged using AFM. This would eliminate the need to exchange the nanotool tip for an unmodified sharp AFM probe.

In this way, it is possible to have a single AFM probe which can perform multiple specialised functions, being suitable for both AFM imaging and manipulation. This can be regarded as a "multitool" probe, with extra tools which can be folded away when not needed. An example of such a probe is shown in figure 5-14.

5.9 Conclusions

The width and thickness of nanoscale carbon blades fabricated using the EBID techniques described in chapter 4 decreases in the case of more rapid growth using a higher beam spot velocity. At large beam spot velocities, the resulting structure is a thin needle-like carbon filament. Optimisation of this growth process allows the growth of filaments ideal for use as high-aspect ratio AFM probes, allowing the imaging of steep gradients on the surface of a sample. High resolutions are attainable using these probes, as tips with radii of $\sim$13 nm were successfully used for imaging, and needles with tip radii of $<$5 nm could be fabricated. Our group

a)

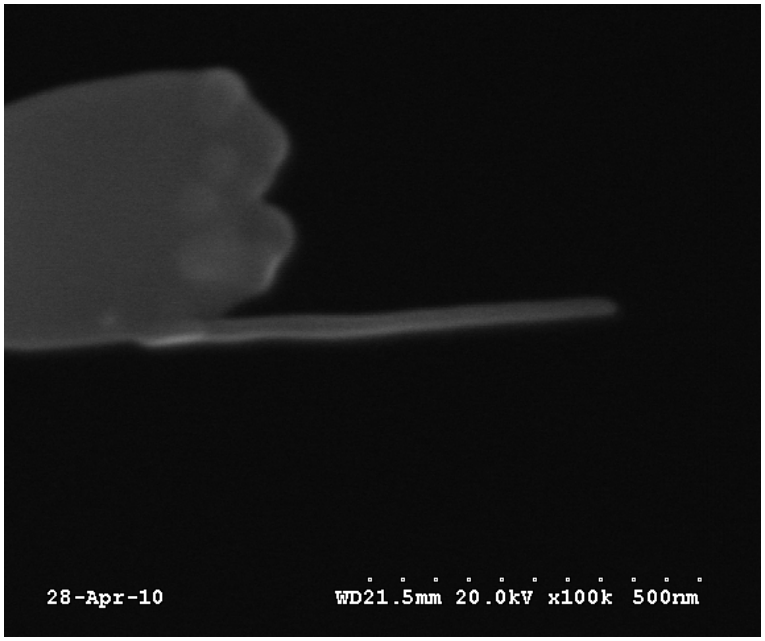

b)

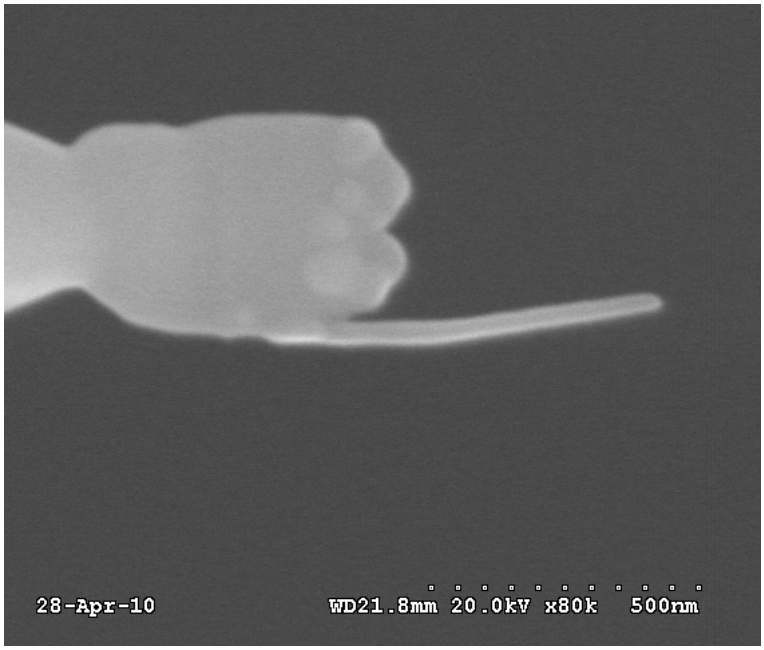

Figure 5-14: a) Needle fabricated on a (damaged) nanoscalpel blade. b) Needle after nanoscalpel tip was moved 1 μm over silicon surface with large force applied so that needle was deformed enough to bring nanoscalpel into contact with surface.

refer to such structures as "nanoneedles".

It was discovered that under large axial loads, nanoneedles were subject to

buckling instabilities in a similar manner to carbon nanotube probes. This protects the tip and sample from damage by preventing the tip-sample force becoming too large. The elasticity of the needle allows it to recover from deformations, preventing it from becoming permanently damaged. While the tip radius of these AFM probes is larger than that of carbon nanotube-tipped probes, the fabrication of carbon nanotube probes is much more complex and requires multiple processing stages. In contrast, nanoneedles fabricated using EBID require only a single deposition stage, and there is potential to produce nanoneedle probes with tip radii as small as those of carbon nanotube probes.

The critical buckling forces of nanoneedle probes were found to be in accordance with those calculated using the Euler model. From this model, the elastic modulus of the needle material was calculated to be $E = 18$ GPa, a value similar to that of 28 ± 10 GPa calculated for EBID structures in chapter 6. The lower value calculated for the needle material may be due to different deposition conditions or surface effects as discussed in this chapter and chapter 6.

Needles resistant to buckling can be fabricated if the needle diameter is increased by exposure to the electron beam after growth to deposit additional material onto the tip. As predicted by the Euler model, a small increase in needle diameter drastically increases the maximum axial load, allowing the needle to exert large forces during nanomanipulation. Such needles can be applied as rigid nanoindenter probes, capable of determining the elastic modulus of soft samples including biological cells. Due to their high aspect ratio these probes are able to penetrate deep into a sample for mechanical testing of internal structures. Their use for this application is discussed in more detail in chapter 7. It should be noted, however, that the low elastic modulus of the needles means that they are probably unsuitable for indentation on harder materials e.g. metals or silicon which have elastic moduli comparable to or greater than that of the needle material. Potentially, deposition of harder materials by EBID or ion-beam induced deposition could be used to create nanoneedle indenters suitable for these applications.

These needles have much smaller diameters than those previously fabricated for biological applications using techniques such as focussed ion beam milling. Similar-sized needles have been fabricated by using carbon nanotube probes which have been coated with carbon or polymer to stabilise them against buckling ef-

fects; however, the fabrication process for such tips is more complex, expensive and time-consuming. Both of these needle types have been used for microscale injection of small quantities of material (such as DNA) into cells, and have demonstrated the ability to target individual intracellular organelles such as the cell nucleus. [130, 131, 134, 135]

It can be concluded that EBID nanoneedle probes have several advantages for imaging and biological applications.

Chapter 6

Characterisation of Nanotools

AFM nanotools are subject to significant forces during their using in nanomanipulation or indentation. It is essential that they be sufficiently resilient to withstand the forces applied to them without breaking, detaching from the AFM tip or deforming so that their specialised shape is altered. Therefore, experiments were designed to measure the effect of applied bending forces on electron-beam deposited structures.

There are few previous studies of the mechanical properties, including elastic modulus, of structures fabricated using EBID. Ding et al. used a method of nanoindentation on areas of EBID carbon deposited on a graphite substrate to determine the elastic modulus and hardness of the deposited material. [64] This study noted that both elastic modulus and hardness tended to increase with increasing primary electron beam energy; this was attributed to different ratios of sp^2 to sp^3-bonded carbon in the deposited material. Controlled bending studies have also been used to measure the elastic modulus of pillars deposited using focused ion beam induced deposition (IBID). [65, 168, 169] However, there are currently few studies of the mechanical properties of free-standing EBID nanostructures; those that have been performed were based on determination of the structure's resonant frequency and did not examine the effect of large deformations on the structures. [76]

This section describes a series of experiments to measure the elastic modulus of electron beam deposited nanostructures. This is achieved by controlled bending of the structures using AFM nanomanipulation. In the course of these experiments, it was discovered that the deposited carbon structures are extremely flexible. It

was possible to bend carbon blades up to 75% of their total length without either breaking the blade or detaching it from the AFM tip.

This flexibility indicates that the nanotools fabricated on AFM probe tips using electron beam deposition are extremely robust, capable of withstanding large deformations. As shown in chapter 5, this flexibility allows slender high-aspect ratio "nanoneedle" probes fabricated by EBID to buckle elastically under large applied forces. This behaviour is well known for carbon nanotubes used as AFM probes; however, this is the first observation of this effect in high-aspect ratio probes produced by EBID. This effect is considered advantageous as it prevents the tip-sample force from becoming too large and damaging the sample surface, while the elastic recovery of the needle prevents the tip from becoming permanently damaged.

In addition, this flexibility suggests a number of other potential applications for these structures, such as nanoscale springs, force-transducing cantilevers or components of nanoscale resonator devices. These structures are currently of great interest for a large number of nanotechnological applications. [170–172]

6.1 Elastic Modulus of EBID Nanostructures

This section describes the methodology used to determine the elastic modulus of free-standing carbon nanostructures fabricated using EBID. This technique uses AFM nanomanipulation to apply a force perpendicular to the long axis of a carbon blade, bending the blade while allowing measurement of its deflection and the applied bending force. The bending of the carbon blade is then modelled using a numerical technique which allows determination of the deflection of the free end of the blade, and its elastic modulus.

In order to allow manipulation of a free-standing carbon nanostructure, carbon blades were fabricated on AFM probes, close to the tip apex, such that the blade lies parallel to the plane of the sample surface when the probe is used for AFM imaging. An example of a carbon blade fabricated for this experiment is shown in figure 6-1. The tip can then be used to image a standard AFM calibration grid in Tapping Mode. If an approach-retract force curve is recorded when the tip is close to a 200 nm step on the sample surface, the carbon blade comes into contact with the upper edge of the step, and the force acting on the

blade causes it to bend. This process is illustrated schematically in figure 6-2. The deflection of the AFM cantilever and the vertical position of the piezoelectric scanner are recorded during the bending of the blade, and allow calculation of the loading force applied and deflection of the blade at the load point. This provided the information necessary to model the blade bending process and calculate its material properties.

a) 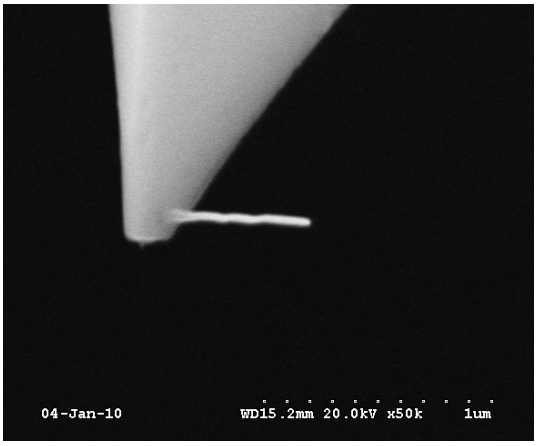

b) 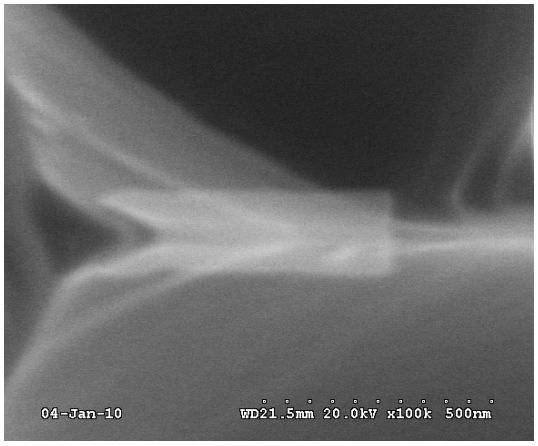

Figure 6-1: SEM images of a carbon blade fabricated on the side of an AFM probe. Image a) shows the blade immediately after growth. Image b) shows the same carbon blade observed from beneath the tip apex.

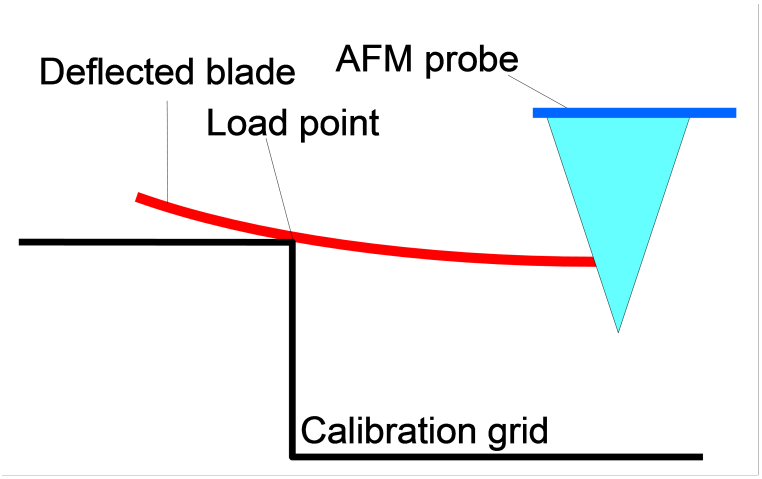

Figure 6-2: Setup for bending of a carbon blade against the edge of a pit in the surface of a calibration grid.

The AFM profiles of the calibration grid allow the position of the AFM tip

relative to the step to be determined. The modification of the tip shape alters the profile of the step, as shown in figure 6-3; the single edge appears as a double step. The lower step is measured as the carbon blade contacts the upper edge of the step during imaging. It is clear that there is some deformation of the blade during normal imaging as this step is profiled, as evidenced by the characteristic periodic artefacts visible in figure 6-3, which are often observed when imaging soft samples which are deformed by the probe. As the approach-retract curve is measured from the centre of the image, the load point position x_0 can be determined from the position of this step with reference to an AFM image recorded just before each approach-retract cycle.

The force curves recorded during the cantilever bending allow the calculation of the vertical deflection of the carbon blade by comparison to a calibration curve recorded on the calibration grid surface far from any step features, so that only the rigid silicon tip (and not the carbon blade) came into contact with the sample. This curve also allows the calibration of the AFM photodiode output, from which the deflection of the cantilever can be calculated, as described in Chapter 3. Determination of the AFM cantilever spring constant, using the method described by Sader *et al* [147] allows calculation of the applied bending force (see section 3.4 for details).

From the gradient of a force-deflection curve recorded as the carbon blade is deflected, an "effective spring constant" for the carbon blade can be calculated. An example of a force curve, and the effective spring constants calculated from approach and retract curves recorded for a single blade are show in figure 6-4. Using this to calculate the applied bending force from the cantilever deflection, the value of E can be determined using the models described below. To calculate E it also necessary to determine the second moment of inertia, I. This property is calculated from the carbon blade dimensions measured using SEM imaging immediately after growth, assuming a rectangular cross-section, using the relationship [173]

$$I = \frac{wt^3}{12} \tag{6.1}$$

where w and t are the width and thickness of the carbon blade respectively.

In many force curves, inflection points are noted. These can be attributed to the rapid slipping of the carbon blade down the step, altering the load point

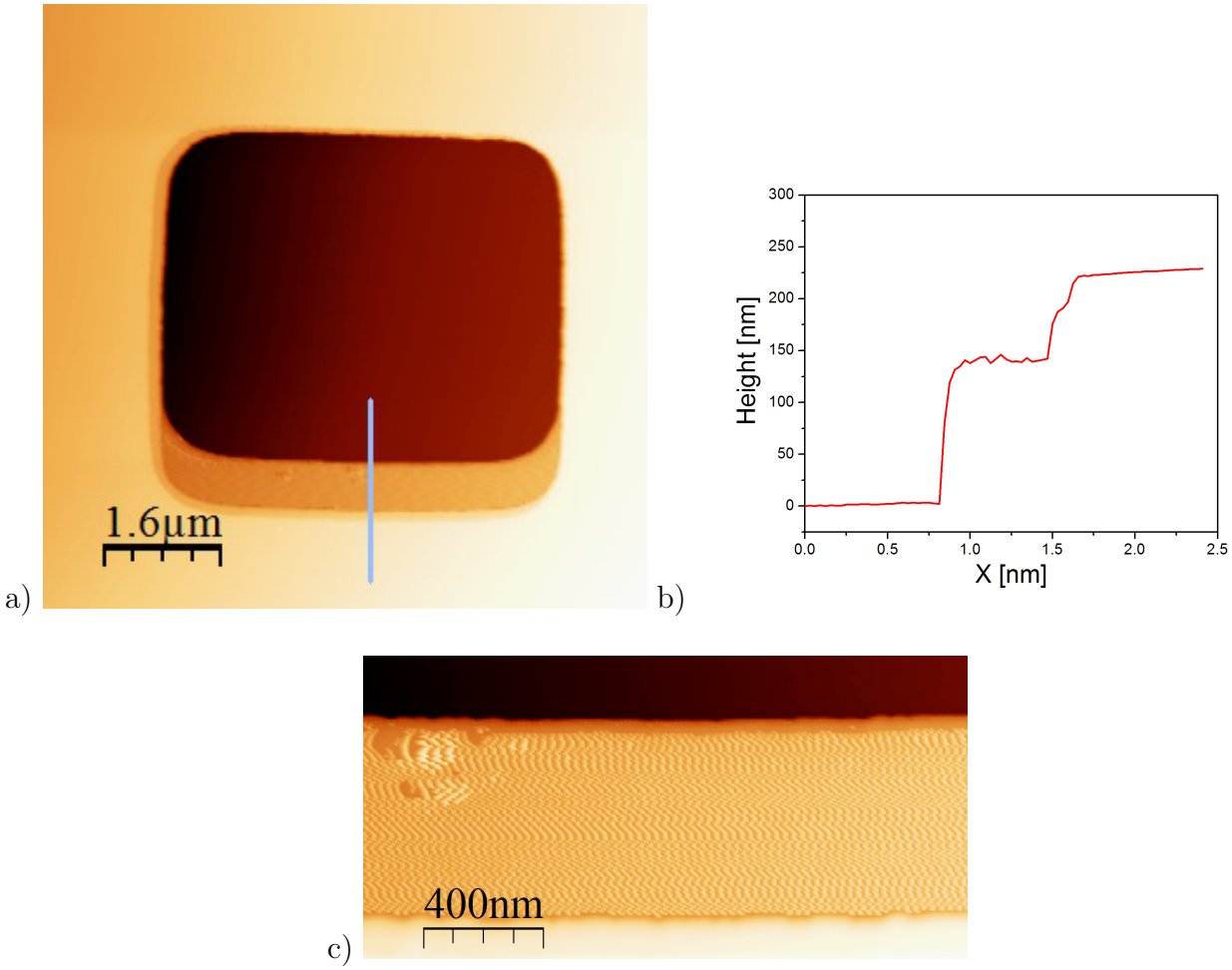

Figure 6-3: a) AFM image of AFM calibration grid taken using a probe with attached carbon blade, causing a "double step" to appear on one edge of the grid. b) Profile along the blue line in a) showing the step structure. c) Close up of double step showing periodic artefacts caused by deformation of the carbon blade during normal imaging mode.

position on the carbon blade.

6.2 Modelling the Bending of a Cantilever Beam

The bending of macroscopic cantilever beams is a subject which has been studied in much detail, and is of great importance in many fields of engineering. The basis of the standard model of such beams is the "Euler-Bernoulli Beam Bending Equation" derived c. 1727 [174]; its discovery allowed significant advances in

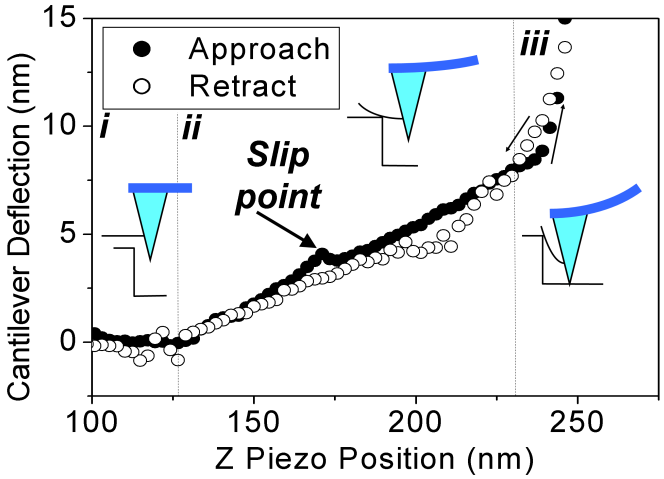

a)

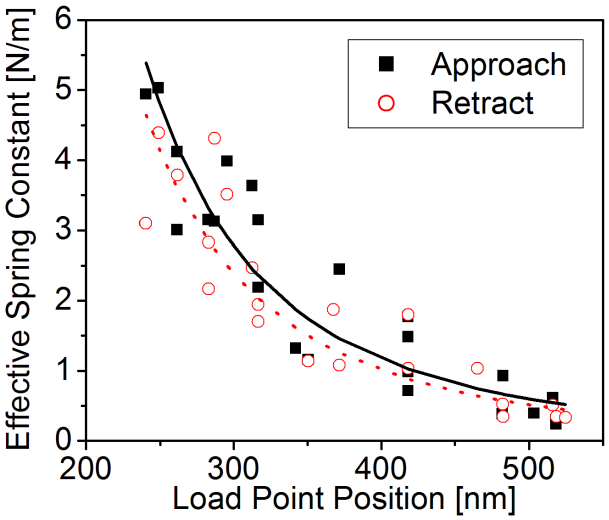

b)

Figure 6-4: a) Approach-retract deflection curve. Smaller inset diagrams show deflection of carbon blade at different regimes of the curve; in (i), the carbon blade is not in contact, in (ii) a small increase in the AFM cantilever deflection occurs as the blade is bent, and in (iii) the rigid silicon tip comes into contact with the sample surface, causing a rapid increase in the AFM cantilever deflection. Note the inflection in the curve caused by slipping of the blade down the step during the approach-retract cycle. b) Effective spring constants of carbon blade calculated from force-deflection curves.

the field of architecture and mathematics [175], including the construction of the Eiffel Tower. This equation can be written as [173]

$$EI\frac{d\varphi}{ds} = M \tag{6.2}$$

where E is the elastic modulus of the beam, φ is the angle of the beam with the horizontal, s is the length of the curved beam (such that $d\varphi/ds$ is the curvature of the beam), M is the bending moment, and I is the second moment of inertia, which is defined by the geometry of the beam cross-section. Solving the equation can be used to relate the deflection of the beam to the applied bending force.

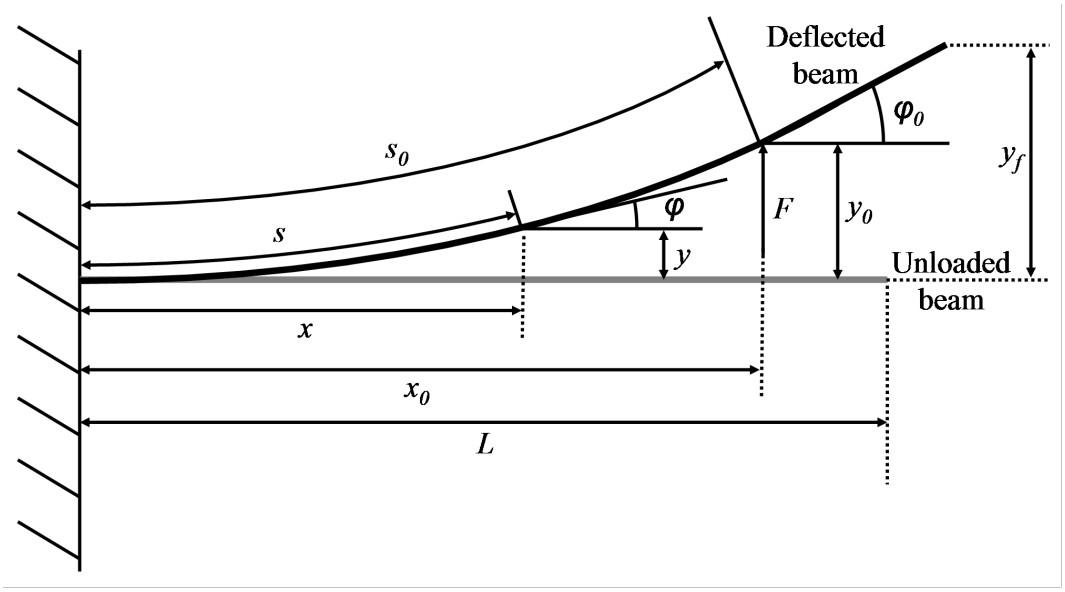

Figure 6-5: Geometry of a deflected cantilever beam.

A commonly encountered situation is that of a beam fixed at one end and with the other free to move due to bending of the beam under a force applied at a point some distance from the fixed end. Such a beam is termed a "cantilever". A macroscopic example of such a beam would be a the horizontal arm of a construction crane lifting a heavy load. An example from the field of nanotechnology is the flexible cantilever used as a force sensor in AFM; the Euler-Bernoulli model can be used to determine the effective spring constants of AFM probe cantilevers

based on their dimensions and known material properties. [176] It has also been applied to determine the elastic properties of carbon nanotubes and other rod-like nanoscale structures [177–179] illustrating its applicability to nanoscale objects. The geometry of a cantilever deflected by an applied force F is shown in figure 6-5.

The solutions to the equation are simple for small deflections of the beam. For small deflections, the applied force can be related to the deflection by

$$y_0 = \frac{Fx_0^3}{3EI} \tag{6.3}$$

Solutions to this equation for larger deflections have also been derived for a cantilever beam loaded at one end. [180] This model was originally derived by Bisshop *et al* and has been shown to be in good agreement with experimental results. [181, 182] In our case the beam is not loaded at the free end but instead some distance between the free end and fixed base; however, if it is assumed that there is no strain in the cantilever between the free end and the load point, this model can still be applied. Bisshop showed that equation 6.2 can be solved to find s in terms of φ:

$$s = \sqrt{\frac{EI}{2F}} \int_0^{\varphi} \frac{d\varphi}{\sqrt{sin\varphi_0 - sin\varphi}} \tag{6.4}$$

$$s_0 = \sqrt{\frac{EI}{2F}} \int_0^{\varphi_0} \frac{d\varphi}{\sqrt{sin\varphi_0 - sin\varphi}} \tag{6.5}$$

$$x = \sqrt{\frac{2EI}{F}} (\sqrt{sin\varphi_0} - \sqrt{sin\varphi_0 - sin\varphi}) \tag{6.6}$$

$$y = \sqrt{\frac{EI}{2F}} \int_0^{\varphi} \frac{sin\varphi d\varphi}{\sqrt{sin\varphi_0 - sin\varphi}} \tag{6.7}$$

If $x = x_0$, then $\varphi = \varphi_0$. Therefore, from equation 6.6

$$x_0 = \sqrt{\frac{2EI}{F}} \sqrt{sin\varphi_0} \tag{6.8}$$

To calculate E based on the experimental data, it was necessary to find φ_0

from the values of x_0 and y_0, which could be determined from the experimentally recorded AFM images and force curve data respectively. Rearranging for E gives

$$E = \frac{Fx_0^2}{2Isin\varphi_0} \tag{6.9}$$

Substituting this equation into equation 6.5 and 6.7 gives y and s_0 in terms independent of E,F, and I.

$$y = \sqrt{\frac{x_0^2}{4sin\varphi_0}} \int_0^{\varphi} \frac{sin\varphi d\varphi}{\sqrt{sin\varphi_0 - sin\varphi}} \tag{6.10}$$

$$s_0 = \sqrt{\frac{x_0^2}{4sin\varphi_0}} \int_0^{\varphi_0} \frac{d\varphi}{\sqrt{sin\varphi_0 - sin\varphi}} \tag{6.11}$$

From this equation, it is possible to find the angle φ_0 given the load point position, x_0, and the deflection at the load point, y_0. Given φ_0, the value of s_0 can also be found. Using the relationship derived by Bisshop *et al.* [180]

$$\int_0^{\varphi_0} \frac{d\varphi}{\sqrt{sin\varphi_0 - sin\varphi}} - 2\sqrt{\alpha} = 0 \tag{6.12}$$

where

$$\alpha = \sqrt{\frac{Fs_0^2}{2EI}} \tag{6.13}$$

the elastic modulus can be determined.

The evaluation of the integrals in equations 6.10, 6.11 and 6.12 to determine α and s_0 was implemented using a simple program written in C. The source code for this program is shown in appendix B. For each force curve recorded during deflection of a carbon blade a distance x_0 from the blade base, values of φ_0 from 0 to $\pi/2$ were tested, and equation 6.10 evaluated for each value of φ_0 until a value of φ_0 corresponding to the final deflection, y_0, was found. Equation 6.11 can then be evaluated by the program to find s_0, and then equation 6.12 evaluated to find E.

6.3 Experimental Results

The calculated spring constants of a carbon blade were fitted to equation 6.3. Fits for spring constants calculated from approach and retract force curves are shown in figure 6-4. These fits were performed using Origin, to the function

$$\frac{F}{y_0} = \frac{A}{x_0^3} \tag{6.14}$$

where $A = 3EI$ and is the only variable which is adjusted to fit the data, and F/y_0 is the calculated spring constant for the carbon blade. The resulting values of A were used to calculate values for E for the approach and retract curves of 27.6 ± 1.4 GPa and 23.8 ± 1.5 GPa respectively. The errors on these values are estimated from the possible range of A coefficients which would fit the experimental data.

Figure 6-6 shows values of the elastic modulus calculated for a carbon blade deflected by forces applied over a range of distances from the blade base (x_0). These results were calculated by numerical evaluation of equations 6.11 and 6.12 using experimentally measured values of x_0, F and y_0. The results show good agreement between values determined from the approach and retract curves and that the calculated value of E do not vary much even for very large deflections resulting from loading the beam at a small x_0. This indicates that the model used to determine the elastic modulus remains accurate even for large deflections of the carbon blade. The average value of E calculated was 28 ± 10 GPa for this carbon blade. This value of elastic modulus is in good agreement with the values of E determined using a fit to equation 6.14. It is also close to the value of 18 GPa fitted to the results for the buckling of EBID nanoneedle AFM probes in chapter 5.

There is, however, significant scatter of the calculated elastic moduli around the average value. This can be attributed to several factors; firstly, there is significant noise in many of the approach-retract curves from which the carbon blade effective spring constant was calculated, resulting in error in this value. Furthermore, there is uncertainty in the position of the loading point since it varies during the bending process and must be calculated using equation 6.11. Finally, the Euler model assumes a thin beam whose thickness is much smaller than its length; this is not necessary true for the carbon blades investigated in

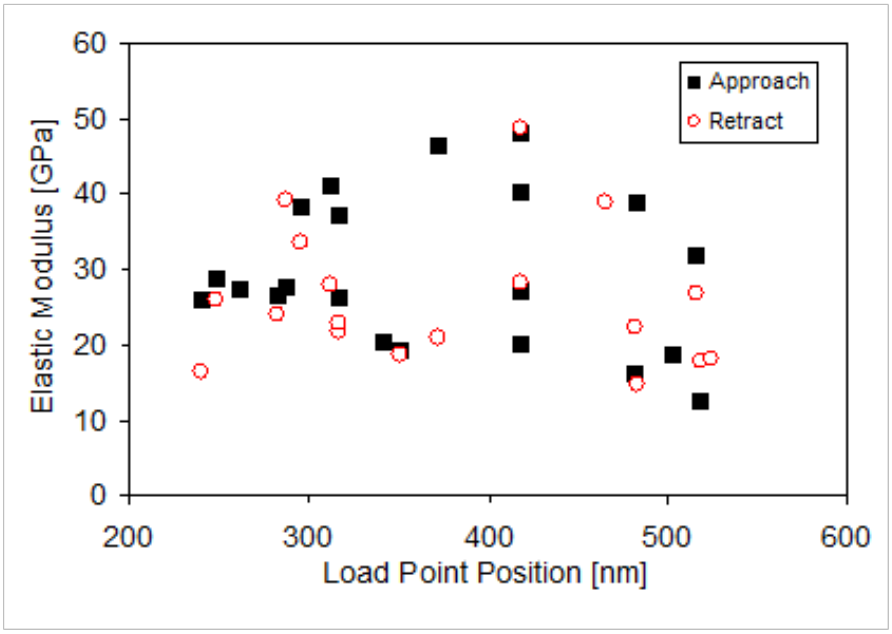

Figure 6-6: Elastic moduli calculated from experimental results for a single carbon blade using numerical model.

these experiments, and could introduce significant variation of the beam bending behaviour which, combined with the other uncertainties in the experimental parameters, could cause variation of the calculated elastic modulus. It is possible that the different elastic moduli calculated for the approach and retract curves using equation 6.14 is also due to variation in the load point position during the bending of the blade, resulting in inaccuracies in the value of x_0.

The numerical model also allows calculation of the final angle, φ_0, of the carbon blade, and the deflection at the free end of the blade, y_f. These results showed that the carbon blade could be deflected by large distances; in one case, a blade ~480 nm in length was deflected up to ~365 nm by applying a force ~65 nm from the blade base. This indicates a lateral deflection of ~75% of the cantilever length at its free end. In this case, the carbon blade did not break and the force curve recorded during the indent shows very little hysteresis, indicating that the majority of the deflection recovered elastically (see Figure 6-7).

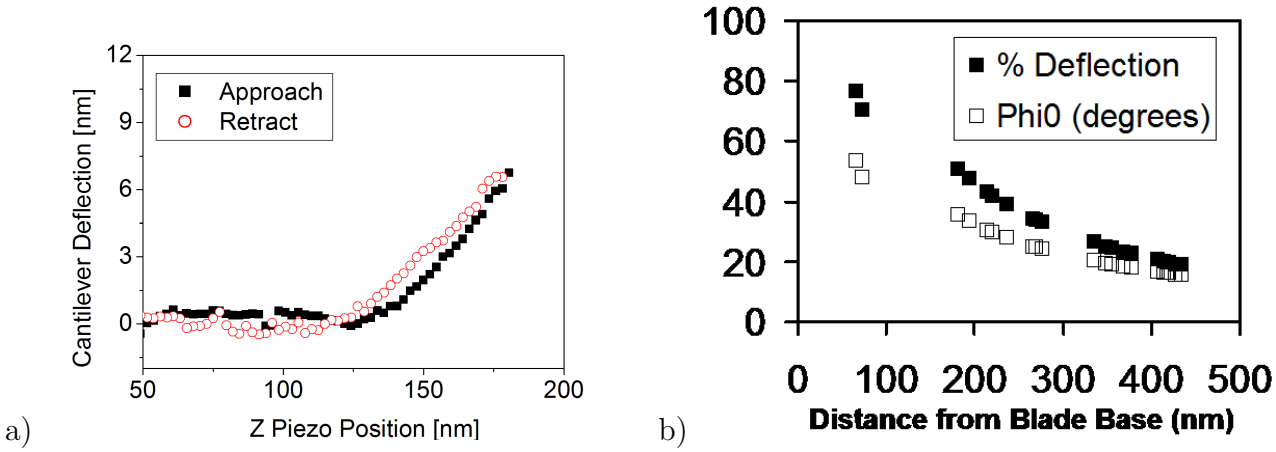

Figure 6-7: a) AFM force curve recorded during lateral deflection of a 480 nm length carbon blade up to 75% of its total length. Only weak hysteresis is visible in the curve, indicating that most of the deflection recovers elastically. b) Final angle and percentage deflection of carbon blade.

6.4 Shape of Deflected Blades

Knowing φ_0, the shape of the deflected blade between the base and load point can be calculated from equation 6.10 and

$$x = \sqrt{\frac{x_0^2}{sin\varphi_0}}(\sqrt{sin\varphi_0} - \sqrt{sin\varphi_0 - sin\varphi}) \tag{6.15}$$

which is derived by substituting equation 6.9 into equation 6.6. From equation 6.15 and 6.10, values of x and y can be found in terms of φ. These equations were also evaluated using a C program to simulate the shape of the deflected carbon blades under the conditions of some of the indents performed in these experiments. The calculated blade shapes are shown in figure 6-8; it is assumed that the blade remains straight between the loading point and the free end.

6.5 Discussion of Results

These experimental results indicated that the nanoscale EBID structures described here are highly robust, capable of withstanding large deflections and recovering their shape elastically. In chapter 5, the fabrication by EBID of high-aspect ratio "nanoneedle" probes ideal for imaging samples with high steep fea-

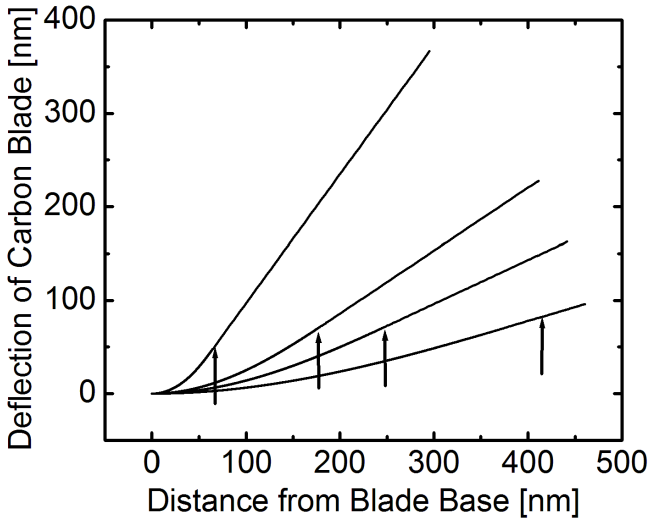

Figure 6-8: Calculated shapes of deflected carbon blades for different load point positions (arrowed).

tures is discussed. The flexibility of the deposited structures means that if the tip-sample force becomes too large, the needle will buckle elastically rather than break. This prevents the force increasing beyond this needle's critical buckling force and so protects both the tip and sample from damage.

In addition, the buckling of these probes can be exploited to create a "multitool" probe, incorporating a nanoneedle tip which can fold under a large tip-sample force, allowing a more rigid silicon tip or EBID nanotool tip fabricated on the same probe to be brought into contact with the sample surface and used for manipulation. The fabrication and testing of such a probe is also described in chapter 5.

The calculated value of the elastic modulus E of the amorphous carbon presented here is 28 $\pm$ 10 GPa, smaller than that measured by nanoindentation on larger EBID amorphous carbon deposits by Ding *et al* who reported E values of $\sim$60 GPa for the same primary beam energy (20 kV). [64] However, they also found that the hardness and elastic modulus of the deposited material tended to increase with increasing primary beam energy; this would indicate that the mechanical properties of the deposit are strongly dependent on the deposition conditions. In addition, Ding's group used a different measurement technique

(nanoindentation) which may have lead to variation in the measured parameters.

In support of the idea that the properties of EBID carbon are dependant on the deposition conditions, Ding *et al* also found that the proportion of sp^2 to sp^3 bonds in the carbon deposit varied with the primary beam energy. In their study, more "diamond-like" sp^3 bonding was detected in the harder deposits fabricated with higher beam energies. Other experimenters have also demonstrated that electron bombardment can significantly alter the bond structure of amorphous carbon. [167]

The deposition of free-standing structures occurs under different conditions to those used to deposit over larger areas, as in the paper by Ding *et al.* In particular, during area deposition the entire deposit is exposed to the primary beam and generated secondary electrons for the whole duration of the deposition. In the case of free-standing structures grown laterally from an edge, as in our experiments, the time over which any part of the deposit is exposed to the beam is much shorter. This could result in a different sp^2/sp^3 bond ratio.

Previous experiments have shown that the elastic modulus of amorphous carbon is dependent on sp^2/sp^3 bond ratio in the material. [183] These different deposition conditions, and the associated difference in bond structure within the carbon blade, could therefore explain the discrepency between the elastic modulus measured in our experiments and that reported by Ding *et al.*

It has also been noted that the measured elastic modulus of nanostructures can decrease with decreasing structure size. For nanoscale structures, different mechanical properties of the surface layers tend to reduce the overall stiffness of the structure. [165, 166] The surface effect becomes more and more significant as the structure becomes smaller and the surface layer represents more and more of its overall volume. Surface effects can be highly significant during beam bending since the surfaces undergo the largest stresses during the bending of the beam. Important surface effects which can affect the stiffness of the structure include residual surface stress [164] and dangling bonds at the surface. These effects can be modelled by a decrease in the effective elastic modulus of the material close to the surface, reducing the overall stiffness and therefore the elastic modulus measured by beam bending studies. This size-dependent effect could also account for the smaller elastic modulus of 18 GPa determined for nanoneedle probes in chapter 5, as these structures have even smaller dimensions than the carbon blades

and so surface effects would be more significant for the nanoneedle structures.

6.6 Other Applications

The flexibility of the carbon structures fabricated by EBID suggests several applications other than their use as AFM probes. They could be employed as mechanical components in nanoelectromechanical systems (NEMS) such as nanoscale springs or as nanoscale AFM cantilevers. Additionally, a free-standing elastic structure can be employed as a mechanical resonator.

There is considerable interest in using resonating cantilevers and other microscale or nanoscale resonating structures as sensing devices. In particular, they can be used as chemical or biochemical sensors. In order to act as a chemical sensor, a resonating microcantilever or nanoscale cantilever is functionalised with binding sites appropriate to the a target molecule [170–172]. The cantilever is then oscillated close to its resonant frequency using periodic electrical or mechanical excitation. The binding of a target molecule to the cantilever causes a change in the cantilever effective mass, shifting its resonant frequency. This shift can then be detected as a change in cantilever resonant frequency, oscillation phase or amplitude. The sensitivity of these devices increases with higher resonant frequencies and so is improved for smaller, stiffer cantilevers; mass changes equivalent to a single molecule can be detected by such devices. [184, 185] Using carbon nanotubes as cantilevers, it has been shown that mass changes of 100 zeptograms (100×10^{-21} g) can potentially be detected. [186]

Fabrication of cantilevers for these sensing devices is usually performed using a complex multistage process, involving patterning of the a substrate by electron-beam lithography or photolithography and multiple etching stages to free the cantilever from the base to form a free-standing structure. EBID fabrication of a free-standing cantilever is a much simpler and therefore quicker process, which can also produce much smaller structures.

6.7 Conclusions

A novel method for the measurement of the elastic modulus of deposited amorphous carbon structures has been developed, using controlled bending of cantilever-

like carbon blades fabricated on AFM probes. A numerical model based on the Euler-Bernoulli beam bending equation was used to determine the elastic modulus of the blades based on the deflection and applied force determined from the AFM force curves.

The elastic modulus measured by this method differed significantly from that measured on similar materials by other experiments. [64] However, the values of elastic modulus here are supported by experiments to determine the elastic modulus of EBID nanoneedle probes by measuring their critical buckling force, which determined a similar (though slightly smaller) elastic modulus. The variation in elastic modulus between these experiments could be due to variation of mechanical properties for nanoscale structures compared to the bulk due to the increased significance of surface effects. It may also be due to different deposition conditions for the free-standing structures; for instance, the time in which any part of the carbon deposit is exposed to the electron beam and associated secondary electrons is much shorter in our experiments. Further experiments on structures of different sizes, deposited under a range of beam energies, would further clarify the effect of the deposition conditions and scale of the structures on their mechanical properties.

It was discovered that the carbon blades could be deflected up to $\sim$75% of their length without breaking, and that most of this deformation would recover elastically. Similar behaviour was noted in high-aspect ratio "nanoneedle" AFM probes fabricated using EBID, which would buckle and recover elastically under large axial loads, similar to carbon nanotube-tipped probes. This behaviour would protect both the tip and sample from damage during imaging.

This is the first description of this high flexibilty in EBID structures. Elastic flexibility has been observed (for smaller deflections) in amorphous carbon structures deposited by ion beam induced deposition (IBID) and was attributed to the bending and rotation of the carbon bonds. [65]

The large flexibility of these structures suggests that they can be used for other applications. Their elasticity could be exploited in spring-like components in nanoelectromechanical systems, and they could also be applied as nanocantilever sensors for the detection of chemical and biological substances. Their single-stage fabrication by EBID is simpler than the multi-stage etch processes typically used to create such devices, and also allows the creation of smaller structures.

Chapter 7

Nanoindentation

Nanoindentation is a technique which has been widely applied to determine the mechanical properties, such as hardness and elastic modulus, of many different structures and materials. Originally developed as a technique to measure the properties of inorganic materials, it has become a widely used technique for the measurement of these properties in biological cells. [90, 92, 93] A large variety of different models have been developed to describe the force-deformation response of different materials, incorporating different indenter shapes and taking into account elastic, inelastic and viscous deformations. [80–82, 89] These properties are of great interest as they reflect the internal organisation of the cell, and have been shown to vary significantly between healthy cells and those in disease states e.g. cancerous cells. [88, 95–98] It is therefore likely that the study of these properties will provide new insight into the organisation of biological cells and the pathology of different diseases. The cell structure is highly complex and inhomogeneous, and much of it consists of nanoscale structures; therefore it is desirable to study its mechanical properties on scales ranging from whole cells to the nanoscale level of individual structures such as cytoskeleton filaments.

This chapter describes experiments examining the penetration and deformation of corneocyte cells using nanoneedle AFM probes fabricated using electron beam induced deposition (EBID). These probes represent a novel and attractive tool for the nanomanipulation and investigation of cells; previous studies using high aspect ratio needle-like structures on AFM probes produced by other nanofabrication techniques have shown that they allow penetration deep into the cell without significant damage to the cell structure as a whole. [130–135] Cor-

neocytes are an ideal target for these experiments as they can be easily isolated (using the protocols described in appendix A) and imaged in air using AFM without dehydration or fixation. They also have a relatively simple structure lacking internal organelles such as nuclei; this lack of inhomogeneities simplifies analysis of the experimental data. Corneocytes have previously been imaged under ambient conditions using AFM [187, 188] and their surface mechanical properties studied using AFM indentation techniques. [189]

The results presented here suggest that nanoneedle probes can be used to penetrate to large depths within the corneocyte cells, piercing their outer layers to probe mechanical properties of their internal structures. Experiments have been carried out on these cells to determine their elastic modulus at various depths below the surface. It is shown that the depth of penetration of the needle into the structure can be determined and controlled by varying the applied indentation force.

Results are presented which suggest that the elastic modulus of structures below the corneocyte's outer layers can be determined using this technique. Both the depth of penetration and measured elastic modulus are also shown to vary significantly with the approach-retract velocity of the AFM probe, indicating viscoelastic behaviour of the corneocyte structure. The observed variation of elastic modulus measured as a function of depth can be related to the different layers known to make up the corneocyte structure. In future, this technique could be used to investigate the mechanical properties of intracellular structures such as single organelles, or to perform "mechanical tomography", measuring the elastic properties of the cell structure or other biological structures at a range of depths below its surface.

It is also demonstrated that the indentation techniques described in this chapter can detect changes in the elastic modulus of the internal corneocyte structure similar to those which occur in corneocytes as a result of skin conditions such as dermatitis. This suggests that indentation using nanoneedles could be used to investigate the changes in cell structure and mechanical properties associated with disease states in cells, and in future could be used to investigate the pathology of these diseases.

7.1 Procedure

In order to create an indent on a cell, the AFM piezoelectric scanner is used to move the sample at a constant velocity, such that the AFM probe is pressed into the sample surface. When the deflection of the AFM cantilever (measured by the photodiode sensor in the AFM system) reaches a chosen value (corresponding to the peak indentation force F_{max}) then the approach is stopped and the probe is retracted at the same rate. During the approach and retract process the amplitude of the oscillating cantilever, and its deflection, are recorded by the AFM system. The data recorded during the indent (referred to as a "force curve") can be used to determine the force applied to the cell, and its associated overall and inelastic deformation in the vertical direction, using the methods described in chapter 3. Figure 7-1 shows images of a typical indent created on a corneocyte surface using a nanoneedle probe.

7.2 Force Curves

An example of a force curve recorded on a corneocyte is shown in figure 7-2. From the force curves, the deformation of the corneocyte h at any point during indentation can be calculated by comparison to a calibration curve recorded by indentation on a rigid substrate (see section 3.5.2 in chapter 3 for details). The applied indentation force F can be determined from the cantilever deflection and spring constant, and the residual inelastic indentation depth from the curve hysteresis.

In many of the approach curves recorded on corneocytes, peaks and steps are noted at small cantilever deflections. Similar inflections have been noted by other experimenters in force curves recorded while using AFM probes to penetrate the membrane of living cells, and are thought to correspond to the rapid yielding of the cell membrane as the tip penetrates through it. [130, 190] It could also be attributed to rapid depolymerisation of the cellular cytoskeleton; however, we do not believe that this is the case in corneocyte cells as these are rather inactive compared to many other cell types. The yielding of the cell surface causes a relaxation of the deflection of the AFM cantilever, causing a decrease in the slope of the approach curve. We refer to these points as "penetration events". When

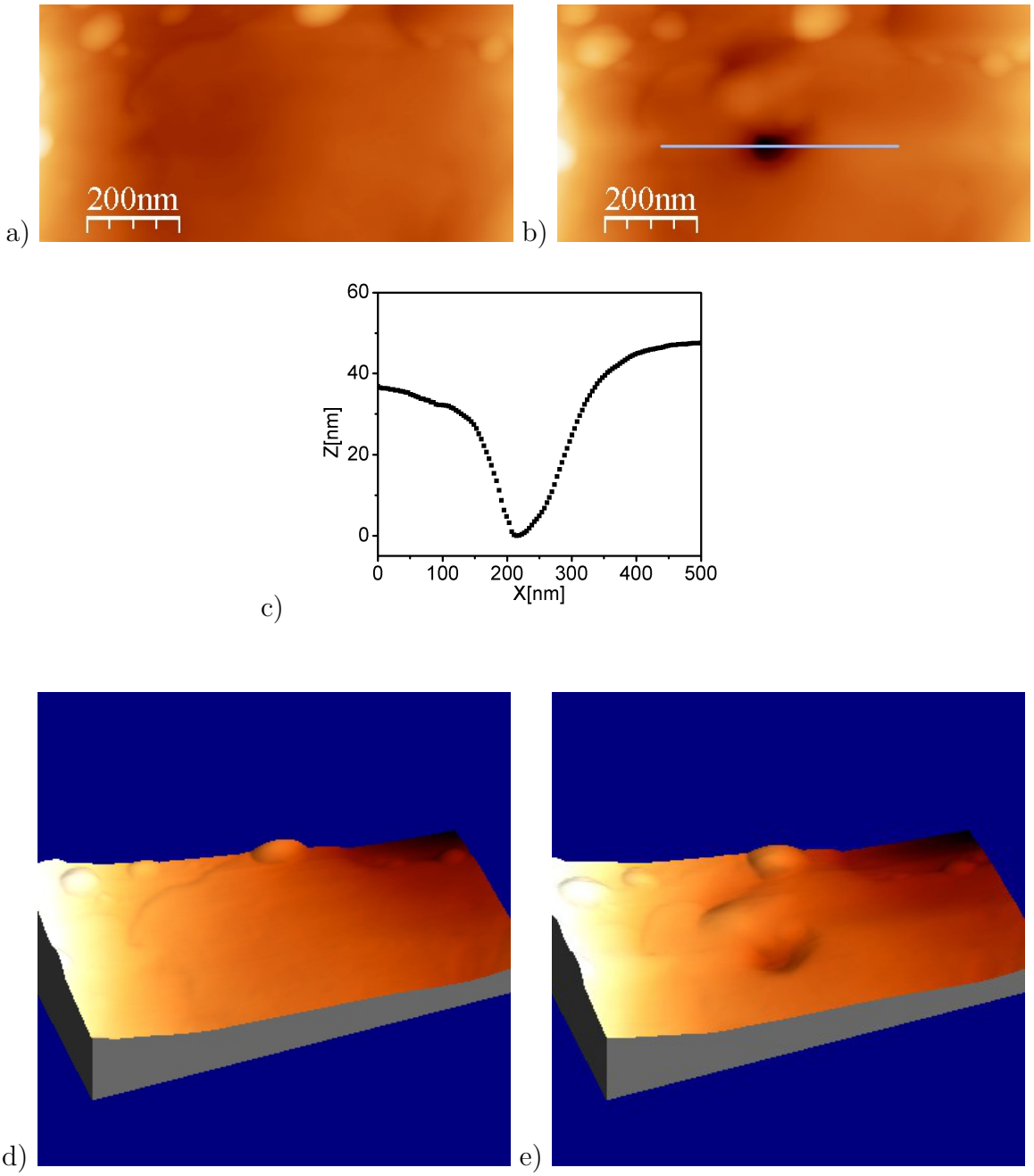

Figure 7-1: a) Surface of corneocyte before indentation. b) Surface including indent. c) Profile across indent in b). d) and e) Pseudo-3D view of surface before (d) indentation and (e) afterward.

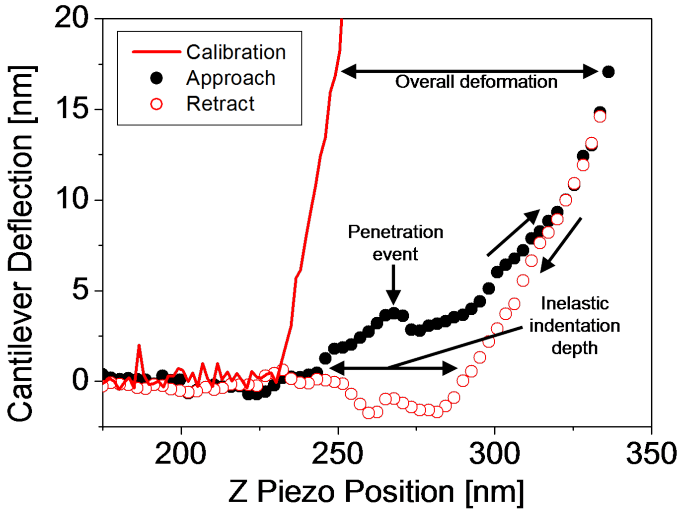

a)

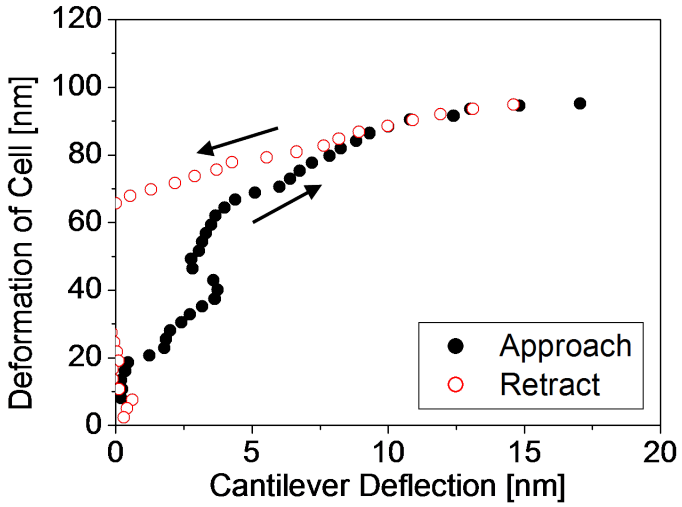

b)

Figure 7-2: a) Example of approach-retract curve recorded on corneocyte cell using a nanoneedle probe. The penetration of the AFM probe through the outer cornified protein envelope is seen as a peak in the force curve at low cantilever deflection. Comparison to the calibration curve recorded on a rigid substrate allows calculation of the overall deformation of the sample while the residual inelastic deformation can be calculated from the hysteresis between the approach and retract curves (see section 3.5.2 for details). b) Calculated deformation of the sample during the approach and retraction of the AFM probe.

indenting on corneocytes, it is likely that these penetration events correspond to the nanoneedle tip breaking through the outer cornified envelope which surrounds the corneocyte, indicating that the nanoneedle is able to pierce this layer.

It is also clear that there is significant adhesion of the needle to the sample during the retract, as can be seen by the region of negative deflection during the retraction of the AFM probe in figure 7-2. This is likely due to frictional forces between the needle and the sides of the hole created in the cell which resist the pull-out of the needle from the cell material, and also adhesion forces between the tip and sample material. These forces might vary with the tip-sample wetting properties (hydrophilic and hydrophobic interaction between tip and sample materials), dependent on the composition of different structures within the cell. Potentially, this could be used to investigate these properties in intracellular structures.

The tip-sample adhesion could also lead to the attachment of contaminant from the sample to the AFM tip. This would tend to change the tip-sample interaction, altering the adhesion effects between tip and sample, as well as altering the specialised tip shape. It could potentially also lead to the contaminant deforming as well as the sample during indentation, leading to inaccuracies in the measurement of the sample mechanical properties. To avoid contamination effects becoming too significant the AFM probes were cleaned every 6-10 indents using organic solvents, as described in section 3.5.3.

7.3 Depth of Penetration

As described in chapter 3, it is possible to determine overall, elastic and inelastic deformation of the sample in the vertical direction by reference to the force curve recorded during the indent. The residual inelastic deformation will approximate to the depth of penetration of the needle tip into the corneocyte structure. Indents with different peak indentation forces were recorded on corneocyte cells in order to determine the depth of penetration of the needle into the cell.

As might be expected, both the overall deformation and force curve hysteresis (related to the inelastic deformation of the cell) are observed to increase with increasing applied force (see figure 7-3a). Indentation with needles of different radii showed that the indentation depth was a function of the applied pressure

beneath the needle tip. The pressure P is approximated here as

$$P = \frac{F}{2\pi R^2} \tag{7.1}$$

where R is the tip radius and F is the applied force. This equation assumes uniform distribution of the force over a hemispherical tip surface. Figure 7-3b shows the inelastic deformation as a function of pressure; the similarity between the pressure-deformation relationships indicates that the deformation is a function of pressure rather than purely a function of the applied force.

In these experiments, it was also observed that the depth of penetration is related to the indentation approach rate. This effect is shown in figure 7-4. At slower velocities, the tip penetrates deeper into the corneocyte for a given applied indentation force. This suggests a significant viscous effect, as the cell's deformation under the needle tip is time-dependent. With a force applied over a longer period of time, the needle sinks deeper into the cell. This effect is often observed in polymers and other viscoelastic materials; when it occurs under constant applied force, the deformation observed is known as "creep". Cells and biological tissues are often also reported to deform in a viscous or viscoelastic manner with associated creep effects, and it is likely that this is the source of the variation in deformation as a function of the loading rate observed in our experiments. [5, 83–88, 191]

Figure 7-5a shows the elastic deformation recorded on cells from 4 volunteers as a function of applied force; part b of the same figure compares the elastic, inelastic and overall deformation. For low forces, the inelastic deformation recorded on the cells is low; with increasing applied force, the inelastic deformation increases while the elastic deformation saturates as the force exceeds the elastic limit of the corneocyte material, as shown in figure 7-5a. However, there is still some elastic recovery of the sample material even after indentation with a large applied force, as can be seen in figure 7-5b.

It should be noted that in all the measurements of the overall, inelastic and elastic deformation of the cell there is a distribution of values of the measured deformation under a given tip-sample force or pressure. This occurs most likely due to variation between individual volunteers, individual corneocytes, and at different sites on the corneocyte surface due to variations in its structure and mechanical properties.

a)

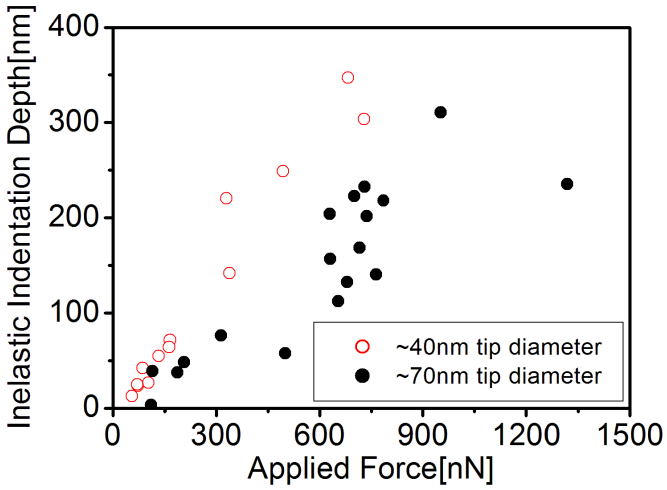

b)

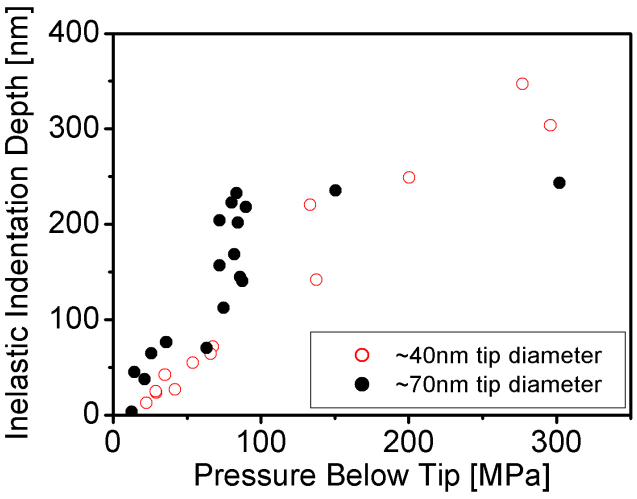

Figure 7-3: a) Inelastic penetration into a corneocyte (as measured from curve hysteresis) as a function of applied indentation force for different needle diameters. b) Inelastic penetration as a function of applied pressure; data compiled for 4 volunteers.

7.4 Elastic Moduli at Surface

At small deformations (less than the radius of curvature, R, of the nanoneedle tip), much of the deformation is elastic as required by the Hertz model. Fitting the initial region of the approach curves to equation 2.1 shown in section 2.3.1 allowed calculation of the reduced elastic modulus at small deformations using this model. An example of a fit to the Hertz model is shown in figure 7-6.

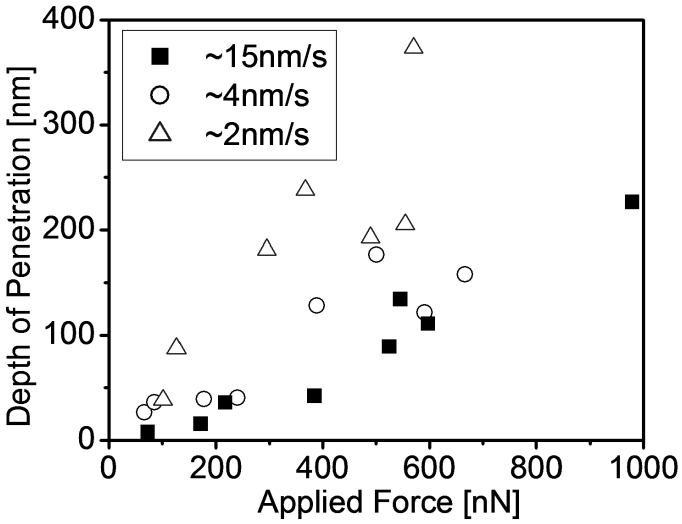

Figure 7-4: Inelastic deformation of corneocytes cells recorded for a ∼40 nm diameter needle for different approach-retract velocities. Data shown here is a typical example from a single volunteer.

The Hertz model does not take into account time-dependent (viscoelastic) properties of the sample, and therefore the elastic modulus calculated using the Hertz model for a viscoelastic sample should vary significantly for different approach-retract rates. Elastic moduli calculated for a range of approach-retract velocities from 2-1000 nm/s are shown in table 7.1 and figure 7-7. It is clear from this result that there is significant variation of the calculated elastic modulus with the rate of deformation.

Table 7.1: Measured elastic modulus using Hertz model. Data is compiled from indents on corneocytes from 5 volunteers; N indicates number of indents. SD is standard deviation, SE is standard error.

Velocity [nm/s]	Mean E_r [MPa]	SD	SE	N
2	85.15	47.91	15.15	10
4	135.25	116.0	19.34	36
15	232.20	132.04	28.81	21
1000	838.95	529.34	176.445	9

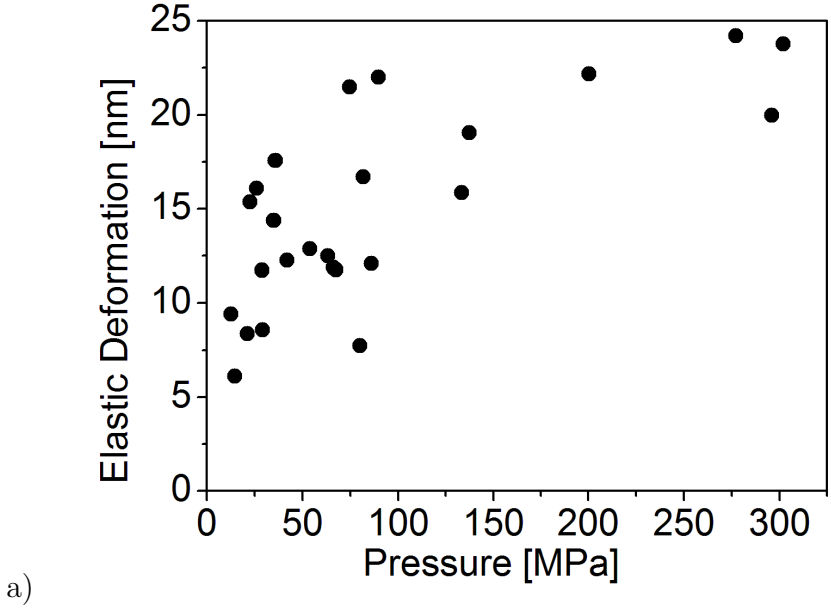

a)

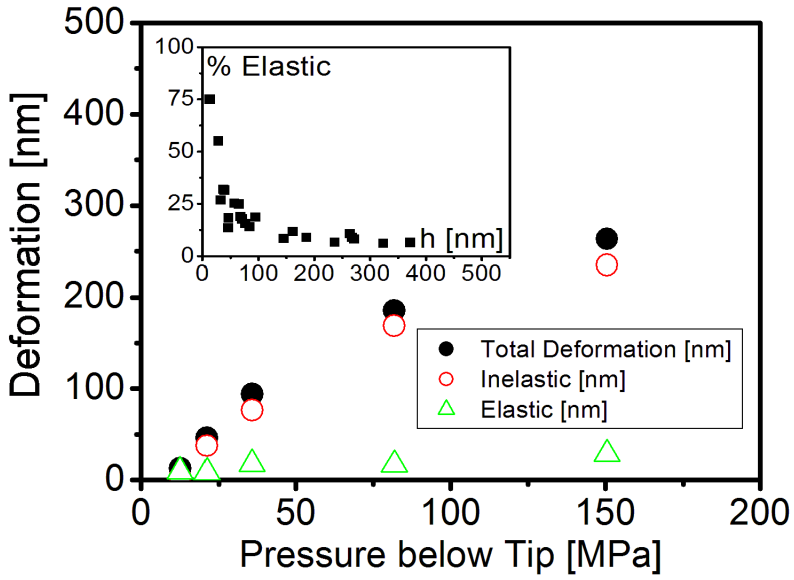

b)

Figure 7-5: a) Elastic deformation of corneocyte cells by nanoneedle probes as a function of pressure below probe tip; data compiled for 4 volunteers. b) Comparison of elastic, inelastic and overall deformation as a function of pressure for corneocytes from a single volunteer. Inset shows compiled data from volunteers showing percentage of deformation which recovers elastically as a function of depth of penetration; this data is compiled from 4 volunteers.

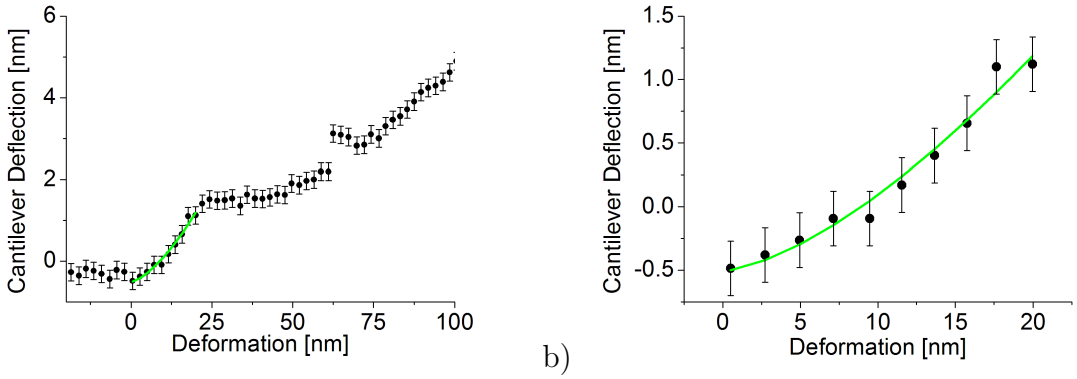

a) b)

Figure 7-6: a) Deformation-force curve calculated for approach on a corneocyte using a ~75 nm diameter nanoneedle AFM probe. b) Enlarged region showing fit to Hertz model. Error bars calculated from noise in deflection signal of cantilever when the tip is not in contact with the sample surface.

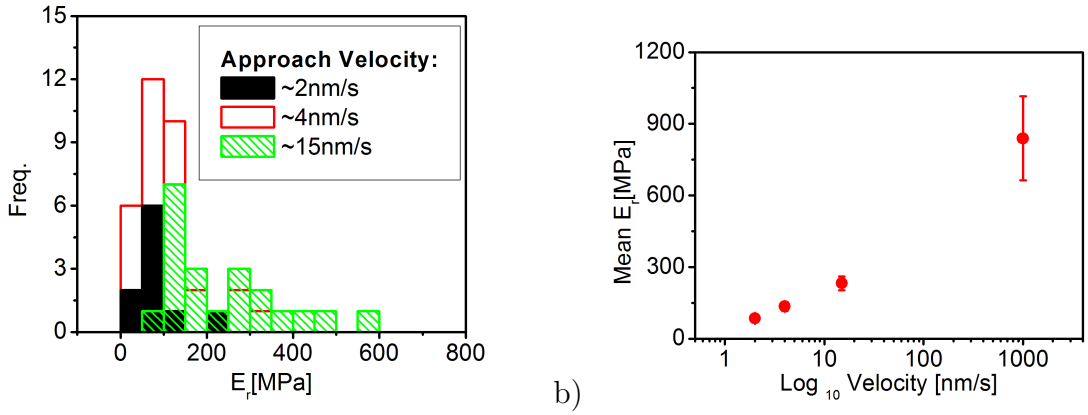

a) b)

Figure 7-7: a) Histogram of measured elastic moduli calculated using the Hertz model for different approach-retract velocities at the surface of corneocytes. Note that data for 1000 nm/s approach-retract velocity is not shown so that the other sets can be shown more clearly. b) Average elastic moduli as a function of approach-retract velocity. Error bars show standard error from averaged results; data compiled for 5 volunteers.

The significant variation in the measured elastic modulus of the corneocyte surface with the approach-retract velocity indicates the viscoelastic nature of the sample material, and therefore is consistent with the viscous behaviour of the corneocyte mentioned in section 7.3 above. It should be noted that there is a distribution of measured elastic moduli over a significant range for each velocity,

most likely again due to variation between individual cells, individual volunteers, or between different sites on the surface of a cell.

The values of elastic modulus presented here are rather different to those reported by a study of surface mechanical properties of corneocytes by Gaikwad *et al.* [189] However, this study used extremely low penetration depths (<10 nm). At these depths, Gaikwad *et al* determined much lower values of elastic modulus (24-70 MPa at fast approach rates) using a modification of the Hertz model incorporating adhesion effects.

The surface of corneocytes is coated with lipid molecules, consisting of ceramides, fatty acids, cholesterol and cholesterol sulphate. [141] These molecules are covalently bound to the corneocyte protein envelope, creating a thin outer layer of lipids. Due to the small penetration depth in the experiments of Gaikwad *et al*, much of what was measured in their experiments may have been these very soft lipids on the outer surface of the corneocyte. In our study, therefore, it is likely that the larger depth of penetration has led to detection of a convolution of the properties of the stiffer internal structure and softer outer structure even at small indentation depths, increasing the measured elastic modulus.

7.4.1 Effect of Indenter Diameter

An important parameter for analysis using the Hertz model is the radius of curvature of the indenter. In our experiments, nanoneedles of two different diameters were used; ∼40 nm and ∼70 nm, which have radii of curvature of half these values. The Hertz model should compensate for the different pressure beneath indenters of different radii, resulting in similar derived elastic modulus for similar samples.

The graph in figure 7-8 shows the elastic moduli calculated from approach-retract curves at an approach rate of ∼4 nm/s for two different needle tip diameters. The overlap of this data would seem to indicate that the needle diameter does not have a strong effect on the calculation of elastic moduli at the corneocyte surface using the Hertz model, suggesting that this model is able to adequately compensate for the different tip radii of the nanoneedle indenters.

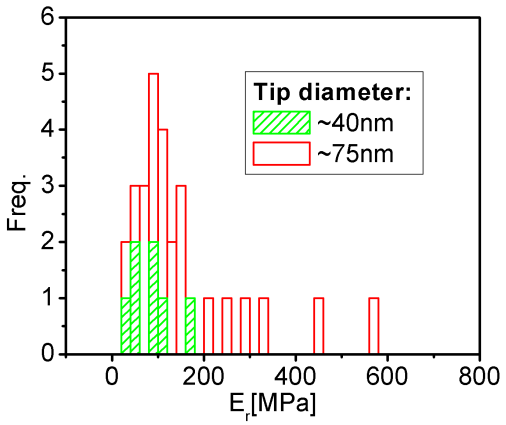

a)

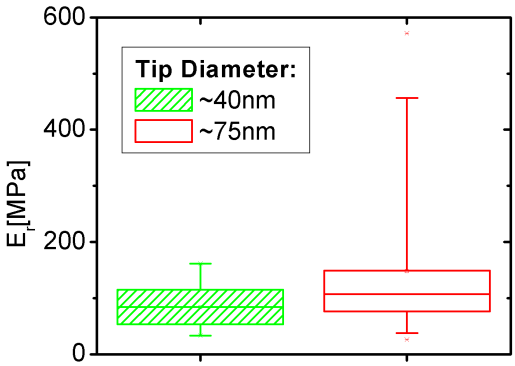

b)

Figure 7-8: a) Histogram and b) box plot of elastic moduli calculated for needles of two different diameters. The Hertz model produces similar values of elastic modulus in either case.

7.5 Multiple Indents

One application of the nanoneedle AFM probes that we propose is "mechanical tomography", recording the mechanical properties as a function of depth beneath a chosen site on the cell surface. If such a measurement can be carried out for multiple sites on a cell, a three-dimensional map of the mechanical properties of the cell could be constructed.

In order to examine mechanical properties at a range of depths below the surface of a sample, a process was designed which indented multiple times at the same site on a cell, allowing the applied force to return to zero before the next indent but without withdrawing the probe from contact with the cell surface. This process allowed multiple approach-retract curves to be recorded for indentation at a single site. An example of a force curve recorded using this multiple indentation technique is shown in figure 7-9.

In this process, each indent was carried out using a larger force than the previous one, and the needle penetrated further into the cell with each indent. However, the force curves appeared to show that further inelastic deformation would only occur when the force exceeded that of the previous indent. This is shown by the lack of hysteresis between each retract curve and the following approach curve (see figure 7-9); the inflection of the approach curve and onset of

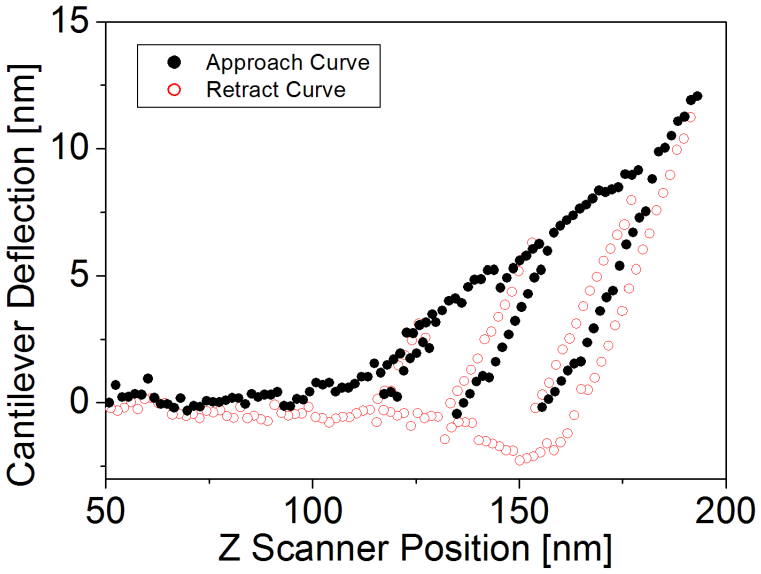

Figure 7-9: Force curve recorded using multiple indentation on a single site on the surface of a corneocyte cell, with an approach-retract rate of ~4 nm/s. The onset of hysteresis indicating inelastic deformation during each approach occurs only when the applied force (which is proportionate to the cantilever deflection) exceeds the peak force of the previous approach.

hysteresis indicative of inelastic deformation occurs only once the peak load of the previous indent has been surpassed.

This would appear to indicate that once the cell material has undergone inelastic deformation during the approach process, in which the applied indentation force is raised from zero to a peak loak, the material will then behave elastically until an indentation force greater than the peak load is applied again. A purely elastic response during the unloading of a sample is often assumed in models of indentation, such as the "compliance model" described in chapter 2. This would suggest that these models can be used to determine the elastic properties of the sample.

When performing these multiple indents, it was often clear that there were two regimes of principally elastic deformation (where very little hysteresis was visible in the force curve) separated by a single approach-retract cycle exhibiting large inelastic deformation (as evidenced by its large hysteresis). Figure 7-10 shows an example of this effect. This would seem to indicate two layers of elastic

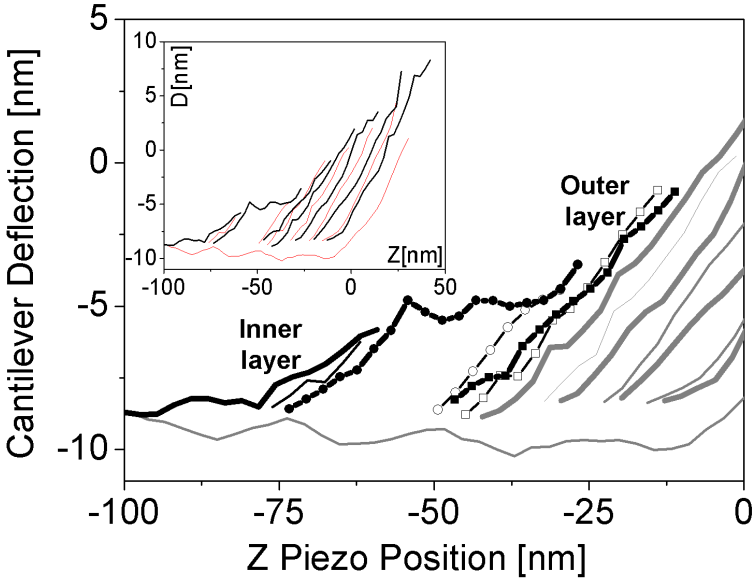

Figure 7-10: Force curves recorded during multiple indentation. Note that these curves appear to show that the sample consists of two layers of elastic material, separated by a penetration event and a single approach-retract cycle with large hysteresis indicating inelastic deformation (circle symbols). An example of an approach-retract curve on the outer layer (solid black line), and one recorded on the inner layer (square symbols) are shown. Inset graph shows the full curve recorded by the AFM; the main graph shows an enlarged view.

material, with the tip eventually breaking through the outer surface layer when the applied force becomes large enough and afterward making contact with the layer underneath. This outer layer is likely to be the corneocyte's cornified envelope, while the inner layer is probably the internal keratin matrix which is known to make up the corneocyte intracellular structure (see chapter 2 for a detailed description of this structure).

This would support the results from single indents showing clear inflections corresponding to penetration through an outer layer (see section 7.2). It would also suggest that the nanoneedle can indeed be used for mechanical tomography of a biological sample, penetrating its outer layers to detect intracellular structures present beneath the sample surface.

7.6 Elastic Moduli of Internal Structure

Previous studies of the mechanical properties of corneocytes using AFM were limited to the surface. [189] The nanoneedles in our experiments penetrated cells to depths of >300 nm, causing significant inelastic deformation. Even at these large deformations, there was some recovery of the deformation of the corneocyte material, which we attributed to elastic recovery of the cell structure. It is also possible that some of the recovery may have been due to the regeneration and repair of the cellular material by processes within the corneocyte, but this can be expected to be negligible for corneocytes over the time period of the probe retraction as the cells are not particularly active. The elastic recovery of the cell material allowed the estimation of the elastic modulus using the compliance model, which was performed for some corneocyte samples. However, the calculated elastic modulus of corneocytes was found to vary strongly with the rate at which the corneocyte is deformed, due to the time-dependent viscous properties of the sample material.

In order to separate time-dependent and time-independent components of the deformation of the corneocyte, a model was derived for indentation using a nanoneedle based on that derived by Oyen and Cook for viscoelastic-plastic deformation of samples. [89] Oyen and Cook used the "Maxwell model" to derive expressions for the force-deformation behaviour of viscoelastic-plastic materials under conical indentation (see diagram in figure 2-4 in section 2.3.1).

7.6.1 Derivation of Model

In the model derived here, the nanoneedle is assumed to be cylindrical. Sneddon [80] showed that elastic deformation using a cylindrical indenter is directly proportionate to the applied force, such that

$$F_e = kh_e \tag{7.2}$$

In this case k is the spring constant of the elastic spring element in a "Maxwell model", F_e is the force on the spring element, and h_e is the deformation of the spring element. The Maxwell model is illustrated in figure 2-4 in section 2.3.1. The cylindrical approximation can be applied since, for deformations greater

than the radius of curvature of the nanoneedle tip, the cylindrical shape of the nanoneedle means that the projected contact area will not change with depth of penetration and so the value of A in equation 2.4 (see section 2.3.1) remains constant, as for a perfectly cylindrical indenter.

Oyen and Cook assumed that for conical indenters

$$F_e = k_Q h_e^2 \tag{7.3}$$

$$F_v = \mu_Q (\frac{dh_v}{dt})^2 \tag{7.4}$$

where k_Q is the "quadratic spring constant" of the spring element, μ_Q is the "quadratic coefficient of viscous damping" in the damping element in the Maxwell model, F_v is the force on the damper element, t is time and h_v is the deformation of the damper element. Oyen and Cook assumed equation 7.4 is the case for time-dependent deformation of the sample material by a conical indenter, based on the derivation of 7.3 by Sneddon. In other words, they assumed that the viscoelastic deformation will have a similar variation with applied force to that for the elastic deformation. In our derivation for a cylindrical indenter, we make the similar assumption based on 7.2 that

$$F_v = \mu \frac{dh_v}{dt} \tag{7.5}$$

where μ is the damping coefficient of the damper element in the Maxwell model. For a linear combination of the elastic spring and viscous damper, the total deformation h is given by

$$h = h_e + h_v + h_i \tag{7.6}$$

where h_i is the inelastic (plastic) deformation of the sample. As with the compliance model, it is assumed that all inelastic deformation occurs during the initial approach, and that deformation during the retraction of the probe is elastic i.e. $\frac{dh_i}{dt} = 0$ during the retraction of the AFM probe. This is shown to be the case for the corneocyte material in the results presented in section 7.5. Therefore during the retraction of the AFM probe

$$\frac{dh}{dt} = \frac{dh_e}{dt} + \frac{dh_v}{dt} \tag{7.7}$$

Since the spring and damper elements are linked in series, both experience equal force (therefore $F = F_e = F_v$). Substituting this, 7.2 and 7.5 into 7.7 gives

$$\frac{dh}{dt} = \frac{F}{\mu} + \frac{1}{k}\frac{dF}{dt} \tag{7.8}$$

If we assume a constant "loading rate" $\mathcal{R}$, then, during the retraction of the probe

$$F = \mathcal{R}(2t_f - t) \tag{7.9}$$

and

$$\frac{dF}{dt} = -\mathcal{R} \tag{7.10}$$

where t_f is the time taken to for the force to decrease from the peak load to zero, then equation 7.8 becomes

$$\frac{dh}{dt} = \frac{\mathcal{R}(2t_f - t)}{\mu} - \frac{\mathcal{R}}{k} \tag{7.11}$$

Integrating equation 7.11 with respect to t gives

$$h = -\frac{\mathcal{R}t^2}{2\mu} + \frac{2\mathcal{R}t_f t}{\mu} - \frac{\mathcal{R}t}{k} + C \tag{7.12}$$

where C is a constant of integration. This equation can be written as the 2nd-order polynomial

$$h = p_1 + p_2 t + p_3 t^2 \tag{7.13}$$

where

$$p_1 = C \tag{7.14}$$

$$p_2 = \mathcal{R}(\frac{2t_f}{\mu} - \frac{1}{k}) \tag{7.15}$$

$$p_3 = -\frac{\mathcal{R}}{2\mu} \tag{7.16}$$

By fitting the curve of the deformation of the corneocyte sample as a function to time to the function 7.13, the coefficients p_1, p_2 and p_3 can be determined. From equation 7.16, μ can be determined. Knowing μ, equation 7.15 can be used to determine k.

The relationship defined in the compliance model (see equation 2.4 in section 2.3.1) for elastic deformation can be used to find E. This equation is

$$k = \frac{dF_e}{dh_e} = \frac{2}{\sqrt{\pi}} E_r \sqrt{A} \tag{7.17}$$

where E_r is the "reduced elastic modulus" $E_r = \frac{E}{1-\nu^2}$ where ν is the Poisson ratio (see section 2.3.1) and A is the projected contact area of the indenter. If the nanoneedle is assumed to have a circular cross section then $A = \pi R^2$ where R is the needle radius. Therefore

$$k = \frac{2}{\sqrt{\pi}} E_r \sqrt{\pi R^2} = 2E_r R \tag{7.18}$$

Therefore, the reduced elastic modulus can be determined from the deformation-time curve corresponding to the retraction of the AFM probe. In section 7.6 this model is used to determine the elastic modulus of structures at depths of >300 nm below the surface of corneocytes.

7.6.2 Results from Analysis Incorporating Viscoelasticity

Figure 7-11 shows an example of a fit of the calculated deformation of a corneocyte during the retraction of the AFM probe to the viscoelastic model derived in section 7.6.1. Examination of data from nanoneedle indentation on corneocytes showed less variation of the calculated elastic modulus with the approach-retract velocity compared to analysis using the compliance model, as illustrated in figure 7-12. This would indicate that the viscoelastic model is able to compensate reasonably well for the time-dependence of the deformation of the viscoelastic material of the corneocyte. However, there is still some variation indicating that this model does not completely separate the time-dependent viscous effects from the time-independent effects.

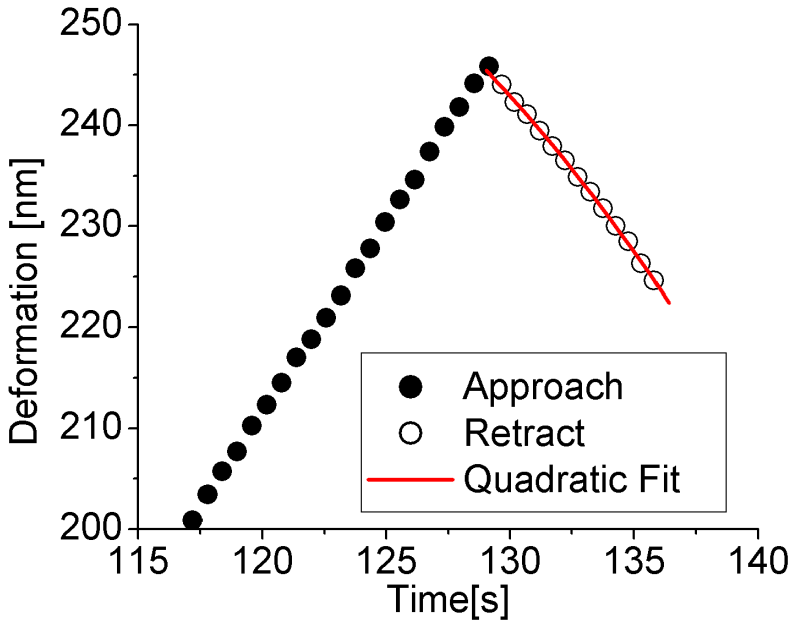

Figure 7-11: Deformation as a function of time for indentation on a corneocyte using nanoneedle probe, including fit to viscoelastic model described in section 7.6.1.

Elastic moduli calculated using the model incorporating viscoelasticity for 5 volunteers over a range of depths and applied forces are shown in figure 7-13. At small indentation depths, the elastic moduli calculated using this method agree reasonably well with those calculated using the Hertz model for the same approach-retract velocity (∼4 nm/s), as described in section 7.4. However, as the nanoneedle penetrates deeper into the cell the elastic modulus appears to increase over the range of inelastic deformation from 0-100 nm. For inelastic deformations greater than ∼100 nm, the elastic modulus becomes relatively constant again at a value of ∼500 MPa.

This variation in elastic modulus may occur as the needle encounters different structures within the corneocyte. The lower elastic modulus at the surface may correspond to the softer external cornified protein envelope, while the higher elastic modulus is measured once the needle penetrates the outer layers of the corneocyte and deforms the stiffer keratin fibrils within the corneocyte. This result is discussed in more detail in section 7.8.

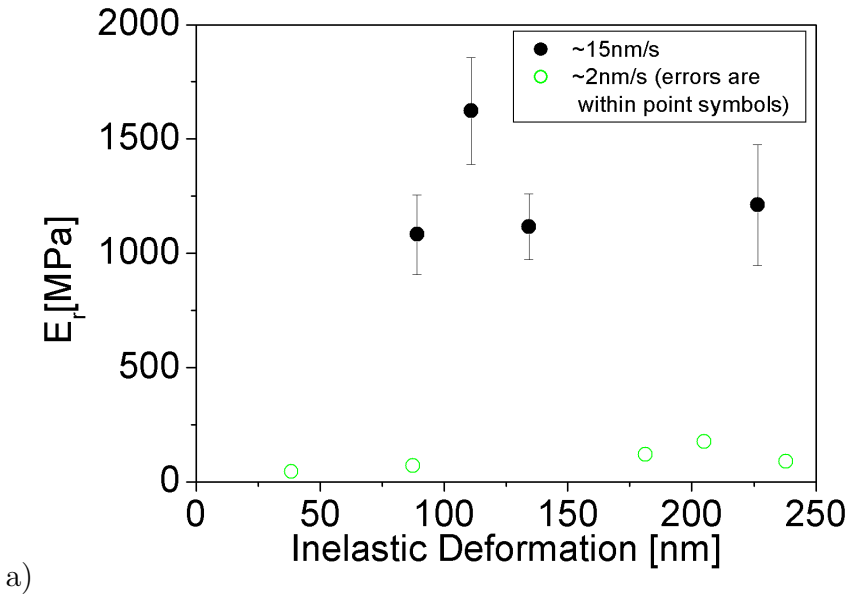

a)

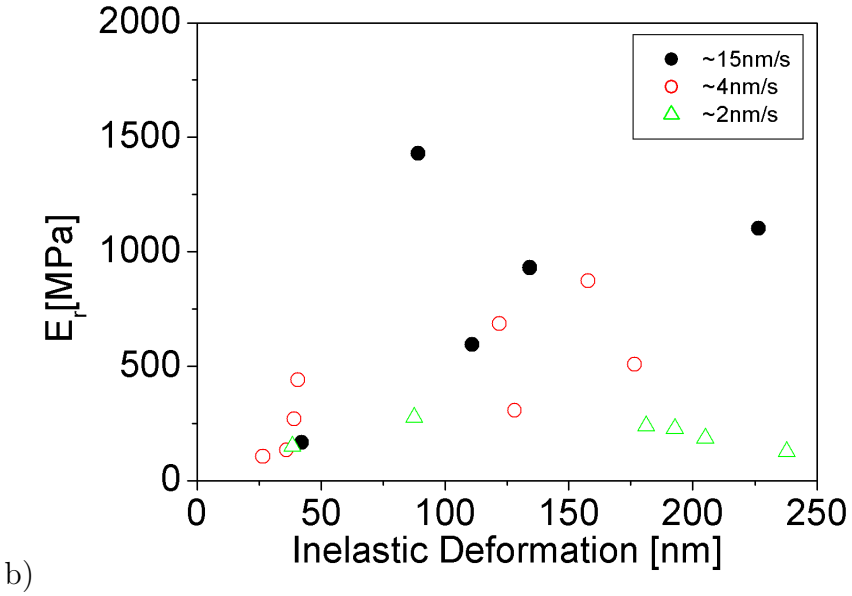

b)

Figure 7-12: Elastic moduli calculated for indents on a corneocyte sample for different approach-retract velocities for a) the compliance model based on the gradient of the retract curve b) the model incorporating viscoelastic effects. Significant variation of elastic modulus is observed at different indentation velocities in (a) due to viscoelasticity of the sample. In (b) there is less variation of the calculated elastic modulus for different approach rates. Data shown is for a single volunteer.

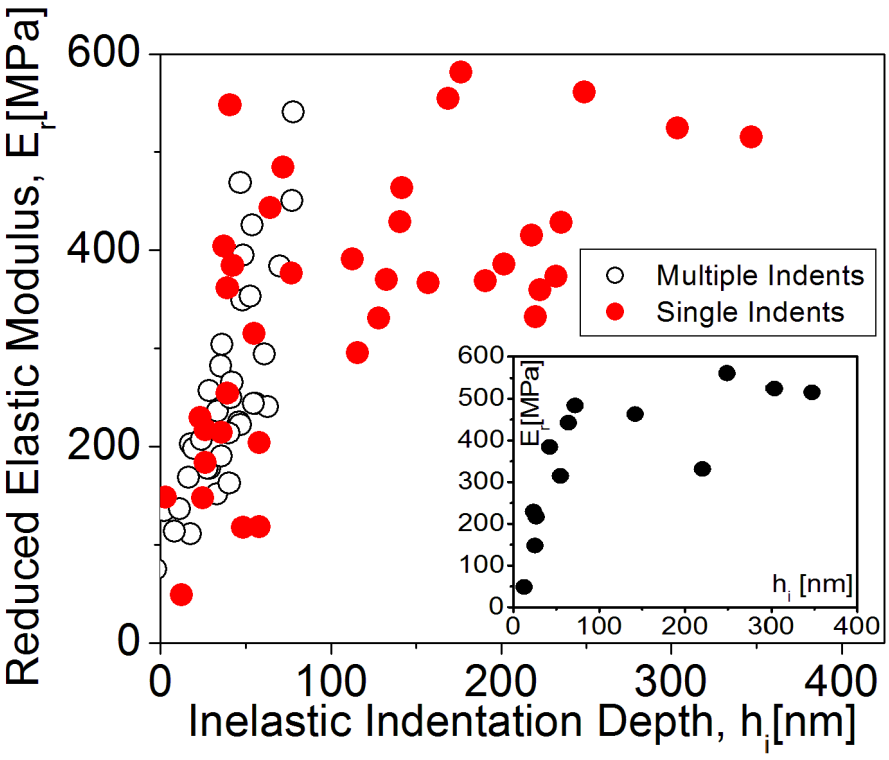

Figure 7-13: Elastic moduli calculated from multiple and single indentation as a function of the calculated inelastic deformation (indentation depth) for an approach-retract velocity of ~4 nm/s. Data is compiled from 5 volunteers. Data for both single and multiple indents is shown to be in good agreement. Inset graph shows example of trend of data for one volunteer.

These results demonstrate that indentation using a nanoneedle probe allows the determination of the elastic modulus of structures at a known depth below the surface of the corneocyte. This indicates its usefulness as a tool to study the internal mechanical properties of biological cells. However, it is clear from the variation of calculated elastic moduli with approach-retract velocity that the viscous and elastic deformation of the structures cannot be completely separated using the models described here; it is likely that more complex models will be needed to more accurately describe the deformation of biological structures during indentation.

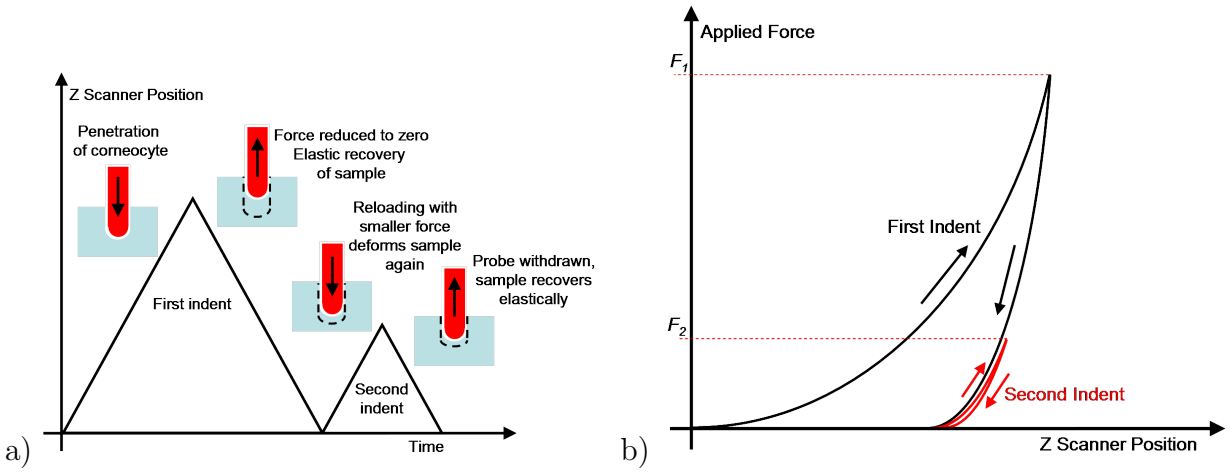

Figure 7-14: Schematic of method of double indentation. a) shows the movement of the AFM scanner while the tip is in contact with the sample, while b) shows the applied force as a function of scanner position.

7.7 Double Indentation

As a test of the usefulness of the model incorporating viscoelastic deformation described here, a new indentation technique was developed in which a second indent of much lower force is made at the same site as the first indent, before the needle is fully withdrawn from the sample surface. This is achieved by first lowering the probe until the tip-sample force reaches the target deflection value corresponding to an applied force F_1, then raising the probe until the cantilever deflection returns to zero, and then repeating the process with a much lower target force F_2 (see figure 7-14).

The purpose of this was to test if the increased elastic modulus occurred due to hardening of the corneocyte material under the increased pressure necessary to penetrate the corneocyte. The second indent was therefore performed at a similar depth to the first, with a much smaller final force (and therefore much smaller pressure). An example of a force curve recorded using this technique is shown in figure 7-15.

From the first indentation cycle with large deformation and strong viscous effects, the elastic modulus of the material beneath the nanoneedle tip can be determined using the viscoelastic model. The force-deformation curve of the second indent was highly linear and therefore the second indent was fitted to the compliance model for elastic deformation using a cylindrical indenter, which predicts a

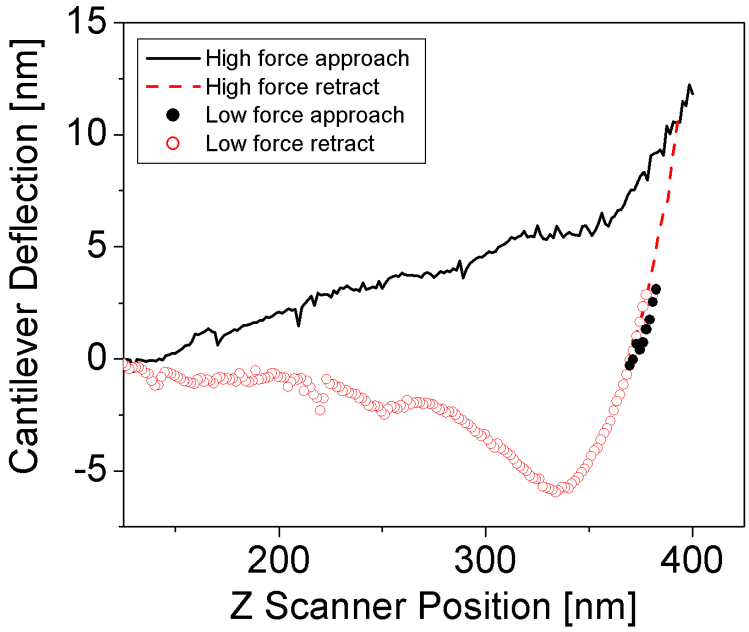

Figure 7-15: Example of force curve recorded during double indentation on a corneocyte. The second indent follows the path of the retract curve of the first indent, indicating that deformation after the initial inelastic deformation during the approach is elastic.

linear relationship between force and deformation under these conditions. Figure 7-16 shows the results of applying this method to indentation on a corneocyte sample.

There are two important points to note from these results. Firstly, using a linear fit to the force-deformation curve during the second indent, the compliance model gives values of E_r similar to those calculated using the viscoelastic model. This would indicate that the measured elastic modulus is not a function of the pressure applied to the corneocyte; rather, it is a function of the inelastic deformation, which reflects the depth of penetration into the cell.

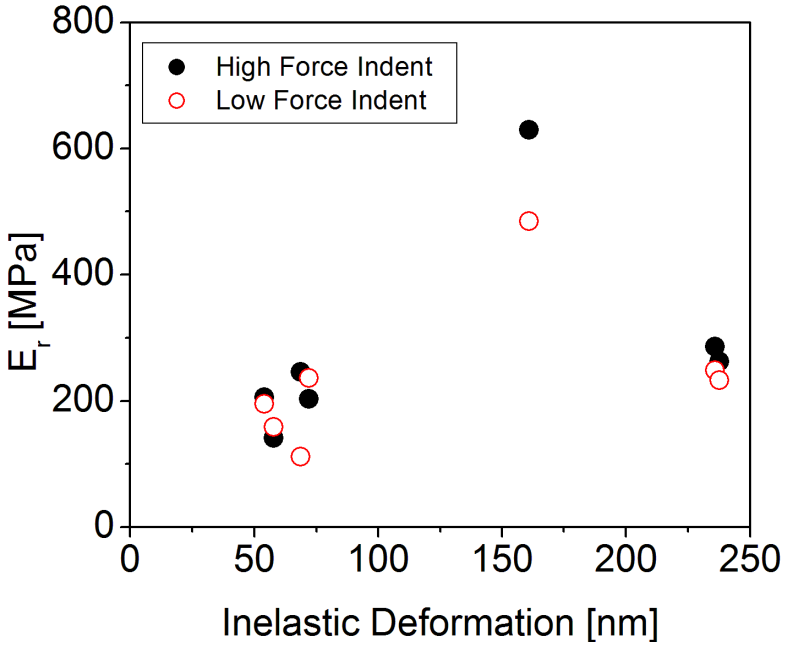

Figure 7-16: Comparison of elastic moduli E_r calculated from application of viscoelastic model to first indentation (at high force) and from the application of the compliance model to the second indentation (at low force); both indents are recorded on corneocyte cells. Data shown is from a single volunteer.

7.8 Discussion of Mechanical Tomography of Corneocytes

The results discussed in this chapter support a "two-layer model" of the corneocyte structure. In this model, the corneocyte surface is composed of a softer outer layer, which deforms elastically under small applied indentation forces. This is supported by the data for multiple indentation at the same site on the cell surface, shown in section 7.5, which indicates elastic deformation of the outer layer at small forces and inelastic deformation at larger forces. The inelastic deformation of the outer layer corresponds to the penetration of the needle tip through this layer; this is the cause of the inflections and peaks in the AFM approach curves described as "penetration events" in section 7.2. Upon penetration of the surface layer, the needle makes contact with an internal layer; calculation of the elastic modulus using the viscoelastic model, as described in section 7.6, shows

this layer to be stiffer than the outer layer, and also thicker (with increased elastic modulus detected over a range of 100-300 nm below the surface).

It is possible that this effect arises from the different layers of material known to exist below the corneocyte surface. Electron microscope studies have shown that corneocytes have an external protein envelope covalently bonded to lipid molecules which fill the intracellular spaces of the stratum corneum. This envelope surrounds a matrix of keratin intermediate filaments which make up the corneocyte cytoskeleton. [141,192] Keratin is a structural protein known to have a high stiffness (1.7-2.5 GPa). [193] The elastic modulus of the keratin network will also depend on the filament density within the cytoskeleton and the mechanical properties of the proteins which bind the filaments to the cornified envelope, so may be lower than this value. However, it is still likely that the measured elastic modulus of the keratin intracellular structure of the corneocyte would be higher than that of the softer protein envelope. One interpretation of the results shown in figure 7-13 is that the lower elastic modulus measured at small indentation depths corresponds to that of the outer protein envelope, while that at larger depths indicates that of the keratin intermediate filaments.

It is noted that figure 7-13 shows a smooth transition from the elastic modulus measured at the outer layer to that of the inner layer as the indentation depth increases, rather than an abrupt transition as might be expected from a system with two distinct layers. This may be due to increasing deformation of both the inner and outer layer as the deformation of the outer layer by the needle increases, with the stiffer internal layer providing a greater resistance to the deformation of the whole structure. This would mean that the needle increasingly detects a convolution of the mechanical properties of the inner and outer layers as it penetrates deeper into the outer layer, resulting in a smooth transition of the measured elastic modulus from one to the other. It is possible that a more sophisticated analysis (e.g. incorporating a finite element model of the corneocyte structure) would allow the properties of these layers to be determined more accurately.

However, the results presented here indicate that the needle can be used to measure the elastic properties of structures over a range of depths within a corneocyte, and therefore could potentially be used to probe mechanical properties of other intracellular structures e.g. nuclei, mitochondria, or cytoskeletal struc-

tures. The process of determining mechanical properties over a range of depths below the surface of a sample has been termed "mechanical tomography". It has been shown here that EBID nanoneedles fabricated on AFM probes can be used for mechanical tomography of biological samples. This could be used to construct three-dimensional maps of the elasticity or other mechanical properties of the cell. The small diameter and high aspect ratio of the nanoneedle probes would allow this mapping to be performed with high spatial resolution and without causing significant damage to the overall cell structure.

7.9 Effect on Corneocyte

It was noted that penetration events, recorded as steps or peaks in the approach curve, were most likely to be observed during the first indent on an individual corneocyte. This was effect was confirmed by examination of 70 force curves recorded on corneocytes from 5 different volunteers. As shown in figure 7-17, the probability of observing a step decreased with each indent.

It is unlikely that the surface of the cell was not penetrated by the subsequent indents, since there is still large hysteresis between the approach and retract curves, indicative of inelastic deformation. However, it is possible that the penetration occurs without an observable step in the force curves as the needle was able to penetrate more smoothly into the cell, without as much resistance from the corneocyte surface.

This would indicate that each indent perturbs the integrity of the corneocyte lipid-protein envelope, decreasing the resistance of the envelope as a whole to deformation. This would seem to suggest that the needle is changing the cell surface as a whole rather than on a local level, which would be a problem if the nanoneedle is to be used to investigate the cell organisation as the presence of the needle would disrupt the cell.

However, the same level of disruption would not be expected on other cell types which lack the cornified envelope of the corneocyte but instead have a lipid-based cell membrane. This membrane is organised by hydrophobic and hydrophilic interactions between the phospholipids which make up the membrane; these tend to form a continuous bilayer with the hydrophilic parts of the molecule exposed to the cell's aqueous environment and cytoplasm and the hydrophobic

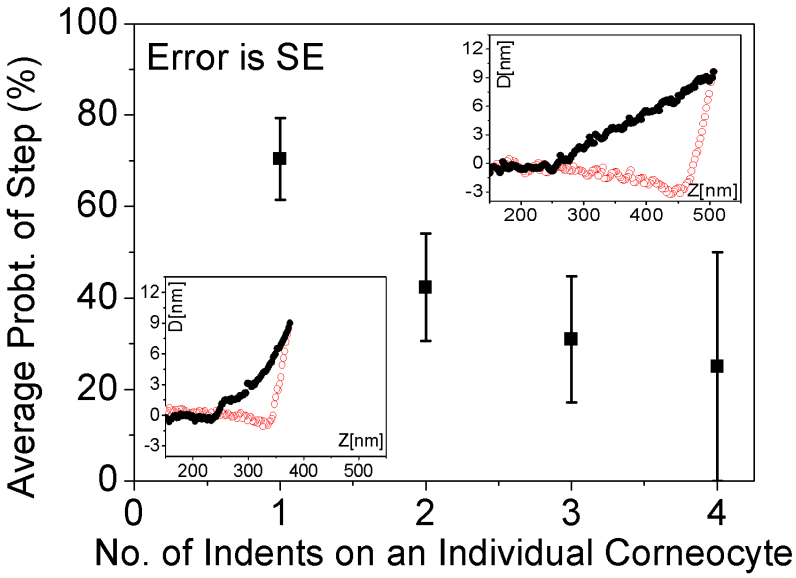

Figure 7-17: The probability of observation of a step corresponding to a penetration event in force curves decreases with increasing number of indents on the same cell. Inset graphs show typical curves with (upper) and without (lower) detectable penetration events. Error bars show standard error on the average probability of observing a penetration event.

parts within the membrane itself. A hole in such a membrane represents an energetically unfavourable state and the lipid molecules around the hole will tend to move to reseal it. This would allow local damage to the membrane by the nanoneedle tip to be repaired, allowing the cell to remain viable after indentation. [94] It is also likely that the perturbation of the corneocyte internal structure is likely to be much less than that of the surface, as the corneocyte surface is composed of a single continuous protein layer while the internal structure is composed of individual keratin fibrils.

As the approach curves suggest a change in the mechanical behaviour of the surface following the initial indent, it could be expected that the measured elastic modulus of the surface would change. However, we were not able to detect any difference in the surface mechanical properties as measured using the Hertz model (as described in section 7.4), nor in the internal mechanical properties as measured using the model incorporating viscoelasticity (see section 7.6) between force curves with and without visible penetration events. Graphs comparing

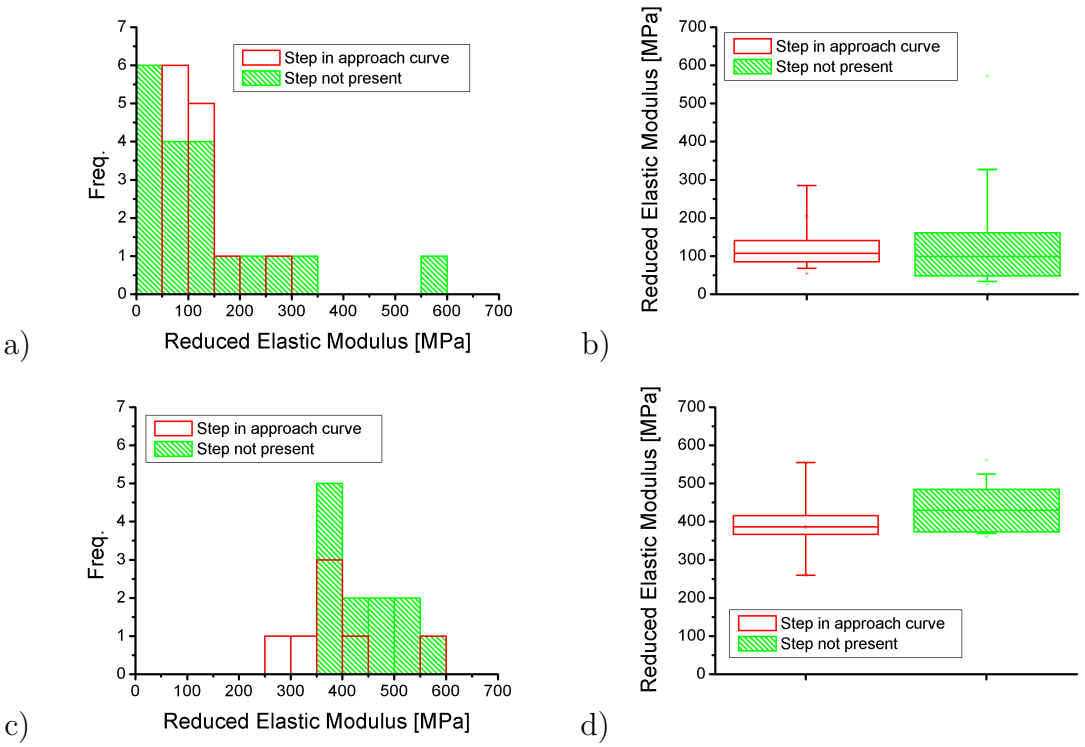

Figure 7-18: a) Histogram and b) box chart comparing elastic moduli determined at the corneocyte surface using the Hertz model for approach curves with and without penetration events. c) Histogram and d) box chart comparing internal elastic moduli of corneocytes determined using the viscoelastic model.

the measured elastic moduli for curves with and without steps corresponding to penetration events are shown in figure 7-18; there is significant overlap between the elastic moduli measured in these two cases.

One reason that there is no detectable change in mechanical properties may be that these indentation techniques are not sensitive enough to pick up this change in properties. However, it is also possible that while the surface mechanical behaviour been affected over large areas of the corneocyte surface, the properties of the surface material at a very local level (immediately beneath the needle tip) may not have been significantly altered. Any change which is present might become clearer if more experiments were performed to increase the sample size.

7.10 Changes in Elastic Modulus of SLS-Treated Corneocytes

The elastic modulus and other mechanical properties of biological cells are known to vary significantly in disease states, such during oncogenesis (the onset of cancer). [88,95–98] These changes in mechanical properties are thought to arise from changes in the cell's internal organisation.

Sodium lauryl sulphate (SLS, also known as sodium dodecyl sulphate) is a mild irritant to skin present in many hygiene products e.g. toothpastes, shampoos, hand washes and shaving foam. It is known to disrupt lipids in the skin and is often used as a "model irritant" in dermatological studies. [194] Use of low concentration SLS over a period of several weeks can induce irritation which can function as a model for chronic irritant contact dermatitis; this is similar to the widespread skin condition of atopic dermatitis. SLS-treated skin can therefore serve to simulate changes in the skin and stratum corneum arising from atopic dermatitis.

Sites on the forearms of a group of volunteers were treated with 0.1% SLS over a period of 3 weeks to induce these changes. This was carried out as part of a study in the Department of Pharmacy and Pharmacology studying biochemical changes in the treated skin using AFM, infrared spectroscopy, mass spectrometry and fluorescence microscopy. Sampling of corneocytes was carried out on this arm, with samples taken from the other (untreated) arm of the same volunteer which acted as controls. Full details of these experiments can be found in appendix A.

Indentation to depths of up to 300 nm was carried out on these samples using nanoneedle probes with tip diameters of $\sim$75 nm. The elastic moduli of these samples were calculated using the viscoelastic model described in this chapter. The calculated reduced elastic modulus shows systematically lower mean values for SLS-treated samples compared to controls (see table 7.2 and figure 7-19) for all but one of the volunteers.

Although the elastic modulus of the treated cells is lower than that of the control cells for all but one of the volunteers, there is significant variation of elastic modulus of both control and treated cells between individual volunteers. Therefore, in order to compare the data between the treated and control cells a

Volunteer	1	2	3	4
Control Samples				
Mean E_r	526	185	256	150
SD	352	38	56	27
SE	144	17	23	11
N	6	5	6	6
SLS Treated Samples				
Mean E_r	296	163	191	270
SD	97	43	38	77
SE	40	18	16	31
N	6	6	6	6

Table 7.2: Elastic moduli calculated from SLS-treated and control samples.

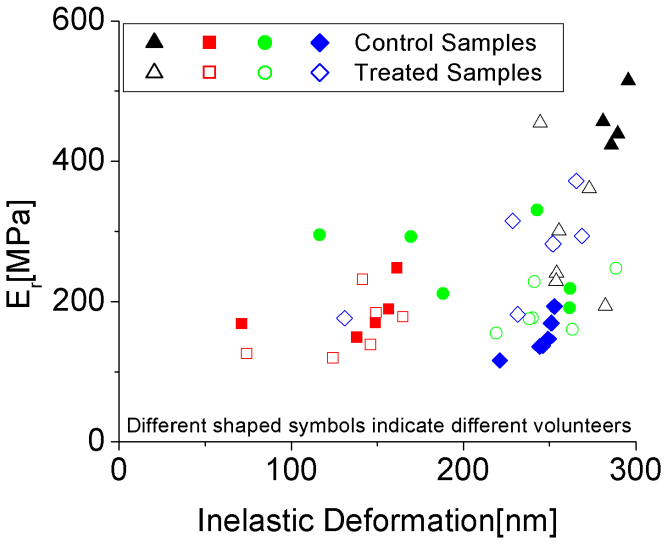

Figure 7-19: Calculated elastic moduli for 4 volunteers as function of indentation depth.

normalised elastic modulus $E_{normalised}$ was calculated using

$$E_{normalised} = \frac{E_r}{\bar{E}_{r\,control}} \tag{7.19}$$

where $\bar{E}_{r\,control}$ is the mean elastic modulus for the control sample for a given volunteer. $E_{normalised}$ can be regarded as the fractional change in elastic modulus for the SLS treated cells compared to the control cells for a given volunteer.

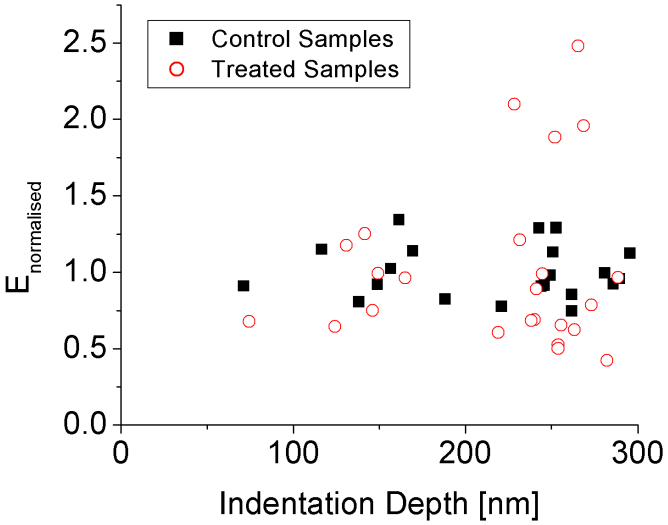

Figure 7-20: Calculated elastic moduli normalised to the control values for 4 volunteers as function of indentation depth.

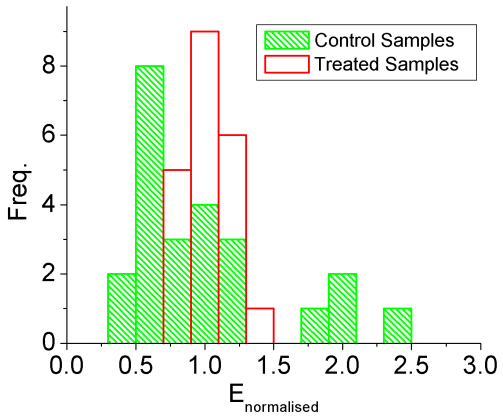

Figure 7-21: Histogram showing normalised elastic moduli for treated and control samples.

Figures 7-20 and 7-21 show the values of normalised elastic modulus. Figure 7-21 suggests a significant difference between the elastic moduli of the SLS-treated and untreated cells. However, an independent t-test on these data sets suggested that there was no significant difference between the these cells (p=0.885, see table 7.3).

If data from volunteer 4 (the only volunteer who did not show a decrease

Table 7.3: T-test results comparing normalised elastic moduli for control and treated samples.

	Mean	Variance	N
SLS Treated	1.02	0.30	24
Control	1.00	0.03	21
t = -1.146			
p = 0.885			

in elastic modulus between control and SLS-treated cells) is treated as outliers and ignored, an independent t-test comparing the treated and control cells shows a clear difference between the data sets for SLS-treated and untreated cells (p=0.001, see table 7.4). It is possible that this volunteer was less susceptible to the effect of the SLS treatment on the cells.

Table 7.4: T-test results comparing normalised elastic moduli for control and treated samples, ignoring data from volunteer 4.

	Mean	Variance	N
SLS Treated	0.76	0.05	18
Control	1.00	0.03	15
t = 3.524			
p = 0.001			

This data suggests that the internal structure of the treated cells is rendered much softer by the treatment compared to the controls, although it is likely that further experimental data is needed to confirm this effect.

7.10.1 Discussion of Results from SLS Treated Skin

The changes observed in the elastic modulus of corneocytes from skin treated with sodium lauryl sulphate (SLS) are likely related to changes known to be induced in the keratinocytes of the basal layer of the epidermis. These cells are responsible for the production of corneocytes, and electron microscope studies have shown them to undergo changes in morphology after treatment with SLS. SLS treatment can also cause parakeratosis of the stratum corneum (the appearance of nucleated cells in the stratum corneum, which is unusual as corneocytes lack nuclei). [195] It is likely that these changes lead to the formation of an abnormal

keratin cytoskeleton in the corneocytes, decreasing their stiffness and so lowering their elastic modulus. SLS is also known to act as a protein denaturant [196–198] and may have directly caused breakdown of the intracellular cytoskeleton in the corneocytes themselves, either by affecting the keratin filaments themselves or the proteins which anchor the keratin filaments to the cornified envelope. This would also reduce the overall integrity and measured stiffness of the intracellular structure.

In a broader context, this experiment illustrates that indentation using nanoneedle AFM probes is sensitive to changes in the mechanical properties of the intracellular structure of cells, particularly to those associated with changes in the cell's internal organisation due to disease. This indicates the suitability of the nanoneedle probes as a tool to detect and investigate these conditions, suggesting they could be used in many areas of biological and medical research.

7.11 Conclusions and Summary of Results

This chapter discusses experiments to study the penetration of EBID-modified AFM probes into isolated corneocyte cells. The probes were modified to create rigid, high-aspect ratio "nanoneedle" structures on the probe apex.

The experiments shown here demonstrate that the needle is able to penetrate the outer layers of these cells, and these "penetration events" are visible in the AFM force curves as peaks or inflections in the approach curve. By analysis of the force curve using the methods discussed in chapter 3 it was possible to determine the overall vertical deformation of the cell and separate it into elastic and inelastic components. The inelastic deformation can be viewed as the depth of penetration of the needle into the cell. Our measurements showed that the needles could penetrate the corneocyte structure to depths of $\sim$300 nm. It is likely that penetration to larger depths is possible; the depth of penetration is likely limited principally by the length of the nanoneedle.

The overall and inelastic deformation is a function of the applied pressure beneath the needle tip. This permits the depth of penetration of the needle to be controlled; by setting a maximum applied force, the needle will penetrate to the corresponding depth and probe the intracellular structure of the cell. Our experiments also showed that the deformation is also increased for slower approach-

retract velocities of the AFM probe. This suggests that the corneocyte material deforms in a time-dependent viscous manner, appearing harder and stiffer if a deforming force is applied to it more rapidly. This property is common in many materials, including polymers as well as biological cells and tissues. [5,83–88,191]

Using the Hertz model for an indenter with a spherical surface (approximating to the hemispherical tip of the needle) the elastic modulus at the corneocyte surface was determined and found to also vary significantly with the approach-retract velocity, with much higher elastic moduli calculated at high approach-retract velocities. This is also consistent with viscoelastic behaviour of the corneocyte material.

As mentioned above, the needle tip is able to penetrate beyond the corneocyte surface and indent on structures deeper inside the corneocyte. This occurs in the presence of significant inelastic deformation of the cell; to analyse the mechanical properties of structures inside, two models were compared. The compliance model of Doerner and Nix [81] showed significant variation in elastic modulus with the approach-retract velocity, consistent again with viscoelastic behaviour. In order to try to separate the time-dependent viscoelastic and time-independent elastic deformations of the intracellular material, a model was derived based on that of Oyen and Cook, incorporating viscoelastic effects. Effective reduced elastic moduli calculated using this model showed smaller variation with approach-retract velocity. However, there was still some variation of the elastic modulus with velocity; it is likely that a more sophisticated model than the relatively simple one used here is needed to fully compensate for viscous effects.

In order to investigate mechanical properties at a range of depths below the surface of the corneocyte, indentation was performed multiple times on the same site, with steadily increasing force and therefore increasing penetration into the cell. It was noted that after an approach-retract cycle of indentation, further indentation was elastic until the applied tip-sample pressure became larger than that of the previous indent. This effect indicates that deformation during the retraction of the AFM probe (where the tip-sample decreases from the peak value at the end of the approach) is elastic, as required by the models used here.

In order to determine if the measured elastic modulus was a function of the pressure applied to the corneocyte material (due to hardening of this material under pressure) double indents were also performed, with a large pressure exerted

during the first indent to allow the needle to penetrate deep into the corneocyte, and a smaller pressure exerted in the second indent. Analysis of these two indents showed good agreement between the elastic moduli measured at large and small pressures. It would seem from this result that the elastic modulus is a function of the depth below the surface of the corneocyte at which the measurement is made, rather than the applied pressure.

The elastic modulus measured using these different techniques showed an increase from ∼100 MPa to ∼500 MPa from the corneocyte surface (zero inelastic deformation) to ∼100 nm below the corneocyte surface. Following this depth the elastic modulus did not vary much, remaining at the value of ∼500 MPa. This suggests that the needle probes a softer outer layer of the corneocyte at low deformations, sensing the harder internal structure as the deformation increases and the probe penetrates through the outer layer. This two-layer model is supported by the presence of penetration events in the approach curves (indicating penetration through the outer layer). The force curves recorded during multiple indents on the same indentation site also suggest the presence of two layers of material, both of which deform elastically, with the needle able to inelastically deform and penetrate the outer layer to make contact with the internal layer.

This proposed two-layer model is supported by the known structure of corneocytes. The corneocyte possesses an external protein envelope covalently bonded to lipid molecules. This layer is likely to be softer than its internal structure, which is composed of bundles of keratin intermediate filaments. The cornified envelope, therefore, is likely to be the softer external layer detected in our experiments, while the more rigid homogeneous internal layer is probably the intracellular keratin filament structure.

It was noted that the resistance to penetration of the outer layer of the corneocyte apparently decreased following an initial penetration by the needle; there was less chance of observation of a peak or step in the approach curves of single indents with each new indentation on the cell. This would suggest that the pore created by the first indent disrupted the integrity of the cornified envelope, at least locally, and there was thereafter less resistance to the penetration of the needle in subsequent indents. This would seem to indicate that indentation using the nanoneedle damages the cell on a wider level than its small size would suggest. This is a problem as it was hoped that small size and high aspect ratio of the

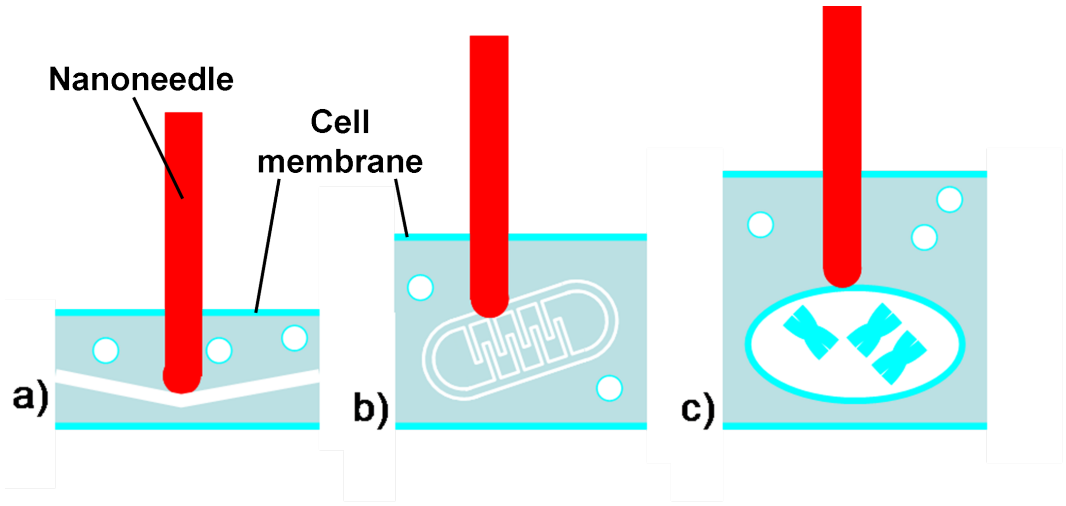

Figure 7-22: Examples of potential targets for manipulation using nanoneedle probes, in order to investigate mechanical properties of the target structure. a) shows the bending of a cytoskeleton fibre bundle b) shows the manipulation of a mitochondrion c) shows deformation of the nuclear envelope surrounding a cell nucleus.

needle would allow it to penetrate cells to large depths without significant damage to their structure as a whole. However, as discussed further in section 7.9, it is likely that other cell types would be less affected than corneocytes as they are more able to regenerate their outer surfaces. That there is little negative effect on these cell types has been demonstrated in other studies using nanoneedles fabricated by techniques other than EBID. [130–135]

The experiments shown here demonstrate that nanoneedles fabricated on AFM tips using EBID can be used to penetrate the outer layers of biological structures. Force curves recorded during this process reflect the internal structure of the cell as it is penetrated by the nanoneedle. Results are presented here showing that the mechanical properties of intracellular structures can be investigated using indentation with nanoneedles. In future, nanoneedles could be used to probe these properties in more complex structures in other cell types, for example cytoskeleton filament structures, and organelles such as mitochondria or the cell nucleus (see figure 7-22). Their small size and high aspect ratio would allow them to penetrate to large depths within the cell without significant damage to the cell structure as a whole, and to break through the cell membrane and outer layers of the cell to make contact with structures deeper inside. This overcomes

a limit of conventional AFM tips whose pyramidal shape means that they will cause significant damage to a larger area of the cell surface if they penetrate deep inside. The nanoneedles therefore demonstrate similar advantages in cellular manipulation to high-aspect ratio AFM probes fabricated by other techniques e.g. focussed ion beam milling [130–133] or attachment of carbon nanotubes to the tip. [134, 135] Integrating the EBID needles into an AFM system allows them to be used for the imaging and investigation of living cells at a nanoscale level under physiological conditions, a major advantage of AFM over other imaging techniques (e.g. electron microscopy).

It was demonstrated that the indentation techniques described here are sensitive to changes in elastic modulus of the corneocyte internal structure which are associated with disease symptoms. In particular, we demonstrated a decrease in elastic modulus at depths of 50-300 nm below the corneocyte surface after treatment of the skin with low concentration sodium lauryl sulphate to induce symptoms similar to those of atopic dermatitis. This suggests that nanoneedle indentation could be used to investigate changes in cell structure and mechanical properties associated with harmful diseases.

In future, the needles could also be used to perform "mechanical tomography" on cells, mapping the elastic modulus and other mechanical properties of structures at a range of depths below the cell surface. There is also potential to use nanoneedle probes for microinjection into cells, as demonstrated by several groups. [130–134], or, if coated with conductive material, as probes of intracellular electrical activity. High aspect ratio "nanoneedle" probes of this type could therefore become powerful tools for the investigation of many aspects of the internal structure of biological cells.

Chapter 8

Manipulation of Biological Structures

In recent years there has been great interest in the capability to manipulate individual cells, and the smaller biological structures which make up their fine structure. Using the atomic force microscope as a dissecting tool, a variety of biological structures have been targeted. These have included collagen fibrils, [125] chromosomes, [117] protein complexes, [123] plasmids, [120, 121] virus particles, [122] and bacterial cell walls. [126] In some of these previous studies, AFM has been successfully applied to manipulate the outer layers of these structures to expose their internal structural details for *in situ* AFM imaging. [125, 126]

This chapter describes experiments performed to expose sub-surface structures in biological cells by manipulation of the surface using AFM. Using a number of different techniques, it has been possible to remove upper layers from smooth muscle cells and corneocytes, and expose structures underneath, which were successfully imaged *in situ* using AFM.

In these experiments we have made use of AFM probes modified to create "nanotool" structures on the AFM tip. We show in this chapter that it is possible to use "nanoscalpel" probes (the fabrication of which is described in chapter 4) to create incisions in biological materials, and that this manipulation can attain narrower incisions than those attainable using either unmodified AFM probes or laser microscalpels. It is also demonstrated that the "nanotome" probes (also described in chapter 4) can be used to separate the upper layers of a corneocyte cell from those lying underneath, and that the separated layer can be manipulated

using the AFM tip to expose the underlying structure.

These "nanosurgical" techniques have the potential to be used to dissect biological structures on very small scales to investigate their internal organisation, as well as for other applications in biological research.

8.1 Incisions

The cutting and manipulation of biological structures using AFM probes is limited by the pyramidal shape of the probe, which necessarily increases the cut width as it penetrates deeper into the sample. In addition, the crystalline materials, such as silicon, used to fabricate AFM probes are relatively brittle and so can be easily damaged during manipulation; [119] this further reduces the precision of the manipulation by blunting the probe tip.

Our experiments demonstrated that probes modified using an EBID process to fabricate "nanoscalpel" blades on the probe tip (as described in chapter 4) can be used to make incisions in the surface of biological structures. The high aspect ratio of these probes allows them to create deep cuts into biological structures without loss of lateral precision. In addition, as shown in chapter 6, the amorphous carbon nanoscalpel blade is highly robust; the structure will bend rather than break and can recover from such deformations elastically.

In order to demonstrate the capability of nanoscalpel AFM probes to make incisions in biological materials, experiments were carried out to create parallel incisions in the surfaces of fixed cells. The protocols used for the isolation, culture and fixation of these cell samples are described in detail in appendix A. We were also able to make incisions in the outer protein envelope of non-fixed corneocyte cells. Incisions were made using both unmodified AFM probes and nanoscalpel probes, in order to compare the relative advantages of these techniques; this work is described in a paper published by our group. [77] Examples on incisions on fixed cells and non-fixed corneocytes are shown in figure 8-1.

Figure 8-2 shows incisions made on the surface of a fixed cell using an unmodified silicon probe, and using a nanoscalpel probe. The incisions created by the nanoscalpel probe are much narrower, approximating to the width of the scalpel blade itself. The nanoscalpel AFM probes therefore demonstrate improved lateral precision compared to both unmodified AFM probes and to previous experiments

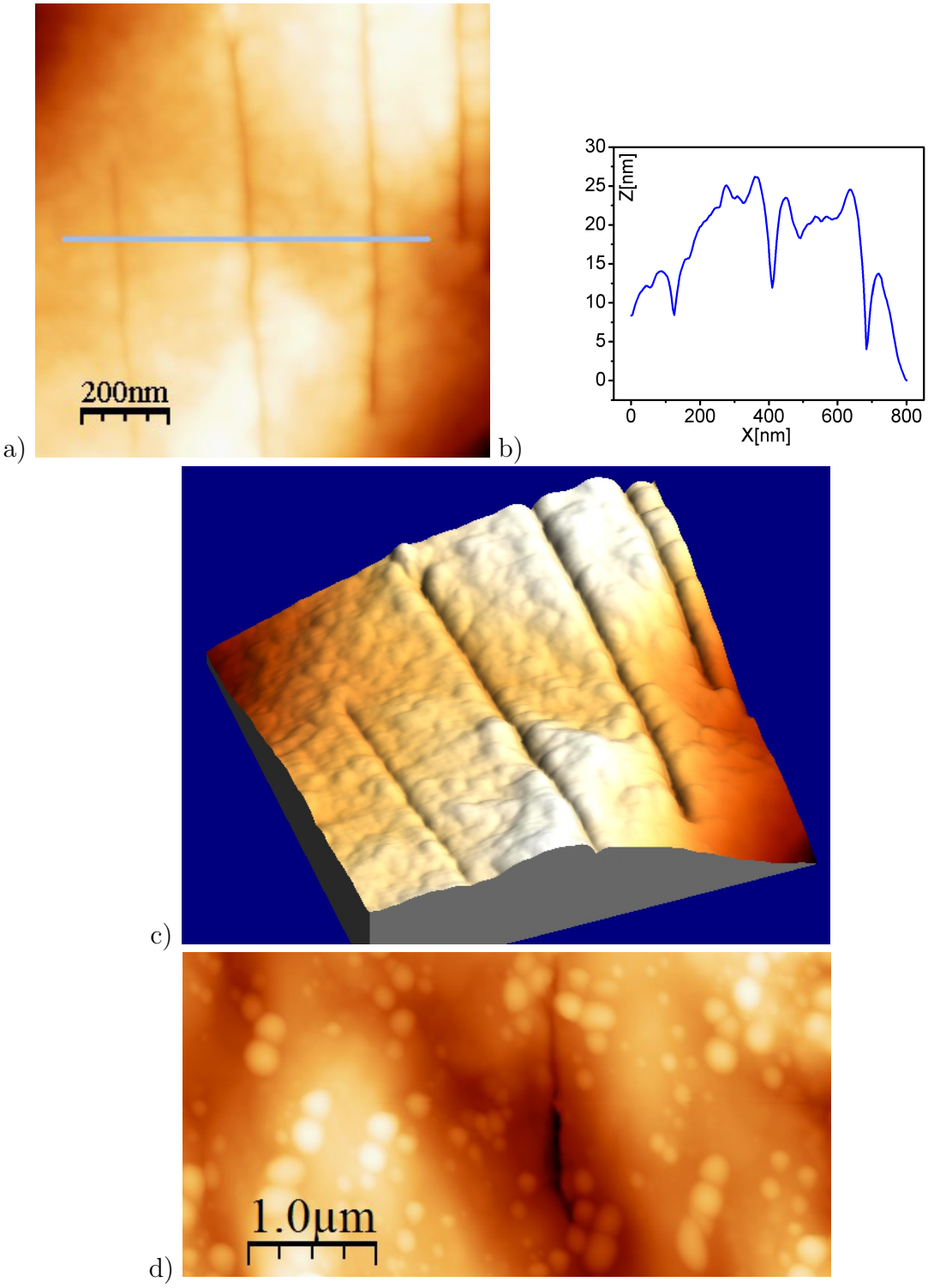

Figure 8-1: a) AFM image of incisions on the surface of a fixed megakaryocyte cell, performed and then imaged using the same AFM nanoscalpel probe. b) Topographic profile across the blue line in (a), showing width of incisions. c) Pseudo-3D AFM image of cuts. d) Nanoscalpel incision on a corneocyte.

a)

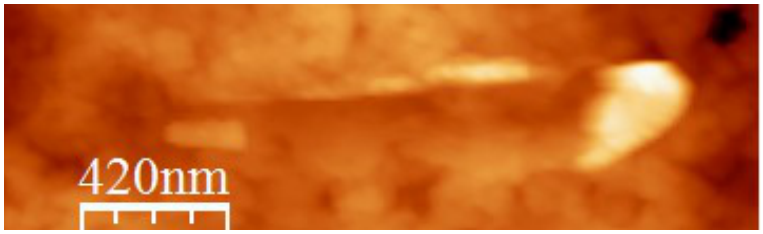

b)

Figure 8-2: a) Incision made on a fixed smooth muscle cell using an unmodified silicon probe. b) Incisions made on fixed megakaryocyte cell using a nanoscalpel probe.

using laser microscalpels, which can attain a minimum incision width of ∼200 nm. [118]

It would probably not be possible to make an incision in the plasma membrane of a living cell using this technique. The membrane is composed of amphipathic phospholipid molecules, which self-assemble in aqueous environments to form a two-molecule thick "lipid bilayer". This structure exposes the hydrophilic "heads" of the molecules to the cell's aqueous environment and cytoplasm, with their hydrophobic "tails" inside the membrane. A hole in this bilayer represents an energetically unfavourable configuration for these molecules, and so the molecules in the bilayer will very rapidly move to close any such hole. [199]

However, it has been shown that AFM probes can penetrate the membrane [6,128,130–134,190]; nanoscalpel probes could therefore be used to cut structures below the membrane, such as the polymerised protein filaments which make up the cytoskeleton and nuclear envelope. These filaments have been successfully severed using laser microscalpel techniques. [113, 114] The filaments and other structures do not regenerate as fast as plasma membranes, and can be located in AFM images since they become visible as the tip deforms or weakly penetrates the cell membrane. [5–10] It has been shown in some cases that rather than regenerating, they tend to recoil due to the release of tension, and then retract further after this elastic recoil, as though depolymerising at the cut ends. [118]

Henderson *et al* reported the formation of a "hole" through a cell after penetration with an AFM tip, without loss of cell viability. [6] This was explained as the penetration of both upper and lower membrane bilayers by the AFM tip, with the membrane sealing at the edges of the hole to maintain a continuous surface. This would imply that using AFM manipulation it would be possible to isolate a section of the cell using the nanoscalpel, especially in the case of cells with long cytoplasmic protrusions (e.g. megakaryocytes).

Manipulation of the internal structures of the cell using nanoscalpels (and other specialised nanotools) could provide insight into their mechanical and biochemical function within the cell. Combined with optical techniques and fluorescent labelling, specific structures within the cell could be targeted and ablated or manipulated using the nanoscalpel probe. These structures could potentially be isolated from the cell using AFM manipulation for further investigation, or selectively damaged in order to observe the response of the cell as a whole.

8.1.1 Force feedback

During an incision on a rough surface such as the surface of a biological structure, the cantilever deflection can vary considerably. This can result in the tip-sample force becoming too large, which can break the nanoscalpel blade or detach it from the AFM tip. During normal AFM imaging, the tip-sample force is controlled using a feedback loop which repositions the tip or sample using the piezoelectric scanner to maintain the tip-sample force at a constant value. This is achieved by using the cantilever deflection (or amplitude, phase or resonance frequency) as the input signal for a feedback loop which controls the piezoelectric scanner.

Such a feedback loop can be implemented in the manipulation program to control the force applied to the nanoscalpel during the cutting process, maintaining it at a chosen setpoint value. The feedback loops used in AFM systems are often complex, employing proportionate and integral gain controls.

In our experiments, a simple proportionate gain-type correction step was implemented using the NanoScript software controlling the AFM system, with the correction of the piezoelectric scanner position being proportionate to the deviation of the cantilever deflection signal from a chosen setpoint voltage.

Figure 8-3 compares the cantilever deflection during cuts made on cell sur-

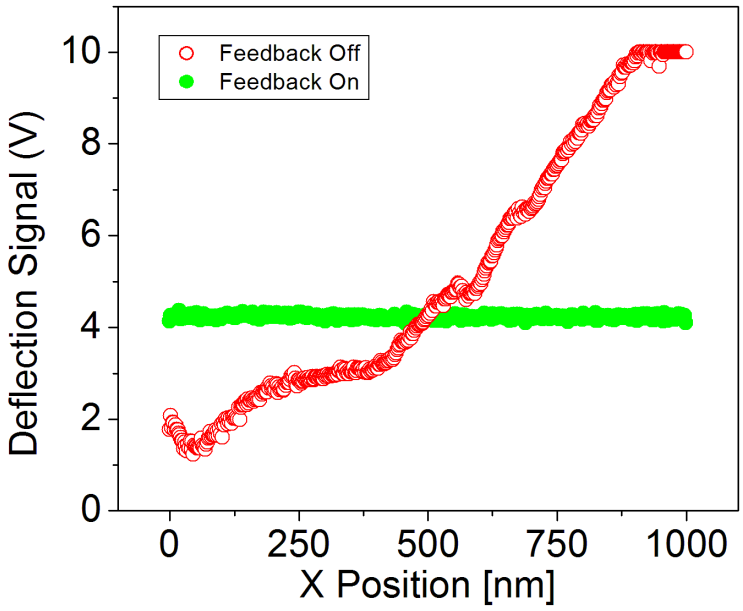

Figure 8-3: Cantilever deflection during cuts on a fixed cell. Without feedback, the rough surface of the cell causes large variation in the cantilever deflection (and therefore the tip-sample force), which eventually causes saturation of the photodiode signal. With feedback active, the cantilever deflection is held at a fixed setpoint value.

faces with and without feedback control. Without feedback, there is significant variation in deflection due to the roughness of the sample. With feedback active, the cantilever deflection is held constant throughout the cutting process. Controlling the cantilever deflection, and therefore the applied cutting force, in this way prevents the nanoscalpel from breaking. It also allows the depth of the cut to be controlled, as the cut depth increases with the vertical tip-sample force applied during an incision. This is described in more detail in subsection 8.1.2.

8.1.2 Depth of Incisions

In the course of our experiments, we investigated the relationship between the force applied during cutting and the depth of the incision created in the cell. This required the design and implementation of a technique to accurately measure the depth of incisions.

Unfortunately it is not generally possible to accurately determine the depth of an incision by imaging it in the AFM system after manipulation; it is unlikely that the AFM probe will penetrate back into the incision during normal imaging, and so its depth will not be accurately profiled. It is also likely that the elastic recovery of material at the sides of the incision will push the sides together, closing the gap created by the nanoscalpel blade.

Therefore it is necessary to determine the vertical deformation of the cell by the scalpel using data recorded from the AFM system during the cut. If the cantilever deflection and the vertical position of the scanner during normal imaging and during cutting are compared, this can be used to track the position of the nanoscalpel blade during the cutting process, and so determine the distance below the surface to which the nanoscalpel penetrates.

In order to allow the cut depth to be calculated using this technique, the manipulation program first moves the AFM probe along the path of the incision with normal feedback enabled, recording the surface topography. After this has been performed, the probe repeats the profile as it returns along the same path, creating trace and retrace profiles of the undamaged topography.

Following this, the cantilever is pressed down into the sample until the target cantilever deflection (corresponding to the desired cutting force) is measured at the AFM photodiode. After this, the tip is moved along the cut path with the cantilever deflection held at this value by the feedback loop implemented in the nanomanipulation program (as described in subsection 8.1.1) This allows the nanoscalpel blade to create an incision in the surface. During this processes, the z-position of the scanner is recorded as it is controlled by the feedback loop, allowing the vertical position of the AFM tip to be determined.

In a similar manner to the calculation of the deformation of a sample during indentation, the deformation of the cell at any point along the cut can be determined by

$$\delta = z_t - z_c - D \tag{8.1}$$

where δ is the deformation of the sample, z_t is the scanner z-position during the initial topographic profile, z_c is the scanner z-position during the cut, and D is the cantilever deflection.

Figure 8-4 shows that the depth of incisions made on the surface of a corneo-

cyte increases in approximate proportion to the applied force. It should be noted that, while the majority of the deformation is inelastic (as noted in chapter 7), some elastic recovery of the deformation is likely to occur. Therefore, the values in the graph shown in figure 8-4 are likely to be slight over-estimates of the depth of penetration of the nanoscalpel. However, these results indicate that by controlling the cutting force using a feedback system, the depth of the cut can therefore also be controlled.

8.2 Surface Removal

Previous studies have used AFM to remove the surface of biological structures by two routes; increasing the tip-sample force to displace material from an area of the surface during scanning, [126] or separating part of the sample by making incisions in the surface and then using the tip to move part of the surface to expose internal structures. [125]

In our experiments, we attempted to use these techniques for the removal of surface layers from biological objects. Initial experiments were carried out on fixed cells to determine if it would be possible to expose internal structures by AFM manipulation.

The first technique which we used was line-by-line displacement of surface material, by increasing the tip-sample force during AFM scanning with a low scan rate. Initially, we tried increasing the applied force during the "retrace" scan line only, by applying a negative lift height in Retrace Lift Mode in the Interleave control in the Nanoscope software which controls the AFM system. By setting a negative lift height, the probe tip is moved downward into the sample surface at the beginning of each retrace scan line, therefore displacing material as it scans. This process is described in more detail in chapter 3.

Figures 8-5 and 8-6 show part of the surface of a fixed aortic smooth muscle cell (SMC) on which two areas of surface material have been removed using this technique. By replacing the AFM probe (which was damaged during the manipulation) with a new, sharp probe, the exposed sites could be imaged in detail. In both cases, the removal process began at the lower edge of the target area, and material was displaced by cutting from the right-hand side of the figure to the left-hand side. The area labelled B in figure 8-5 was exposed by cutting

a)

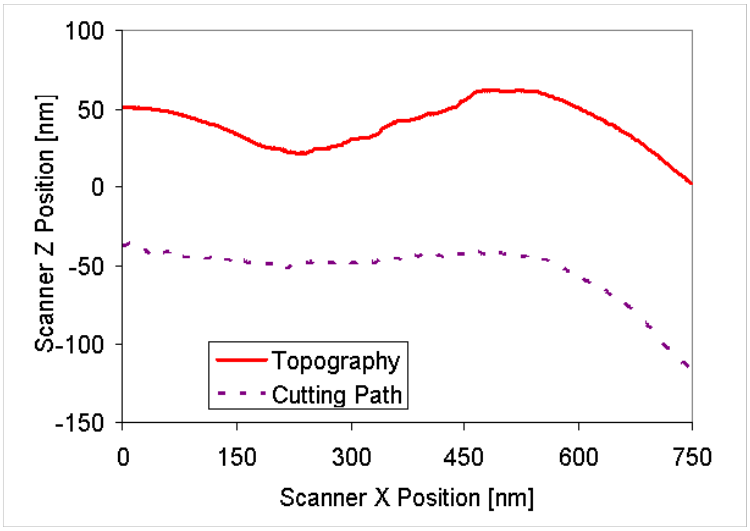

b)

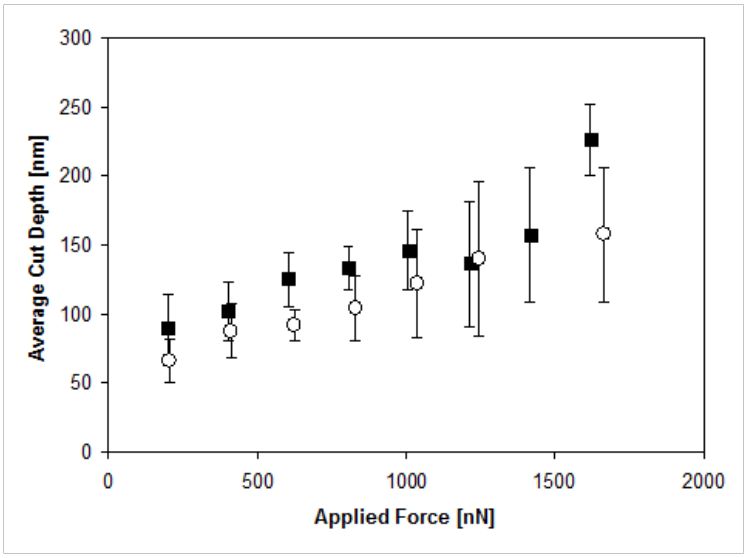

Figure 8-4: a) Comparison of z-position of scanner during initial topographic profile along cut path and during incision. b) Depths of nanoscalpel cuts measured on corneocyte surfaces as a function of applied cutting force. Open and closed circles indicate data from 2 different corneocytes; error bars indicate variation in depth during cut.

with the angle of the AFM scan rotated 45 degrees.

It was noted that in both cases raised areas are present at the upper and left-hand edges of the exposed areas. These can be explained as surface material "piling up" ahead of the probe as it is displaced, and being deposited at the edge of the exposed areas.

In both areas A and B, filament-like structures can be seen in the target area after manipulation. These would appear to be present below the surface of the SMC. It is of interest that, although the direction of the retrace scan in area B was at 45 degrees to that in area A, the filaments appear to run in a similar direction in both areas. This would suggest that they are actual subsurface features rather than an artefact created by damage to the surface caused by the AFM probe, as such an artifact could be expected to take the form of furrows running parallel to the direction of cutting in both cases. It is known that parallel bundles of filaments, composed of actin and myosin proteins, are indeed present within SMCs; it is possible that this nanodissection has exposed parts of a filament bundle, allowing it to be imaged using AFM. [136] A comparison of the filament structures between the two exposed areas is shown in figure 8-7.

A second technique which was used was an increase in tip-sample force using a slow raster scan, with the increased force applied during both trace and retrace scan lines. Figure 8-8 shows the result of applying this technique to a corneocyte, in an attempt to remove its outer protein envelope and expose the internal keratin structures. As in the previous experiment, the AFM images were taken after manipulation by replacing the AFM probe used for manipulation with a new, sharp probe. This revealed that the manipulation had again successfully removed the surface layer, exposing some ultrastructural details beneath.

These experiments suggested that AFM manipulation can be used to expose internal cellular structures for AFM imaging *in situ*. However, the manipulation processes in these experiments were very time-consuming due to multiple passes of the AFM probe tip required. It would be useful to demonstrate the removal of an area of surface with a single pass of the tip, during which the cutting force can be controlled using the feedback loop as in the manipulation program used for the incisions, as this process would be relatively quick. This would be especially advantageous if larger areas of the outer surface are to be removed. This was achieved using a "nanotome" probe, modified using EBID to include a specialised

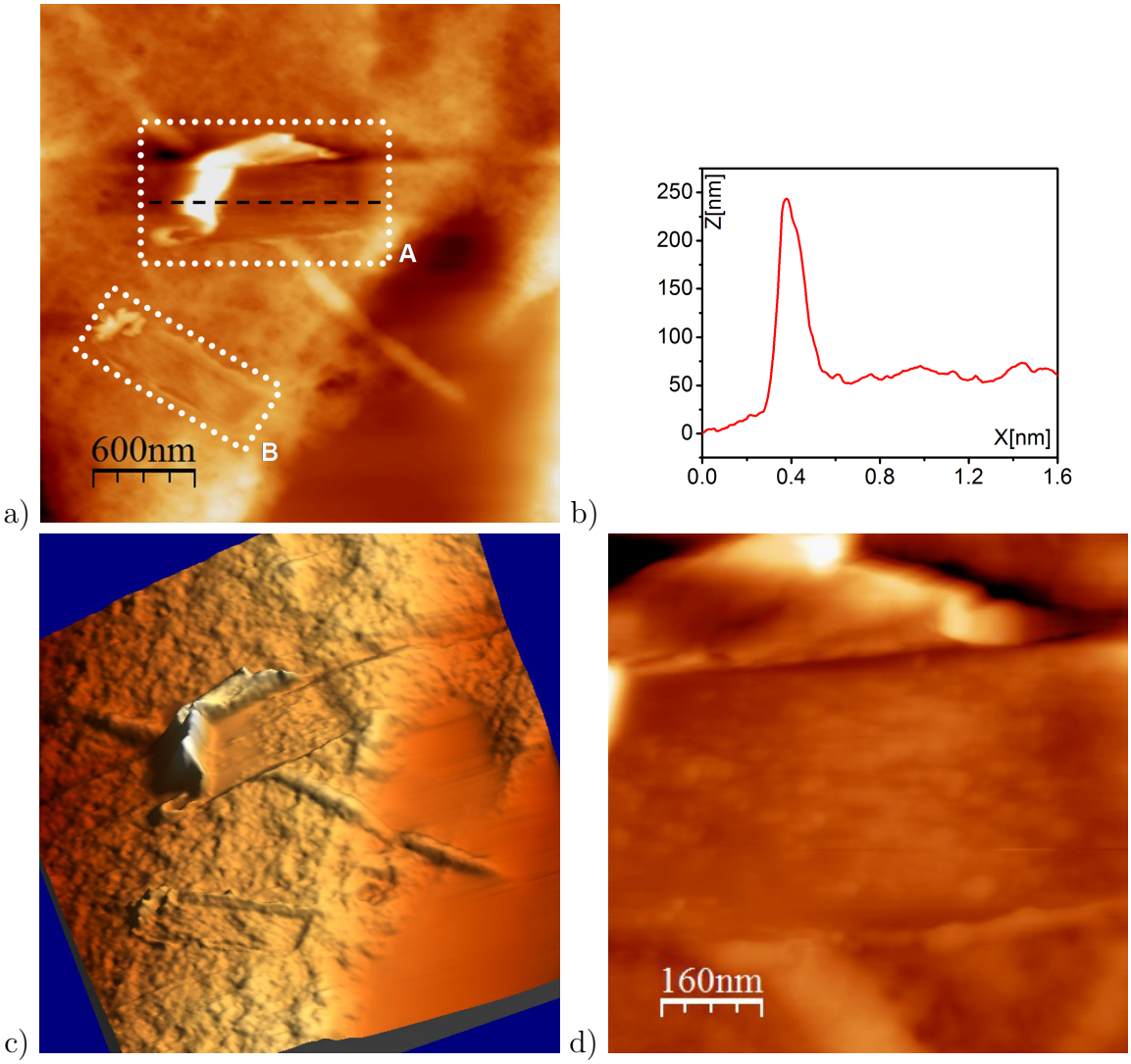

Figure 8-5: a) Area of surface of fixed aortic smooth muscle cell, showing two rectangular regions whose surface has been removed by multiple passes of the AFM probe in "Retrace Lift" mode. b) Profile across area A (along dashed line in a)), showing raised area at one edge of the exposed region where surface material has been deposited. c) Pseudo-3D view of area shown in (a). d) Image of area A with increased magnification, showing filament-like structures exposed below surface.

nanotool which can separate the upper layer of a sample from those underneath using a single pass of the probe tip. This process is described in the next section.

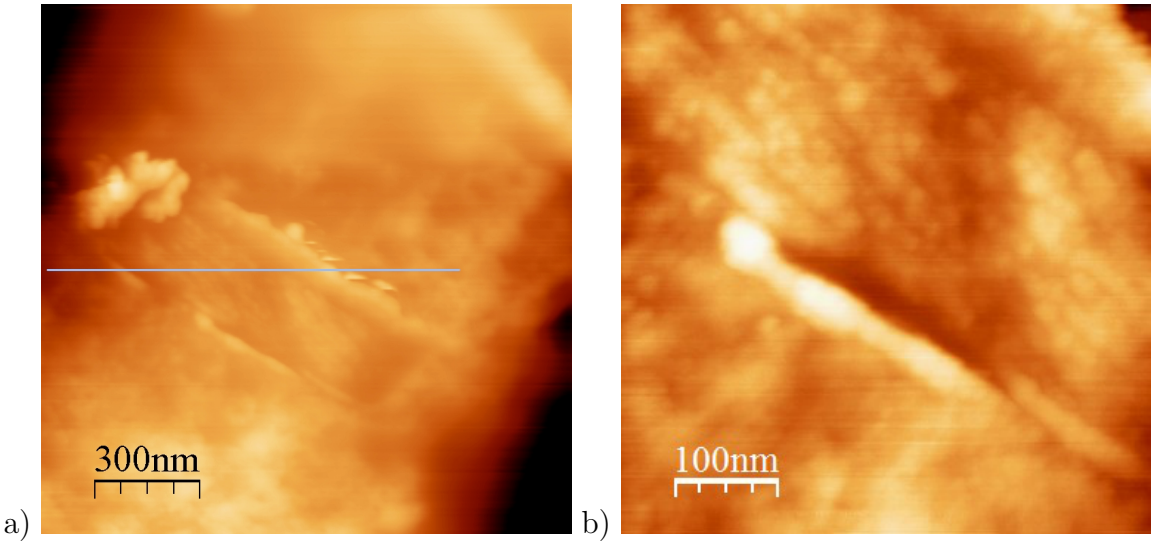

Figure 8-6: a) Image of area B highlighted in figure 8-5. b) Magnified image showing filament-like structures. c) Topographic profile along line in a).

8.2.1 Nanotome

In chapter 4, the fabrication of a "nanotome" probe is described. This probe was modified using EBID to deposit two parallel nanoscalpel blades on the probe tip, and then to fabricate a single suspended filament between them. The probe is designed to separate the outer layers of a target structure from those underneath, with the suspended filament cutting beneath the outer layer. This process is illustrated in figure 8-9.

Moving a nanotome probe across the surface of a corneocyte created two parallel cuts due to the twin amorphous carbon blades. Unfortunately, in this experiment the nanotome was detached from the AFM probe when it withdrew

A

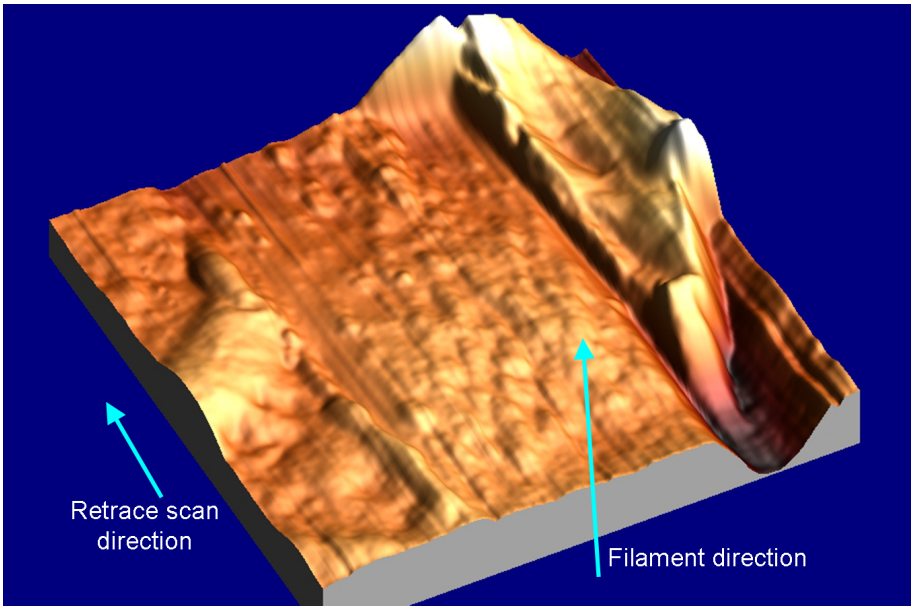

B

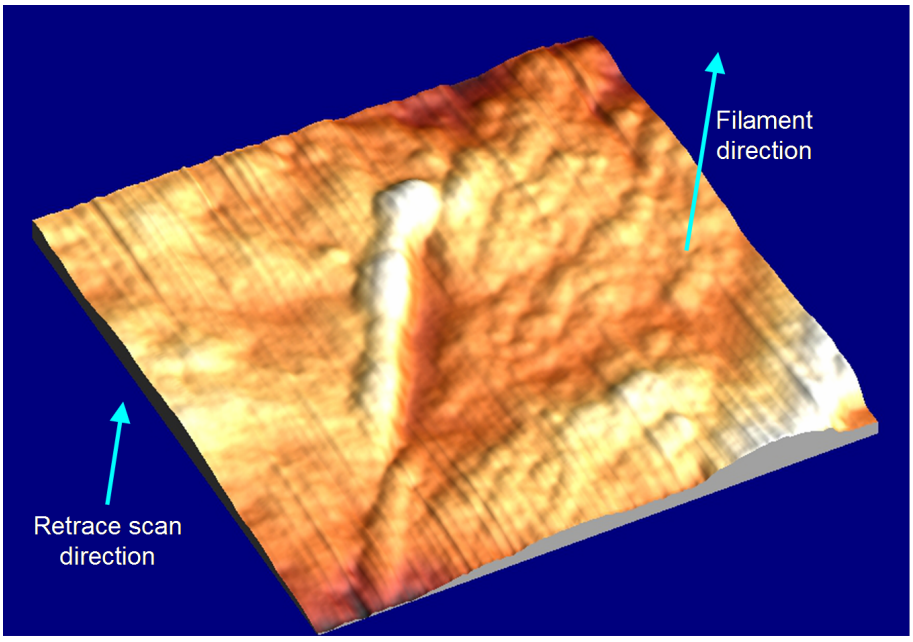

Figure 8-7: Pseudo-3D images of areas A and B shown in figures 8-5 and 8-6. These images have the same orientation relative to one another. The subsurface filaments revealed by nanodissection using AFM manipulation are visible. The filaments run in a similar direction (into the page) in both areas, even though the retrace scan direction during the surface removal was performed in a different direction between the two areas.

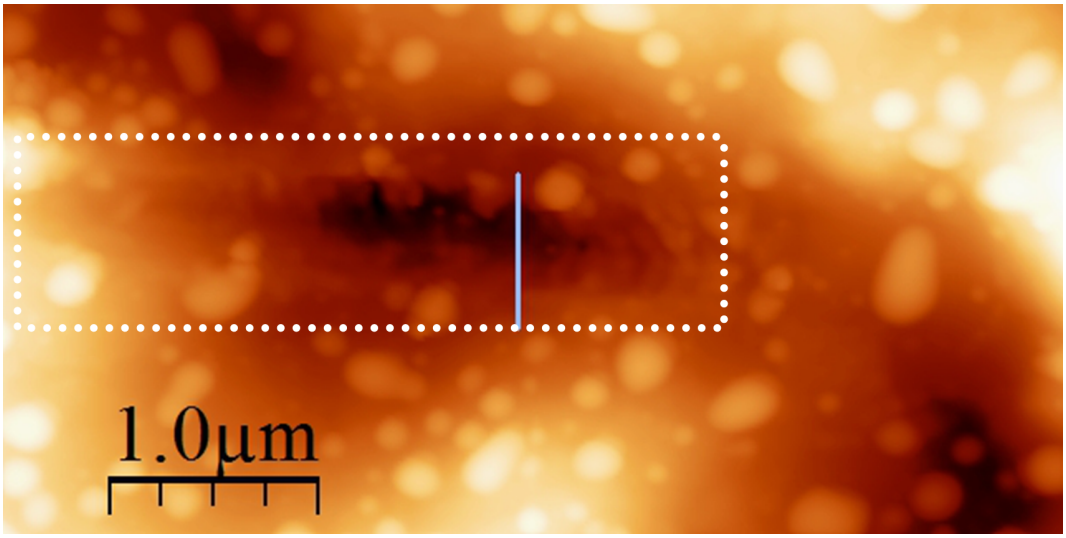

a)

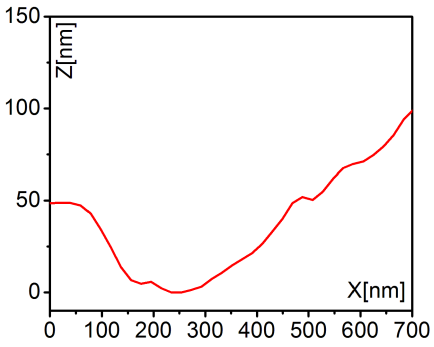

b)

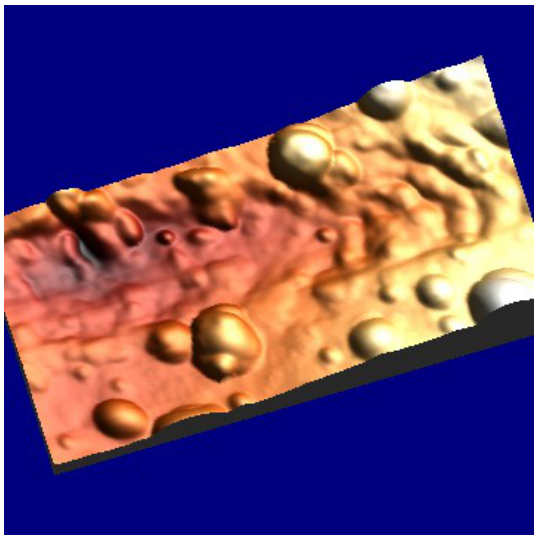

c)

Figure 8-8: a) AFM image of area of corneocyte surface highlighting area exposed by multiple passes using AFM probe. b) Profile across removed area. c) Enlarged pseudo-3D view of exposed area, showing exposed internal structure.

from the corneocyte surface after making these cuts; fragments of the broken blades are visible as the bright regions in figure 8-10a.

Passing the (damaged) probe tip across the cuts appeared to remove parts of the surface layer between the two cuts. This process is shown in figure 8-10a and b. It also removed the fragments of the damaged probe; as these were not visible on the surface after manipulation then it is likely that they adhered to the probe tip.

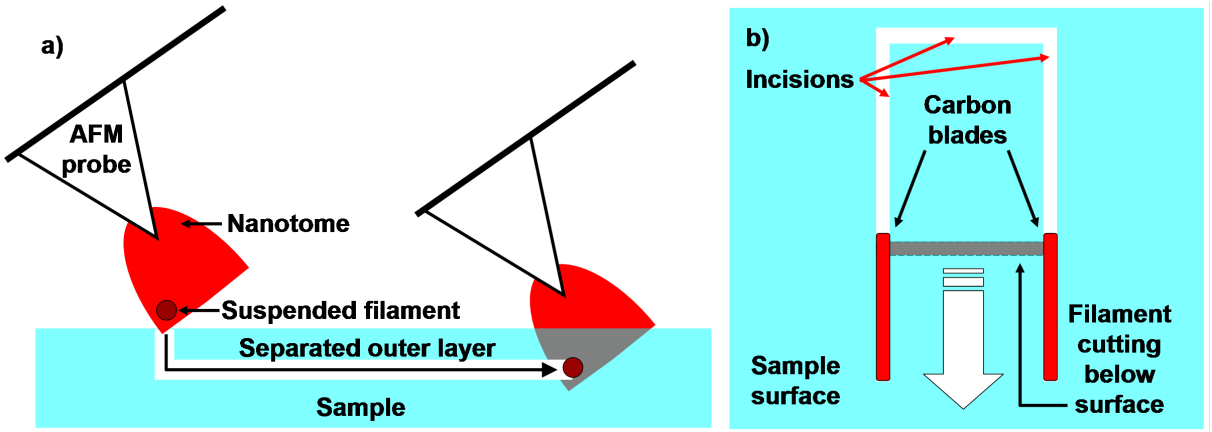

Figure 8-9: Schematic of nanotome operation. a) Cross-sectional view. b) View from above.

The removal of the surface layer would seem to indicate that the suspended filament between the two blades of the nanotome probe was able to separate this layer from the structures beneath. Imaging of the area of the corneocyte interior which was revealed was then be carried out by replacing the nanotome probe with a sharp unmodified AFM probe. Figure 8-11 shows a three-dimensional view of the site where manipulation was performed. It is clear in this image that the surface layer has been successfullly removed, and that some of the structure beneath is visible.

This experiment showed that the nanotome probe can be used to separate the upper layers of a biological sample from those beneath. It has been shown here and by previous studies that removal of these layers by AFM manipulation can expose internal structures for imaging using AFM. [125, 126] Nanotome probes could find application in the investigation of the ultrastructure of biological structures, including cells, with the potential to expose large areas of their internal organisation for AFM imaging.

8.3 Manipulation with Nanoneedles

In some of our experiments, indents using nanoneedles were performed on the small circular structures visible on the surface of almost all the imaged corneocytes, as described in chapter 7. It was theorised that these might be the outer structures of corneodesmosomes, structures spanning the surface envelope of cor-

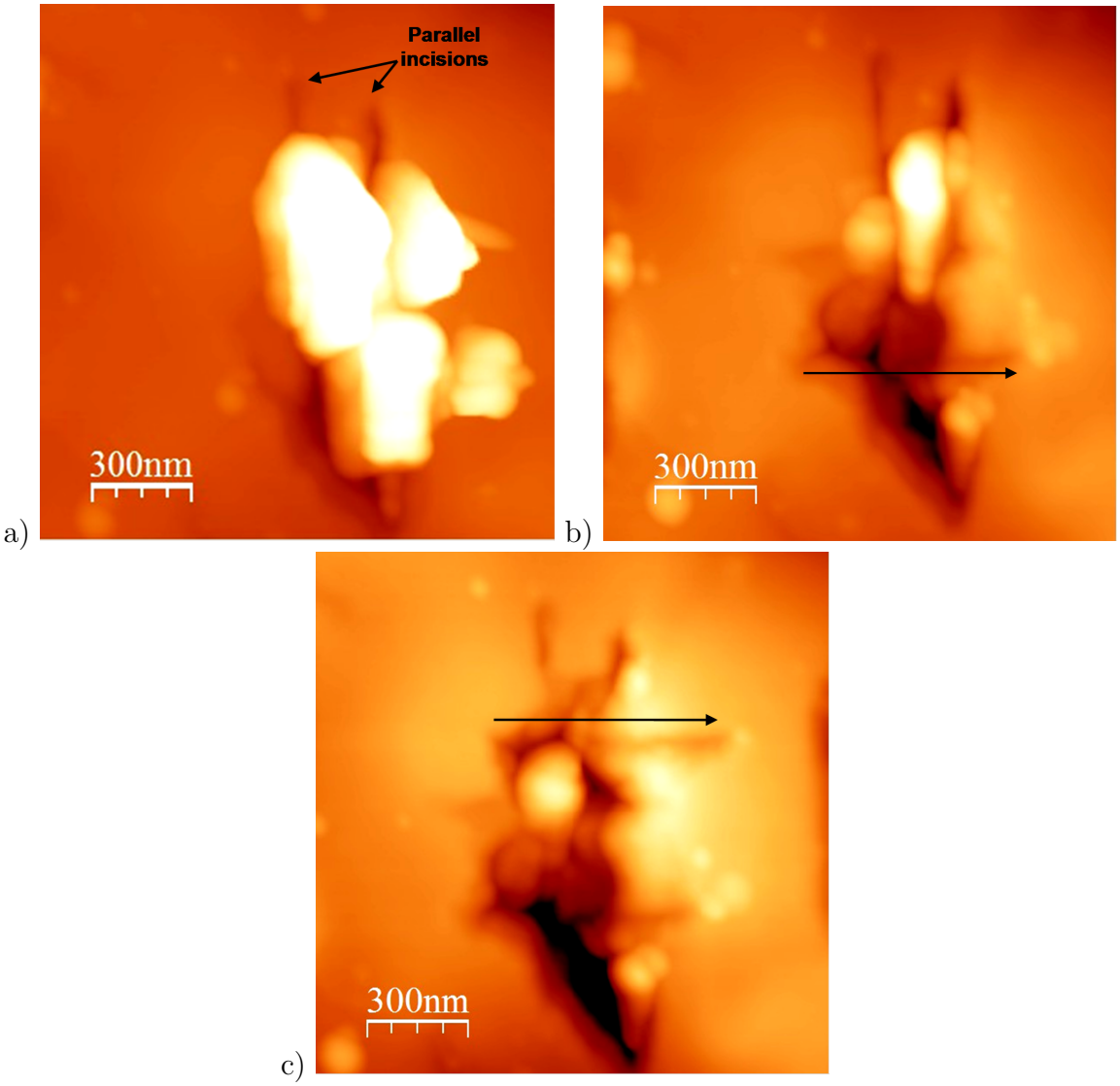

Figure 8-10: a) Parallel cuts created using nanotome. b) and c) Passing the AFM tip across the corneocyte surface perpendicular to the initial cuts (along the paths of the arrows) removes the surface layer between the cuts.

neocytes which function as site of adhesion for the corneocyte to the surrounding cells. [140] It was shown that indentation using a nanoneedle probe on such a structure initially caused it to disappear, leaving an indent or pore in the surface as with other indentation experiments.

However, after this indent had been performed, a second indent at approximately the same site appeared to deposit an object on the cell surface. Images of the cell surface before and after these indents are shown in figure 8-12. There

a) 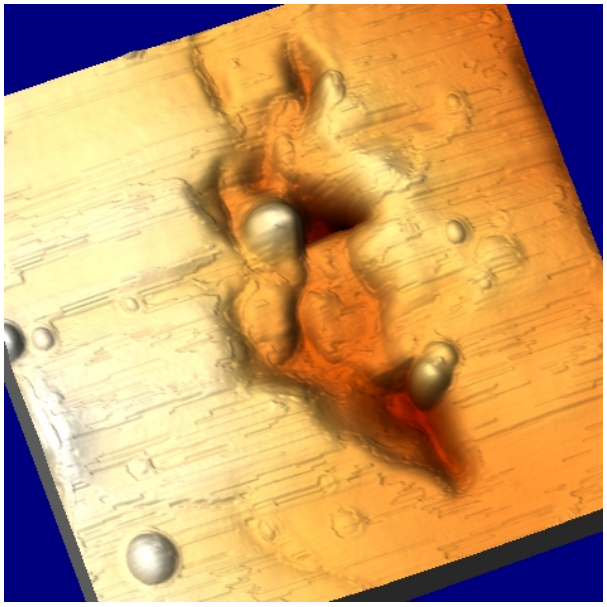 b) 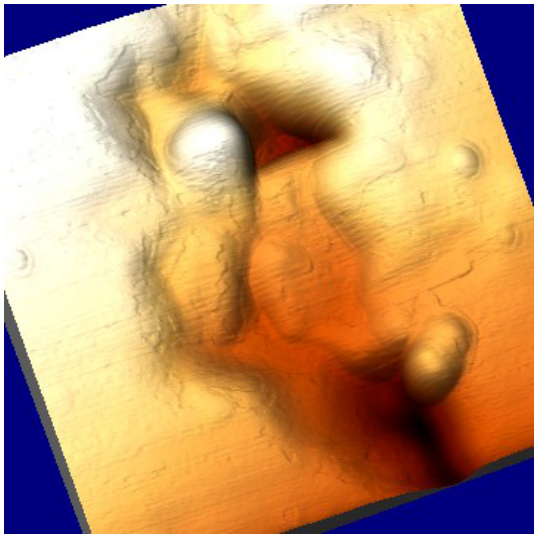

Figure 8-11: a) Pseudo-3D image of corneocyte after removal of an area of surface material using a nanotome. Imaged area is 1.6x1.5 μm. b) Image of the removal region with increased magnification, showing structures beneath surface layer. Imaged area is 1x1 μm.

was no damage to the probe during this process, so the object cannot be a part of the probe which has detached; it must have originated as contamination from the cell.

The general appearance and size of the object deposited suggests it is actually the initial target structure. This would suggest that it was pulled out of the cell surface by the first indent and adhered to the probe until it was detached during the second indent.

This process illustrates that the nanoneedle probes can be used for sampling of material from surface of biological cells, and potentially also from inside the cell. This process has been achieved in the past using unmodified AFM probes to extract genetic material from the cytoplasm of cells [128] and from isolated chromosomes [119]. To improve its suitability as a sampling tool, the needle could be functionalised with biological molecules to improve its binding or adhesion to the target structure, as often used for AFM imaging of molecular binding sites on cells [13]. The observation of extraction of material from corneocytes is of particular interest as the strongly cross-linked cornified envelope is often highly

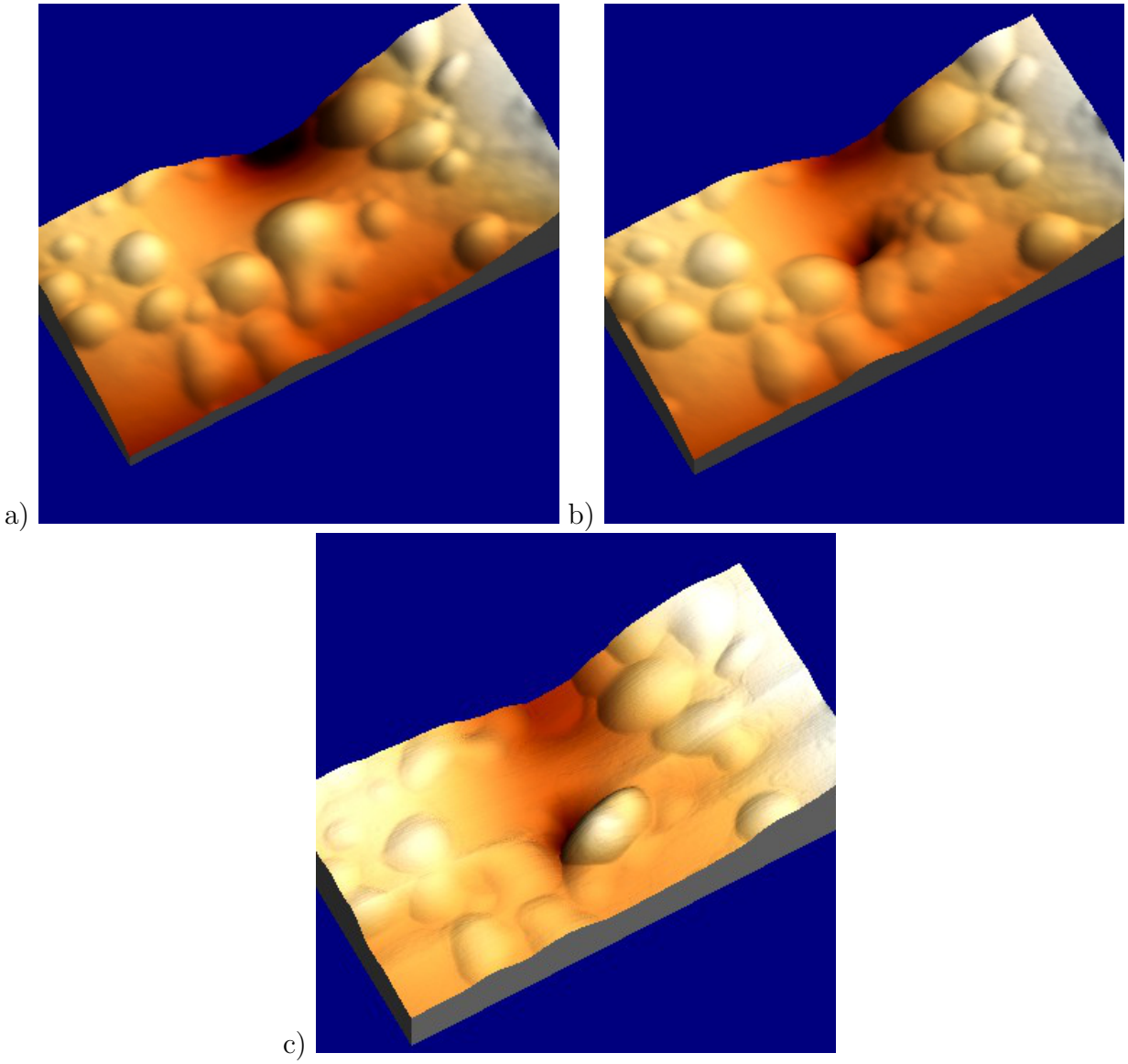

Figure 8-12: a) Surface of corneocyte before indentation using nanoneedle. b) Surface after indentation on structure in centre of image a). c) Surface after second indent, showing object (possibly original surface structure in a) deposited on surface.

resistant to typical chemical extraction techniques, requiring the use of high temperature treatment to remove molecules for biochemical assays. [140] Sampling by mechanical removal using AFM would represent an alternative technique with high spatial selectivity which could extract small quantities of material from the corneocyte.

8.4 Conclusions

In this chapter, experiments to manipulate biological structures using AFM manipulation are described. It has been shown that EBID nanotools can be used for specialised manipulation of these structures.

High-aspect ratio "nanoscalpel" probes can be used to create incisions in the surface of biological structures. This has been demonstrated by making incisions on the surface of fixed cells and on non-fixed corneocytes. These incisions are narrower than those which can be attained using either unmodified AFM probes or laser microscalpels. Unmodified probes are limited by the low aspect ratio shape of the probe, while laser microscalpels are limited in precision by the focussing limits of the beam and the threshold energy needed to ablate biological materials; the nanoscalpel is able to overcome both these limitations. While other high-aspect ratio probes exist and have been applied to the manipulation of biological cells, their needle-like shape limits them to exerting force along the needle axis; they would be too brittle for lateral manipulation. [130–133]

The use of an AFM system for manipulation allows the force applied to the probe to be controlled. Use of a force-feedback control while making an incision allows the applied cutting force to be maintained at a setpoint value, controlling the depth of penetration of the nanoscalpel below the surface of the structure and preventing the tip-sample force becoming too large (which could damage the nanoscalpel).

AFM manipulation was also successfully applied to remove surface material from cells, exposing structures beneath. This was achieved using both line-by-line removal of material using a large tip-sample force during normal scanning, and also the separation of the surface layer from the underlying structures using a specialised EBID-modified "nanotome" probe.

Extraction of material from the surface of a cell using a nanoneedle was also

demonstrated, indicating that high-aspect ratio nanotool probes can be applied for this purpose as well. This could potentially be used to sample locations within cells deep beneath the cell surface to extract material from the nucleus or other organelles. These extraction sites could be highly localised due to the high aspect ratio and small diameter of the probe, allowing the location of sampling to be precisely controlled.

The successful application of these techniques demonstrates that EBID-modified probes can be used for sophisticated nanomanipulation of biological structures. In future, these tools could be used for a variety of different applications; for example, the isolation of individual cells, ablation or isolation of single organelles or cytoskeletal structures, and the dissection of biological structures to expose internal structures for AFM imaging.

In future, AFM nanomanipulation with nanotool probes could be combined with laser microscalpel, optical imaging, and fluorescent labelling techniques. This could be applied for highly sophisticated nanosurgery and dissection, targeting both internal and surface structures in cells and other biological structures.

Chapter 9

Conclusions

This chapter summarises the most important results and conclusions from this thesis. The experiments described in this work have concentrated on the fabrication and application of specialised novel AFM probes, created from standard AFM probes modified using electron beam induced deposition. Experiments have also been carried out to determine the mechanical properties of the deposited structures, which have not been previously studied. These "nanotool" probes represent a new approach to nanomanipulation; combined with optical imaging and manipulation, these tools could be used in new techniques for the investigation of biological cells.

9.1 Summary of Results and Conclusions

In this thesis we have investigated the use of electron beam induced deposition (EBID) for the modification of atomic force microscope probes for advanced nanomanipulation applications. This work builds on that already performed in our group, which focused on the use of specialised EBID probes for nanolithography on soft metal films. [67, 77]

The EBID process is highly versatile, allowing the creation of a wide variety of nanoscale tools for different nanomanipulation applications. The deposited material (amorphous carbon) proved highly robust, able to withstand large lateral and vertical forces without damage or breaking free of the AFM tip, making it more suitable for nanomanipulation applications than the comparatively brittle silicon or silicon nitride that is generally used for AFM probes.

A number of different nanotool structures were fabricated and investigated for different nanomanipulation applications. Blade-like nanoscalpel tools were fabricated and their application for making incisions on fixed animal cells and non-fixed corneocyte cells demonstrated. Using a force feedback program, it was shown that the applied force on the nanoscalpel probe could be controlled during manipulation, allowing the control of the penetration depth of the nanoscalpel into biological structures. The lateral and vertical resolution of the nanoscalpel was shown to be better than that attainable using current "nanosurgical" techniques such as laser microscalpels. These nanoscalpels have the potential to be used for the nanoscale surgery of biological structures, for instance to isolate parts of cells, delete specific intracellular structures, or dissect biological structures to expose their internal organisation for further examination.

The nanoscalpel blades provided the basis for other nanotools. Experiments were carried out to determine the effect of deposition conditions (principally the primary beam dwell time and beam current) on the dimensions of the carbon blades. These parameters could be controlled to create a variety of different shapes from a flat blade to a cylindrical high-aspect ratio "nanoneedle".

These structures are grown by beginning the deposition close to an edge of a growth substrate and moving the electron beam spot beyond the edge into empty space, growing a nanostructure perpendicular to the beam axis. While similar structures have been fabricated using the same electron beam induced deposition technique by other groups, our group is the first to investigate their use as probes for AFM imaging and manipulation. In particular, the work presented in this thesis represents the first use of EBID nanoneedle probes fabricated by this method for imaging and manipulation; previously high-aspect ratio EBID probes had been fabricated by growing pillars on AFM tips parallel to the electron beam using a stationary beam spot. The technique of growth perpendicular to the beam allows for more versatility in the structures that can be fabricated as well as allowing high-aspect ratio pillars of much smaller diameters to be created.

These experiments also added to the body of previously existing evidence that the principle source of replenishment for the EBID hydrocarbon precursor molecules is the diffusion of adsorbed molecules across the surface of the growth substrate. It was also shown that it is essential to have a single well-defined growth site for the fabrication of an EBID structure with a particular shape.

These are important factors which must be considered if EBID is to become a more widely-used techique for nanofabrication. In our case, these insights into the careful control of the EBID process allowed the fabrication of complex nanotools such as "nanotweezers" and a "nanotome" incorporating a single suspended filament deposited between two nanoscalpel blades. This nanotome was designed to separate a thin outer layer from a sample by AFM manipulation, similar to a macroscopic vegetable peeler. The fabrication of different nanotools is described in detail in chapter 4.

Nanoneedle probes fabricated using nanofabrication methods other than EBID have been used by other groups for a variety of manipulation applications in biological cells, particularly in the injection of biomolecules into cells. In our experiments, the high-aspect ratio nanoneedles fabricated by EBID were demonstrated to be capable of penetration into biological structures, using corneocyte cells as a test sample. The small size and high aspect ratio of these needles would allow them to penetrate deep into cells and other biological structures in order to investigate their internal structure, without causing damage to the cell structure as a whole. The fabrication of the needles is discussed in chapters 4 and 5.

The vertical deformation of the cell could be determined from the approach-retract force curve recorded by the AFM system during penetration of a needle into the cell. The inelastic and elastic components of this deformation could also be determined from the force curve. Experiments demonstrated that the penetration of the needle into the corneocyte depended strongly on the rate at which the tip-sample force was applied, indicating viscoelastic or viscoplastic properties of the corneocyte material. These experiments are described in chapter 7.

The nanoneedle probes function as a high-aspect ratio AFM probe with a small tip radius which can be used for the accurate imaging of samples with steep, high features. These probes are shown to buckle elastically if the tip-sample force becomes too large, preventing damage to the tip or sample. This behavior is similar to that of high-aspect ratio AFM probes fabricated by the attachment of a carbon nanotube (CNT) to the probe apex, but the single-stage fabrication of EBID tips is much simpler than the multi-stage processes needed to produce CNT probes.

In order to exert forces larger than the critical buckling force for thin needles

the needles could be strengthened by carbon coating using EBID. This was implemented by imaging the needle at high magnification and beam current in the SEM, which resulted in an even coating of amorphous carbon on the needle tip. This allowed "tuning" of the needle diameter, making it more rigid and increasing the maximum force which it could exert on a sample.

In chapter 7, it is shown how analysis of the force curves recorded during penetration of the nanoneedles into corneocyte cells was performed using models based on those derived for determination of the elastic modulus of materials by nanoindentation. These experiments showed increase in elastic modulus with increasing rate of application of the indentation force, indicating viscoelastic behaviour in the corneocytes. The process also indicated the presence of a layered structure within the corneocyte; there was evidence of a sudden penetration through an outer layer with a lower elastic modulus, with the nanoneedle able to detect a second layer of stiffer material beneath. This reflects the known structure of corneocyte cells, with an outer cornified envelope surrounding a stiffer intracellular keratin filament structure.

This study indicates that the nanoneedle probes can be used for "mechanical tomography" of biological cells, probing deep into the cell structure to determine elastic modulus or other mechanical properties of intracellular structures. This application has not previously been investigated using nanoneedle probes. It was also demonstrated that the measured elastic properties of corneocytes changed significantly upon treatment with sodium lauryl sulphate to simulate irritation of the skin. This indicates that indentation using nanoneedles can be used to investigate the changes in mechanical properties of the internal structures of cells which are associated with disease states; these changes reflect alterations to the nanoscale internal ultrastructure of the cell.

Using both unmodified AFM probes and nanotool probes, experiments were carried out to investigate the removal of surface layers from fixed cells and unfixed corneocytes in order to expose internal structures for AFM imaging. These experiments are described in chapter 8. It was shown that this removal was possible; AFM images taken afterwards suggested that the internal structure of the cells could be observed using this technique. This kind of "nanosurgery" has been previously performed on bacterial cell walls and isolated collagen fibrils, but this is the first demonstration of the localised removal of the surfaces of animal cells

by mechanical (rather than chemical) methods. In particular, the "nanotome" tool was sucessfully used to separate the outer layer of a corneocyte from structures beneath; the separated layer was then removed using nanomanipulation with the AFM tip. It is also demonstrated that nanoneedle probes can be used for recovery of samples of material from the cell surface.

Experiments were also carried out to determine the elastic modulus and flexibility of the nanoscale structures fabricating using EBID; this was performed by controlled bending of carbon cantilevers fabricated by EBID using AFM manipulation. This process also demonstrated the flexibility of these structures, which could recover most of their deformation elastically after being deflected up to 75% of their length. This flexibility has not been systematically investigated previously in EBID structures. This result suggests other applications for free-standing EBID structures, such as nanoscale springs, force transducers or nanocantilever oscillators for biological and chemical sensing applications. These experiments are described in chapter 6.

9.2 Concluding Remarks

The work described in this thesis has demonstrated several novel AFM probe designs by EBID, and demonstrated their successful application for nanomanipulation of biological cells. Experiments have been carried out that advance the present understanding of electron beam induced deposited structures and suggest new applications for these structures. These probes open up new capabilities for the investigation of the internal structure of biological cells and are likely to find application in many areas of biology and medicine.

9.3 Publications

The following is a list of the previously published works from the experiments described in this thesis:

J.D. Beard, D.J. Burbridge, A.V. Moskalenko, O. Dudko, P.L. Yarova, S.V. Smirnov and S.N. Gordeev, "An atomic force microscope nanoscalpel for nanolithography and biological applications", *Nanotechnology* 20 (2009) 445302

J.D. Beard, "Dissecting the nanoworld: The atomic force microscope nanoscalpel", *Nanowerk (www.nanowerk.com)* uploaded 30 October 2009

J.D. Beard and S.N. Gordeev, "Large flexibility of high aspect ratio amorphous carbon nanostructures fabricated by electron-beam-induced deposition", *Nanotechnology* 21 (2010) 475702

J.D. Beard and S.N. Gordeev, "Fabrication and Buckling Dynamics of Nanoneedle AFM Probes", *Nanotechnology* 22 (2011) 175303

J.D. Beard, S.N. Gordeev and R.H. Guy, "AFM Nanotools for Surgery of Biological Cells", *Journal of Physics: Conference Series* 286 (2011) 012003

J.D. Beard, S.N. Gordeev and R.H. Guy, "Measuring the Internal Mechanics of Biological Cells with a Nanoneedle", in preparation for submission to *Nature Methods* (2011)

J.D. Beard and S.N. Gordeev, "Simple EBID Process Delivers Robust Nanoneedle Probe", *http://nanotechweb.org/* uploaded 4 May 2011

Appendix A

Biological Protocols

A.1 Isolation of Smooth Muscle Cells

Smooth muscle cells are extracted from aortic tissue. Male Wistar rats were humanely killed by cervical dislocation in accordance with Home Office regulations, and then dissected to remove the aorta (handling and dissection of the rats was performed by a licensed technician). The tissue was immersed in antibiotic/fungicide solution and sectioned and cleaned of external connective tissue. An air bubble was passed through the aorta to destroy its internal layer of epithelial cells and then the tissue was divided into ∼4 mm rings and incubated in a 2 ml Ca2+, Mg2+-free saline buffer solution containing 1 mg/ml bovine serum albumin (BSA), 2 mg/ml collagenase (type XI), 1 mg/ml papain, 1 mg/ml dithiothreitol and 0.5 mg/ml trypsin inhibitor (all from Sigma, UK) for 20 minutes at 37 °C. Using gentle agitation with a pipette, the digested tissue was separated into individual cells. For AFM experiments, cells were deposited on glass cover slips and allowed to adhere for ∼30 minutes. This process is routinely used for tissue isolation at the University of Bath Department of Pharmacy and Pharmacology; this work was performed in collaboration with Dr SV Smirnov in this department. [200]

A.1.1 Cell Culture

Some cells samples were fixed for imaging immediately. However, some were cultured for ∼24 hours, allowing them to adhere to the slides and propagate.

This reduces their overall height (making them easier to image with AFM as our AFM scanner is limited to 5.5 μm vertical displacement). The cells were centrifuged twice at 1100 rpm to separate them from solution, and then transferred to DMEM/F-12 culture media (Invitrogen, UK) and deposited on circular glass cover slips for AFM experiments.

These cells were incubated at 37 °C in a CO_2 atmosphere in culture media for ∼3 days. Before fixation for AFM imaging, the culture media above the cells was removed by aspiration, and the cells were then transferred to clean phosphate-buffered saline (PBS).

A.1.2 Fixation for AFM Imaging

Cultured cells were fixed using 3% paraformaldehyde (PFA) for 40 minutes at room temperature, then dehydrated using increasing concentrations of ethanol (25%, 50%, 75%, 100%) then acetone (25%, 50%, 100%, omitting the 75% step), before rinsing in DI-H_2O and drying in air. Non-cultured cells were not PFA-fixed but were dehydrated using the same protocol.

A.2 Preparation of Megakaryocyte Samples

Preparation of megakaryocyte samples was performed in collaboration with Dr A Mackenzie of the Department of Pharmacy and Pharmacology at the University of Bath.

A.2.1 Preparation of Substrates

In order to improve adhesion by the megakaryocytes, the cover slips which served as substrates for AFM imaging were coated with fibrinogen. This was performed by depositing 200 μl 0.1 mg/ml fibrinogen solution (sterilised by filtration using a 0.22 μm filter) in PBS onto the coverslip under sterile conditions. ∼2 hours was allowed for adhesion of the fibrinogen to the glass slide.

a)

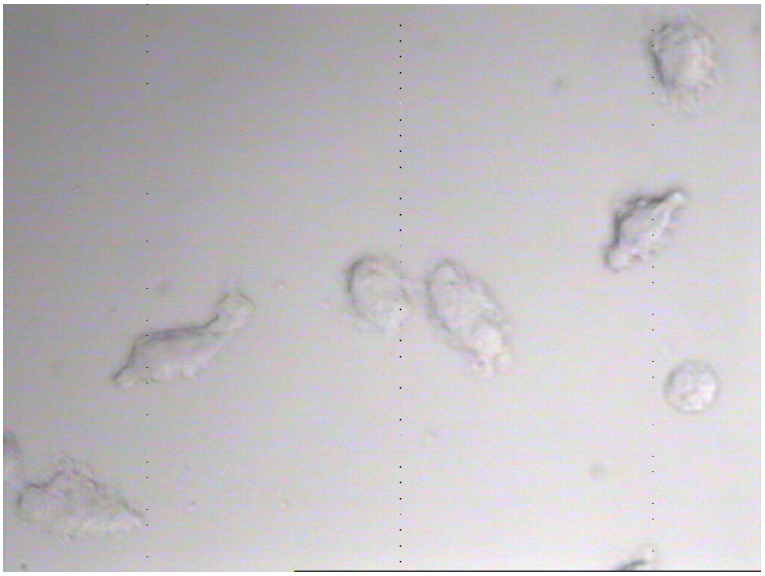

b)

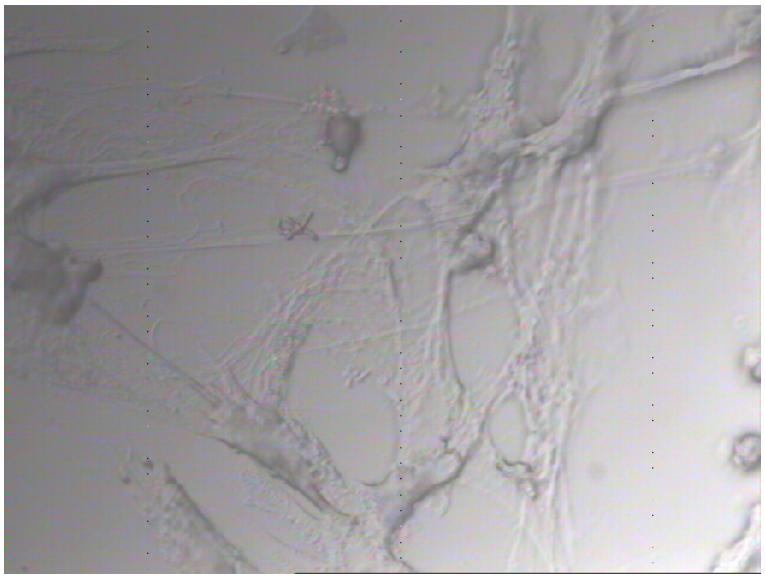

Figure A-1: Optical microscope images of non-cultured (a) and cultured (b) fixed aortic smooth muscle cells. (x1000 magnification)

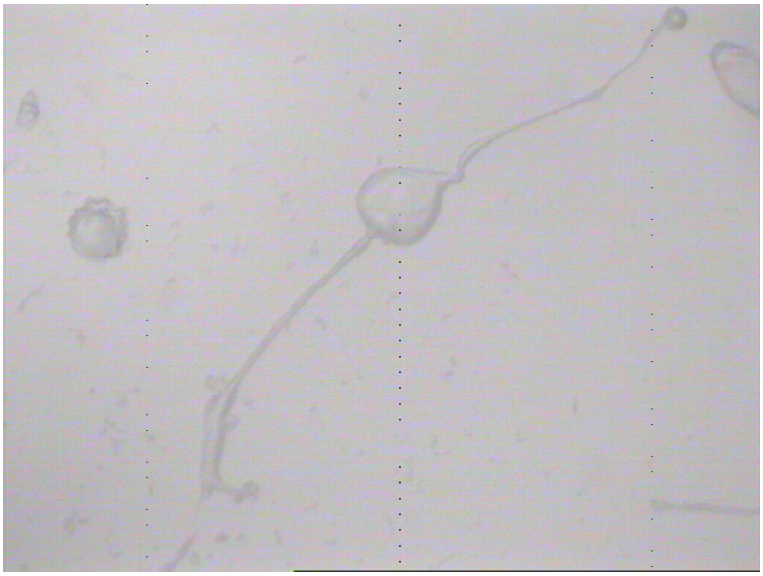

Figure A-2: Optical microscope image of megakaryocyte cell in the process of platelet production. Visible are the long proplatelet protrusions which extend from the cell as it differentiates. (x500 magnification)

A.2.2 Megakaryocyte Preparation

Megakaryocytes suspended in culture media were centrifuged at 1200 rpm for 4 minutes, and the supernatant media removed by aspiration. The cells were resuspended in 4 ml culture media, then 1 ml of the cell suspension added to 4 ml culture media in petri dishes containing the fibrinogen-coated glass slides. The cells were incubated at 37 °C in a CO_2 atmosphere in culture media for ∼3 days, as for the smooth muscle cells. During this time the megakaryocyte cells adhere to the substrate, propagate and form the demarcation membrane system.

The cultured megakaryocytes were fixed using PFA using the same procedure as for the the smooth muscle cells (see section A.1).

A.3 Isolation of Corneocytes

Corneocyte sampling for mechanical testing was performed using a tape- stripping process on the left ventral forearms of 8 healthy human volunteers aged 19-54 years. The subjects were provided with detailed information on the process beforehand and any questions raised were answered appropriately. All subjects gave

written consent beforehand, and the sampling process was performed with approval from the relevant ethics committees (REC references: 04/MRE04/70 from Trent Research Ethics Committee and EP 10/11 54 including amendment EP 10/11 55 from the Research Ethics Approval Committee for Health (REACH)) and was performed in collaboration with Prof RH Guy of the Department of Pharmacy and Pharmacology at the University of Bath. An area 10x10 mm^2 was marked on a hair-free area of skin on the left ventral forearm surface. Commercially available adhesive tape (Scotch Tape from 3M) was then pressed onto this area, and then removed. Tape-stripping was used in combination with Trans-Epidermal Water Loss (TEWL) measurements to determine the depth of removal of the stratum corneum. These TEWL measurements were performed using a Biox AquaFlux Condenser Chamber TEWL probe to monitor and control the depth of removal of the corneocytes (using the method described in chapter 2); these measurements were performed every 1-5 strips. When the desired depth (corresponding to 20% removal of the stratum corneum) had been reached, commercially available hair removal wax (Parissa Strip Free Wax, Boots UK Ltd.) heated to 65 °C was used as an adhesive to remove corneocytes for AFM imaging. This wax hardens on cooling to a rigid substrate for the cell samples. These sampling procedures are routinely used in the Department of Pharmacy & Pharmacology at the University of Bath.

In order to examine differences in mechanical properties in irritated skin, a site on the left ventral forearm of 4 volunteers was treated with a low concentration of the mild irritant sodium lauryl sulphate (SLS) (0.1% w/v concentration, 250 μl, QMX Laboratories, UK) for 6 hours per day for 4 days per week (Tuesday-Friday) over a 3-week period. SLS treatment of the skin was performed by Mrs Q Yang of the Department of Pharmacy and Pharmacology at the University of Bath as part of a larger study examining biochemical changes in the irritated stratum corneum using infrared spectroscopy, mass spectroscopy and fluorescence microscopy on the isolated corneocytes (approved under Ref: EP10/11 54 including amendment Ref: EP 10/11 55 from the Research Ethics Approval Committee for Health (REACH)). During this period, TEWL measurements were carried out to mitigate against strong irritation; if an increase in TEWL of >50 g/m^2hr^{-1} was detected, the applied SLS concentration was halved. The right arm was not exposed to SLS and therefore was used to provide control samples. Tape stripping

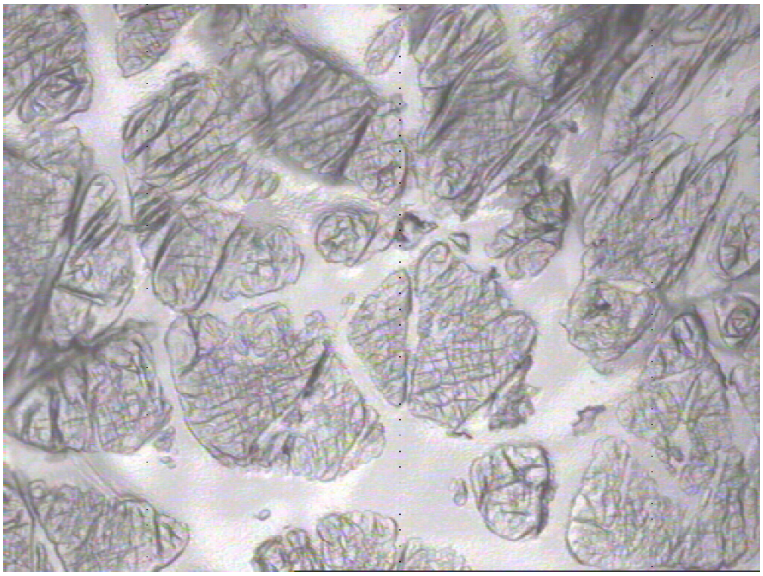

Figure A-3: Optical microscope image of isolated corneocytes on wax surface. (x100 magnification)

was then used to remove 75% of the stratum corneum on both control and treated sites, before wax was again used to remove samples for AFM measurements as described above.

Appendix B

Program for Integration of Beam Bending Equations

The program shown below was used to find solutions to the Euler-Bernoulli beam bending equations for large deflections of a cantilever beam as derived by Bishop *et al.* [180] This is performed by integrating equations 6.10 and 6.12 found in section 6. The program is written using C in the CodeBlocks open source development environment and is intended to run in a Windows operating system (Windows 7 and XP were used in our experiments).

```
#include <stdio.h>
#include <stdlib.h>
#include <math.h>
#include <windows.h>

int main()
{
    double phi0_min=0, phi0_max=M_PI/2;
    double phi, d_phi, phi0, d_phi0;
    double output1=0, output2=0, phi0_output=0;
    double output1_0, output2_0;
    int E_found;
    double i1, i0;
    int i, j, k, fp;
    int n=25,phi0_n=256, phi_n=2.0e6;
```

```
// x and y arrays hold experimentally measured values of load point
// position (x) and deflection of beam at the load point (y) for each indent
// x and y are defined in the program code; substitute value1, value2 etc.
// for experimentally measured values

    double x[30]={value1, value2...value29,value30};
    double y[30]={value1, value2...value29,value30};
    double d;
    double output1_min, output2_min, output1_max, output2_max,
phi0_output_min, phi0_output_max;

// Set text colour to green (just a personal preference)
SetConsoleTextAttribute (GetStdHandle(STD_OUTPUT_HANDLE),
FOREGROUND_GREEN);

// Open output file
    fp=fopen("output.txt", "w");

// Write a file header
    fprintf(fp, "x(nm), y(nm), d(nm), phi0(rads) min, phi0(rads) max,
output1 min, output1 max, output2 min,
output2 max\n");

// Set stepsize for phi0
    d_phi0=(phi0_max-phi0_min)/phi0_n;

// Start loop through measured x values
for (k=0;k<n;k++) {

    output1_min=0;
    output2_min=0;
    phi0_output_min=0;
    output1_max=0;
    output2_max=0;
    phi0_output_max=0;
```

```
// Start loop through possible phi0 values
for (j=0;j<phi0_n;j++){

//Calculate phi0 and stepsize for phi

    phi0=j*d_phi0;
    d_phi=(phi0-phi0_min-1.0e-14)/phi_n;

//Store values of output1 and output2 from previous phi0 step

    output1_0=output1;
    output2_0=output2;

//Zero outputs

    output1=0;
    output2=0;
    phi0_output=0;

// Start loop through possible phi values from zero to phi0

    for (i=0;i<phi_n;i++) {

// Calculate phi
        phi=i*d_phi+phi0_min;

// Calculate 2*sqrt(alpha) values at phi, phi+d_phi

        i1=1/sqrt((sin(phi0)-sin(phi)));
        i0=1/sqrt((sin(phi0)-sin(phi+d_phi)));

// Integrate using trapezium method
        output1=output1+(i1+i0)*d_phi/2;

// Calculate output for y values
```

```
        i0=sin(phi)/sqrt((sin(phi0)-sin(phi)));
        i1=sin(phi+d_phi)/sqrt((sin(phi0)-sin(phi+d_phi)));

// Integrate using trapezium method
        output2=output2+(i1+i0)*d_phi/2;

// End loop through phi values
   }

// Calculate 2*sqrt(alpha) values at phi, phi+d_phi

//       i1=1/sqrt((sin(phi0)-sin(phi+d_phi)));
//       i0=1/sqrt((sin(phi0)-sin(phi+1.999999*d_phi)));

// Integrate using trapezium method
//        output1=output1+(i1+i0)*d_phi/2;

// Calculate output for y values
//        i0=sin(phi+d_phi)/sqrt((sin(phi0)-sin(phi+d_phi)));
//        i1=sin(phi+1.999999*d_phi)/sqrt((sin(phi0)
-sin(phi+1.999999*d_phi)));

// Integrate using trapezium method
//        output2=output2+(i1+i0)*d_phi/2;

// Calculate d corresponding to x for this phi0 value
        d=x[k]*sqrt(1/(4*sin(phi0)))*output2;

// If y has passed d, output maximum values
        if(d>y[k]){
            phi0_output_max=phi0;
            output1_max=output1;
            output2_max=output2;
            break;
            }
```

```
    output1_min=output1;
    output2_min=output2;
    phi0_output_min=phi0;

//    fprintf(fp, "%f, %f, %f, %f\n", phi0, d, output1, output2);

// End loop through phi0 values
}

//    fprintf(fp, "\n", "");

// Output results to file and screen
printf("%i, %f, %f, %f, %f, %f, %f \n", j, phi0_output_min,
phi0_output_max, output1_min, output1_max,
output2_min, output2_max);
fprintf(fp, "%f, %f, %f, %f, %f, %f, %f, %f, %f \n", x[k], y[k], d,
phi0_output_min, phi0_output_max, output1_min,
output1_max, output2_min, output2_max);

// End loop through x values
}

// Close output file
    fclose(fp);

// End program
    return 0;
}
```

Bibliography

[1] Nobel Media AB, "The Nobel Prize in Physics 1986. NobelPrize.org." `http://nobelprize.org/nobel_prizes/physics/laureates/1986/`, accessed 31 Jan 2011.

[2] G. Binnig, C. Quate, and C. Gerber, "Atomic force microscope," *Physical review letters*, vol. 56, no. 9, pp. 930–933, 1986.

[3] F. Giessibl, "Advances in atomic force microscopy," *Reviews of modern physics*, vol. 75, no. 3, pp. 949–983, 2003.

[4] Y. Martin, C. Williams, and H. Wickramasinghe, "AFM-force mapping and profiling on a sub 100-A scale," *Journal of Applied Physics*, vol. 61, no. 10, pp. 4723–4729, 1987.

[5] C. Putman, K. Van der Werf, B. De Grooth, N. Van Hulst, and J. Greve, "Viscoelasticity of living cells allows high resolution imaging by tapping mode atomic force microscopy," *Biophysical journal*, vol. 67, no. 4, pp. 1749–1753, 1994.

[6] E. Henderson, P. Haydon, and D. Sakaguchi, "Actin filament dynamics in living glial cells imaged by atomic force microscopy," *Science*, vol. 257, no. 5078, p. 1944, 1992.

[7] L. Chang, T. Kious, M. Yorgancioglu, D. Keller, and J. Pfeiffer, "Cytoskeleton of living, unstained cells imaged by scanning force microscopy," *Biophysical journal*, vol. 64, no. 4, pp. 1282–1286, 1993.

[8] C. Grimellec, E. Lesniewska, M.-C. Giocondi, E. Finot, and J.-P. Goudonnet, "Simultaneous imaging of the surface and submembranous cytoskeleton in living cells by tapping mode atomic force microscopy," *Biophysics*, vol. 320, pp. 637–643, 1998.

[9] H. You, J. Lau, S. Zhang, and L. Yu, "Atomic force microscopy imaging of living cells: a preliminary study of the disruptive effect of the cantilever tip on cell morphology," *Ultramicroscopy*, vol. 82, no. 1-4, pp. 297–305, 2000.

[10] T. Ushiki, S. Yamamoto, J. Hitomi, S. Ogura, T. Umemoto, and M. Shigeno, "Atomic force microscopy of living cells," *Jpn. J. Appl. Phys*, vol. 39, pp. 3761–3764, 2000.

[11] J. Saenz, N. Garcia, P. Grutter, E. Meyer, H. Heinzelmann, R. Wiesendanger, L. Rosenthaler, H. Hidber, and H. Guntherodt, "Observation of magnetic forces by the atomic force microscope," *Journal of Applied Physics*, vol. 62, no. 10, pp. 4293–4295, 1987.

[12] Y. Martin and H. Wickramasinghe, "Magnetic imaging by force microscopy with 1000 Å resolution," *Applied Physics Letters*, vol. 50, no. 20, pp. 1455–1457, 1987.

[13] C. Stroh, A. Ebner, M. Geretschläger, G. Freudenthaler, F. Kienberger, A. Kamruzzahan, S. Smith-Gill, H. Gruber, and P. Hinterdorfer, "Simultaneous topography and recognition imaging using force microscopy," *Biophysical journal*, vol. 87, no. 3, pp. 1981–1990, 2004.

[14] R. Stewart, "Insulating films formed under electron and ion bombardment," *Physical Review*, vol. 45, no. 7, pp. 488–490, 1934.

[15] J. Watson, "An effect of electron bombardment upon carbon black," *Journal of Applied Physics*, vol. 18, p. 153, 1947.

[16] V. Cosslett, "Particle "Growth" in the Electron Microscope," *Journal of Applied Physics*, vol. 18, p. 844, 1947.

[17] J. Hillier, "On the investigation of specimen contamination in the electron microscope," *Journal of Applied Physics*, vol. 19, no. 3, pp. 226–230, 1948.

[18] R. Hart, T. Kassner, and J. Maurin, "The contamination of surfaces during high-energy electron irradiation," *Philosophical Magazine*, vol. 21, no. 171, pp. 453–467, 1970.

[19] A. Ennos, "The origin of specimen contamination in the electron microscope," *British Journal of Applied Physics*, vol. 4, p. 101, 1953.

[20] R. Christy, "Formation of thin polymer films by electron bombardment," *Journal of Applied Physics*, vol. 31, no. 9, pp. 1680–1683, 1960.

[21] A. Baker and W. Morris, "Deposition of metallic films by electron impact decomposition of organometallic vapors," *Review of Scientific Instruments*, vol. 32, p. 458, 1961.

[22] A. Broers, W. Molzen, J. Cuomo, and N. Wittels, "Electron-beam fabrication of 80-Å metal structures," *Applied Physics Letters*, vol. 29, p. 596, 1976.

[23] W. Van Dorp and C. Hagen, "A critical literature review of focused electron beam induced deposition," *Journal of Applied Physics*, vol. 104, no. 8, p. 081301, 2008.

[24] G. Hornyak, J. Dutta, H. Tibbals, and A. Rao, *Introduction to nanoscience*. CRC Press, 2008.

[25] N. Silvis-Cividjian, C. Hagen, L. Leunissen, and P. Kruit, "The role of secondary electrons in electron-beam-induced-deposition spatial resolution," *Microelectronic Engineering*, vol. 61, pp. 693–699, 2002.

[26] N. Silvis-Cividjian, C. Hagen, and P. Kruit, "Spatial resolution limits in electron-beam-induced deposition," *Journal of Applied Physics*, vol. 98, p. 084905, 2005.

[27] D. Alman, D. Ruzic, and J. Brooks, "A hydrocarbon reaction model for low temperature hydrogen plasmas and an application to the Joint European Torus," *Physics of plasmas*, vol. 7, p. 1421, 2000.

[28] J. Bieber, J.A. Pulecio and W. Moreno, "Applications of electron beam induced deposition in nanofabrication," in *Proceedings of the 7th International Carribean Conference on Devices, Circuits and Systems*, 2008.

[29] J. Fowlkes, S. Randolph, and P. Rack, "Growth and simulation of high-aspect ratio nanopillars by primary and secondary electron-induced deposition," *Journal of Vacuum Science & Technology B: Microelectronics and Nanometer Structures*, vol. 23, p. 2825, 2005.

[30] Y. Akama, E. Nishimura, A. Sakai, and H. Murakami, "New scanning tunneling microscopy tip for measuring surface topography," *Journal of Vacuum Science & Technology A: Vacuum, Surfaces, and Films*, vol. 8, p. 429, 1990.

[31] D. Keller and C. Chih-Chung, "Imaging steep, high structures by scanning force microscopy with electron beam deposited tips," *Surface Science*, vol. 268, no. 1-3, pp. 333–339, 1992.

[32] M. Yamaki, T. Miwa, H. Yoshimura, and K. Nagayama, "Efficient microtip fabrication with carbon coating and electron beam deposition for atomic force microscopy," *Journal of Vacuum Science & Technology B: Microelectronics and Nanometer Structures*, vol. 10, no. 6, pp. 2447–2450, 1992.

[33] K. Schiffmann, "Investigation of fabrication parameters for the electron-beam-induced deposition of contamination tips used in atomic force microscopy," *Nanotechnology*, vol. 4, p. 163, 1993.

[34] F. Zenhausern, M. Adrian, B. ten Heggeler-Bordier, F. Ardizzoni, and P. Descouts, "Enhanced imaging of biomolecules with electron beam deposited tips for scanning force microscopy," *Journal of Applied Physics*, vol. 73, p. 7232, 1993.

[35] M. Wendel, H. Lorenz, and J. Kotthaus, "Sharpened electron beam deposited tips for high resolution atomic force microscope lithography and imaging," *Applied Physics Letters*, vol. 67, p. 3732, 1995.

[36] Chen, I-C and Chen, L-H and Orme, C and Quist, A and Lal, R and Jin, S, "Fabrication of high-aspect-ratio carbon nanocone probes by electron beam induced deposition patterning," *Nanotechnology*, vol. 17, pp. 4322–4326, 2006.

[37] N. Kislov, I. Khodos, E. Ivanov, and J. Barthel, "Electron-beam-induced fabrication of metal-containing nanostructures," *Scanning*, vol. 18, no. 2, pp. 114–118, 1996.

[38] K. Mølhave, D. Madsen, A. Rasmussen, A. Carlsson, C. Appel, M. Brorson, C. Jacobsen, and P. Bøggild, "Solid gold nanostructures fabricated by electron beam deposition," *Nano Letters*, vol. 3, no. 11, pp. 1499–1503, 2003.

[39] Z. Liu, K. Mitsuishi, and K. Furuya, "Effects of focus change on the fabrication of tungsten nanowire by electron-beam-induced deposition," *Nanotechnology*, vol. 15, p. S414, 2004.

[40] Z. Liu, K. Mitsuishi, and K. Furuya, "Three-dimensional nanofabrication by electron-beam-induced deposition using 200-keV electrons in scanning transmission electron microscope," *Applied Physics A: Materials Science & Processing*, vol. 80, no. 7, pp. 1437–1441, 2005.

[41] K. Mitsuishi, M. Shimojo, M. Takeguchi, M. Tanaka, and K. Furuya, "Proximity effect in electron-beam-induced deposition," *Japanese Journal of Applied Physics*, vol. 45, no. 6B, pp. 5517–5521, 2006.

[42] G. Gazzadi, S. Frabboni, and C. Menozzi, "Suspended nanostructures grown by electron beam-induced deposition of Pt and TEOS precursors," *Nanotechnology*, vol. 18, p. 445709, 2007.

[43] I. Utke, A. Luisier, P. Hoffmann, D. Laub, and P. Buffat, "Focused-electron-beam-induced deposition of freestanding three-dimensional nanostructures of pure coalesced copper crystals," *Applied Physics Letters*, vol. 81, no. 17, pp. 3245–3247, 2002.

[44] F. Banhart, "Laplacian growth of amorphous carbon filaments in a non-diffusion-limited experiment," *Physical Review E*, vol. 52, no. 5, pp. 5156–5160, 1995.

[45] M. Song, K. Mitsuishi, M. Tanaka, M. Takeguchi, M. Shimojo, and K. Furuya, "Fabrication of self-standing nanowires, nanodendrites, and nanofractal-like trees on insulator substrates with an electron-beam-induced deposition," *Applied Physics A: Materials Science & Processing*, vol. 80, no. 7, pp. 1431–1436, 2005.

[46] Y. Chu, J. Hu, W. Yang, C. Wang, and J. Zhang, "Growth and characterization of highly branched nanostructures of magnetic nanoparticles," *J. Phys. Chem. B*, vol. 110, no. 7, pp. 3135–3139, 2006.

[47] M. Song and K. Furuya, "Fabrication and characterization of nanostructures on insulator substrates by electron-beam-induced deposition," *Science and Technology of Advanced Materials*, vol. 9, p. 023002, 2008.

[48] G. Xie, M. Song, and K. Furuya, "Fabrication and characterization of Au-nanoparticle/W-nanodendrite structures on Al_2O_3 substrate," *Journal of Materials Science*, vol. 41, no. 14, pp. 4537–4542, 2006.

[49] G. Xie, M. Song, K. Mitsuishi, and K. Furuya, "Characterization of nanometer-sized Pt-dendrite structures fabricated on insulator Al_2O_3 substrate by electron-beam-induced deposition," *Journal of Materials Science*, vol. 41, no. 9, pp. 2567–2571, 2006.

[50] L. Reimer and M. Wachter, "Contribution to the contamination problem in transmission electron microscopy," *Ultramicroscopy*, vol. 3, pp. 169–174, 1978.

[51] M. Amman, J. Sleight, D. Lombardi, R. Welser, M. Deshpande, M. Reed, and L. Guido, "Atomic force microscopy study of electron beam written contamination structures," *Journal of Vacuum Science and Technology-Section B-Microelectronics Nanometer Structur*, vol. 14, no. 1, pp. 54–62, 1996.

[52] S. Matsui, "Three-Dimensional Nanostructure Fabrication by Focused Ion Beam Chemical Vapor Deposition," *Springer Handbook of Nanotechnology*, pp. 211–229, 2010.

[53] S. Randolph, J. Fowlkes, and P. Rack, "Focused, nanoscale electron-beam-induced deposition and etching," *Critical Reviews in Solid State and Materials Sciences*, vol. 31, no. 3, pp. 55–89, 2006.

[54] K. Mitsuishi, M. Shimojo, M. Han, and K. Furuya, "Electron-beam-induced deposition using a subnanometer-sized probe of high-energy electrons," *Applied Physics Letters*, vol. 83, p. 2064, 2003.

[55] P. Crozier, J. Tolle, J. Kouvetakis, and C. Ritter, "Synthesis of uniform GaN quantum dot arrays via electron nanolithography of DGaN," *Applied Physics Letters*, vol. 84, p. 3441, 2004.

[56] I. Utke, P. Hoffmann, B. Dwir, K. Leifer, E. Kapon, and P. Doppelt, "Focused electron beam induced deposition of gold," *Journal of Vacuum Science & Technology B: Microelectronics and Nanometer Structures*, vol. 18, p. 3168, 2000.

[57] N. Silvis-Cividjian, C. Hagen, P. Kruit, M. vd Stam, and H. Groen, "Direct fabrication of nanowires in an electron microscope," *Applied Physics Letters*, vol. 82, p. 3514, 2003.

[58] K. Mølhave, D. Madsen, S. Dohn, and P. Bøggild, "Constructing, connecting and soldering nanostructures by environmental electron beam deposition," *Nanotechnology*, vol. 15, p. 1047, 2004.

[59] G. Boero, I. Utke, T. Bret, N. Quack, M. Todorova, S. Mouaziz, P. Kejik, J. Brugger, R. Popovic, and P. Hoffmann, "Submicrometer Hall devices fabricated by focused electron-beam-induced deposition," *Applied Physics Letters*, vol. 86, p. 042503, 2005.

[60] C. Umbach, S. Washburn, R. Webb, R. Koch, M. Bucci, A. Broers, and R. Laibowitz, "Observation of h/e Aharonov–Bohm interference effects in submicron diameter, normal metal rings," *Journal of Vacuum Science & Technology B: Microelectronics and Nanometer Structures*, vol. 4, no. 1, pp. 383–385, 1986.

[61] H. Koops, O. Hoinkis, M. Honsberg, R. Schmidt, R. Blum, G. Böttger, A. Kuligk, C. Liguda, and M. Eich, "Two-dimensional photonic crystals produced by addi-

tive nanolithography with electron beam-induced deposition act as filters in the infrared," *Microelectronic Engineering*, vol. 57, pp. 995–1001, 2001.

[62] T. Liang, A. Stivers, M. Penn, D. Bald, C. Sethi, V. Boegli, M. Budach, K. Edinger, and P. Spies, "Demonstration of damage-free mask repair using electron beam-induced processes," in *Proc. SPIE*, vol. 5446, p. 291, 2004.

[63] M. Yu, O. Lourie, M. Dyer, K. Moloni, T. Kelly, and R. Ruoff, "Strength and breaking mechanism of multiwalled carbon nanotubes under tensile load," *Science*, vol. 287, no. 5453, p. 637, 2000.

[64] W. Ding, D. Dikin, X. Chen, R. Piner, R. Ruoff, and E. Zussmann, "Mechanics of hydrogenated amorphous carbon deposits from electron-beam-induced deposition of a paraffin precursor," *J. Appl. Phys.*, vol. 98, p. 014905, 2005.

[65] H. Tanaka, M. Shinkai, Y. Shibutani, and Y. Kogo, "Nonlinear large deflection of nanopillars fabricated by focused ion-beam induced chemical vapor deposition using double-cantilever testing," *Journal of Vacuum Science & Technology B: Microelectronics and Nanometer Structures*, vol. 27, no. 5, pp. 2161–2165, 2009.

[66] F. Banhart, "The formation of a connection between carbon nanotubes in an electron beam," *Nano Letters*, vol. 1, no. 6, pp. 329–332, 2001.

[67] D. Burbridge, *Nanofabrication Techniques: Novel Applications of Electron Beam Induced Deposition.* PhD thesis, University of Bath, 2009.

[68] Z. Liu, K. Mitsuishi, and K. Furuya, "The growth behavior of self-standing tungsten tips fabricated by electron-beam-induced deposition using 200 keV electrons," *Journal of Applied Physics*, vol. 96, p. 3983, 2004.

[69] M. Tanaka, M. Shimojo, M. Han, K. Mitsuishi, and K. Furuya, "Ultimate sized nano-dots formed by electron beam-induced deposition using an ultrahigh vacuum transmission electron microscope," *Surface and Interface Analysis*, vol. 37, no. 2, pp. 261–264, 2005.

[70] S. Frabboni, G. Gazzadi, L. Felisari, and A. Spessot, "Fabrication by electron beam induced deposition and transmission electron microscopic characterization of sub-10-nm freestanding Pt nanowires," *Applied Physics Letters*, vol. 88, p. 213116, 2006.

[71] A. Botman, J. Mulders, R. Weemaes, and S. Mentink, "Purification of platinum and gold structures after electron-beam-induced deposition," *Nanotechnology*, vol. 17, p. 3779, 2006.

[72] S. Frabboni, G. Gazzadi, and A. Spessot, "Transmission electron microscopy characterization and sculpting of sub-1 nm Si–O–C freestanding nanowires grown by electron beam induced deposition," *Applied Physics Letters*, vol. 89, p. 113108, 2006.

[73] W. van Dorp, B. van Someren, C. Hagen, P. Kruit, and P. Crozier, "Approaching the resolution limit of nanometer-scale electron beam-induced deposition," *Nano Lett*, vol. 5, no. 7, pp. 1303–1307, 2005.

[74] C. Hagen, N. Silvis-Cividjian, and P. Kruit, "Resolution limit for electron beam-induced deposition on thick substrates," *Scanning*, vol. 28, no. 4, pp. 204–211, 2006.

[75] K. Furuya, "Nanofabrication by advanced electron microscopy using intense and focused beam," *Science and Technology of Advanced Materials*, vol. 9, p. 014110, 2008.

[76] J. Fujita, M. Ishida, T. Ichihashi, Y. Ochiai, T. Kaito, and S. Matsui, "Carbon nanopillar laterally grown with electron beam-induced chemical vapor deposition," *Journal of Vacuum Science & Technology B: Microelectronics and Nanometer Structures*, vol. 21, p. 2990, 2003.

[77] J. Beard, D. Burbridge, A. Moskalenko, O. Dudko, P. Yarova, S. Smirnov, and S. Gordeev, "An atomic force microscope nanoscalpel for nanolithography and biological applications," *Nanotechnology*, vol. 20, p. 445302, 2009.

[78] J. Beard and S. Gordeev, "Fabrication and Buckling Dynamics of Nanoneedle AFM Probes," *Nanotechnology*, 2011, in press.

[79] M. Oyen and R. Cook, "A practical guide for analysis of nanoindentation data," *Journal of the Mechanical Behavior of Biomedical Materials*, vol. 2, no. 4, pp. 396–407, 2009.

[80] I. Sneddon, "The relation between load and penetration in the axisymmetric Boussinesq problem for a punch of arbitrary profile," *International Journal of Engineering Science*, vol. 3, no. 1, pp. 47–57, 1965.

[81] M. Doerner and W. Nix, "A method for interpreting the data from depth-sensing indentation instruments," *J. Mater. Res*, vol. 1, no. 4, pp. 601–609, 1986.

[82] W. Oliver and G. Pharr, "An improved technique for determining hardness and elastic modulus using load and displacement sensing indentation experiments," *Journal of materials research*, vol. 7, no. 6, pp. 1564–1583, 1992.

[83] G. Schmid-Schönbein, K. Sung, H. Tözeren, R. Skalak, and S. Chien, "Passive mechanical properties of human leukocytes," *Biophysical Journal*, vol. 36, no. 1, pp. 243–256, 1981.

[84] R. Tran-Son-Tay, D. Needham, A. Yeung, and R. Hochmuth, "Time-dependent recovery of passive neutrophils after large deformation," *Biophysical journal*, vol. 60, no. 4, pp. 856–866, 1991.

[85] M. Radmacher, R. Tillamnn, M. Fritz, and H. Gaub, "From molecules to cells: imaging soft samples with the atomic force microscope," *Science*, vol. 257, no. 5078, p. 1900, 1992.

[86] R. Hochmuth, H. Ting-Beall, B. Beaty, D. Needham, and R. Tran-Son-Tay, "Viscosity of passive human neutrophils undergoing small deformations," *Biophysical journal*, vol. 64, no. 5, pp. 1596–1601, 1993.

[87] M. Oyen and C. Ko, "Examination of local variations in viscous, elastic, and plastic indentation responses in healing bone," *Journal of Materials Science: Materials in Medicine*, vol. 18, no. 4, pp. 623–628, 2007.

[88] Q. Li, G. Lee, C. Ong, and C. Lim, "AFM indentation study of breast cancer cells," *Biochemical and biophysical research communications*, vol. 374, no. 4, pp. 609–613, 2008.

[89] M. Oyen and R. Cook, "Load-displacement behavior during sharp indentation of viscous-elastic-plastic materials," *Journal of Materials Research*, vol. 18, no. 1, pp. 139–150, 2003.

[90] A. Weisenhorn, M. Khorsandi, S. Kasas, V. Gotzos, H. Butt, *et al.*, "Deformation and height anomaly of soft surfaces studied with an AFM," *Nanotechnology*, vol. 4, p. 106, 1993.

[91] N. Tao, S. Lindsay, and S. Lees, "Measuring the microelastic properties of biological material," *Biophysical journal*, vol. 63, no. 4, pp. 1165–1169, 1992.

[92] J. Hoh and C. Schoenenberger, "Surface morphology and mechanical properties of MDCK monolayers by atomic force microscopy," *Journal of Cell Science*, vol. 107, no. 5, pp. 1105–1114, 1994.

[93] M. Radmacher, "Measuring the Elastic Properties of Biological Samples with the AFM," *IEEE Engineering in Medicine and Biology*, vol. 16, pp. 47–57, 1997.

[94] B. Alberts, D. Bray, A. Johnson, J. Lewis, M. Raff, K. Roberts, and P. Walter, *Essential cell biology*. Garland Science New York, 1998.

[95] M. Lekka, P. Laidler, D. Gil, J. Lekki, Z. Stachura, and A. Hrynkiewicz, "Elasticity of normal and cancerous human bladder cells studied by scanning force microscopy," *European Biophysics Journal*, vol. 28, no. 4, pp. 312–316, 1999.

[96] S. Cross, Y. Jin, J. Rao, and J. Gimzewski, "Nanomechanical analysis of cells from cancer patients," *Nature nanotechnology*, vol. 2, no. 12, pp. 780–783, 2007.

[97] B. Lincoln, H. Erickson, S. Schinkinger, F. Wottawah, D. Mitchell, S. Ulvick, C. Bilby, and J. Guck, "Deformability-based flow cytometry," *Cytometry Part A*, vol. 59, no. 2, pp. 203–209, 2004.

[98] G. Lee and C. Lim, "Biomechanics approaches to studying human diseases," *Trends in biotechnology*, vol. 25, no. 3, pp. 111–118, 2007.

[99] J. Celis, "Microinjection of somatic cells with micropipettes: comparison with other transfer techniques.," *Biochemical Journal*, vol. 223, no. 2, p. 281, 1984.

[100] R. Hochmuth, "Micropipette aspiration of living cells," *Journal of Biomechanics*, vol. 33, no. 1, pp. 15–22, 2000.

[101] A. Ashkin, J. Dziedzic, J. Bjorkholm, and S. Chu, "Observation of a single-beam gradient force optical trap for dielectric particles," *Optics Letters*, vol. 11, pp. 288–290, 1986.

[102] A. Lucio, R. Santos, and O. Mesquita, "Measurements and modeling of water transport and osmoregulation in a single kidney cell using optical tweezers and videomicroscopy," *Physical Review E*, vol. 68, no. 4, p. 41906, 2003.

[103] C. Xie, M. Dinno, and Y. Li, "Near-infrared Raman spectroscopy of single optically trapped biological cells," *Optics letters*, vol. 27, no. 4, pp. 249–251, 2002.

[104] H. Zhang and K. Liu, "Optical tweezers for single cells," *Journal of the Royal Society Interface*, vol. 5, no. 24, p. 671, 2008.

[105] L. Ikin, D. Carberry, G. Gibson, M. Padgett, and M. Miles, "Assembly and force measurement with SPM-like probes in holographic optical tweezers," *New Journal of Physics*, vol. 11, p. 023012, 2009.

[106] E. Florin, J. Hörber, and E. Stelzer, "High-resolution axial and lateral position sensing using two-photon excitation of fluorophores by a continuous-wave Nd: YAG laser," *Applied physics letters*, vol. 69, p. 446, 1996.

[107] E. Florin, A. Pralle, J. Heinrich Hörber, and E. Stelzer, "Photonic Force Microscope Based on Optical Tweezers and Two-Photon Excitation for Biological Applications* 1," *Journal of structural biology*, vol. 119, no. 2, pp. 202–211, 1997.

[108] E. Florin, A. Pralle, E. Stelzer, and J. Hörber, "Photonic force microscope calibration by thermal noise analysis," *Applied Physics A: Materials Science & Processing*, vol. 66, pp. S75–S78, 1998.

[109] J. Shelby, J. Edgar, and D. Chiu, "Monitoring Cell Survival After Extraction of a Single Subcellular Organelle Using Optical Trapping and Pulsed-Nitrogen Laser Ablation," *Photochemistry and photobiology*, vol. 81, no. 4, pp. 994–1001, 2005.

[110] A. Vogel, J. Noack, G. Hüttman, and G. Paltauf, "Mechanisms of femtosecond laser nanosurgery of cells and tissues," *Applied Physics B: Lasers and Optics*, vol. 81, no. 8, pp. 1015–1047, 2005.

[111] M. Berns *et al.*, "Laser microsurgery in cell and developmental biology," *Science*, vol. 213, no. 4507, p. 505, 1981.

[112] R. Amy and R. Storb, "Selective mitochondrial damage by a ruby laser microbeam: an electron microscopic study.," *Science (New York, NY)*, vol. 150, no. 697, p. 756, 1965.

[113] N. Shen, D. Datta, C. Schaffer, P. LeDuc, D. Ingber, and E. Mazur, "Ablation of cytoskeletal filaments and mitochondria in live cells using a femtosecond laser nanoscissor," *Mech. Chem. Biosyst*, vol. 2, no. 1, pp. 17–25, 2005.

[114] V. Kohli, A. Elezzabi, and J. Acker, "Cell nanosurgery using ultrashort (femtosecond) laser pulses: Applications to membrane surgery and cell isolation," *Lasers in Surgery and Medicine*, vol. 37, no. 3, pp. 227–230, 2005.

[115] T. Shimada, W. Watanabe, S. Matsunaga, T. Higashi, H. Ishii, K. Fukui, K. Isobe, and K. Itoh, "Intracellular disruption of mitochondria in a living HeLa

cell with a 76-MHz femtosecond laser oscillator," *Optics Express*, vol. 13, no. 24, pp. 9869–9880, 2005.

[116] U. Tirlapur and K. König, "Femtosecond near-infrared laser pulses as a versatile non-invasive tool for intra-tissue nanoprocessing in plants without compromising viability," *The Plant Journal*, vol. 31, no. 3, pp. 365–374, 2002.

[117] R. Stark, F. Rubio-Sierra, S. Thalhammer, and W. Heckl, "Combined nanomanipulation by atomic force microscopy and UV-laser ablation for chromosomal dissection," *European Biophysics Journal*, vol. 32, no. 1, pp. 33–39, 2003.

[118] I. Maxwell, S. Chung, and E. Mazur, "Nanoprocessing of subcellular targets using femtosecond laser pulses," *Medical Laser Application*, vol. 20, pp. 193–200, 2005.

[119] S. Thalhammer *et al.*, "The atomic force microscope as a new microdissecting tool for the generation of genetic probes," *Journal of structural biology*, vol. 119, no. 2, pp. 232–237, 1997.

[120] H. Hansma, J. Vesenka, C. Siegerist, G. Kelderman, H. Morrett, R. Sinsheimer, V. Elings, C. Bustamante, and P. Hansma, "Reproducible imaging and dissection of plasmid DNA under liquid with the atomic force microscope," *Science*, vol. 256, pp. 1180–1184, 1992.

[121] E. Henderson, "Imaging and nanodissection of individual supercoiled plasmids by atomic force microscopy," *Nucleic acids research*, vol. 20, no. 3, p. 445, 1992.

[122] M. Falvo, S. Washburn, R. Superfine, M. Finch, F. Brooks Jr, and V. Chi, "Manipulation of individual viruses: friction and mechanical properties," *Biophysical Journal*, vol. 72, no. 3, pp. 1396–1403, 1997.

[123] S. Scheuring, J. Seguin, S. Marco, D. Lévy, B. Robert, and J. Rigaud, "Nanodissection and high-resolution imaging of the Rhodopseudomonas viridis photosynthetic core complex in native membranes by AFM," *Proceedings of the National Academy of Sciences of the United States of America*, vol. 100, no. 4, p. 1690, 2003.

[124] D. Fotiadis, D. Müller, G. Tsiotis, L. Hasler, P. Tittmann, T. Mini, P. Jenoè, H. Gross, and A. Engel, "Surface analysis of the photosystem I complex by electron and atomic force microscopy," *Journal of molecular biology*, vol. 283, no. 1, pp. 83–94, 1998.

[125] C. Wen and M. Goh, "AFM nanodissection reveals internal structural details of single collagen fibrils," *Nano letters*, vol. 4, no. 1, pp. 129–132, 2004.

[126] M. Firtel, G. Henderson, and I. Sokolov, "Nanosurgery: observation of peptidoglycan strands in Lactobacillus helveticus cell walls," *Ultramicroscopy*, vol. 101, no. 2-4, pp. 105–109, 2004.

[127] R. Afrin, U. Zohora, H. Uehara, T. Watanabe-Nakayama, and A. Ikai, "Atomic force microscopy for cellular level manipulation: imaging intracellular structures and DNA delivery through a membrane hole," *Journal of Molecular Recognition*, vol. 22, no. 5, pp. 363–372, 2009.

[128] H. Uehara, T. Osada, and A. Ikai, "Quantitative measurement of mRNA at different loci within an individual living cell," *Ultramicroscopy*, vol. 100, no. 3-4, pp. 197–201, 2004.

[129] R. Singhal, Z. Orynbayeva, R. Sundaram, J. Niu, S. Bhattacharyya, E. Vitol, M. Schrlau, E. Papazoglou, G. Friedman, and Y. Gogotsi, "Multifunctional carbon-nanotube cellular endoscopes," *Nature Nanotechnology*, vol. 6, no. 1, pp. 57–64, 2010.

[130] I. Obataya, C. Nakamura, S. Han, N. Nakamura, and J. Miyake, "Nanoscale operation of a living cell using an atomic force microscope with a nanoneedle," *Nano Lett*, vol. 5, no. 1, pp. 27–30, 2005.

[131] S. Han, C. Nakamura, I. Obataya, N. Nakamura, and J. Miyake, "Gene expression using an ultrathin needle enabling accurate displacement and low invasiveness," *Biochemical and biophysical research communications*, vol. 332, no. 3, pp. 633–639, 2005.

[132] I. Obataya, C. Nakamura, S. Han, N. Nakamura, and J. Miyake, "Direct insertion of proteins into a living cell using an atomic force microscope with a nanoneedle," *NanoBiotechnology*, vol. 1, no. 4, pp. 347–352, 2005.

[133] S. Han, C. Nakamura, I. Obataya, N. Nakamura, and J. Miyake, "A molecular delivery system by using AFM and nanoneedle," *Biosensors and Bioelectronics*, vol. 20, no. 10, pp. 2120–2125, 2005.

[134] I. Vakarelski, S. Brown, K. Higashitani, and B. Moudgil, "Penetration of living cell membranes with fortified carbon nanotube tips," *Langmuir*, vol. 23, no. 22, pp. 10893–10896, 2007.

[135] A. Patil, J. Sippel, G. Martin, and A. Rinzler, "Enhanced functionality of nanotube atomic force microscopy tips by polymer coating," *Nano Letters*, vol. 4, no. 2, pp. 303–308, 2004.

[136] J. Small and M. Gimona, "The cytoskeleton of the vertebrate smooth muscle cell," *Acta Physiologica Scandinavica*, vol. 164, no. 4, pp. 341–348, 1998.

[137] S. Patel, J. Hartwig, and J. Italiano Jr, "The biogenesis of platelets from megakaryocyte proplatelets," *Journal of Clinical Investigation*, vol. 115, no. 12, pp. 3348–3354, 2005.

[138] J. Italiano, P. Lecine, R. Shivdasani, and J. Hartwig, "Blood platelets are assembled principally at the ends of proplatelet processes produced by differentiated megakaryocytes," *The Journal of cell biology*, vol. 147, no. 6, p. 1299, 1999.

[139] A. Kalinin, A. Kajava, and P. Steinert, "Epithelial barrier function: assembly and structural features of the cornified cell envelope," *Bioessays*, vol. 24, no. 9, pp. 789–800, 2002.

[140] P. Koch and D. Roop, *Skin Barrier*, ch. 8, pp. 97–110. 2006.

[141] D. Swartzendruber, P. Wertz, K. Madison, and D. Downing, "Evidence that the corneocyte has a chemically bound lipid envelope," *Journal of Investigative Dermatology*, vol. 88, no. 6, pp. 709–713, 1987.

[142] P. Elias, "Epidermal lipids, barrier function, and desquamation," *Journal of Investigative Dermatology*, vol. 80, pp. 44S–49S, 1983.

[143] H. Pinkus, "Examination of the Epidermis by the Strip Method of Removing Horny Layers," *Journal of Investigative Dermatology*, vol. 16, pp. 383–386, 1951.

[144] Y. Kalia, F. Pirot, and R. Guy, "Homogeneous transport in a heterogeneous membrane: water diffusion across human stratum corneum in vivo," *Biophysical journal*, vol. 71, no. 5, pp. 2692–2700, 1996.

[145] Y. Kalia, I. Alberti, N. Sekkat, C. Curdy, A. Naik, and R. Guy, "Normalization of stratum corneum barrier function and transepidermal water loss in vivo," *Pharmaceutical research*, vol. 17, no. 9, pp. 1148–1150, 2000.

[146] J. Sader, "Frequency response of cantilever beams immersed in viscous fluids with applications to the atomic force microscope," *Journal of applied physics*, vol. 84, p. 64, 1998.

[147] J. Sader, J. Chon, and P. Mulvaney, "Calibration of rectangular atomic force microscope cantilevers," *Review of Scientific Instruments*, vol. 70, p. 3967, 1999.

[148] Digital Instruments Veeco Metrology Group, *MultiMode SPM Instruction Manual Version 4.31ce.* 1997.

[149] G. Möllenstedt, "Die entstehung einer vielzahl von konatminationsfäden unter der elektron-mikrosonde," *Optik*, vol. 78, pp. 132–143, 1988.

[150] Z. Liu, K. Mitsuishi, and K. Furuya, "Features of self-supporting tungsten nanowire deposited with high-energy electrons," *Journal of Applied Physics*, vol. 96, p. 619, 2004.

[151] K. Kanaya and H. Kawakatsu, "Secondary electron emission due to primary and backscattered electrons," *Journal of Physics D: Applied Physics*, vol. 5, p. 1727, 1972.

[152] M. Dapor, "Monte Carlo simulation of backscattered electrons and energy from thick targets and surface films," *Physical Review B*, vol. 46, no. 2, pp. 618–625, 1992.

[153] T. Ooi, K. Matsumoto, M. Nakao, M. Otsubo, S. Shirakata, S. Tanaka, and Y. Hatamura, "3D nano wire-frame for handling and observing a single DNA fiber," in *Micro Electro Mechanical Systems, 2000. MEMS 2000. The Thirteenth Annual International Conference on*, pp. 580–583, IEEE, 2000.

[154] H. Dai, J. Hafner, A. Rinzler, D. Colbert, and R. Smalley, "Nanotubes as nanoprobes in scanning probe microscopy," *Nature*, vol. 384, pp. 147–150, 1996.

[155] J. Hafner, C. Cheung, A. Woolley, and C. Lieber, "Structural and functional imaging with carbon nanotube AFM probes," *Progress in Biophysics and Molecular Biology*, vol. 77, no. 1, pp. 73–110, 2001.

[156] S. Timoshenko, *Vibration problems in engineering.* Wolfenden Pr, 2008.

[157] S. Akita, Y. Nakayama, S. Mizooka, Y. Takano, T. Okawa, Y. Miyatake, S. Yamanaka, M. Tsuji, and T. Nosaka, "Nanotweezers consisting of carbon nanotubes operating in an atomic force microscope," *Applied Physics Letters*, vol. 79, p. 1691, 2001.

[158] P. Kim and C. Lieber, "Nanotube nanotweezers," *Science*, vol. 286, no. 5447, p. 2148, 1999.

[159] P. Bøggild, T. Hansen, C. Tanasa, and F. Grey, "Fabrication and actuation of customized nanotweezers with a 25 nm gap," *Nanotechnology*, vol. 12, p. 331, 2001.

[160] Q. Ye, A. Cassell, H. Liu, K. Chao, J. Han, and M. Meyyappan, "Large-scale fabrication of carbon nanotube probe tips for atomic force microscopy critical dimension imaging applications," *Nano letters*, vol. 4, no. 7, pp. 1301–1308, 2004.

[161] E. Yenilmez, Q. Wang, R. Chen, D. Wang, and H. Dai, "Wafer scale production of carbon nanotube scanning probe tips for atomic force microscopy," *Applied Physics Letters*, vol. 80, p. 2225, 2002.

[162] J. Vesenka, S. Manne, R. Giberson, T. Marsh, and E. Henderson, "Colloidal gold particles as an incompressible atomic force microscope imaging standard for assessing the compressibility of biomolecules," *Biophysical journal*, vol. 65, no. 3, pp. 992–997, 1993.

[163] S. Timoshenko and J. Gere in *Theory of elastic stability*, pp. 46–70, McGraw-Hill, New York, 2nd ed., 1961.

[164] R. Miller and V. Shenoy, "Size-dependent elastic properties of nanosized structural elements," *Nanotechnology*, vol. 11, p. 139, 2000.

[165] X. Li, T. Ono, Y. Wang, and M. Esashi, "Ultrathin single-crystalline-silicon cantilever resonators: fabrication technology and significant specimen size effect on Young's modulus," *Applied Physics Letters*, vol. 83, p. 3081, 2003.

[166] Q. Jin, T. Li, P. Zhou, and Y. Wang, "Mechanical researches on Young's modulus of SCS nanostructures," *Journal of Nanomaterials*, vol. 2009, pp. 1–6, 2009.

[167] S. Liang, A. Yajima, S. Abe, Y. Mera, and K. Maeda, "Evolution kinetics of sp_2 ordering in tetrahedral amorphous carbon films induced by electron irradiation," *Surface Science*, vol. 593, no. 1-3, pp. 161–167, 2005.

[168] M. Ishida, J. Fujita, and Y. Ochiai, "Density estimation for amorphous carbon nanopillars grown by focused ion beam assisted chemical vapor deposition," *Journal of Vacuum Science & Technology B: Microelectronics and Nanometer Structures*, vol. 20, p. 2784, 2002.

[169] Y. Shibutani and T. Yoshioka, "Inelastic deformability of nanopillar by focused-ion-beam chemical vapor deposition," *Journal of Vacuum Science & Technology B: Microelectronics and Nanometer Structures*, vol. 26, p. 201, 2008.

[170] T. Thundat, E. Wachter, S. Sharp, and R. Warmack, "Detection of mercury vapor using resonating microcantilevers," *Applied Physics Letters*, vol. 66, p. 1695, 1995.

[171] C. Ziegler, "Cantilever-based biosensors," *Analytical and bioanalytical chemistry*, vol. 379, no. 7, pp. 946–959, 2004.

[172] N. Lavrik, M. Sepaniak, and P. Datskos, "Cantilever transducers as a platform for chemical and biological sensors," *Review of Scientific Instruments*, vol. 75, p. 2229, 2004.

[173] J. Gere and S. Timoshenko, *Mechanics of Materials*. Stanley Thornes, 4th ed., 1999.

[174] C. Truesdell, *The Rational Mechanics of Flexible or Elastic Bodies*. Orell Fussli, 1960.

[175] C. Truesdell, "The influence of elasticity on analysis: The classic heritage," *B. Am. Math. Soc.*, vol. 9, pp. 293–310, 1983.

[176] D. Sarid, *Scanning Force Microscopy: with Applications to Electric, Magnetic, and Atomic Forces*. Oxford University Press, 1991.

[177] E. Wong, P. Sheehan, and C. Lieber, "Nanobeam mechanics: elasticity, strength, and toughness of nanorods and nanotubes," *Science*, vol. 277, no. 5334, p. 1971, 1997.

[178] G. Singh, P. Rice, and R. Mahajan, "Fabrication and mechanical characterization of a force sensor based on an individual carbon nanotube," *Nanotechnology*, vol. 18, p. 475501, 2007.

[179] L. Niu, X. Chen, S. Allen, and S. Tendler, "Using the bending beam model to estimate the elasticity of diphenylalanine nanotubes," *Langmuir*, vol. 23, no. 14, pp. 7443–7446, 2007.

[180] K. Bisshop and D. Drucker, "Large deflection of cantilever beams," *Q. Appl. Math.*, vol. 3, pp. 272–275, 1945.

[181] T. Belendez, C. Neipp, and A. Belendez, "Large and small deflections of a cantilever beam," *Eur. J. Phys.*, vol. 23, pp. 371–379, 2002.

[182] W. Ding, Z. Guo, and R. Ruoff, "Effect of cantilever nonlinearity in nanoscale tensile testing," *Journal of Applied Physics*, vol. 101, p. 034316, 2007.

[183] F. Marques, R. Lacerda, A. Champi, V. Stolojan, D. Cox, and S. Silva, "Thermal expansion coefficient of hydrogenated amorphous carbon," *Applied Physics Letters*, vol. 83, p. 3099, 2003.

[184] N. Lavrik and P. Datskos, "Femtogram mass detection using photothermally actuated nanomechanical resonators," *Applied Physics Letters*, vol. 82, p. 2697, 2003.

[185] P. Poncharal, Z. Wang, D. Ugarte, and W. de Heer, "Electrostatic deflections and electromechanical resonances of carbon nanotubes," *Science*, vol. 283, no. 5407, p. 1513, 1999.

[186] M. Nishio, S. Sawaya, S. Akita, and Y. Nakayama, "Carbon nanotube oscillators toward zeptogram detection," *Applied Physics Letters*, vol. 86, no. 13, p. 133111, 2005.

[187] N. Kashibuchi, Y. Hirai, K. O'Goshi, and H. Tagami, "Three-dimensional analyses of individual corneocytes with atomic force microscope: morphological changes related to age, location and to the pathologic skin conditions," *Skin Research and Technology*, vol. 8, no. 4, pp. 203–211, 2002.

[188] C. Gorzelanny, T. Goerge, E. Schnaeker, K. Thomas, T. Luger, and S. Schneider, "Atomic force microscopy as an innovative tool for nanoanalysis of native stratum corneum," *Experimental dermatology*, vol. 15, no. 5, pp. 387–391, 2006.

[189] R. Gaikwad, S. Vasilyev, S. Datta, and I. Sokolov, "Atomic force microscopy characterization of corneocytes: effect of moisturizer on their topology, rigidity, and friction," *Skin Research and Technology*, vol. 16, no. 3, pp. 275–282, 2010.

[190] E.-Y. Kwon, Y.-T. Kim, and K. D-E, "Investigation of the penetration force of living cell using an atomic force microscope," *Journal of Mechanical Science and Technology*, vol. 23, pp. 1932–1938, 2009.

[191] D. Ebenstein and L. Pruitt, "Nanoindentation of biological materials," *Nano Today*, vol. 1, no. 3, pp. 26–33, 2006.

[192] L. Norlén and A. Al-Amoudi, "Stratum corneum keratin structure, function, and formation: the cubic rod-packing and membrane templating model," *Journal of Investigative Dermatology*, vol. 123, no. 4, pp. 715–732, 2004.

[193] R. Bonser and P. Purslow, "The Young's modulus of feather keratin," *The Journal of experimental biology*, vol. 198, no. Pt 4, p. 1029, 1995.

[194] R. Tupker, C. Willis, E. Berardksca, C. Lee, M. Fartasch, T. Atinrat, and J. Serup, "Guidelines on sodium lauryl sulfate (SLS) exposure tests," *Contact Dermatitis*, vol. 37, no. 2, pp. 53–69, 1997.

[195] C. Willis, C. Stephens, and J. Wilkinson, "Epidermal damage induced by irritants in man: a light and electron microscopic study," *Journal of Investigative Dermatology*, vol. 93, no. 5, pp. 695–699, 1989.

[196] F. Putnam and H. Neurath, "Interaction between proteins and synthetic detergents," *Journal of Biological Chemistry*, vol. 159, no. 1, p. 195, 1945.

[197] R. Ward and C. Ashley, "pH modification of the effects of detergents on the stability of enteric viruses.," *Applied and Environmental Microbiology*, vol. 38, no. 2, p. 314, 1979.

[198] J. Bestman-Smith, J. Piret, A. Desormeaux, M. Tremblay, R. Omar, and M. Bergeron, "Sodium lauryl sulfate abrogates human immunodeficiency virus infectivity by affecting viral attachment," *Antimicrobial agents and chemotherapy*, vol. 45, no. 8, p. 2229, 2001.

[199] B. Alberts, A. Johnson, J. Lewis, M. Raff, K. Roberts, and P. Walter, *Molecular Biology of the Cell, Fourth Edition.* Garland Science, 2002.

[200] P. Tammaro, A. Smith, S. Hutchings, and S. Smirnov, "Pharmacological evidence for a key role of voltage-gated K+ channels in the function of rat aortic smooth muscle cells," *British journal of pharmacology*, vol. 143, no. 2, pp. 303–317, 2004.